

Additive and digital manufacturing of transient sensors and bioelectronics

Présentée le 10 novembre 2023

Faculté des sciences et techniques de l'ingénieur
Laboratoire des Microsystèmes Souples
Programme doctoral en microsystèmes et microélectronique

pour l'obtention du grade de Docteur ès Sciences

par

Nicolas Francis FUMEAUX

Acceptée sur proposition du jury

Prof. L. G. Villanueva Torrijo, président du jury
Dr D. Briand, directeur de thèse
Dr G. Nyström, rapporteur
Prof. I. Minev, rapporteur
Prof. J. Brugger, rapporteur

The essence of strategy is choosing what not to do.

— Michael Porter

Acknowledgements

First of all, I wish to particularly thank my supervisor Dr. Danick Briand for the valuable comments on the manuscript of the thesis and, of course, for the continued guidance and support in conducting the research presented here.

I would like to also express my deepest gratitude to the jury members of the private defense: Prof. Guillermo Villanueva from EPFL, Prof. Ivan Minev from TU Dresden, Dr. Gustav Nyström from EMPA and Prof. Jürgen Brugger from EPFL. I was honored to have you on the jury to review my scientific work and the thesis manuscript and thank you for the valuable comments and suggestions.

I would like to give special thanks to Dr. Peter van der Waal, whose infinite expertise in chemistry, kindness and availability helped countless people at Microcity, including me. I thank Dr. Matthieu Rüegg and Prof. Clémentine Boutry for their early help and guidance on this project as experts of bioresorbable electronics, as well as Maria Marcinek, Sophia Thiele and Sabrina Sant for introducing me to synthetic chemistry.

I thank all the students that I had the pleasure to supervise or co-supervise during my thesis and provided invaluable contributions and interesting discussions: Julien Hurni, Laurent Bertherin, David di Stadio, Mélissa Kossairi, Aurèle Schlegel, Marie Sanglé-Ferrière, Monika Stasytyte and Claudio Almeida Pinto. Special thanks go to Claudio, who is still making the lab a better place thanks to his work ethic and GIF-making abilities.

The LMTS was a wonderful environment to carry out a PhD thesis, full of supportive and knowledgeable people, always willing to help with a machine or a measurement or debate scientific and unscientific ideas. Many thanks to Prof. Herbert Shea for fostering this environment and to Myriam Poliero, who is not only very competent as the lab's administrative assistant but also always available for some moral support or just a fun chat. I want to thank each of the many talented scientists that were part of LMTS at one point or another and with whom I shared an office, a beer or a BBQ by the lake. I thank the little group of cryptocurrency aficionados, including Jean-Baptiste Chossat, Fabio Albuquerque as well as the skeptics such as Sylvain Schaller and Mehdi Benbedda for the interesting debates at coffee break. I would like to give the warmest thanks to the Green Team/Printing Crew for their friendship and advice during this thesis: James Bourely, Morgan Monroe, Silvia Demuru, Ryan van Dommelen, Alessio Mancinelli and Jaemin Kim.

Thanks to all the friends who showed unwavering support, for the dinners, drinks, hikes and adventures that help one keep a sane mind while doing a PhD: the Bisca/Schmadri gang, Hugo, Aileen, Paul, Ece, Clem, Niko and Isa, the Valais people, Christophe, Maxime, Quentin, Margaux, Kim and Adrien, who even if I see them after a long time I feel like we just talked last week, the Boston people, Maurice, Moret, Fadhel, Noaf, and the fantastic people of Lausanne, in particular Adele, Gianfranco, Valentina, Nicolas, Andrea, Dani, Selin and Fabien. Thanks to Tonino, Marina and Betta, my Italian family, for their warm welcome and infinite kindness.

Je remercie surtout ma famille, mes parents Jean-Yves et Geneviève qui m'ont soutenu à travers toutes mes études et sans qui je n'aurait certainement pas obtenu de doctorat, ainsi que mes fantastiques frères et sœur, Simon, Mathieu et Yasmina.

Last but not least, my deepest gratitude goes to Eleonora, my partner in crime, for her constant support, advice and for the adventures we went on together. Thank you for keeping me grounded in stressful times with your optimism and levelheadedness, and instilling joy, spontaneity and enthusiasm in my life. You make me a better person, and I could not have wished for a better teammate to share this PhD journey with.

Abstract

Transient electronics have emerged as a promising class of devices, capable of breaking down without harmful side effects to their environment. They have tremendous potential as bioresorbable electronics for temporary applications in the human body, and as disposable or biodegradable eco-friendly devices. However, transient materials are challenging to pattern, due to their sensitivity to heat, humidity and solvents. Additive manufacturing techniques can help solve this challenge, and allow for large-area fabrication of electronics on sensitive substrates with a reduced environmental footprint. Moreover, their adaptability enables the fast prototyping and customization of electronic devices. In this thesis, several advances in printed transient electronics are presented, leading to devices integrating sensing functions for biomechanical, environmental and biochemical monitoring.

Firstly, a novel two-step sintering process for screen-printed zinc is introduced. Combining electrochemical and photonic methods results in unprecedented conductivity ($5.6 \cdot 10^6$ S/m). The process is compatible with bioresorbable substrates such as polylactic acid (PLA) and polyvinyl alcohol (PVA). The degradation of zinc on PLA is studied, demonstrating exceptional electrical stability in air. Fully bioresorbable implantable pressure capacitive sensors are fabricated, using (poly(octamethylene maleate (anhydride) citrate); POMaC) as a soft dielectric. The integration of these sensors into a chipless wireless configuration as well as a power receiver is also demonstrated.

Next, we fabricate bioresorbable and ecoresorbable temperature sensors enabled by the zinc hybrid sintering process, respectively on PLA and paper. The influence of photonic sintering parameters on the temperature coefficient of resistance (TCR) is carefully studied to enhance the stability and linearity of sensor responses to temperature changes, leading to a TCR of 0.00316 $1/^\circ\text{C}$. The use of a degradable beeswax encapsulant offers protection against the interference of humidity allowing the sensors to operate reliably from -20°C to 40°C .

As a next study, we fabricate organic electrochemical transistors (OECTs) from degradable materials, fully by printing on a PLA substrate. Highly electrically conductive zinc interconnects are integrated with a water-resistant carbon-shellac composite as contacts and poly(3,4-ethylenedioxythiophene) polystyrene sulfonate (PEDOT:PSS) to form the channel of the transistor. The disposable OECTs are evaluated as biochemical sensors for ion and glucose detection, exhibiting sensitivity to ion concentration changes in the order of 10 %/dec and a limit of detection of 5 μM for glucose.

Lastly, we explore the 3D digital printing of customizable transient bioelectronics using direct ink writing. A meticulous process optimization enables the printing of 3D structures using UV-curable POMaC pre-polymer ink. Flexible conductive patterns made of carbon-shellac ink are embedded in POMaC constructs. We demonstrate fully 3D printed capacitive sensors capable of detecting pressures up to 1500 kPa and strain sensors that operate for axial deformations of up to 20% . Electrode arrays with impedance below 10 k Ω at 1 kHz offer potential applications in transient neuromuscular interfaces.

In conclusion, this research advances the additive manufacturing of transient electronics, opening new avenues for post-surgical monitoring, regeneration applications, and sustainable electronics.

Keywords: Bioresorbable electronics, green electronics, additive manufacturing, 3D printing, digital fabrication, sensors, biochemical sensing

Résumé

L'électronique transitoire est une nouvelle classe de dispositifs ayant la capacité de se dégrader sans effets nocifs sur leur environnement. Elle présente un potentiel considérable pour des applications temporaires dans le corps humain, ainsi que comme électronique jetables ou biodégradable. Cependant, les matériaux transitoires sont difficiles à structurer en raison de leur sensibilité à la chaleur, à l'humidité et aux solvants. Les techniques de fabrication additive peuvent aider à résoudre ce défi et permettent une fabrication plus durable, à grande échelle et sur des substrats sensibles. De plus, ces méthodes permettent un prototypage rapide et une personnalisation des dispositifs électroniques. Dans cette thèse, plusieurs avancées dans le domaine de l'électronique dégradée imprimées sont présentées, aboutissant à des capteurs biomécaniques, environnementaux et biochimiques.

Tout d'abord, une méthode de recuit pour le zinc imprimé en sérigraphie est introduite. La combinaison de mécanismes électrochimiques et photoniques conduit à une conductivité sans précédent ($5.6 \cdot 10^6$ S/m). Le processus est compatible avec des substrats biorésorbables tels que l'acide polylactique (PLA) et l'alcool polyvinylique (PVA). La dégradation du zinc est étudiée, démontrant une stabilité électrique exceptionnelle dans l'air. Des capteurs capacitifs de pression entièrement biorésorbables sont fabriqués, utilisant le poly(octaméthylène maléate (anhydride) citrate) (POMaC) comme diélectrique souple. L'intégration de ces capteurs dans une configuration sans fil est également démontrée.

Ensuite, nous présentons des capteurs de température biorésorbables et écoresorbables, fabriqués respectivement sur du PLA et du papier. L'influence des paramètres du recuit photonique du zinc sur le coefficient de température de résistance (TCR) est soigneusement étudiée, aboutissant à un TCR de 0.00316 $1/^\circ\text{C}$. L'utilisation d'un encapsulant en cire d'abeille biodégradable offre une protection contre l'humidité, permettant aux capteurs de fonctionner de manière fiable de -20°C à 40°C .

Dans une autre étude, nous réalisons des transistors organiques électrochimiques (OECT) à partir de matériaux dégradables, par impression sur du PLA. Le zinc est intégré avec un composite carbone-shellac résistant à l'eau en tant que contacts et du poly(3,4-éthylènedioxythiophène) polystyrène sulfonate (PEDOT:PSS) pour former le canal du transistor. Les OECT jetables sont évalués en tant que capteurs biochimiques pour la détection d'ions et de glucose, montrant une sensibilité à la concentration ionique de 10 %/décade et une limite de détection de $5 \mu\text{M}$ pour le glucose.

Enfin, nous explorons l'impression 3D numérique de dispositifs dégradables personnalisables en utilisant une technique d'écriture directe et digitale. Une optimisation méticuleuse permet l'impression de structures 3D à l'aide d'une encre de POMaC. Des motifs conducteurs flexibles en encre de carbone sont intégrés dans le POMaC. Nous démontrons des capteurs de pression capables de détecter jusqu'à 1500 kPa, et des capteurs de déformation pouvant fonctionner jusqu'à 20%. Des réseaux d'électrodes avec une impédance inférieure à 10 k Ω à 1 kHz offrent des possibilités dans les interfaces neuromusculaires transitoires.

En conclusion, cette recherche présente la fabrication additive de capteurs dégradables, ouvrant de nouvelles perspectives pour les mesures post-opératoires, les applications de régénération et l'électronique durable.

Mots-clés: Électronique biorésorbable, électronique écologique, fabrication additive, impression 3D, fabrication numérique, capteurs, détection biochimique

Contents

Acknowledgements	ii
Abstract	iv
Résumé	v
List of Figures	viii
List of Tables	xi
Chapter 1	Introduction 13
1.1	Background and motivation..... 13
1.2	Thesis objectives and contributions 14
1.3	Thesis outline 15
Chapter 2	State of the art..... 18
2.1	Materials for transient electronics 18
2.1.1	Substrate and dielectric materials..... 19
2.1.2	Conductive and semiconductor materials..... 21
2.2	Bioresorbable devices and systems 22
2.3	Additive manufacturing for bioresorbable electronics 25
2.3.1	Ink formulation and printing methods..... 25
2.3.2	Printed bioresorbable electronics 28
2.4	Summary and contributions 31
2.4.1	Status of the research on printed bioresorbable electronics 31
2.4.2	Research approach and contributions 32
Chapter 3	Zinc hybrid sintering for printed transient sensors and wireless electronics 34
3.1	Introduction..... 35
3.2	Results and discussion 36
3.2.1	Hybrid sintering of printed zinc films 36
3.2.2	Optimization of sintering parameters 37
3.2.3	Flexibility and stability of fully degradable zinc traces 40
3.2.4	Resistive and capacitive wireless transient sensors..... 42
3.3	Conclusions..... 44
3.4	Experimental section..... 45
3.5	Supporting information 47
Chapter 4	Printed ecoresorbable temperature sensors for environmental monitoring..... 55
4.1	Introduction..... 56

4.2	Material and methods.....	57
4.2.1	Fabrication	57
4.2.2	Samples characterization	58
4.3	Results and Discussion.....	59
4.3.1	Influence of flash annealing parameters on temperature behavior	59
4.3.2	Influence of ambient humidity on the temperature sensors	62
4.4	Conclusions.....	63
4.5	Supporting information	64
Chapter 5	Organic electrochemical transistors printed from degradable materials as disposable biochemical sensors	67
5.1	Introduction.....	68
5.2	Results and discussion	69
5.2.1	OECTs design and materials.....	69
5.2.2	Influence of gate material and geometry	70
5.2.3	Integration on a biodegradable substrate	72
5.2.4	Cation sensing experiments	74
5.2.5	Glucose detection and integration with degradable circuits	75
5.3	Conclusions.....	77
5.4	Experimental section.....	78
5.5	Supporting information	79
Chapter 6	Digital manufacturing of customizable 3D bioresorbable electronics	83
6.1	Introduction.....	84
6.2	Results and Discussion.....	85
6.2.1	Approach and materials.....	85
6.2.2	Synthesis and printing of POMaC pre-polymer	86
6.2.3	Integration of conductive carbon-based ink.....	90
6.2.4	Fabrication and characterization of 3D printed transient devices.....	90
6.3	Conclusions.....	93
6.4	Experimental Section	93
6.5	Supporting information	95
Chapter 7	Conclusion	99
7.1	Summary and conclusion.....	99
7.2	Outlook.....	101
References	103	
Curriculum Vitae	120	

List of Figures

Figure 1.1: Digital manufacturing of bioresorbable implants with customizable form and function.....	14
Figure 2.1: Mechanisms of degradation and bioresorption of various types of materials that have been used for implantable transient bioelectronics.	19
Figure 2.2: Examples of bioresorbable implantable electronics, where the main method used for fabrication is clean-room processes (a-c), shadow-mask evaporation (d-f), lamination of films and foils (g-i).....	24
Figure 2.3: Examples of printed biosensors and bioelectronics. (a) Screen-printed strain sensor for cardiovascular monitoring.	27
Figure 2.4: Examples of printed bioresorbable conductors and devices.	29
Figure 3.1: Description of the hybrid zinc sintering process.	37
Figure 3.2: Study of the sintering process on screen-printed zinc layers.	38
Figure 3.3: Hybrid sintering of Zn and durability of the traces on transient substrates.....	40
Figure 3.4: Transient resistive physical sensors fabricated from printed Zn encapsulated in PLA ($R_0 = 89.6 \pm 56.4 \Omega$, $n = 4$).	42
Figure 3.5: Bioresorbable capacitive sensors based on zinc hybrid sintering and soft elastomer POMaC.....	43
Figure S3.1: Electrical conductivity of lines treated by electrochemical acetic acid sintering as a function of the weight of PVP per weight of Zinc in the solution.	47
Figure S3.2: Pulses delivered by the PulseForge 1200 photonic sintering lamp as a function of lamp voltage, given as irradiance during the pulse delivery time.	47
Figure S3.3: Electrical conductivity of the hybrid sintered Zn traces from this work compared to the conductivity of bulk zinc and to examples from the literature for printed zinc using different sintering methods.	48
Figure S3.4: Study on profile geometry and microstructure for sintered screen-printed traces.....	48
Figure S3.5: Peel test according to ASTM F1842-15 on polyimide, paper and polylactic acid substrates.....	49
Figure S3.6: Optimization of the hybrid sintering process for paper substrates.	49
Figure S3.7: Proposed mechanism for the longer durability of photonic sintered Zn in air. The enhanced particle cohesion obtained with hybrid sintering decreases the impact of the zinc reoxidation on the electrical conductivity.	50
Figure S3.8: Relative change of resistance for Zn lines on PLA after hybrid sintering in air over a period of 31 days, with and without encapsulation.	50
Figure S3.9: Bending of a printed and encapsulated Zn resistor on PLA (50 × 0.5 mm) at different bending radii. All scale bars are 20 mm.	51
Figure S3.10: Temperature behavior of Zn lines as a function of the sintering process. .	51
Figure S3.11: ¹ H-NMR for the synthesized POMaC pre-polymer. ¹ H NMR spectra were recorded on a Bruker AVANCE-400 Ultra Shield instrument at room temperature using	

(CD ₃) ₂ SO as solvent. ¹ H NMR chemical shifts are reported relative to the residual proton signal of the solvent.....	52
Figure S3.12: Real-time data processing for the S ₁₁ data of pressure-sensitive wireless circuits.	52
Figure S3.13: Peak-to-peak recorded voltage at the secondary coil (degradable power receiver) as a function of the distance to the primary coil.....	53
Figure 4.1: Fabrication process of the biodegradable RTD.	57
Figure 4.2: Influence of the flash energy and number of pulses on the linearity and repeatability of the temperature response of zinc resistors (n = 3).....	59
Figure 4.3 Dynamic behavior of the temperature sensors.	61
Figure 4.4: Effect of beeswax encapsulation on the interference of humidity.....	62
Figure 4.5: Temperature sensing at different humidity levels.	63
Figure S4.1: Measurement setup and data extraction for the assessment of the degradable RTDs.	64
Figure S4.2: SEM images of the zinc layer after different photonic treatments: only electrochemical sintering by application of acetic acid (left), 1 light pulse of 5.8 J/cm ² (middle) and 3 light pulses of 6.6 J/cm ² (right).....	64
Figure S4.3: Relative change in resistance with respect to change in temperature for different sintering parameters, at room temperature, 40 and 60°C (n = 3).....	65
Figure S4.4: Relative change of resistance for temperatures below room temperature. Sensor response (blue) and reference temperature (orange), when cooling the sensor down to 0 °C (a) and -20°C (b).....	65
Figure S4.5: Relative change of resistance (top graphs) when varying ambient humidity from 30 to 70 %rH (bottom graphs), for Zn resistors printed on polyimide and without encapsulation, with an ambient temperature of: a) 20 °C and b) 40 °C (n = 3).	65
Figure 5.1: Design and fabrication of the degradable OECTs.	70
Figure 5.2: Influence of the gate material and dimensions on the behavior of the transistors.	72
Figure 5.3: Surface modification of PLA to enable to fabrication of fully degradable OECTs.	73
Figure 5.4: Characterization of the OECTs for ion concentrations measurements.	74
Figure 5.5: Characterization of the OECTs for the enzymatic detection of glucose.	76
Figure 5.6: Integration of the OECTs with zinc metal traces.....	77
Figure S5.1: Capacitance of the PEDOT:PSS and carbon gates measured in phosphate-buffered saline.....	79
Figure S5.2: Delamination (pointed out by the arrow) of PEDOT:PSS channel and gate in PBS solution, when inkjet printed on a polylactic acid film.	79
Figure S5.3: Influence of oxygen plasma treatment on a polyimide film on the contact angle of a water droplet, with 40W, 40 kHz oxygen plasma treatments with variable time.	80
Figure S5.4: Output characteristics of the OECTs (PEDOT:PSS-gated) for different modifications to the fabrication process (with the standard process as a control experiment	

on the left): changing the curing of the PEDOT:PSS layer to 80 °C for 3 hours (middle) and introducing Zn contacts using the same PEDOT curing protocol (right)..... 80

Figure S5.5: Transfer characteristics of the OECTs on PLA after cycling transfer measurements for one hour. 80

Figure S5.6: Calibration curves for the OECTs for use in ion detection applications, for PEDOT:PSS-gated ((a) and (b)) and carbon-gated ((c) and (d)) devices. 81

Figure S5.7: Response dynamics and stability of the devices..... 82

Figure 6.1: Additive manufacturing of customizable transient electronics. 85

Figure 6.2: Optimization of POMaC patterning by direct ink writing. 88

Figure 6.3: 3D direct ink writing of POMaC polymer..... 89

Figure 6.4: Integration of carbon conductors with POMaC. 90

Figure 6.5: Mechanical sensors printed by DIW. 91

Figure 6.6: Transient printed electrode array and materials degradation study. 92

Figure S6.1: Lines of printed POMaC with the same parameters as in Figure 6.2(b) (printing speeds from 10 to 50 mm/s (from bottom to top), for a pressure of 60 psi and a dispense gap of 60 μm) when curing is delayed by 30 minutes..... 95

Figure S6.2: POMaC squares printed with increasing number of layers. 95

Figure S6.3: 3D design of the POMaC pyramid array, with each pyramid having a 2 x 2 mm base and a height of 2 mm (left). Side view of the pyramids compared to a confocal laser microscope scan of the printed POMaC pyramids, in yellow (right). 96

Figure S6.4: Mechanical properties of the POMaC (Young’s modulus, failure stress and failure strain) as a function of the esterification time..... 96

Figure S6.5: Influence of the printing parameters (printing speed and dispense gap) on the shape of printed carbon-shellac lines, for a fixed pressure of 10 psi..... 97

Figure S6.6: SEM image of carbon-shellac conductive ink embedded in POMaC polymer. 97

Figure S6.7: Linear sweep voltammetry measurement of a carbon electrode in PBS with potential difference with Ag/AgCl reference between -2 and 2 V. 98

List of Tables

Table 2.1: Bioresorbable substrate materials and their relevant characteristics.	20
Table 2.2: Transient metals with their relevant degradation characteristics, tolerance in the human body and most common deposition methods used.....	21
Table 2.3: Printing methods mentioned in this review with their figures of merit, numbers from [15,16,161,173,174].	26
Table 2.4: Conductive pastes based on transient metals, with the particle size as well as the printing and sintering methods used, and the conductivities obtained.	30

Chapter 1 Introduction

1.1 Background and motivation

Transient electronics refer to devices and components that break down into their constituent parts in a given environment, after a short and controlled lifetime, without any harmful effects on that environment. This concept has emerged, principally in the last 10 years, in the biomedical field. Temporary bioelectronics with monitoring, stimulation or actuation capabilities can be implanted and fulfill their function for a controlled period of time and then resorb in the body through endogenous or exogenous triggers [1–3]. This concept has generated interest thanks to the potential to circumvent the need for re-operation [4], therefore potentially reducing the risk for the patient while allowing for unprecedented functionality, for instance in the context of post-operative monitoring. Moreover, the degradability of the implant could facilitate integration in the body, reducing short- and long-term foreign body response [5], the inflammatory reaction of the body to the introduction of a foreign material. More recently, the concept of transient electronics has attracted attention in response to the growing challenge of electronic waste. Indeed, 53.5 megatons of electrical and electronic equipment is discarded each year, representing the fastest growing stream of waste, and less than 20 % of it is recycled [6]. This comes with dire consequences on the environment and the health of the communities that are exposed to the unrecycled waste [7]. These components are largely based on materials such as fiberglass, fossil-based plastics and rare metals, with environmental degradation times of several decades or more [8]. Efforts have been undertaken to render the fabrication of some electronic devices by using more sustainable manufacturing techniques such as printing, which is an additive fabrication process [9]. More recently, there has been a notable focus in replacing these materials with environmentally benign or degradable alternatives, in particular for applications where a short lifecycle is acceptable or even desirable.

The concept of transient implants originates with absorbable sutures [5], that have been made from biomaterials (e.g. catgut, wound animal intestine) or synthetic polymers such as polyvinyl alcohol or polyglycolic acid [10]. In more recent years, various resorbable structural implants have been proposed, such as orthopedic screws and attachments [11] as well as stents [12], which were developed with the aim to prevent vessel remodeling and late-stage thrombosis. Moreover, bioresorbable materials have been incorporated in non-transient implants for mechanical support, for instance to facilitate the manipulation of extremely thin brain implants [13], or to permit the insertion in the brain of a neural probe through the dura without buckling [14]. However, the fabrication of functional electrical devices fully with bioresorbable materials poses a radical challenge. Indeed, the reactivity of these materials and their instability under certain process conditions (solvents, humidity, temperature, light, etc.) renders their manufacturing into complex devices difficult. This is particularly true for MEMS (microelectromechanical systems) fabrication methods, which, while having revolutionized the field of bioelectronics [4], rely on the use of photolithography for the patterning of functional electronics. Several methods and workarounds have been proposed to address this challenge, which are detailed in Chapter 2. Among these methods, additive manufacturing presents several advantages which are of interest for the fabrication of transient electronics. Additive manufacturing refers to fabrication methods that consist in the addition of material to attain the desired shape and function. Typically, the addition of material is performed in a layer-by-layer fashion in order to create thin film devices or 3D structures. Additive manufacturing presents the following advantages [2,15]:

- Only the necessary amount of material is deposited, thereby participating in reducing costs and leading to more sustainable fabrication;
- By avoiding subtractive fabrication methods such as etching, it allows to considerably reduce the use of solvents and higher temperatures;
- 2D & 3D digital additive manufacturing enables straightforward customization of bioelectronics and implantable systems based on *in silico* optimization performed in a patient-specific way. This customization process is illustrated in **Figure 1.1**.

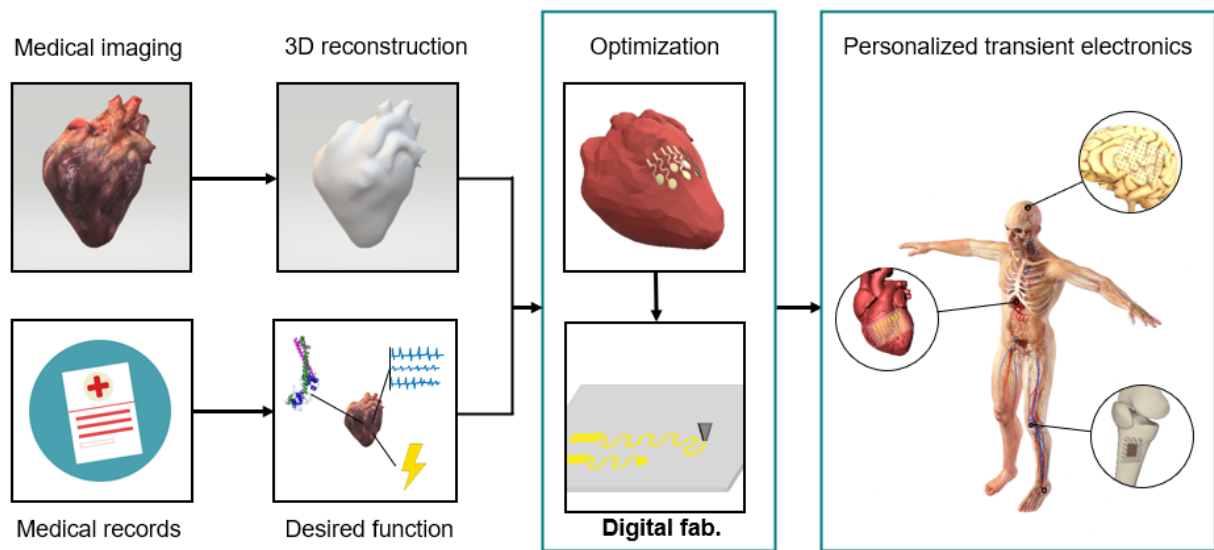


Figure 1.1: Digital manufacturing of bioresorbable implants with customizable form and function.

Despite these advantages, the fabrication of transient implants and electronics using additive manufacturing remains sparsely investigated. Indeed, digital additive fabrication of transient implants requires the joint optimization of the materials, inks, layer deposition, post-processing methods and device architecture. Structural and functional material inks must be developed while ensuring the compatibility between the materials and solvents as well as the potential treatment that is applied to the printed inks. As such, fully 3D printed transient bioelectronics have not yet been proposed. For this aim to be achieved, the following challenges must be addressed:

- **Materials stability:** The materials that can degrade within the human body without generating harmful byproducts in a reasonable amount of time are in general, by definition, more sensitive to environmental and process conditions which may cause a degradation of the materials properties during processing and operation.
- **Ink formulations:** While commercial inks are available for various 3D printable structural and conductive materials [16], transient polymeric and metallic inks remain challenging to formulate in a stable manner [17]. Moreover, the rheology of the ink must be adapted to the chosen printing technique. Finally, the choice of the ink solvent is important, as it must be compatible with the layer the ink is printed on and have sufficient wetting.
- **Layer printing:** As transient materials represent a new frontier in additive manufacturing, their printing behavior is mostly unknown and must be characterized. Due to the limited choice of transient materials, printability may be a challenge.
- **Layer treatments:** The printed layers may require heat or light curing/annealing. The post-treatments of the layers must be appropriately optimized or developed and studied, as the treatment is paramount for achieving printed layers with the desired properties, and their treatment may affect the properties of the underlying materials.

1.2 Thesis objectives and contributions

The overarching objective of this thesis is the study and development of methods for the additive manufacturing of transient materials for the realization of bioresorbable electronics, embedding sensing features. The translation of these technological developments and results to ecoresorbable sensing devices was also addressed. Methodologies for the reliable printing of transient electronics with a controlled lifetime are currently limited, and we sought to establish and optimize methods that allow this to be achieved. Studies are needed to better understand the current material and process limitations regarding printed transient electronics and overcome

them. The bioresorbable electronics that are produced as an outcome are to be characterized in terms of their sensing behavior and functional lifetime. By achieving multi-material 3D printing of structural and electrically conductive degradable materials, the fields of additive manufacturing and transient electronics can be advanced, leading to the facile fabrication of customizable transient electronic implants. In order to tackle this challenge, several sub-objectives for this thesis were explored and are outlined below, separated into two sections pertaining to processes investigation and devices development.

To tackle these objectives, several investigations were conducted. This includes the development of printing inks and study of processing/curing methods that are compatible with degradable materials and temperature sensitive substrates. Furthermore, with these methods established, devices were fabricated and characterized, to ensure the appropriateness of the fabrication methods for the creation of functional sensors with different sensing modalities and functional lifetimes. Physical sensors based on resistive and capacitive mechanisms as well as organic electrochemical sensors for biochemical sensing were fabricated and characterized. The degradation kinetics and the deterioration of the devices and materials' performance were studied in relevant test environments. Finally, the advancements mentioned previously were integrated together for the 3D printing of transient bioelectronics and sensors that advantageously leverage the possibilities of digital additive manufacturing. The outcomes of these investigations are summarized in several submitted or accepted publications, which are presented in the next section and will form the structure of this thesis.

1.3 Thesis outline

Following the current chapter that serves as Introduction, the thesis is organized in the following way:

Chapter 2: This chapter aims to cover the state-of-the-art of transient electronics, with a focus on bioresorbable electronics. A perspective is provided for the application of additive manufacturing for transient electronics. The main discoveries and achievements from the published literature are summarized, and the challenges for the advancement of the domain are presented. It concludes with an outline of the contributions to the field of transient electronics that are presented in this thesis.

Chapter 3: This chapter reports on the development and use of a screen printable high conductivity zinc-based ink for the realization of transient sensors, interconnects and antennas. In order to circumvent the need for high annealing temperatures for the zinc layer, which are incompatible with low-temperature degradable substrates, a two-step annealing process combining electrochemical and photonic sintering is developed and studied. The first step is based on the use of acetic acid to trigger an electrochemical sintering of zinc, involving the reduction of the zinc hydroxide/oxide layer, and self exchange of zinc ions at the particles interface. This process relies on the open circuit voltage of zinc in acetic acid being at levels where the passivation layer can be reduced and Zn deposition can occur, as presented previously [18]. The second step relies on photonic delivery of energy in the form of intense pulsed light with a xenon lamp. We demonstrate that the reduction of the native oxide on the zinc microparticles is crucial to facilitate photonic sintering, allowing to reach the highest conductivity in the state of the art for printed transient metal ($>5 \cdot 10^6$ S/m). The process is compatible with bioresorbable substrates with a limited thermal budget and with the integration of multiple solution-processible materials. The flexibility of the transient devices is characterized down to a radius of 2 mm and under cycling conditions. The resistive transducers are tested as temperature and strain sensors. We demonstrate bioresorbable capacitive wireless force sensors based on printed zinc on PLA and utilizing a soft polymer, poly(octamethylene maleate (anhydride) citrate) (POMaC) as dielectric layer. The sensors are implemented in chip-less configuration on a small footprint by taking advantage of the high conductivity of the zinc. The zinc-based electronics on a transient polymeric substrate (PLA) are assessed in terms of functional lifetime in phosphate-buffered saline at 37 °C over one month.

Paper 1: This chapter is based on the following article: [N. Fumeaux](#) and D. Briand, "Zinc hybrid sintering for printed transient sensors and wireless electronics," *npj Flex. Electron.*, vol. 7, no. 1, p. 14, Mar. 2023, doi: 10.1038/s41528-023-00249-0.

Contribution: As main author, I contributed to all the aspects of this work. This includes the original idea of hybrid sintering to improve the properties of printed zinc, studying and optimizing the process, designing and fabricating the devices, performing the sensing and degradation experiments, analyzing the data and writing the manuscript.

Chapter 4: This chapter is dedicated to further investigating the properties of the printed zinc presented in the previous chapter to develop resistive temperature detectors (RTDs) for environmental monitoring. The influence of the sintering process parameters, in particular the light pulse energy and count, is studied to maximize the linearity and temperature coefficient of printed zinc resistors on paper. The ecoresorbable zinc resistors on paper reach a TCR of 3160 ppm/K (80% of that of bulk zinc) and a highly linear temperature response is obtained ($r^2 > 0.99$). The relative sensitivity of the zinc RTDs is lower than that of biodegradable sensors based on carbonized silk or porous carbon [19,20], but higher than that of magnesium-based transient RTDs [21]. A biodegradable beeswax encapsulation is applied to the paper and zinc sensors by dip-coating, in order to extend the lifetime of the sensors and offer protection against the interference of ambient humidity. The resistance temperature detectors are shown to operate accurately for temperatures ranging from -20 to 40 °C at relative humidity between 30 and 70 %RH.

Paper II: This chapter is based on the following article: [N. Fumeaux](#), M. Kossairi, J. Bourely, and D. Briand, "Printed ecoresorbable temperature sensors for environmental monitoring," *Micro and Nano Engineering*, vol. 20, p. 100218, Sep. 2023, doi: 10.1016/j.mne.2023.100218.

Contribution: As main author, I contributed to all the aspects of this work. This includes designing the experiments to study the influence of sintering parameters on the TCR, fabricating and characterizing the temperature sensors, implementing and evaluating the beeswax coating and writing the manuscript.

Chapter 5: This chapter focuses on the development of biochemical sensors made of biocompatible, degradable and environmentally benign materials. The developments in terms of solution-processible substrate and conductive materials presented in the last chapters are built upon for the development of degradable organic electrochemical transistors based on poly(3,4-ethylenedioxythiophene) polystyrene sulfonate (PEDOT:PSS) printed on an eco- and bioresorbable polylactic acid substrate. Due to the oxide layer of the printed zinc and the PEDOT:PSS forming a Schottky barrier, a carbon-shellac ink is used to create an interface. The fabrication and design of the OECTs is optimized as a function of the gate dimensions and material, and the adhesion of the PEDOT:PSS channel to the substrate is ensured thanks to a silanization process. We characterize the electrical behavior of the transistors and their usability for the detection of ions and glucose, and their degradation in soil is demonstrated. The transistors show a linear sensing behavior to ions, with relative responses in the order of -10%/dec and can detect glucose for concentrations between 5 μ M to 1 mM. The obtained sensitivity for ions and limit of detection for glucose are in a similar range to previous investigations on OECT-based sensors [22,23].

Paper III: This chapter is based on the following article: [N. Fumeaux](#), C. P. Almeida, S. Demuru, and D. Briand, "Organic electrochemical transistors printed from degradable materials as disposable biochemical sensors," *Sci. Rep.*, vol. 13, no. 1, Art. no. 1, Jul. 2023, doi: 10.1038/s41598-023-38308-1.

Contribution: As main author, I contributed to all the aspects of this work. This includes studying and optimizing the processibility of PEDOT:PSS on PLA, fabricating the samples, measuring the electrical and sensing behavior of the transistors and writing the manuscript.

Chapter 6: This chapter presents the fully digital fabrication of bioresorbable electronic implants by 3D printing. The printability of inks presented in previous chapters, namely POMaC and the carbon-shellac composite, is studied for direct-ink writing (DIW). DIW allows the highly customizable multi-nozzle printing of a wide range of materials and inks. The deposition by printing of the POMaC pre-polymer is studied and optimized for the realization of 3D structures, and the degradation of the prints in phosphate-buffered saline is studied. The carbon ink is integrated with the POMaC as electrical tracks, and their flexibility over 10'000 cycles is characterized. The physical degradation of both the POMaC and carbon materials is studied in phosphate-buffered

saline. Exploiting the possibilities offered by the multi-material printing, force sensors based on a parallel plate capacitor design are fabricated and assessed for applications in knee joint monitoring. Finally, electrodes for electrophysiology are fabricated, leveraging the high effective area and electron transfer characteristics of the carbon composite.

Paper IV: This chapter is based on the following article: [N. Fumeaux](#), A. Schlegel, D. Briand , “Digital manufacturing of customizable 3D bioresorbable electronics,” *Manuscript in preparation*.

Contribution: As main author, I contributed to all the aspects of this work. This includes the idea for the bioresorbable electronics manufactured by 3D additive manufacturing, conducting the study and optimization of the deposition processes, the degradation tests, performing the devices design, fabrication and characterization and writing the manuscript.

Chapter 7: This chapter concludes the thesis, summarizes the results that were presented, and provides an outlook on future research that this project enables.

Chapter 2 State of the art

This chapter covers the state of the art of the manufacturing of transient electronics, with a focus on implantable bioresorbable systems and addressing transient materials and their additive manufacturing. It aims to provide sufficient context for this thesis work having the goal of developing printed bioresorbable electronics. First, we introduce the transient materials that have been used for the fabrication of degradable electronics, and provide operative definitions for the terms that describe these degradable components, and rapidly outline their most common mechanisms of degradation. Secondly, we present examples of functional transient devices and systems with a focus on the fabrication methods employed, highlighting the inherent challenges of multi-material fabrication of transient electronics. The next section focuses on the additive manufacturing of transient electronics. An introduction is given on additive manufacturing, with particular interest for the use of printing techniques for the development of 3D, soft and/or implantable sensors, and the limited existing examples of printed bioresorbable electronics are presented. Finally, the challenges that emerge from the current state of the research are summarized, in order to highlight the contributions this thesis aims to achieve.

2.1 Materials for transient electronics

A large set of materials has been utilized for the fabrication of transient electronics. To better understand the field of transient electronics, however, we need to provide some definitions and distinguish these materials by their environment of application. The concept of transient electronics was championed by the group of Prof. John Rogers, where they developed very thin silicon membranes (silicon nanomembranes; SiNMs) which can dissolve in physiological solutions over a period ranging from hours to days [1]. The SiNMs can be used as conductors or semi-conductors for transient electronics. In this work, transient electronics are described as “systems that physically disappear at prescribed times and at controlled rates”. Therefore, transient electronics describe degradable systems with an electrical function, that will physically break down in a controlled amount of time, triggered or accelerated by a specific environmental stimulus [1,24]. Stimuli or environmental causes for the degradation include light, heat, moisture, bacteria, water, enzymes, etc. [25]. Degradable or transient electronics can be further divided as a function of the desired environment of use. Biodegradable or ecoresorbable electronics describe transient electronics which degrade in the natural environment, e.g. in soil, or in a controlled composting system, without harm to that environment [26]. To be considered biodegradable, a material must have broken down by at least 90 % in a period of 6 months [27]. Bioresorbable, or bioabsorbable [28] in turn, refers to material that undergo degradation through metabolic or hydrolytic processes, without eliciting harmful effects in the body [5]. Usually, it is admitted that the use of “-resorbable” or “fully degradable” refers to systems that entirely degrade into their simplest possible building blocks or derivatives such as monomers, metabolism byproducts, water-soluble metal oxides/hydroxides, etc. In opposition, some materials or composites are considered partially degradable, that is, they break down in their constituent parts, such as matrix and active material. We focus the following review on bioresorbable materials, and touch on their degradation mechanisms and rates. Ideally, these materials should provide a level of function that is comparable to their non-degradable counterparts.

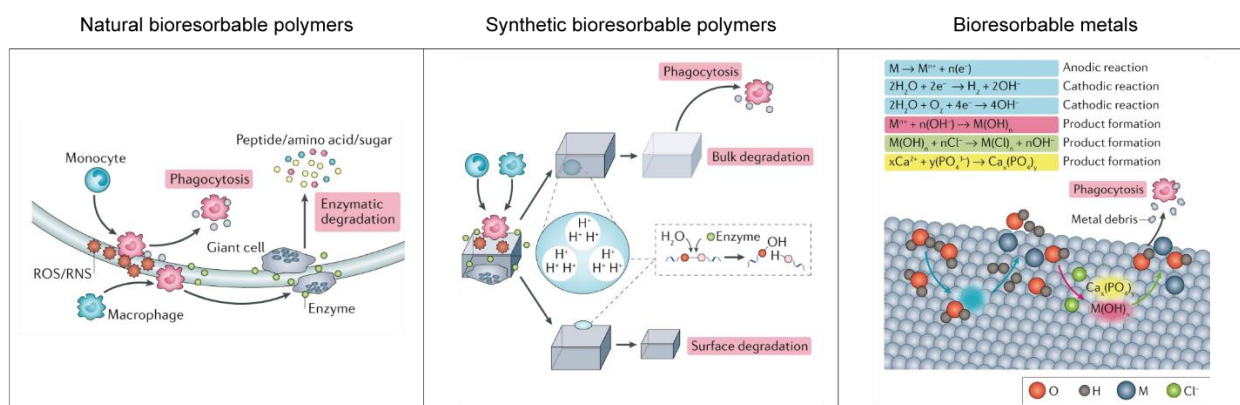


Figure 2.1: Mechanisms of degradation and bioresorption of various types of materials that have been used for implantable transient bioelectronics. Adapted with permission [29]. Copyright (2019), Springer Nature Limited. Natural bioresorbable polymers degrade mainly through the action of enzymes such as proteases secreted by macrophages or giant cells (in the case of silk for example). Their degradation can be modulated by reactive oxygen species. Synthetic bioresorbable polymers generally degrade by hydrolysis, sometimes catalyzed by enzymatic processes. As a function of the dimensions of the polymer, the degradation rate of its functional group and its water diffusivity, surface or bulk degradation may occur [30]. Metals degrade as the result of corrosion processes to oxides, hydroxides and hydrogen. Ions present in the solution influence the degradation process and degradation products can be metabolized by phagocytes.

2.1.1 Substrate and dielectric materials

Materials most commonly used as transient substrates are polymers, both natural and artificial [5,25,31]. They may also be used as encapsulation layers for the devices, with the degradation rate of the polymer being critical in determining the lifetime of the system [32]. Both synthetic and natural polymers exist, and their degradation mechanisms are illustrated in **Figure 2.1**. Synthetic water-soluble polymers include poly(vinyl alcohol) (PVA) and polyvinylpyrrolidone (PVP), which can also serve as binding additives in printed inks [25] and dissolve very rapidly in water (minutes to hours). Metabolizable synthetic polymers, such as poly(lactic acid) (PLA) [33], poly(glycolic acid) (PGA) [34], poly(lactic-co-glycolic acid) (PLGA) [35], polycaprolactone (PCL) [36] are also used. Their degradation usually relies on the hydrolysis of the ester linkages in their backbone in water or biofluids, and the rate of breakdown (over several months) can be adjusted by controlling the molecular weight. Bioresorbable elastomers have been engineered, generally through cross-linking of polymer chains made of absorbable monomers, e.g. poly(1,8-octanediol-co-citrate) (POC) [37], poly(octamethylene maleate (anhydride) citrate) (POMaC) [38] and poly (glycerol sebacate) (PGS) [39]. These thermoset elastomers generally require heat curing from the pre-polymer state (before cross-linking), and the presence of vinyl bonds in POMaC grants it a dual curing mechanism, where both thermal and UV curing can be used to cross-link the polymer [38]. Similar modifications have been proposed for PGS, rendering the polymer photocurable by acrylation [40], methacrylation [41] or by addition of a cinnamate reactive group [42]. These modifications, however, complexify the synthesis and require the use of toxic reagents. The degradation of bioresorbable elastomers is similar to other degradable polyesters, with full degradation being observed after several months [43], and lifetime can be adjusted by modifying chain length or chemical composition. This is the case for POMaC, for instance, where a higher proportion of maleic anhydride in the synthesis slows down degradation [38]. Various degradable biomaterials have also been investigated as substrates or encapsulants.

Silk is a natural bioresorbable polymer produced by the larvae of the silkworm *Bombyx Mori* [44]. Transient films can be formed from the fibroin protein extracted from the natural silk, and their degradation time is adjustable from seconds to weeks with post-treatments that modify their crystallinity [45]. Silk-based biomaterials have been investigated in great depth by Prof. Kaplan at Tufts University, and post-treatments based on ethanol or methanol immersion [46] or water vapor annealing [47] have been studied. The mechanical properties of silk fibroin can be adjusted by controlling their hydration state [48] or by addition of plasticizers such as glycerol [49]. Beeswax, largely composed of wax esters, hydrocarbons and fatty acids, is a material of interest for lifetime-controlled transient electronics, owing to its excellent water barrier properties and relatively slow

degradation [50]. Beeswax has been used as an encapsulant for ecoresorbable electronics and several publications study the complex mechanisms of its degradation in soil [51]. Beeswax has also been used as binder in printable inks [52] and its degradation was characterized in conditions reproducing an implanted setting, indicating full degradation in 80 days. Other bio-derived bioresorbable polymers include shellac [53] and chitosan [54], derived from lac bug secretions and crustacean shells, respectively. Shellac benefits from favorable water-barrier properties [55] and degrades by surface hydrolysis (at a rate of 0.5% weight loss per hour at room temperature [56]). Polyhydroxyalkanoates (PHAs) are transient polyesters produced by various microorganisms, and the most investigated are polyhydroxybutyrate (PHB) and poly(3-hydroxyvalerate) (PHV) and their co-polymers. PHAs degrade in vivo by hydrolysis, and their degradation is influenced by molecular weight, chain length, crystallinity and formulation [57]. Cellulose derivatives are widely used as green polymers for degradable electronics [58] and their degradability in soil or a composting setting have been thoroughly investigated [59] and largely depend on the composition of the paper and crystallinity of the cellulose fibers [60]. Its degradation in soil or compost requires the presence microbial and fungal enzymes [61]. To be bioresorbable, they must be rendered water soluble via etherification, as is the case for sodium carboxymethylcellulose (Na-CMC) [62]. The organic substrates mentioned above have also found applications as dielectrics [63] or triboelectric friction layers [64] or in some cases as piezoelectric transduction or sensing layer [65]. Inorganic dielectrics commonly used in microelectronics such as silicon dioxide (SiO_2) and silicon nitride (Si_3N_4) show sufficient degradation rates in physiological solution to be used in ultrathin films [37,66]. Silicon dioxide, in particular, showed promise as encapsulation for transient implantable devices, as its slow degradation rate allows to precisely control the functional lifetime of the device and limit water permeation [32]. Magnesium oxide has been used as well, due to its high temperature stability and optical transparency [25]. Thanks to their processability in thin film forms, these materials have been used as dielectrics for degradable transistors [3,67]. The most prominent transient substrate materials for the fabrication of eco- and bioresorbable electronics are shown in **Table 2.1**, with their most relevant properties.

Table 2.1: Bioresorbable substrate materials and their relevant characteristics.

Complete name	Common name	E [MPa]	ϵ_{break} [%]	σ_{yield} [MPa]	ρ [g/cm ³]	T_m [°C]	Tg [°C]	Degradation	Printable	References
<i>Poly(lactic acid)</i>	PLA	350-3500	2.5-6	21-60	1.21-1.25	150-162	45-60	Hydrolysis	2D/3D	[25,33]
<i>Poly(l-lactic acid)</i>	PLLA	2700-4140	3-10	15.5-150	1.24-1.3	170-200	55-65	Hydrolysis (12-18 w)	2D/3D	[33,34]
<i>Poly(d, l-lactic acid)</i>	PDLLA	1000-3450	2-10	27.6-50	1.25-1.27	am	50-60	Hydrolysis	2D/3D	[33]
<i>Polyglycolide</i>	PGA	6000-7000	1.5-20	60-99.7	1.50-1.71	220-233	35-45	Hydrolysis (6-12 w)	2D/3D	[33,34]
<i>Poly(lactic-co-glycolic acid)</i>	PLGA	2000	3-10	41-55	1.2-1.7	am	>37	Hydrolysis (1-6 w)	2D/3D	[34,35]
<i>Poly(vinyl alcohol)</i>	PVA		700	37	1.19-1.31	200	85	Hydrolysis	2D/3D	[68-70]
<i>Polycaprolactone</i>	PCL	210-440	300-1000	20.7-42	1.11-1.15	58-65	(-60)-(-65)	Hydrolysis	2D/3D	[25,33]
<i>Polyhydroxybutyrate</i>	PHB	3500-4000	5-8	40	1.18-1.26	162-182	15-5	Bacteria, Macrophages	2D/3D	[33,71,72]
<i>Polyhydroxybutyrate/polyhydroxyvalerate</i>	PHB/PHV	Different blends						Bacteria, Macrophages	-	[71]
<i>Polybutylene succinate</i>	PBS	250-650	170-380	17-40	1.24-1.26	84-115		Bacteria	2D/3D	[73]
<i>Silk fibroin</i>	Silk	2000-4000	1.9-3.9	47.2-100	-	250-350	178	Enzymiatic degradation, hydrolysis (tunable)	2D/(3D)	[74,75]
<i>Shellac</i>	Shellac	340	3	-	1.04-1.11	75-80	45-56	Hydrolysis	2D/3D	[76,77]
<i>Sodium carboxymethyl cellulose</i>	Na-CMC	>250	10.54-17.67	14,18-27.10	-	-	-	Hydrolysis	2D/3D (composites)	[78]
<i>Poly(octamethylene maleate (anhydride) citrate)</i>	POMaC	0.03-1.54	48-534	0.245-0.994	1.08-1.17	-	-	Hydrolysis (tunable)	-	[38,79]
<i>Poly(glycerol-sebacate)</i>	PGS	0.08-2.3	60-510	0.25-1.5	-	5.23, 37.62	<80	Hydrolysis, tunable, up to -60 d	2D/3D	[39,80]

2.1.2 Conductive and semiconductor materials

Most bioresorbable electronic devices make use of metals as conductors, specifically those that are present in a normal human adult diet and naturally occur in the body [66]. So far, magnesium (Mg), iron (Fe), zinc (Zn), tungsten (W) and molybdenum (Mo) have been used for the fabrication of electrodes and interconnects [81]. They present the advantage of much higher conductivities and more stable properties than conductive polymers. Their electrical dissolution behavior (based on the measured change in electrical resistance) was systematically studied by Yin et al. [82]. The mechanism for dissolution of transient metals in biofluids is corrosion, which is dependent on the salts present in the solution, the temperature and the grain sizes, porosity and general morphology of the metal film [28,82,83]. In general, the metals will convert to water-soluble oxides or hydroxides that can be metabolized or excreted by the body [29]. Magnesium dissolves in water and forms water-soluble $Mg(OH)_2$. Zn dissolves at a slower rate and forms principally the water-soluble and non-toxic ZnO and $Zn(OH)_2$. The corrosion of iron in biofluids is more complex [66] and the products are not water-soluble. Zinc and iron have been combined in bilayers for transient electronics [84], with the presence of iron causing galvanic corrosion of the zinc, thereby speeding up its otherwise relatively slow dissolution rate. While the aforementioned metals and their alloys have been proposed for implantable resorbable stents or screws [85], tungsten remains a less investigated bioresorbable metal. Tungsten has been used in neural probes [86], and its corrosion rate was found to be $\sim 100 \mu\text{m}/\text{year}$ in vivo, with the rate of degradation increasing with the presence of oxygen and hydrogen peroxide. Finally, molybdenum has been recently studied for in vivo degradation in a rat model, with an approximate rate of degradation of $13.5 \mu\text{m}/\text{year}$, and no significantly elevated amount of Mo was found in the kidney or liver of the animals. The electrical degradation rates measured by Yin et al. are reported in **Table 2.2** below, the in vivo degradation rate (if known) as well as the normal serum levels for each metal and their upper daily intakes, which provide guidelines for their application to bioresorbable electronics. The local tissue tolerance for hydrogen must also be considered ($<10 \mu\text{L}/(\text{cm}^2 \cdot \text{day})$), as the corrosion of the aforementioned metals releases hydrogen gas [87]. We note that these metals are usually deposited with methods stemming from the semi-conductor industry, such as e-beam evaporation and magnetron sputtering, and additive manufacturing has been scarcely used thus far. In general, Mg and Zn are favored as they are easier to process and generally better tolerated [66]. However, Mo and W exhibit lower degradation rates and are more amenable to applications where a longer lifetime is needed, or direct contact with biofluids is required. Bioresorbable metals generally display a negative electrode potential, indicating their tendency to corrode in a pH neutral aqueous environments, with the exception of tungsten, whose corrosion is aided by the presence of oxygen [88].

Table 2.2: Transient metals with their relevant degradation characteristics, tolerance in the human body and most common deposition methods used.

Metal	Bulk Conductivity [S/m]	Electrical dissolution rate [$\mu\text{m}/\text{h}$]	In vivo dissolution rate [$\mu\text{m}/\text{h}$]	Normal blood serum level [$\mu\text{g}/\text{dL}$]	Upper daily intake [mg/day]	Deposition methods	References
Mg	$2.15 \cdot 10^7$	4.8 ± 2.2	≈ 10	1700 - 2200	350	Electron-beam evaporation, sputtering	[1,66,82,89]
Fe	$1.04 \cdot 10^7$	$\approx 2 \cdot 10^{-4}$	-	50 - 175	40 - 45	Electron-beam evaporation, magnetron sputtering	[66,82,90,91]
Zn	$1.68 \cdot 10^7$	0.3 ± 0.2	$\approx 5 \cdot 10^{-3}$	60 - 120	23 - 40	Magnetron sputtering	[82,92,93,66]
Mo	$1.91 \cdot 10^7$	$(2 \pm 0.3) \cdot 10^{-4}$	≈ 0.0015	8 - 30	1.2 - 2	Magnetron sputtering	[66,82,94-96]
W	$1.82 \cdot 10^7$	$(8 \pm 2) \cdot 10^{-3}$	≈ 0.01	0.1 - 0.3	-	Magnetron sputtering	[66,82,86,91,95]

Conductive polymers, although they exhibit much lower conductivities, have been synthesized in water-soluble forms and proposed for use as transient materials [25]. Despite these polymers not being inherently bioresorbable, they are biocompatible and have been deposited on or blended in bioresorbable matrices for uses in tissue regeneration [97]. Conductive polymers polyaniline (PAni) [98], polypyrrole (PPy) [99] and in particular poly(3,4-ethylenedioxythiophene) (PEDOT) [100] are the most researched. PEDOT is usually found in a

mixture with polystyrene sulfonate (PSS), which acts as dopant for the PEDOT. Although biocompatible and degradable, there is no evidence that these polymers dissolve in the body into metabolizable elements. PEDOT:PSS is insoluble in water but was found to break down in the presence of moisture [101] and hydrogen peroxide has been hypothesized to cause degradation of PEDOT:PSS [102]. Moreover, although the potential mechanisms of degradation of PEDOT:PSS in vivo are unclear, it was shown to cause only minimal glial scarring when implanted in the brain on a bioresorbable substrate (polycaprolactone) [103] and is considered for transient implantable electronics [104]. Polyaniline is not fully bioresorbable, and adverse effects (cytotoxicity, reactive oxygen species) has been observed during in vivo breakdown [105]. Polypyrrole, in the form of degradable PPy nanoparticles-PLA blends, has been hypothesized to be cleared renally without harmful effects [106]. A strategy to better control the breakdown of conductive polymers is to combine them with some of the aforementioned materials used as bioresorbable substrates (e.g. as block copolymers) [97] at the cost of conductivities orders of magnitude lower.

Carbon-based materials have also been considered for the fabrication of bioresorbable electronics, as well as for environmentally-friendly devices [107,108]. Graphite and carbon particles have been used for the development of biodegradable printable inks [17,55]. Graphite and carbon are natural environmentally benign materials and are compatible with composting [109]. Carbon is largely considered to be biocompatible and edible [110], it is however bioinert and its fate in the body if used in bioresorbable implants remains to be investigated. Carbon nanotubes have been used in the biomedical field, yet their biocompatibility and degradability remain to be further investigated as they are known to be cytotoxic [111], although functionalization approaches had some success in fostering enzymatic degradation [112]. Their use in bioresorbable electronics requires further research on approaches to render them biocompatible and to enable their degradation or disposal from the human body.

Finally, some research efforts have also focused on semiconductor materials, for the realization of more complex bioresorbable systems featuring e.g., transistors or diodes. Silicon (Si) exhibits low hydrolysis rates, which, in the case of ultrathin membranes, is significant enough for it to be considered bioresorbable [1]. Germanium (Ge) and SiGe alloy [37] have also been used, as well as zinc oxide (ZnO) [25]. The group of Zhenan Bao synthesized biocompatible and degradable semi-conductors with mobility values comparable to standard organic semiconductors ($0.34 \text{ cm}^2 \text{ V}^{-1} \text{ s}^{-1}$) [58,113]. However, the fact that their dissolution has been observed only in acidic solutions makes their use in bioresorbable electronics less straightforward. A wide array of natural and bioresorbable materials, including glucose, indigo and beta-carotene, have been proposed, and they are limited by their low mobilities (in the order of $10^{-2} \text{ cm}^2 \text{ V}^{-1} \text{ s}^{-1}$) [114].

2.2 Bioresorbable devices and systems

Bioresorbable implants are already present in the clinic, as for bioresorbable sutures, which have been used for more than 50 years [31]. This is also the case for degradable stents, which were developed to avoid late-stage thrombosis and vessel remodeling [115]. These stents can be made of magnesium and its alloys or bioresorbable polymers, usually PLLA [116], although other transient metals have been investigated as well, such as zinc [12]. Analogously, bone screws made of bioresorbable metals have been proposed [117]. Bioresorbable materials have been used as part of long-term implants, as is the case in [13], where a silk film serves as support to deliver ultrathin polyimide-based electronics onto the brain. Relatively stiff transient polymers, with fast degradation times (minutes to hours) have been used as insertion guides for neural probes, to avoid buckling issues when penetrating the dura [14,118].

Of more interest to us in the context of this work are bioresorbable implants that comprise active electronics. State-of-the-art bioelectronics are increasingly fabricated with techniques from the semi-conductor and microelectromechanical systems (MEMS) industries, allowing unprecedented resolutions and thin layers, to create minimally invasive implants. However, the application of such techniques to transient electronics is challenging due to the unique properties of the materials [25,111]. Indeed, their increased reactivity precludes their patterning by conventional microfabrication steps due to their low thermal budget (e.g., during baking steps) and their limited solvent resistance (e.g., during etching or developing) [111]. To circumvent these challenges,

several methods have enabled the fabrication of multilayer, complex and functional transient implants. These methods can be characterized in four categories [25]: conventional microfabrication in combination with transfer techniques, vacuum-based deposition through a shadow mask, hybrid assembly of films and foils and solution-based processing. For the most part, the first three methods have been used in combination to create functional bioresorbable devices, although, as we will see in Section 2.3, additive manufacturing holds promise for that purpose.

Functional electronic devices based on degradable materials have been proposed in a 2010 paper from Irimia-Vladu et al., using bio-derived semi-conductors to fabricate organic field effect transistors [114]. Boutry et al. presented an early concept of wireless degradable and implantable device based on blends of conducting and biodegradable polymer blends (PLA, PCL and PPy) [119,120]. Another early example of bioresorbable electronics came from the group of Mark Allen. In this work, Luo et al. [84] fabricated a wireless pressure sensor with a combination of transfer by embossing, stencil evaporation and electrodeposition. As introduced before, John Rogers' group pioneered the development of degradable metal-oxide-semiconductor field-effect transistors (MOSFETs) based on bioabsorbable metals and very thin membranes of silicon (silicon nanomembranes; SiNMs) as the semi-conductor [1,82]. The fabrication of these devices relies on a combination of the first two methods mentioned above. The SiNMs are patterned on a silicon-on-insulator wafer by reactive ion etching, released by wet etching in HF and transferred on the transient substrate film of silk fibroin. The transfer of the active components to the transient substrate relies on the aforementioned transfer technique, based on controlled adhesion to an elastomeric stamp [121]. The electrodes and dielectric (Mg and MgO, respectively) are evaporated through high-resolution stencil masks by e-beam evaporation. This made the development of several transient components possible, such as transistors, diodes, capacitors, inductors and interconnects [1,122]. Variation of the methods presented in this paper have enabled the fabrication and in vivo assessment of a variety of bioresorbable sensors and systems, such as a degradable radio-frequency (RF) heater [123], or temperature, pressure and pH sensors for the brain [124] and an electrocorticography array with multiplexing capabilities [125]. The RF heater presented in [123] relies on the same processes for the patterning of Mg and MgO on silk, and the wireless heater is assessed in mice for the mitigation of bacterial infections. The same group developed a multi-sensor platform for the brain [124] based on SiNMs on PLGA. Despite these impressive developments, they highlight some of the challenges with transient electronics. This includes controlling the lifetime of the devices, which in these cases degrade fast (a few hours) and are therefore limited to acute experiments. Yu et al. [125] present a bioresorbable electrocorticography (ECoG) array for the recording of brain surface activity. The array relies on highly-doped SiNMs as interconnects and electrodes and SiO₂ as a dielectric interlayer. Increasing the thickness of the SiNMs and SiO₂ interlayer is shown to allow for a functional lifetime of one month for the device in an implanted setting. The SiNMs electrodes degradation is also shown to be dependent on the presence of protein and calcium ions in the solution, and compared to Mo electrodes, which undergo relatively fast functional degradation in vivo by cracking and fragmenting [24]. Silicon is a very versatile material and can exhibit a wide range of properties as a function of its doping and crystallinity, and the silicon nanomembranes are exploited for the realization of optical waveguides [126]. SiO₂ is also used in further work as a flexible encapsulant to increase the lifetime of implantable pressure sensors [32]. Shadow-mask evaporation and hybrid assembly techniques have been used for the fabrication of bioresorbable electronics. Xu et al. [127] presented a system for brain pressure sensing and electrophysiology based on PLA/PCL as substrate and shadow-mask sputtered Mo as electrodes and interconnects. Ouyang et al. [128] developed a cardiac pressure sensor based on a bioresorbable triboelectric sensor made of laminated PLA and chitosan films. Curry et al. [129] presented a piezoelectric force sensor based on PLA with laser-cut molybdenum foil electrodes. A wireless bioresorbable air-gap pressure sensor was also proposed [130], leveraging electron-beam evaporated magnesium and using melted PCL as adhesive to assemble the sensor. The range of applications for bioresorbable systems has expanded considerably in recent years, spanning various sensing/stimulation mechanisms and targets: nerve stimulation for regrowth [131] or pain suppression [132], remote-controlled drug delivery [133–136], cardiac electrical stimulation [137], impedance sensing at wound site [138], electrostimulation for bone healing [139] etc. The fabrication methods have also been expanded, with the use of direct laser ablation to pattern bioresorbable functional materials on a transient substrate [140], or the development of foundry-compatible fabrication techniques for transient electronics [141].

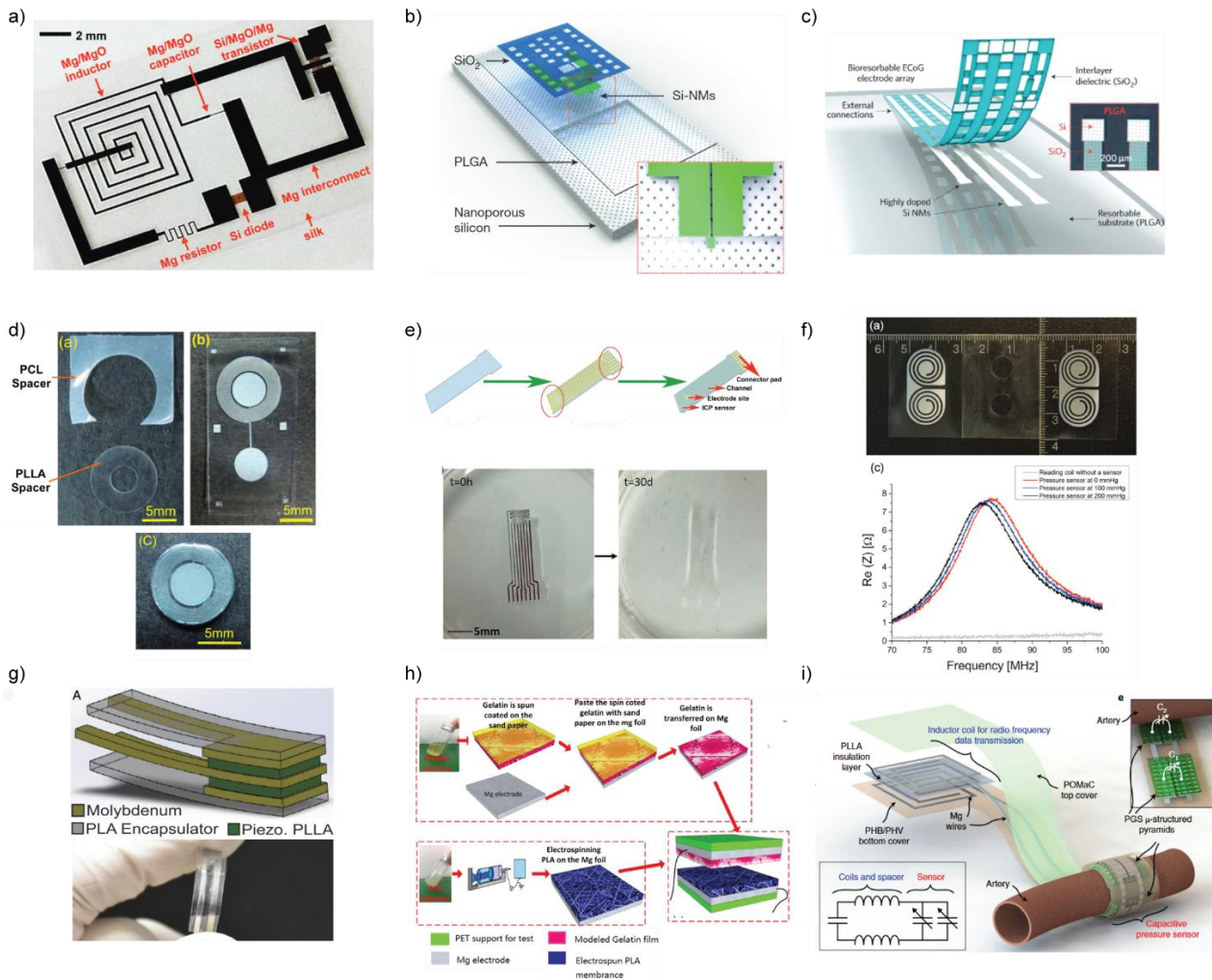


Figure 2.2: Examples of bioresorbable implantable electronics, where the main method used for fabrication is clean-room processes (a-c), shadow-mask evaporation (d-f), lamination of films and foils (g-i). (a) Mg and Si transient electronic circuit on silk. Reproduced with permission [1]. Copyright (2012), the American Association for the Advancement of Science. (b) Silicon electronics as implantable sensors. Reproduced with permission [124]. Copyright (2016), Macmillan Publishers Limited. (c) Bioresorbable ECoG array. Reproduced with permission [142]. Copyright (2016), Macmillan Publishers Limited. (d) Intracranial wireless pressure sensor based on electrodeposited Zn on evaporated Fe. Reproduced with permission [84]. Copyright (2013), IEEE. (e) Electrodes and pressure sensor from evaporated Mo. Reproduced with permission [127]. Copyright (2019), Wiley-VCH GmbH. (f) Wireless intracranial pressure sensor relying on evaporated Mg and assembled with PCL-based adhesive. Reproduced with permission [130]. Copyright (2019), Wiley-VCH GmbH. (g) Bioresorbable piezoelectric force sensor from laminated Mo and PLA. Reproduced with permission [129]. Copyright (2018), National Academy of Sciences. (h) Triboelectric generator fabricated from laminated Mg foil and gelatin and PLA films. Reproduced with permission [143]. Copyright (2017), Elsevier Ltd. (i) Wireless pressure sensor for cardiovascular monitoring, where the antenna and electrodes are made from laser-cut Mg foil. Reproduced with permission [144]. Copyright (2019), Copyright (2019), Springer Nature Limited.

In some cases, it is necessary for medical implants to be able to stretch and deform, following the natural movements of the body, and avoiding a mismatch with soft tissue [145]. Hwang et al. [37] fabricated wavy SiNMs that confer stretchability by design to structures transferred onto bioresorbable elastomer POC. Following a simpler fabrication approach (molding and evaporation of the conductive layer, or alternatively using laser-cut metal foils), researchers from Stanford University created a strain sensor and an arterial pulse sensor [144,146] whose performance was assessed in vivo in rats. To address the issue of device powering, various approaches have been proposed, such as bioresorbable wires [124], self-powered implants (piezoelectric [147], triboelectric [148]), wireless power transmission [122,131,149,150] or batteries [151] or supercapacitors [91]. Examples of bioresorbable biosensors are scarce and limited to our knowledge to the pH sensor in [124] and recent examples using a silk-PEDOT composite [152,153], whose bioresorbability has not been fully

demonstrated. Some limited examples of transistors for biochemical sensing also exist on eco/bioresorbable substrates such as PLA [63], PLGA [154] and diacetate cellulose [155]. However non-transient silver or gold electrodes were used in these investigations. Illustrations of some of the aforementioned bioresorbable electronic devices are provided in **Figure 2.2**.

In conclusion, solution processes are generally limited to the casting of substrates and encapsulation, although some conductive transient polymers have been solution-processed, and examples of transient electronics additive manufacturing are scarce. The publications where additive manufacturing is used are described in more detail in Subsection 2.3.2.

2.3 Additive manufacturing for bioresorbable electronics

Additive manufacturing, or printing, refers to fabrication techniques that rely on layer-by-layer manufacturing by addition of a material ink. These methods generally benefit from being more cost-efficient and sustainable [156], as only the needed amount of material is deposited, and the process can be performed under atmospheric pressure and ambient conditions. The methods are also, in general, characterized by their high scalability, and the capability to fabricate large-area devices [157]. Moreover, with the simplified processes resulting from printing, the possibility for customizable digital additive manufacturing emerges. The design can be personalized to a specific use case to optimize the geometry of the implant to maximize functionality, conformality, etc. [158]. Finally, as printing processes take place at ambient temperatures with limited amounts of solvent, they may prove to be suitable for the fabrication of functional devices from fragile and reactive bioresorbable materials [25]. Additive manufacturing has been used to fabricate wearable and implantable bioelectronics, taking advantage of its benefits and flexibility. In Subsection 2.3.1, we present examples and introduce the commonly used printing techniques in this context. Despite these advances, the field of bioresorbable electronics is still relatively new, and only limited demonstrations of printed bioresorbable electronics exist. They are presented in Subsection 2.3.2, and a perspective on the printability of bioresorbable materials is given.

2.3.1 Ink formulation and printing methods

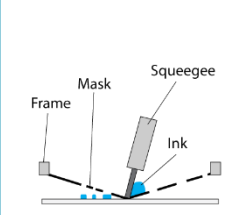
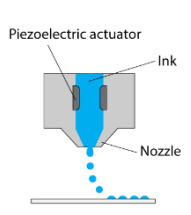
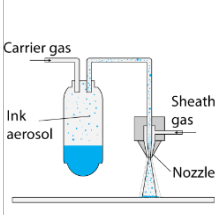
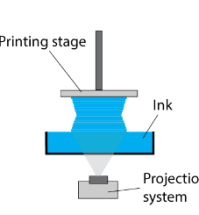
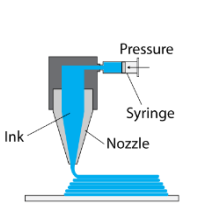
Printing in the context of flexible electronics usually requires two distinct steps: the material deposition in the form of an ink and the densification or curing of the material [159]. The formulation of stable and printable inks or pastes is a crucial challenge in itself [160,161], and their properties must be adjusted in relation to the printing technique to be used. Inks for the printing of dielectrics, conductors and semi-conductors have been developed. Organic materials can often be directly printed in solution with a compatible solvent, provided the appropriate rheological properties can be attained. When this is not the case, or for inorganic materials, inks can be separated in two categories: particle dispersions and precursor inks. In the case of precursor inks, the solution contains compounds that will react during or after printing to form the desired component. An example of such is copper formate, which self-reduces to copper metal under heat [162]. Particle inks consist of micro- or nanoparticles, dispersed in a solvent with the aid of a polymeric dispersant or surfactant [160]. A polymeric binder may be included, or the particles covered with ligands, to maintain the physical integrity of the layer of printing. In both cases, the particle size, viscosity, water tension and density are informed by the chosen printing method.

The printing techniques used differ chiefly by the deposition mechanism, the ink viscosity range, the attainable resolution, and the possibility to realize 3D structures (see **Table 2.3**). Although many printing techniques exist, we focus in this brief review on the most commonly used for the fabrication of flexible or soft electronics for wearable or implantable applications: screen printing, inkjet printing, aerosol jet printing, stereolithography/digital light processing, and direct-ink writing. Screen printing is a versatile technique where a paste or slurry (typically loaded with functional particulates) is dispensed through a metallic or polymeric mesh with the aid of a squeegee. Viscous micro- or nanoparticles dispersions are generally used, resulting in layers in the order of a few microns to dozens of microns. The minimal feature size is limited by the openings in the printing mask and the shape fidelity of the ink and is generally found around 50 μm . Comparably to similar techniques such as flexographic or gravure printing, screen printing is suitable for large-area, high throughput manufacturing

(roll-to-toll production) but requires the use of a pre-fabricated mask or pattern. Screen printing has been widely used for the fabrication of flexible electronics, e.g. biosensors [163] or implantable pressure sensors [164].

Inkjet and aerosol jet printing both rely on lower viscosity ink that are jetted in a non-contact configuration. Due to the low viscosity of inks required, nanoparticles are generally used to maintain ink stability and avoid nozzle clogging. In the case of inkjet or drop-on-demand techniques, distinct droplets of ink are created (typically from a piezoelectric or heated element) [165]. The printability of inks by inkjet printing has been studied in great depth and can be predicted by the values of dimensionless numbers related to the surface tension, density and viscosity of the ink [166]. The thickness of printed layers is in the order of hundreds of nanometers, with resolutions down to dozens of micrometers, as a function of the ink surface tension and rheology, as well as surface wetting and roughness. In the case of aerosol jet, a mist is created from the ink and carried to the substrate by a carrier gas through a nozzle, where aerodynamic focusing allows for the obtention of higher resolutions, down to 10 μm [167]. Resolution is limited by overspray, i.e., functional material particles that are outside of the desired zone of deposition. The thickness of printed layers is generally in the order of one micrometer or less. Both techniques allow for digital additive manufacturing, where a design can be printed without the creation of a mask or modifications to the process. Inkjet printing is a more established technique and has been used to print a variety of devices, such as implantable glucose sensors [168], organic electrochemical transistors [169] and electrocorticography (ECoG) arrays [170]. AJP allows for a wider range of viscosities and is particularly suited for printing on curvilinear surfaces. However, as a less established technique, it faces more issues in terms of process standardization and process drift [167]. As examples, flexible micro-hotplates [171] as well as pH sensors [172] have been fabricated aerosol jet printing.

Table 2.3: Printing methods mentioned in this review with their figures of merit, numbers from [15, 16, 161, 173, 174].

	Screen printing	Inkjet printing	Aerosol jet printing	Stereolithography/ Digital light processing	Direct ink writing
					
Approximate resolution [μm]	10 - 40	30 - 50	10	1 - 50	30
Layer/print thickness [μm]	5 - 100	~ 1	0.1 - 10	5 - 150	30 - 600
Viscosity range [cP]	500 - 5000	< 50	1 - 2500	< 5000	1 - 10^6
Digital	No	Yes	Yes	Yes	Yes
3D capabilities	No	No	No	Yes	Yes

Digital additive manufacturing techniques that allow to produce 3D objects are of interest to unlock a new degree of customizability. Stereolithography (SLA) refers to a family of technology where solid 3D objects are obtained from a photocurable resin. Digital light processing (DLP) is similar to SLA except that the light is delivered through a projected light source instead of a laser. Although the techniques are fast, inexpensive and amenable to the construction of complex 3D shapes, limited material choice is available [16] and multi-material printing requires complex modifications [175]. SLA has been used for the creation of soft robots [16] and structural or drug-loaded passive implants [176]. Finally, direct ink writing (DIW) consists in the extrusion of a viscoelastic ink through a nozzle. This is similar to the more common fused deposition modelling (FDM), but differs in that a fluid ink is used, allowing for more versatility and higher resolutions. Pressure for extrusion

is generated through a piston or pneumatically [15]. A key characteristic of DIW inks in order to achieve high shape fidelity is shear-thinning. This refers to non-Newtonian fluids for which viscosity decreases with increasing shear. This is typically determined by oscillatory rheology measurements, where the cross-over point between the loss and storage moduli determines the transition between a solid paste to a fluid. DIW benefits from the most versatility in terms of materials for printing, with the possibility to print substrate, conductive and even biological materials [177]. Recently, Afanasenkau et al. [158] presented customizable electrodes for neuromuscular interfaces relying on a combination of direct ink writing and inkjet printing. Table 2.3 shows a summary of the printing methods mentioned above, with their attainable smallest features, layer thicknesses and ink viscosities.

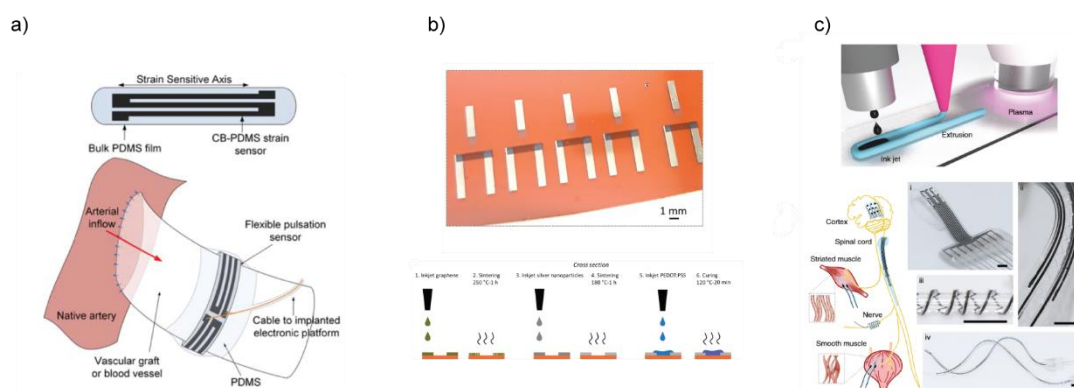


Figure 2.3: Examples of printed biosensors and bioelectronics. (a) Screen-printed strain sensor for cardiovascular monitoring. Reproduced with permission [178]. Copyright (2019), IEEE. (b) Fully inkjet-printed organic electrochemical transistors, with a PEDOT:PSS channel, graphene gate and silver contacts. Reproduced with permission [23]. Copyright (2022), American Chemical Society. (c) Combination of direct ink writing and inkjet printing for the fast prototyping of neuromuscular interfaces. Reproduced with permission [158]. Copyright (2020), Springer Nature Limited.

Often, materials require post-treatment following printing to solidify the material and/or achieve a sufficient degree of functionality. Polymeric inks may necessitate curing for cross-linking, while particle inks need treatment to vaporize polymeric additives that may impede layer functionality or to enhance particle contact via sintering. Sintering refers to the densification of particles by the introduction of energy by thermal, optical or electrical means [18]. As is the case for deposition methods, there exists a wide array of post-treatment techniques used in the context of additive manufacturing. Often, thermal heating is the preferred post-treatment for printed inks. However, many commercial conductive printable inks are sintered by thermal heating at temperatures superior to 200 °C [25]. Thus, in the context of degradable electronics, methods where higher temperatures are avoided are preferred. In the frame of this review, we focus on two types of methods: delivering energy selectively through light, and leveraging chemical reactions to achieve curing. Ultraviolet (UV) light is often used in the context of photopolymerization of polymeric printable inks [177], although UV-curable conductive silver inks have been developed for inkjet printing [179] and for screen printing [180]. Photonic sintering, or flash lamp annealing, consists in the application of high-intensity pulsed light delivered on a short time-scale (in the order of milliseconds). The light is generally in the visible or near-infrared range. This allows to rapidly heat the printed layer while maintaining a much lower temperature in the substrate, preventing damage to temperature-sensitive polymeric or cellulosic substrates [181]. This is dependent on the heat conduction of each layer and their respective thicknesses. This method has been used for the sintering of a wide range of materials from metals [181], metal oxides [182], graphene [183] and ceramics [184]. Laser sintering achieves the same aims, also relying on rapid heating from energetic photons to locally weld the metal particles [185]. As opposed to photonic sintering, laser sintering used a coherent light source, and requires scanning of the surface. This can be detrimental to throughput, but allows for more localized sintering. Finally, chemical approaches have been developed to achieve metallic particles coalescence, triggered for example by contact with oppositely charged polymers or electrolytes [186,187]. Chemical oxide reduction strategies have also been developed to achieve densification of particles films for metals such as copper, e.g. by exposure to formic

acid [188] or silver, in HCl vapor for example [189]. **Figure 2.3** shows examples of functional printed bioelectronics incorporating various sensing functions.

2.3.2 Printed bioresorbable electronics

Until very recently, additive manufacturing of bioresorbable implants has been limited to the 3D printing of structural polymers or metals. Polymeric materials have been 3D printed with multiple techniques, and there is a large collection of published papers on manufacturing resorbable metallic orthopedic implants with selective laser sintering (SLS) [190,191]. Functional materials are printable as well, with satisfying performance through the use of innovative sintering techniques. There are only limited examples, to our knowledge, of integration of functions into a fully printed bioresorbable device or system.

Transient polymers are solution-processible low melting point materials, and they lend themselves well to various forms of printing. Of course, PLA, PLGA and PCL and various composites have been printed, also for medical implants, with fused deposition modeling, inkjet or direct ink writing techniques [33,63,192]. Silk has been inkjet-printed [193,194] and 3D printed in methanol [195] as well by aerosol jet printing [196]. The extraction of silk fibroin from the silkworm cocoon typically results in a 7-9 % aqueous solution of silk fibroin [44]. The characteristics of that solution in terms of surface tension lend themselves well to low-viscosity printing, after dilution to 3 % [193] and the bio-derived inks can be functionalized with antibodies, enzymes, nanoparticles, etc. As mentioned in Subsection 2.1.1, silk fibroin requires treatments that modulate its degradability in aqueous solution. Rider et al. [194] used inkjet printing to deposit silk protein as well as for the subsequent methanol treatment, allowing to locally control crystallinity and avoid potential damage when curing the entire film in a methanol bath. PGS has found various applications in the biomedical field in the form of scaffolds for cell culture or in vivo regeneration, some supported by additive manufacturing techniques [197]. Methacrylated photocurable PGS was 3D printed into cell scaffolds [198] by γ -photon polymerization to form resorbable scaffolds for cell culture. Yeh et al. [199] reported on the 3D printing by direct-ink writing of acrylated PGS to form stretchable biocompatible and bioresorbable scaffolds. The same authors also introduced norbornene-modified PGS for fast UV curing [200], and fabricated scaffold with direct ink writing under constant UV illumination. Finally, digital light processing has been used for the 3D printing of acrylated PGS networks with features below 100 μm . POMaC is readily UV-curable, although its vinyl bonds result in a slower polymerization than the chemistries used in the aforementioned modified PGS polymers [201]. Its printability by DIW has been assessed recently, however in the form of poly(ethylene glycol) diacrylate copolymers [202].

Organic conductors are amenable to solution processing and printable inks are available. Conductive polymer inks based on PEDOT:PSS, PANi and PPy have been used for the fabrication of devices on degradable substrates [8]. PEDOT:PSS has been printed on biodegradable and bioresorbable substrates such as PLA [63], paper [203] or PLGA [154] for the realization of biochemical sensors or electrocardiography (ECG) electrodes. PPy has been used in combination with electrochemically sintered zinc to fabricate supercapacitors which were shown to degrade in vivo with no adverse effects [204]. Carbon materials conductive and semi-conductive printable inks have been formulated and used in ecoresorbable or edible devices. When targeting applications in eco-friendly electronics, the components of the ink are chosen carefully, preferring water as a solvent and renewable binders [205,206]. To address the challenge of stable electrical properties despite using degradable materials, Poulin et al. presented a carbon particles/graphite loaded shellac ink, which maintains conductivity in water and reaches values in the order of 10^3 S/m [55]. This has enabled the fabrication of biodegradable devices such as batteries [107] or humidity sensors [108]. Williams et al. introduced fully-printed thin film transistors using carbon nanotubes as channel, graphene as conductor and a crystalline nanocellulose dielectric on a paper substrate [207].

Examples of printed and degradable inorganic semi-conductors in the literature are scarce. Solution-processing of ZnO and sintering at low temperatures has been demonstrated with laser-sintered ZnO NPs [208,209] as well as with various ZnO precursors inks [210,211], although not on bioresorbable substrates. Relatively low-temperature methods have been developed for the printing and sintering of ZnO (150 $^{\circ}\text{C}$) which could be applicable to the more temperature-resilient bioresorbable substrates, such as silk or Na-CMC, for

the fabrication of thin film transistors [25]. Silicon inks have been developed as well from nanoparticles [212] or precursors [213] as well. However, depending on the printing method used, a timely degradation of the silicon appears incompatible with the thicknesses obtained.

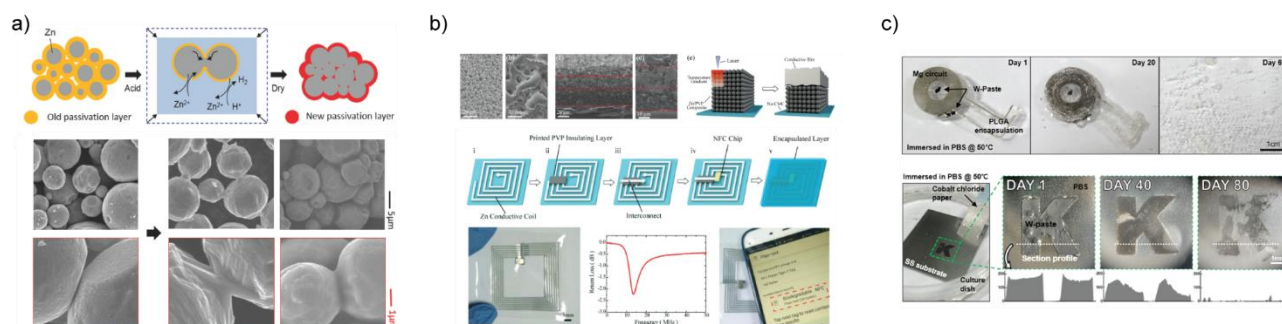


Figure 2.4: Examples of printed bioresorbable conductors and devices. (a) Electrochemical sintering of printed zinc metal, relying on the conversion of zinc oxide and self-exchange of zinc to form bridges between the particles. Reproduced with permission [18]. Copyright (2017), Wiley-VCH GmbH. (b) Laser sintering of printed zinc and demonstration of an antenna using this process. Reproduced with permission [214]. Copyright (2019), Wiley-VCH GmbH. (c) Isotropic conductive paste made of tungsten metal and beeswax. Reproduced with permission under the CC BY-NC-ND license.

The first example of screen-printed bioresorbable metallic conductor are W and Zn microparticles (μ P) pastes that was used for the transient PCB shown in [62]. Conductivity for these pastes is however orders of magnitude lower than the bulk materials, due to the limited contact between the microparticles. The conductivity of the W paste is much higher than that of the Zn paste (in the order of 10^3 S/m versus 10^{-3} S/m). Further examples of screen-printable bioresorbable metal (Zn, Mo, Fe) pastes have been shown, with conductivities below 10^3 S/m. Zn or Fe generally show lower conductivities than those based on W or Mo, due to the lower electronegativities of Zn and Fe causing them to form thicker oxide layers. That being said, other parameters will influence the conductivity of a composite paste, such as volume fraction of metal, particles size and particles morphology [62]. Screen-printable composite pastes based on Mo pastes based on a degradable polyanhydride and metal mixture have also been proposed, with conductivities reaching in the order of 10^3 S/m [215]. More recently, Kim et al. [52] formulated W and Mo pastes with beeswax as a binder, which reach maximal conductivities of $6 \cdot 10^3$ S/m. The use of beeswax allows to increase the functional lifetime of the bioresorbable tracks in solution which is a known problem with bioresorbable electronics [82]. The aforementioned examples of printable pastes have been principally used as soldering paste for connections.

To improve conductivity, sintering, post processing that aims to compact or coalesce the particles in the ink, can be applied [25]. The challenge with these processes is to perform sintering at a low enough temperature so that it is compatible with bioresorbable substrates. This is compounded by the rapid oxidation of transient metals in air and the high melting temperature of their oxides (e.g., ZnO: 1975 °C). The main strategies used for bioresorbable materials include flash sintering and laser sintering, which were described above. These methods have enabled the fabrication of various devices, from humidity sensors to organic electrochemical transistors (OECTs), on substrates with very low glass transition temperatures such as PLA [63,216,217]. In terms of sintering transient printed metals, efforts have focused on zinc, due to its wide availability at low-cost in micro- and nanoparticles form and relatively low melting point (419.5 °C). As a first example of printed bioresorbable conductor, a Zn nanoparticles (NPs) ink was deposited on a glass slide and evaporated with a laser under an inert atmosphere to avoid oxidation. The method is compatible with writing on Na-CMC substrates [218] and yields a satisfying electrical conductivity in the order of 10^6 S/m. Analogously, Zn microparticles were sintered directly on Na-CMC substrates using short laser pulses under argon atmospheres [185], yielding a conductivity in the same order of magnitude. Aerosol-jet printed Zn NPs on resorbable substrates were sintered on Na-CMC using flash sintering, albeit with lower conductivity ($\sim 10^5$ S/m) [219]. This is likely due to thinner layers deposited with AJP (1 $\sim \mu$ m) limiting the energy that can be delivered before excessive heating is caused on the substrate. More recently, an approach was introduced using photonic sintering to vaporize printed zinc NPs from a donor substrate, allowing for freeform conductive zinc deposition with a conductivity reaching $3 \cdot 10^5$ S/m [220].

Room-temperature sintering approaches have also been developed for Zn, making use of acids in the ink to dissolve the native passivation layer [18,221]. The concept of zinc electrochemical sintering was introduced by Lee et al. [18], relying on the interaction between the native oxide layer on the particles and acetic acid. Indeed, acetic acid dissolves the passivation layer and shifts the open-circuit voltage of zinc in water toward the Zn/Zn²⁺ redox reaction. This results in self-exchange of zinc and local welding of the particles. In a similar approach, propionic anhydride, which converts to propionic acid in the presence of water, was also used [221]. Propionic acid is similar to acetic acid, and the use of an acid anhydride allows to activate the reaction with water vapor, reducing potential damage to the zinc traces from the direct acid dispense. To address the same problem, a zinc NPs inkjet printable ink was formulated and the acetic acid solution dispensed by inkjet as well for in situ electrochemical sintering [222]. For all these approaches, the conductivity remains lower than with photonic or laser sintering, reaching values of around 1-3·10⁵ S/m. Another downside of this method is that the electrical properties of the printed layers are unstable and degrade in hot or humid environments [222], likely due to insufficient densification of the particles. These printing and sintering strategies have been utilized to fabricate devices and components such as interconnects or antennas [91,218,221,222]. Some of these processes and devices are illustrated in **Figure 2.4**. **Table 2.4** summarizes recent efforts dedicated to the development of conductive bioresorbable inks, with the printing and sintering strategies used and the resulting electrical conductivities.

Table 2.4: Conductive pastes based on transient metals, with the particle size as well as the printing and sintering methods used, and the conductivities obtained.

<i>Metal</i>	<i>Particles size [μm]</i>	<i>Printing method</i>	<i>Sintering method</i>	<i>Conductivity [S/m]</i>	<i>Reference</i>
<i>Fe</i>	< 10	Screen printing	Electrochemical	10	[18]
<i>W</i>	4 - 6	Screen printing	Drying in air	3.5·10 ³	[62]
	0.5	Screen printing	Drying in air	6.4·10 ³	[52]
<i>Mo</i>	< 10	Screen printing	Electrochemical	6·10 ²	[18]
	1 - 5	Screen printing	Drying in air	1.4·10 ³	[215]
	5 - 100	Screen printing	Drying in air	1.2·10 ³	[223]
<i>Zn</i>	4 - 10	Screen printing	Drying in air	2.4·10 ⁻³	[62]
	0.065 - 0.075	-	Laser evaporation	1.1·10 ⁶	[218]
	< 10	Screen printing	Electrochemical	3·10 ⁵	[18]
	0.5	Screen printing	Heat + photonic sintering	6·10 ⁴	[224]
	0.05	Aerosol jet printing	Photonic sintering	3.5·10 ⁴	[219]
	1.5	Screen printing	Laser sintering	9.7·10 ⁵	[185]
	0.05	Screen printing	Electrochemical	7.2·10 ⁴	[221]
	0.04 - 0.06	Inkjet printing	Electrochemical	1·10 ⁵	[222]
	0.035 - 0.045	-	Flash lamp evaporation	3.5·10 ⁵	[220]

2.4 Summary and contributions

This chapter reviewed the state of the art on bioresorbable electronics, with a perspective on using additive manufacturing techniques for the development of bioresorbable implants embedding electronic functionalities. We introduced the transient materials that can be used, the fabrication methods that have found prevalence in the research on bioresorbable electronics so far, and examples of devices and systems that show their potential in applications where a transient behavior is desirable. Subsequently, we examined additive manufacturing as an alternative approach to fabricate these devices, comprehensively reviewing the techniques employed for the production of implantable and/or degradable electronics. Examples of printed degradable materials and devices were shown, highlighting the approaches that have been taken to circumvent the challenges inherent to the use of these materials. Finally, to conclude this chapter, we will outline the challenges that remain in the field, and the contributions this thesis makes towards digital additively manufactured bioresorbable electronics.

2.4.1 Status of the research on printed bioresorbable electronics

Although a wide range of transient materials has been studied and utilized in the development of both eco- and bioresorbable electronics, fabricating these devices remains in general challenging. Existing methods for overcoming this multifaceted challenge rely on adapting fabrication methods from the semiconductor industry at the cost of scalability. These approaches combining them with assembly processes such as lamination, transfer stamping or using laser-cut metal foils. While, the potential of additive manufacturing techniques for the fabrication of transient electronics has been recognized in recent literature [25,159], examples of functional transient devices remain scarce. Process reliability and repeatability in additive manufacturing remain a problem with respect to more established techniques. Moreover, printed materials often come with lower performance than their conventionally fabricated counterparts, due to imperfections during the deposition or the heterogenous nature of the printed composite layers. These challenges are of course compounded by the use of transient materials, for which inks and processes are not well established. Advancing additive manufacturing for transient materials requires complex optimization and new developments spanning multiple fields: material science, chemistry and ink formulation, printing, electronics, etc. This may explain the relative lack of completely solution-processed functional transient devices that incorporate sensing or actuation functions. Furthermore, the applicability and performance of the printed transient devices shown so far is only minimally characterized, and their functional lifetime is not always clear. Finally, one of the most significant promises of additive manufacturing is the use of digital methods for fast prototyping and customization of transient electronics. Devices can be designed and fabricated seamlessly, without the need for mask fabrication or process adjustment, facilitating the rapid characterization of prototypes. More importantly, 3D digital additive manufacturing allows to create customized devices in terms of form and function, for instance adapting to the complex geometry of internal organs. Despite this, there is no demonstration of the fully digital printing, in a single machine, of multi-material transient bioelectronics.

2.4.2 Research approach and contributions

As highlighted previously, the potential for bioresorbable and ecoresorbable electronics is undeniable, and this novel class of devices may contribute to solving pressing challenges in the next years. The look we had at the state of the art of the research in printed electronics has also highlighted the potential additive manufacturing holds for the cost-effective, facile, scalable, sustainable, and customizable fabrication of transient electronics. In order to realize this vision and address these gaps in the current research, and in agreement with recent reviews [25,159], the following challenges must be addressed:

- **New transient inks must be developed, and their printing and post-processing optimized, notably for metallic layers to reach higher electrical conductivity, repeatability and stability as a goal.** So far, the best printable transient metal methods presented in the literature only reach less than 10 % of the conductivity of bulk zinc, which is still insufficient when compared to the performance of materials deposited by physical vapor deposition. Printed materials exhibiting high electrical conductivity and stability are necessary for the realization of performant antennas, interconnects, electrodes, etc.
- **The range of functionalities for printed bioresorbable electronics must be expanded to go beyond the properties of the materials themselves and include more sophisticated functions like sensing and actuating.** To construct more complex devices, we aim to use several bioresorbable materials (substrates, conductors, dielectrics, encapsulants) integrate them together using additive manufacturing, despite the challenges caused by potential chemical and processing incompatibilities.
- **We aim to achieve the fully digital additive fabrication of bioresorbable electronics.** This would allow to exploit the full potential of 3D digital printing in terms of customizability and versatility. Direct ink writing and treatment parameters need to be thoroughly studied and optimized for the realization of high-resolution structures, with flexible or soft materials that can conform to the inner geometry of the human body.
- **The fabricated functional devices need to be assessed for shelf-life, functional lifetime and mechanical reliability.** The lifetime of transient devices is a key element to determine their applicability as biodegradable or bioresorbable electronics. Previous early reports have shown that printed transient electronics show increased sensitivity to ambient humidity for instance [222]. Further investigations are needed into the topic, and, if necessary, encapsulation/passivation strategies should be developed to ensure sufficient mechanical and electrical stability.

To tackle these challenges and advance the field of printed transient electronics, we carefully evaluated the portfolio of available materials in terms of processibility and printability, and developed printable inks from the resulting selection. A two-step process for the sintering of screen-printed zinc was developed, circumventing the difficulty of achieving high conductivity caused by the native oxide layer, and achieving record conductivity in the published state of the art. The process was confirmed to be compatible with bioresorbable substrates, such as PLA and PVA. We studied the mechanical behavior and the degradation of the electrical properties of the zinc on PLA in air and in saline solution at 37 °C. This demonstrated that the hybrid sintering process results in outstanding electrical stability compared to state-of-the-art electrochemical sintering. The process was utilized to fabricate fully bioresorbable implantable pressure capacitive sensors. We employed a combination of printing and folding techniques, and used POMaC as a soft dielectric layer. These sensors were implemented in a chipless wireless configuration, benefiting from the high electrical conductivity of the processed zinc tracks. A wireless receiver for power transfer was also demonstrated, and an LED and capacitor are integrated on the degradable circuit.

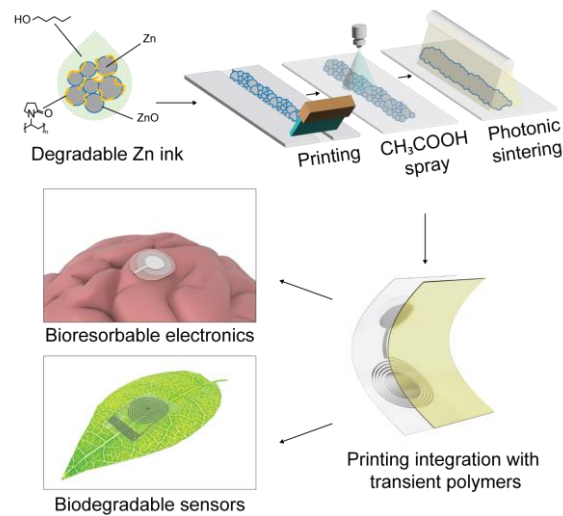
The stability of the printed zinc was exploited for the fabrication of a set of other components such as strain sensor, coils, antenna, interconnects, and, notably, fully degradable and printed resistive temperature sensors. The influence of the photonic sintering parameters on the temperature coefficient of resistance of the printed zinc was studied. They were optimized to maximize the stability and linearity of the response of the sensors to temperature changes. Bioresorbable sensors made of zinc encapsulated in PLA were developed, and shown to appropriately measure temperatures in the physiological range (from 36 to 40 °C) when compared to a

commercial sensor. The sensors were further implemented in an ecoresorbable configuration, on paper with a degradable beeswax encapsulant. The sensors were shown to operate reliably in humid environments from -20° to 40° °C, owing to the beeswax protective coating.

Furthermore, the highly electrically conductive zinc layer was integrated as interconnects with water-resistant carbon-shellac composite and PEDOT:PSS. The fabrication by screen printing and inkjet printing was adapted to produce organic electrochemical transistors (OECTs) on biodegradable PLA substrates. Their electrical characteristics (transistor behavior and transconductance) were found to be in line with those from the non-disposable devices already reported in the literature. These transient OECTs were evaluated as biochemical sensors for ions and glucose detection and shown to degrade in soil over a month. The disposable OECTs were studied with NaCl, KCl, and CaCl_3 , and could detect ion concentration changes from 0.1 to 100 mM with a Nernstian response. We also tested the OECTs for enzymatic glucose detection, and a limit of detection of $5\ \mu\text{M}$ was found.

Finally, the fully 3D printing of transient electronics and sensors by direct ink writing was demonstrated. Materials were assessed for the ink development and carbon the previously introduced carbon-shellac ink was chosen for its resistance to aqueous solution over weeks, allowing functional interfaces in direct contact with bodily fluids. A careful process optimization was conducted to print 3D structures from a UV curable POMaC ink. Multi-material printing was implemented to embed carbon conductors in a POMaC elastomeric matrix. Flexibility of the printed carbon on POMaC at a radius of 3 mm and up to 10000 cycles was demonstrated. The printing process was used to create fully 3D printed multilayer pressure sensors to detect forces up to 1500 kPa. Electrodes array with impedance below $10\ \text{k}\Omega$ at 1 kHz that could be applied for recording of electrical potentials or stimulation for neuromuscular interfaces were also fabricated.

Chapter 3 Zinc hybrid sintering for printed transient sensors and wireless electronics



Transient electronics have emerged in recent years as a potential solution for the increasingly pressing issue of electronic waste, and have shown promise for novel applications in implantable bioelectronics. In this work, we report on a scalable, innovative method, synergistically combining chemical and photonic mechanisms, to sinter printed Zn microparticles and obtain high electrical conductivity. After deposition, the oxide layer around the zinc particles, which impedes particle fusion and conductivity, is reduced using an acidic solution. The removal of the high-melting zinc oxide is followed by a photonic sintering treatment, delivering high-intensity light pulses to the samples, which permits the agglomeration of the zinc particles into a continuous layer. The sintered Zn patterns reach electrical conductivity values as high as $5.62 \cdot 10^6$ S/m. The process allows for reduced energy use and is compatible with temperature-sensitive polymeric and cellulosic substrates. The mechanical flexibility and electrical stability in air and phosphate-buffered solution of the sintered zinc layers are studied. The unprecedented electrical conductivity and durability of the printed zinc traces enable, for the first time, the fabrication of biodegradable sensors and LC circuits fully by printing: temperature, strain, and chipless wireless force sensors, and radio-frequency inductive coils for remote powering. This scalable process enables new avenues for the additive manufacturing of biodegradable electronics and transient implants.

3.1 Introduction

Transient electronics, i.e. electronic components and devices that fully degrade in a given environment without generating harmful byproducts [1,3], show potential in reducing electronic waste [26,225,226], and enable novel bioresorbable implants, eliminating the need for a re-operation [25,31,81]. Different materials such as dissolvable metals [18,82,223], degradable semi-conductors [1,113,227], substrates and dielectrics [24,39,44,63,228] have been proposed. These developments have led to various devices being demonstrated, including batteries [107,151,229], heaters [135,230], transistors [122,142], energy harvesters [64,147], as well as pressure [84,129,144], strain [146], and temperature sensors [21]. Most of these functional biodegradable components and devices rely on microfabrication techniques stemming from the semiconductor industry, and the use of shadow-mask techniques [147] or transfer printing [121] to circumvent the difficulty to pattern functional layers directly onto temperature and solvent-sensitive biodegradable substrates [2]. As an alternative, additive manufacturing techniques have shown promise for the fabrication of flexible transient electronics, especially in domains where large area, cost-effective and low-waste manufacturing is desired. Digital additive manufacturing also presents the advantage of allowing freeform printing on 3D curvilinear surfaces [15] and seamless integration of multi-sensing paradigms [173]. This expands the design possibilities to customizable, deformable or highly conformal sensor networks, which can be self- or remotely powered. These manufacturing methods have the potential to open new possibilities for the fabrication of functional degradable electronic devices, but require joint optimization of printable ink formulation, deposition processes, and post-treatment methods. After deposition of a transient metal micro- or nanoparticles ink, the conductivity is in general very low or non-existent and a sintering step, i.e., a densification of the material without melting to the point of liquefaction, is required [231]. This is especially challenging due to the reactivity of these materials and their tendency to naturally form an oxide layer in air. Only few approaches have been proposed to achieve sintering of printed biodegradable electrically conductive layers. These approaches focus on zinc because of its low melting point and owing to its widespread availability in micro- and nanoparticle forms at affordable prices [18,218,232,219,185,221,222]. Methods applied so far to sinter zinc particles can be classified into two main categories: photonic and electrochemical. Photonic methods are based on the use of high-power lasers or lamps [185,218,219] to selectively heat the metallic layer while minimizing the interaction with the substrate. They are usually restricted by the high-melting ($T_m = 1950\text{ }^\circ\text{C}$) native oxide layer of the Zn particles, which prevents efficient particle agglomeration by maintaining the metallic zinc in a solid shell [214]. Even by applying sintering pulse intensities superior to 10 J/cm^2 , the electrical conductivity reached remains limited [219]. Electrochemical sintering of zinc is a room-temperature method that leverages the interaction between acetic acid [18,222], or analogues such as propionic acid [221], to convert the native oxide layer to Zn ions. The metal ions redeposit between the particles, thereby forming a conductive path. Electrochemical sintering usually yields lower conductivity values (in the order of $1\text{-}3\cdot 10^5\text{ S/m}$) due to the minimal bridging achieved between the particles and the presence of residual binder in the layer. Finally, a recurrent challenge that arises when fabricating complex flexible devices with transient metals is that their reactivity precludes the use of multiple post-processing steps which may damage the metal traces. As a consequence, robust processes need to be developed for the additive manufacturing of eco- or bioresorbable metal traces, compatible with post-processing steps and yielding stable devices with a sufficient time of operation.

In this work, we present a hybrid method for the scalable and additive manufacturing of highly conductive transient metallic zinc traces. After deposition by printing, the native oxide shell of zinc microparticles is reduced by means of an acetic acid solution. The reducing agent is delivered via an optimized spray coating process, with the aim of mitigating the downsides of previously presented dispensing methods [222]. Flash lamp annealing (also referred to as photonic sintering) is used to further sinter the metallic patterns. This approach permits to reach unparalleled electrical conductivities for printed transient metal, up to $5.62\cdot 10^6\text{ S/m}$, only about three times less than the conductivity of bulk zinc ($16.6\cdot 10^6\text{ S/m}$). As an added benefit, the energy delivered to the sample is considerably lower than in previous studies concerning zinc photonic sintering [185,219]. This allows for increased compatibility with lower thermal budget substrates. The mechanical flexibility of the printed traces as well as their stability in environments relevant to their operation are demonstrated. The fabrication of multilayer devices requiring further curing or deposition steps is enabled by the robustness

of the transient metal traces. A set of printed physical sensors, including resistive strain and temperature sensors, as well as a wireless capacitive force and pressure sensor are reported. The process presented in this work advantageously leverages chemical and physical mechanisms to obtain highly conductive (comparable with heat-cured copper or silver inks [233]) transient metal traces. These advances unlock new avenues for environmentally friendly internet-of-things components and bioresorbable electronic implants fabricated by additive manufacturing.

3.2 Results and discussion

3.2.1 Hybrid sintering of printed zinc films

The sintering method that is presented here is compatible with commercially available microparticles obtained through a powder atomization process, and no further step such as ball milling is necessary. These zinc microparticles (2 μm average diameter) are mixed with polyvinylpyrrolidone (PVP) as a binder and pentanol as a solvent to form the printable ink. The hybrid sintering relies on a two-step process as follows (**Figure 3.1(a)**): (i) acetic acid treatment by spray coating, to reduce the oxide layer and (ii) photonic sintering, where energy in the form of high intensity pulsed light is delivered to achieve particle agglomeration into a continuous metallic trace. SEM imaging (**Figure 3.1(b)**) is used to show the evolution of the microstructure of the zinc printed layer between the processing steps. Separated particles can be clearly observed just after printing and solvent drying. The acid sintering only slightly modifies the microstructure, with conductive bridges formed between particles in the order of a few hundreds of nanometers, as observed in previous work [18]. Conversely, after the application of pulsed light, microparticles are shown to have fused and aggregated into a continuous layer. Preliminary experiments conducted on printed zinc resistors on polyimide show that photonic sintering delivers an improvement in conductivity by more than one order of magnitude compared to solely using electrochemical sintering (**Figure 3.1(c)**), whether conducted under air or nitrogen atmosphere. The synergistic interaction between those treatments, i.e. the removal of the oxide layer and the formation of bridges between the particles considerably enhances the effect of the photonic sintering, allowing unprecedented conductivity for printed biodegradable metallic films. The results in air and N_2 atmospheres are comparable, although a higher conductivity (~50 % higher) is reached in an inert atmosphere. This method of sintering is compatible with various substrates used in standard, paper, and degradable electronics (**Figure 3.1(d)**). This versatility as well as the remarkable electric conductivity that is achieved with the hybrid sintering process makes it suitable for the fabrication of degradable radio-frequency devices. Notably, we demonstrate the first fully printed bioresorbable LC circuits applied to chipless pressure sensing as well as a degradable wireless power receiver (**Figure 3.1(e)**).

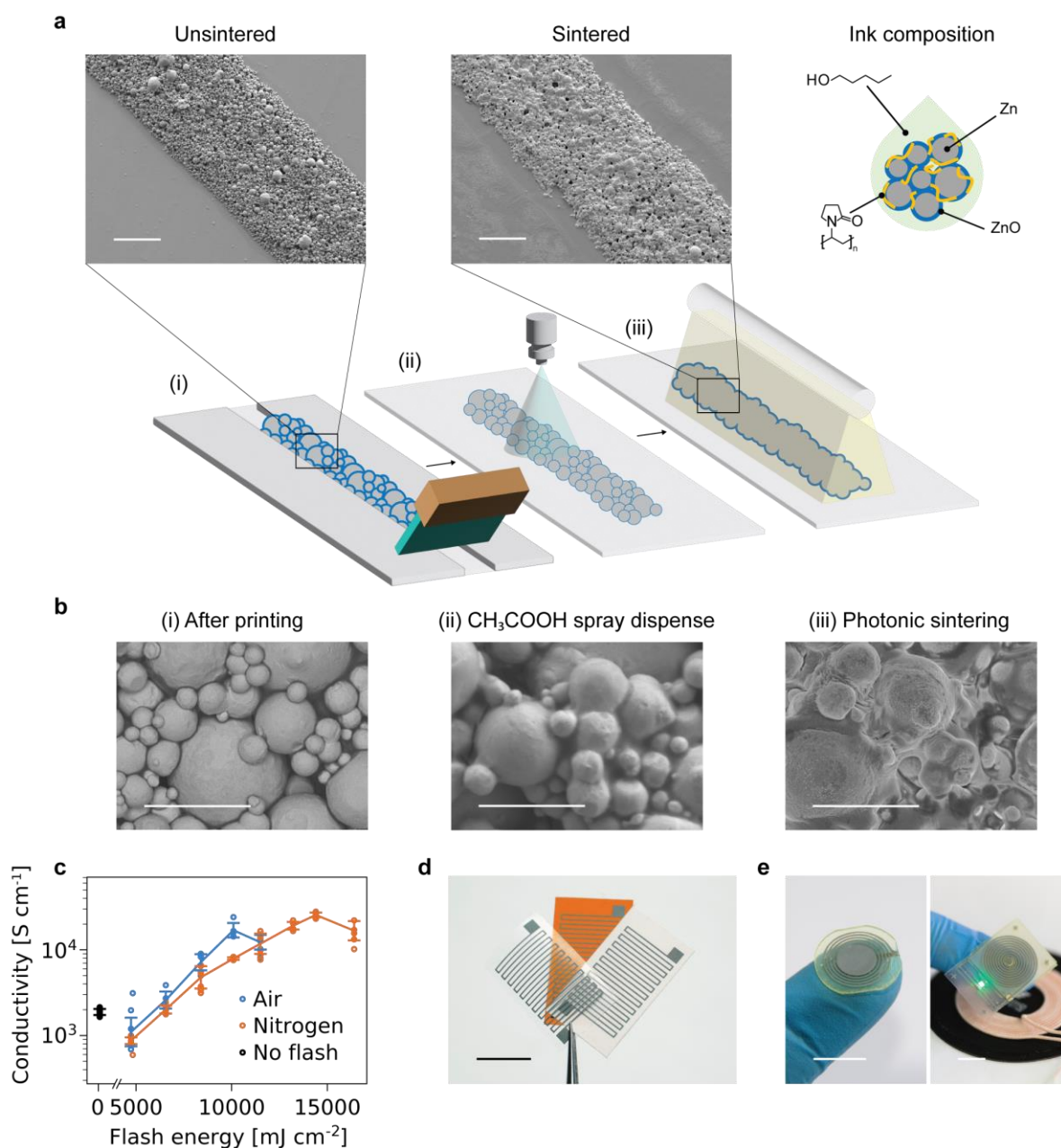


Figure 3.1: Description of the hybrid zinc sintering process. a) Illustration of the steps of the hybrid sintering process (i) deposition by printing (ii) acetic acid spray coating (iii) photonic sintering. Scale bars: $100\ \mu m$. b) Microstructure of the Zn by SEM after each processing step. c) Measured conductivity (with standard deviations) of Zn traces at different pulse energies and under air or nitrogen atmosphere. Scale bars: $10\ \mu m$. d) Printed Zn resistors on polyimide, paper, and polylactic acid substrates. e) (left) Bioresorbable radio-frequency chipless pressure sensor (right) wirelessly powered LED circuit based on a Zn secondary coil on a degradable substrate. Scale bars are $10\ mm$.

3.2.2 Optimization of sintering parameters

A first study on the process parameters used for the electrochemical and photonic sintering steps was performed on resistors printed on polyimide substrates. Firstly, we examined the electrochemical treatment of the printed layers by acetic acid spray coating. The use of spray coating relies on limited and uniform acid deposition to avoid the partial dissolution of the unsintered zinc patterns, which is a known issue when using a drop coating process to deliver the acidic solution [221]. Moreover, the electrochemical sintering process occurs in a short timeframe (less than one minute) [18]. We observed that fast drying (on a hot plate or by application of

a stream of N_2) was critical to avoid damage to the metal traces from prolonged exposure to the aqueous solution. As a consequence, several coatings and drying cycles must be applied to reach a plateau conductivity in the order of $2 \cdot 10^5$ S/m. As shown in **Figure 3.2(a)**, the improvement in conductivity can be obtained only by alternating the application of acetic acid with a drying step in N_2 . As can be seen, the resistance initially increases after dispensing, as the porous track is soaked with the acid solution, and nitrogen drying causes the solution to dry and the Zn ions to deposit between the particles. A saturation in conductivity is reached after the application of 5 to 6 of these cycles (**Figure 3.2(b)**). The concentration of the PVP binder in the inks has an influence not only on its printability but also on the conductivity achieved following the electrochemical sintering step, as observed previously [221]. Therefore, keeping the solvent to solid material ratio constant, the effect of the chain length and the concentration of PVP with respect to the amount of metallic powder on the conductivity of the films was evaluated (**Figure S3.1**, Supporting Information). The chain length was shown to have minimal influence on the conductivity in the chosen range. On the contrary, the concentration of binder was shown to influence the obtained electrical conductivity. A ratio of 0.04 g of PVP per g of Zn was deemed to be optimal and was chosen for further inks formulation. The conductivity obtained with the spray treatment is comparable with results previously obtained with electrochemical methods in the literature [18,221,222]. The conductivity reaching a plateau serves as a validation of the dissolution of the oxide layer, as no more oxide is converted to metallic zinc. This is critical for achieving efficient particle agglomeration and high conductivity by photonic sintering. The cycling of the acid treatment could be seen as a limiting factor for the scalability of the process. However, it is likely that the dispensing could be optimized for throughput outside of a research setting. Moreover, the reducing agent may be incorporated to the ink in future work, to circumvent the necessity of spray dispensing altogether.

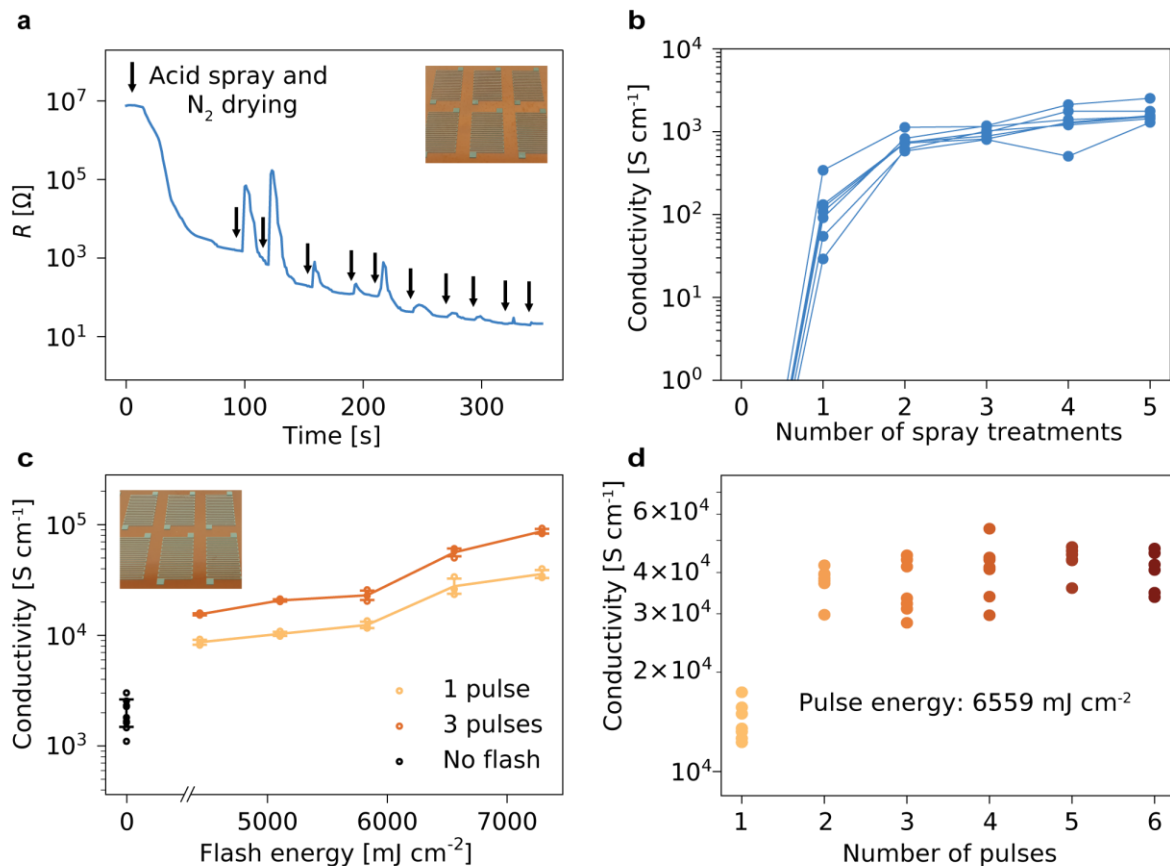


Figure 3.2: Study of the sintering process on screen-printed zinc layers. a) Real-time measurements of the resistance of a Zn line under subsequent acetic acid spray coatings and nitrogen drying. b) Conductivity of Zn resistors (with standard deviations) on polyimide after electrochemical treatment cycles. c) Conductivities of Zn resistors treated with electrochemical and photonic sintering, for 1 and 3 pulses of various energies. d) Influence of the numbers of pulses on the conductivity of sintered Zn for a given pulse energy of $6559\ mJ/cm^2$ ($n = 7$ per pulse).

The second step of the hybrid process, photonic sintering, was studied varying the pulse energy and the number of pulses delivered (**Figure 3.2(c)**). The study was conducted under a nitrogen atmosphere, to avoid re-oxidation effects, notably when studying the effect of multiple photonic pulses. Moreover, as shown above, sintering in a nitrogen atmosphere leads to higher conductivities, which we hypothesize arise from the fact that the inert atmosphere allows to limit zinc oxidation, which may hinder conductivity [234]. As can be seen in **Figure 3.1(c)**, higher pulse energies appear to be necessary to reach maximal conductivity in the case where sintering is conducted under an inert atmosphere. This is however likely due to the increased distance from the lamp caused by the sealed chamber used, therefore decreasing the effective energy delivered to the samples. The energy delivered in one pulse of photonic sintering depends on the voltage supplied to the xenon lamp and the irradiance profiles of the pulses applied are given in **Figure S3.2** in the Supporting Information. The timing between the spray coating and the photonic sintering steps is of importance, however, a precise study of its influence is difficult as it would depend on the exact drying conditions of the acid (atmosphere, flow), as well as on the morphology of the printed layer, notably dimensions and porosity. We observed that if photonic sintering was conducted after more than one hour of drying in ambient air after the acid application, the electrical conductivities obtained started to decline, as a result of the oxide layer reforming. We hypothesize that residual acidic solution in the metallic microparticles layer is critical to avoid re-oxidation before the photonic sintering step. Applying photonic sintering generally increases the electrical conductivity of the zinc traces by one to two orders of magnitude compared to samples that underwent only electrochemical sintering, and the increase is more marked when several light pulses are delivered (**Figure 3.2(c)**). The conductivities that were measured reached average values as high as $5.62 \cdot 10^6$ S/m, when 3 pulses of 6559 mJ/cm² were delivered. To our knowledge, this is the highest conductivity value obtained for printed zinc layers (**Figure S3.3**, Supporting Information). The values obtained for the highest studied pulse energy (7299 mJ/cm²) are not considered as this level of energy was causing partial destruction of the resistors and inferior yield. At this pulse energy, a yield of 25% was observed versus near 100% for lower energies. Indeed, increasing the pulse energy will lead to increased sintering as the metal layer approaches its melting point [235], but an energy that is too high will lead to considerable melting and flowing of the metal, which causes interruptions in the conductive line. Conductivity values for samples sintered above 7300 mJ/cm² could not be measured due to damages and cracks occurring in the layers at these high levels of energy, as observed through optical microscopy. Using several light pulses was observed to improve conductivity for the same pulse energy, however, the improvements started to plateau after two to three light pulses (**Figure 3.2(d)**). This behavior could be explained by an equilibrium being reached between the damage caused to the tracks by further energy being delivered and the improved particle cohesion with more pulses. The variability in conductivity between samples is in line with previous studies on photonic sintering [219], and could be further reduced by using smaller metal particles or a more controlled acid dispensing technique. When observing the cross-section of the sintered Zn thick films under a scanning electron microscope, the particles display a degree of agglomeration that varies across a gradient, with the first 5 to 10 μm forming a cohesive layer independent of thickness (**Figure S3.4**). We note that a more than twice higher conductivity is obtained for screen printed lines (17 μm average thickness) compared to stencil printed lines (41 μm thickness, see **Figure 3.1(c)**), which was measured to be $2.55 \cdot 10^6$ S/m. This may be due to enhanced sintering on the uppermost zinc layer; however, the process is demonstrated to be amenable to varying pattern thicknesses. As can be expected, the energy required for optimal sintering of the thinner layers is lower. In order to verify that the resolution of the lines is maintained throughout the process, the profile of the lines was compared between each treatment step (**Figure S3.4**) and no significant difference in area was observed. Moreover, good adhesion between the sintered zinc layer and polyimide, paper and PLA substrates was observed with a standard peeling scotch test (**Figure S3.5**). In order for this method to be usable for films printed with other deposition methods, it would require to be compatible with the use of nanoparticles, as methods such as aerosol-jet printing, inkjet printing or direct ink writing require smaller particle sizes. We hypothesize our method to be compatible with the processing of nanoparticles films, in particular because photonic methods are amenable to the sintering of nanoparticles [185,219], as the reduction in particle size comes with a reduction of the melting point, and, as a consequence, of the required energy to attain efficient sintering. Preliminary tests with 500 nm Zn particles were conducted and conductivities reaching $3.3 \cdot 10^6$ S/m were obtained, with the same ink formulation as the one aforementioned and using a lower pulse energy (5.1 J/cm²).

3.2.3 Flexibility and stability of fully degradable zinc traces

Importantly, to take full advantage of this process to sinter transient metal, it needs to be compatible with temperature- and solvent-sensitive bioresorbable and biodegradable substrates. This is possible with the two-step sintering method presented here, thanks to the use of flash sintering, which allows to selectively heat the metal tracks with minimal energy being directly transferred to the transparent polymeric substrates [236] as well as cellulosic substrates [237]. Moreover, the use of spray-coating to dispense the acid is also beneficial by limiting the amount of aqueous solution on the water-sensitive substrate, compared to methods such as drop-casting for instance [18]. The hybrid method we introduce here is compatible with flexible paper substrates, which are of interest in the context of biodegradable and eco-friendly electronics [238]. Printed Zn traces processed on paper reach an average electrical conductivity of $2.00 \cdot 10^6$ S/m (**Figure S3.6**). Furthermore, we study the sintering of zinc on thin layers of bioresorbable polymers. The results of zinc hybrid sintering poly(vinyl acetate) (PVA) and polylactic acid (PLA) are shown in **Figure 3.3(a)**. Similar maximal mean conductivities of 2.61 and $2.43 \cdot 10^6$ S/m are obtained, respectively for PVA and PLA, following three light pulses with an energy of 8390 mJ/cm². Remarkably, these high values in electrical conductivities are similar to the results achieved on polyimide. The slight reduction in terms of conductivity that is observed may be due to a degradation of the interface substrate-zinc layer, which could cause deformation and cracking of the zinc resistors.

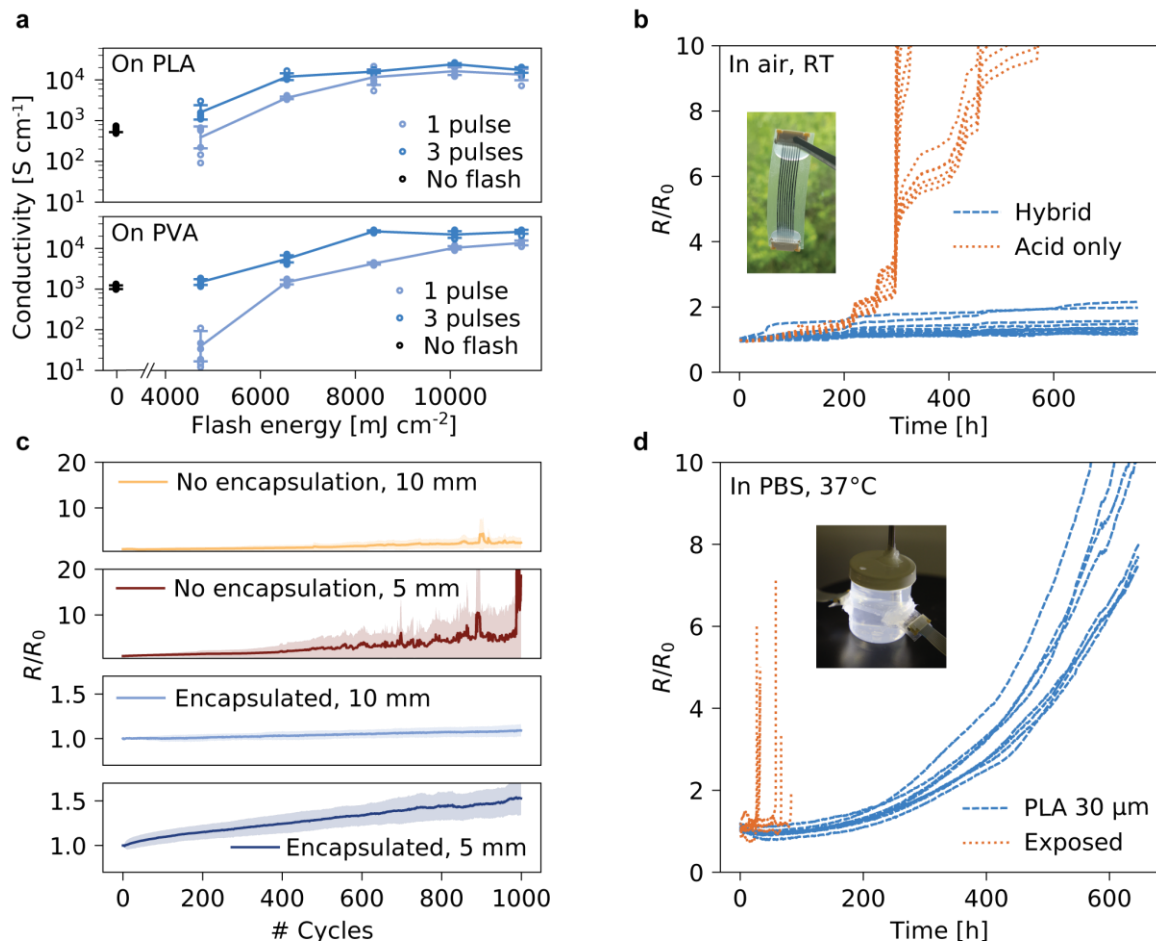


Figure 3.3: Hybrid sintering of Zn and durability of the traces on transient substrates. a) Electrical conductivity (with standard deviations) for sintered Zn traces as a function of energy and number of photonic pulses, on PVA and PLA. b) Evolution of the resistance for unencapsulated Zn samples ($n = 14$ per condition, 40×0.3 mm) stored at ambient conditions, as a function of the sintering protocol. c) Change in resistance for sintered Zn lines on PLA ($n = 5$ per condition, 50×0.5 mm, with a ~ 40 μm thickness), for radii of 5 mm and 10 mm, with and without PLA encapsulation. d) Evolution of the resistance for encapsulated and unencapsulated sintered Zn tracks ($n = 8$ per condition, 40×0.3 mm) in PBS at 37 °C.

Ideally, transient electronic devices would display stable function during their lifetime and rapid degradation upon the introduction of a specific stimulus or at the end of the desired lifecycle [67]. Experiments for zinc samples made on PLA were conducted to assess the electrical durability of the traces in conditions reproducing the operating environments for applications such as biodegradable electronics (e.g., for smart packaging or environmental monitoring) and bioresorbable electronics (e.g., smart implants for post-surgical monitoring). In the case of samples that were only sintered electrochemically, the conductivity of the Zn traces changes in a non-linear way after a week, and a tenfold increase in resistance is already attained after 300 to 500 hours of exposure to ambient air. Conversely, the Zn traces that were fabricated with hybrid sintering and without encapsulation display a much more stable electrical conductivity for the period of measurement (31 days) with the resistance increasing by a factor of 1.4 only, in air at ambient conditions (**Figure 3.3(b)**). This difference can be explained by the increased aggregation of particles in the case of hybrid sintering, which reduces the impact of the reoxidation process, resulting in a lower relative loss of conductivity. For Zn traces that were only electrochemically sintered, the smaller bridges formed between particles are converted back to ZnO, thereby reducing the conductivity of the layer. The proposed mechanism is illustrated in **Figure S3.7**. When aiming for real-world electronic applications, encapsulation is often needed and hybrid sintered Zn samples that were encapsulated with blade-cast PLA displayed an average loss of conductivity of 12 % after 31 days at ambient conditions (**Figure S3.8**). With the aim to study the usability of the process in the fabrication of transient implantable electronic, the durability of hybrid sintered Zn lines was assessed in a sealed vial containing phosphate-buffered solution (PBS) at 37 °C, which emulates *in vivo* experiments (**Figure 3.3(d)**). The conductivity of unencapsulated zinc traces degrades by an order of magnitude within 46.6 h on average, as they disintegrate rapidly in an aqueous medium [82]. With a 30 μm encapsulation considerably reducing water permeation, the resistance gradually increases, and it takes on average 28 days to reach a loss of conductivity of 90%. In line with previous work, the degradation of transient metal is rapid in bodily fluids and the choice of the encapsulation with respect to its water permeability and degradation speed is key to maintain function for the amount of time required by specific applications [24]. It is important to note that the degradation in conductivity in the porous metallic layer does not directly correspond to physical degradation. The rate of zinc corrosion in various environments has been characterized in other studies [82,84]. Considering a layer of zinc with a thickness of 40 μm without encapsulation and a constant mass loss rate per unit area rate in PBS at 37°C of 0.025 mg/(cm² h) [84], the time for the full resorption of the zinc layer could be estimated to 48 days.

In order to fabricate reliable transient devices, the mechanical flexibility of the metallic interconnects is an important feature. In the case of inks that are only chemically sintered at room temperature, the presence of binder in the layer may contribute to the flexibility of the conductive patterns by acting as a plasticizer [221]. However, here, the flash sintering step likely vaporizes the PVP binder [239]. The hybrid sintered Zn tracks can be bent down to a radius of 3 mm without loss in conductivity (**Figure S3.9** in the Supporting Information). The mechanical flexibility of the printed Zn lines, with and without encapsulation, was also evaluated by applying repeated bending cycles (**Figure 3.3(c)**). As expected, encapsulated samples exhibit better resilience to repeated bending, as the neutral plane is shifted closer to the metal line, and the polymeric encapsulation likely reinforces the porous metallic layer [18]. Indeed, in the case of encapsulated samples bent at a radius of 10 mm, the resistance increases by 9 % after 1000 cycles at 0.5 Hz, as shown in **Figure 3.3(c)**, while the resistance of unencapsulated samples more than doubles after 1000 bending cycles. The increase in resistance under fatigue bending is attributed to the formation and propagation of micro-cracks in the metallic line [240].

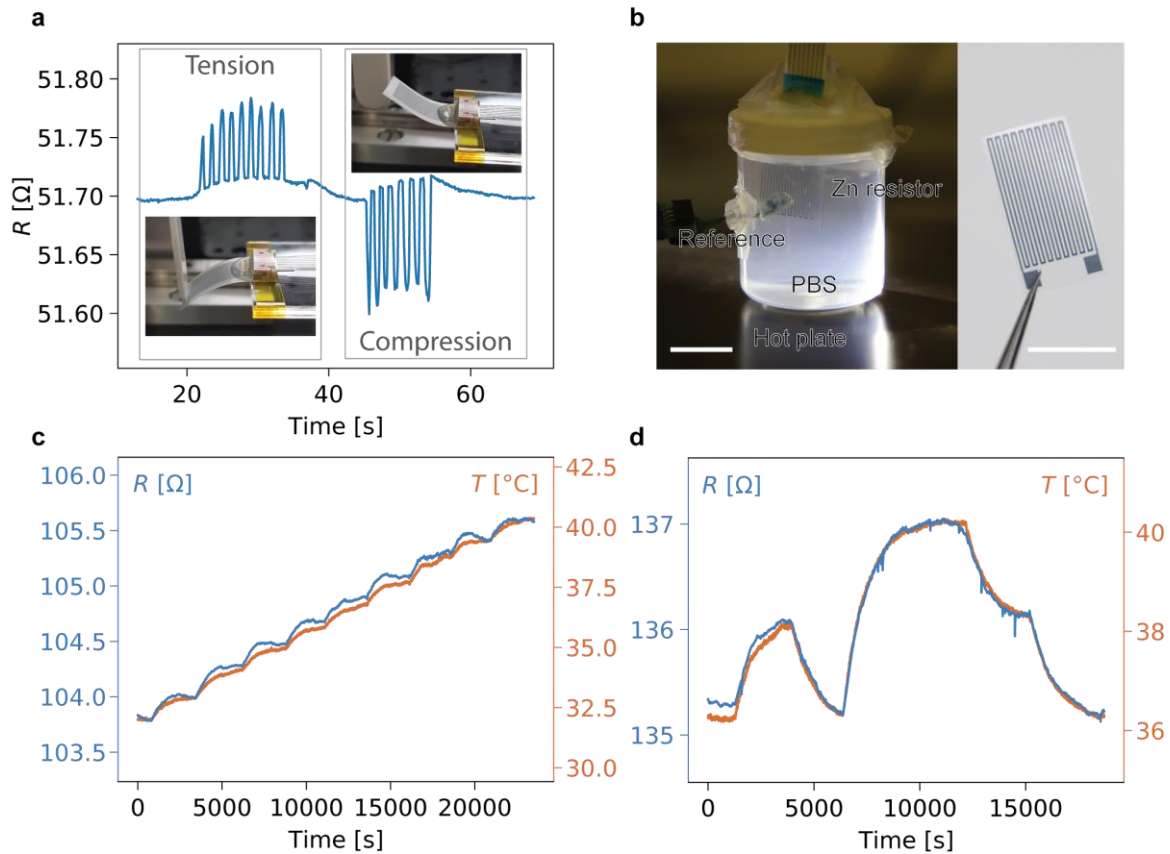


Figure 3.4: Transient resistive physical sensors fabricated from printed Zn encapsulated in PLA ($R_0 = 89.6 \pm 56.4 \Omega$, $n = 4$). a) Zn strain sensor submitted to compressive and tensile cycles (insets). b) Zn temperature sensor in a vial of PBS, with a reference temperature sensor. Scale bars are 10 mm. c) Zn resistance change (blue) following an increasing temperature in PBS (orange). d) Zn resistance change (blue) with an arbitrary change in PBS temperature (orange) around physiological temperatures.

3.2.4 Resistive and capacitive wireless transient sensors

The enhanced electrical conductivity, electrical stability, and flexibility, reached with the hybrid sintering method of the printed zinc films can be exploited to fabricate simple transient resistive sensors on PLA. **Figure 3.4(a)** shows a resistive strain sensor undergoing repeated bending in compression and tension. The resistance value varies by approximately $\pm 0.2\%$ and returns to the baseline value upon release of the sensor. The temperature behavior of the zinc degradable resistors was studied with the aim of fabricating resistance thermometers. The change in resistance for temperatures up to 60°C was measured (**Figure S3.10**, Supporting Information). Zn lines that underwent hybrid sintering show a stable behavior under temperature changes, as opposed to electrochemically sintered traces. A linear relationship between the changes in resistance and temperature was observed for Zn resistors. The temperature coefficient of resistance (TCR) of the printed zinc after hybrid sintering was calculated to be high at $0.00316\ 1/^\circ\text{C}$, which is close to the TCR of bulk zinc [241] ($0.00385\ 1/^\circ\text{C}$) as well as that of standard platinum-based temperature sensors [242], further validating the efficiency of the hybrid sintering method. **Figure 3.4(b)** shows such a temperature sensor operating in PBS solution placed on a hotplate, with the temperature in the solution controlled with the aid of a commercial temperature sensor (Sensirion). The change in resistance of the two sensors was measured for variations of temperature around 37°C . The resistance varies linearly with the temperature and the sensors are sensitive enough to detect small changes in temperature within the physiological range (**Figure 3.4(c)**). The fully degradable zinc-based resistors demonstrate good tracking of the temperature in agreement with the reference data (**Figure 3.4(d)**). Although the proposed resistive sensors are sensitive to various physical inputs, strategies have been proposed to address this challenge [243]. In our case, different designs could be used to obtain

different sensitivities to temperature and strain for instance [244] (e.g. meander and serpentine), with the aim to fabricate a fully bioresorbable multi-sensor platform.

Finally, we demonstrate that the zinc layers as sintered here are compatible with the fabrication of advanced devices requiring further curing and assembly steps, such as multilayer soft wireless sensors. The hybrid sintering of the zinc layer is implemented to realize original device designs, such as those shown in **Figure 3.5**. Transient capacitive pressure sensors relying on a soft bioresorbable elastomer poly(octamethylene maleate (anhydride) citrate) (POMaC) [38] as a dielectric layer are presented. The POMaC pre-polymer was synthesized as in previous works and an exemplary $^1\text{H-NMR}$ spectrum is shown in **Figure S3.11** in the Supporting Information. POMaC is a soft elastomer which has been used in past publications as an transient encapsulation, substrate or structural material [79,144,146,201], owing to its stretchability and ease of processing by ultraviolet (UV) photopolymerization. The design of the uniaxial pressure sensor is based on a parallel plate capacitor architecture, with the POMaC layer acting as a deformable dielectric, which compresses under pressure leading to an increase in capacitance. A facile fabrication process was developed, leveraging the dual cross-linking mechanism of POMaC and the flexibility of the substrate and printed layers. As shown in **Figure 3.5(a)**, the metallic plates and contact pads for the capacitive sensors were printed and treated on PLA, with the POMaC pre-polymer deposited on top by blade casting. The pre-polymer was cured by UV photopolymerization, yielding a solid but tacky polymeric layer. The assembly was then folded with the POMaC layer on the

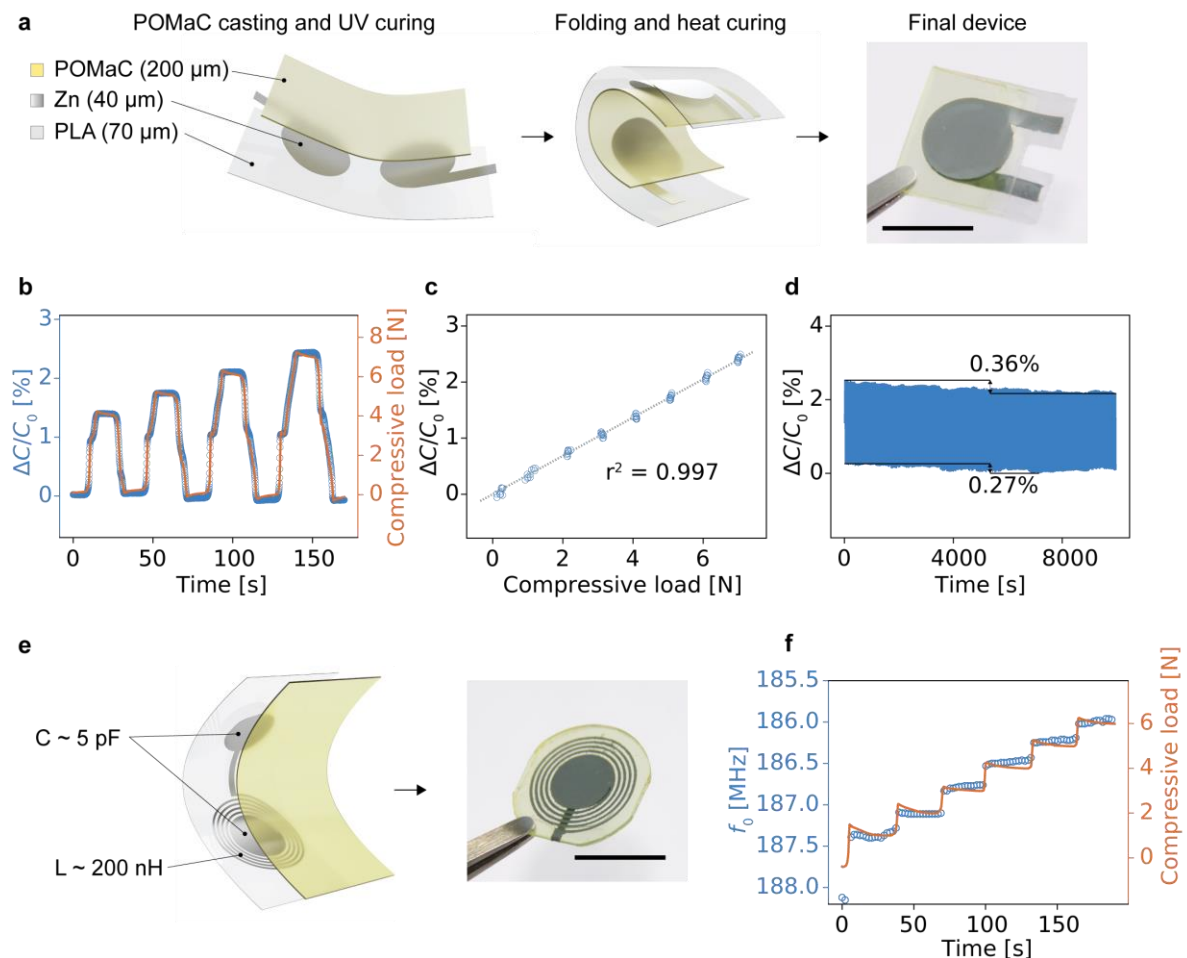


Figure 3.5: Bioresorbable capacitive sensors based on zinc hybrid sintering and soft elastomer POMaC. *a)* Schematic of the fabrication and picture of the Zn-POMaC capacitive sensor. Scale bar: 10 mm. *b)* Capacitive response of the pressure sensor under compressive load. *c)* Relative change in capacitance over 10 cycles for forces up to 7 N. *d)* Cycling of a capacitive sensor for 10000 s (0-4 N, 40 s period). *e)* Schematic and picture of the Zn-based RLC sensing circuit. Scale bar: 10 mm. *f)* Response of the wireless pressure sensor in resonant frequency change under compressive load.

inside and further allowed to cure and bond at 80 °C for 48 h. The Young's modulus of POMaC after UV and heat curing was measured to be 1 ± 0.2 MPa and its relative permittivity ϵ_r was estimated to be 6.9 ± 0.4 . The sensors were tested for forces up to 10 N and the response in capacitance followed the applied force closely and maintained a stable baseline (**Figure 3.5(b)**). The capacitive devices shown here had an initial capacitance of 15.5 ± 3.4 pF ($n = 5$) and the change in capacitance was linear ($R^2 = 0.997$) with the force applied, with a sensitivity of 71.4 fF/N (**Figure 3.5(c)**). This corresponds to a relative sensitivity of 0.00035 1/kPa, which is on the lower end of the state of the art for bioresorbable pressure sensors [245]. However, these sensors rely on micro-/nanostructured dielectrics that could be implemented in future developments to reach higher sensitivity. The device was also evaluated under cycling conditions for 2500 cycles with a duration of 40 seconds and an amplitude of 4 N (**Figure 3.5(d)**). The maximal value of capacitance recorded during the whole cycling period varied by 0.36 % and the baseline by 0.27 %. The change of performance of the sensors over longer periods of time would depend on the evolution of the viscoelastic properties of the POMaC dielectric [246]. This would in turn depend on the encapsulation of the sensor and the conditions of operation [32], and more research on the degradation of bioresorbable elastomers is needed to systematically evaluate the long-term performance of the sensors. Bioresorbable sensors are envisioned for applications in post-operative monitoring or regeneration, and while transient metallic wires and connections can be used to interface them [124], wireless powering and communication are a desirable option to minimize invasiveness. Therefore, a similar design with a zinc coil in series was fabricated (**Figure 3.5(d)**), relying on the same folding process. The sensing relies on the shift in the resonant frequency of the series RLC circuit formed by the Zn-POMaC capacitive element characterized above and the Zn antenna. This allows to create a fully bioresorbable chipless circuit to sense forces and pressures, taking advantage of the higher conductivity obtained with the hybrid sintering process. **Figure S3.12** in the Supporting Information shows the return loss (S_{11}) of typical devices as measured with a custom-made silver antenna on FR4, and they have a resonant frequency of 154.7 ± 3.3 MHz. The response is comparable to the soft capacitors shown above, with the resonant frequency shift (320 kHz/N) being proportional to the applied force (**Figure 3.5(e)**). A similar process was applied to manufacture the degradable wireless power receiver shown in **Figure 3.1(e)**. In order to demonstrate the possibility to integrate silicon-based dies with the degradable electronic receiver and board, an LED and a capacitor were soldered using a room-temperature cure degradable Zn-based paste. The double-sided Zn coil separated with a POMaC layer was measured to have an inductance of 3.2 μ H and the LED could be powered at a distance of up to approximately 60 mm. A similar setup shown in previous research was used to drive the primary coil [131], and the peak-to-peak voltage elicited in the biodegradable receiver as a function of the distance to the primary coil is shown in **Figure S3.13**.

3.3 Conclusions

The hybrid approach for the sintering of printed transient metal traces presented in this work addresses several challenges related to the fabrication of degradable electronic devices on temperature and water-sensitive substrates. The combination of two complementary sintering approaches, namely electrochemical and photonic, allows to overcome the disadvantages of each method and achieve outstanding particle agglomeration. Indeed, hybrid sintering enables the highest electrical conductivity shown thus far for printed transient metal, as well as a high temperature coefficient of resistance, owing to the enhanced particle cohesion. The latter results in electrically durable conductive traces exhibiting unparalleled stability in air, even without encapsulation. The reliability of the sintering process in combination with the stability of the printed zinc enable the realization of a wide range of original and both fully printed and biodegradable physical sensors, notably transient temperature and wireless pressure sensors, as well as RF coils and antennas. The study presented here paves the way to cost-efficient and eco-friendly printed sensors and transducers for applications such as supply-chain or environmental monitoring as well as transient implants processed using digital additive manufacturing.

3.4 Experimental section

Preparation of Zn-based inks

Zn microparticles (2 μm average diameter, Sigma Aldrich), polyvinylpyrrolidone (Sigma Aldrich, $M_w=360\text{K}$ or 2000K) and Pentanol (Sigma Aldrich) were mixed at varying weight ratios (25:1:5 for the final formulation). The ink was homogenized with a planetary mixer (Thinky ARE-250) at 300 rpm for 30 minutes. It was stored at 4 $^{\circ}\text{C}$ and brought to room temperature and homogenized at 300 rpm for 10 minutes before printing.

Preparation of substrates and encapsulation layer

The substrates used in this study are polyimide (DuPont, Kapton[®] 125 μm), biodegradable paper (Arjo-Wiggins Powercoat XD, 200 μm), polylactic acid (Ingeo[™] Biopolymer 4032D) and polyvinyl alcohol (Sigma-Aldrich, Mowiol 4-88). For the preparation of PLA films, pellets were dissolved in 1,4 dioxane (Sigma-Aldrich) overnight at 50 $^{\circ}\text{C}$ under stirring to obtain a 15 wt% solution. Films of PLA were prepared by blade-casting the solution on a standard 4-inch single-side polished silicon wafer at a speed of 2 mm/s with a gap of 1000 μm to obtain films of 70 μm in thickness, after overnight drying. 25 wt% solutions of PVA were prepared by dissolving PVA for 3h in DI water under stirring. The PVA films were cast as described above, with a gap of 600 μm to obtain films with a thickness of 75 μm . Before printing, all substrates, except the paper, were first activated with an oxygen plasma treatment for 60 seconds at 200 W at 40 kHz (Diener). For the encapsulation of the sintered Zn traces, the same PLA solution was blade-casted with a gap of 500 μm , to yield an encapsulation of approximately 35 μm in thickness.

Printing of Zn patterns

For the stencil printing, one-sided polyethylene adhesive tape (Nexus G20, 80 μm) was cut with the desired patterns with a CO₂ laser (Trotec Speedy300). The Zn ink was applied with a silicone squeegee and left to dry for 1 hour, after which the stencil was peeled off from the substrate. For screen printing, custom stainless steel meshes (Serilith) were used, and the ink was applied through the stencil with a silicone squeegee, at a distance of 500 μm from the substrate. The traces were left to dry for one hour before further processing.

Treatment of Zn patterns

Acetic acid (10 vol% in de-ionized water) was spray-coated on the Zn traces using an airbrush (Harder & Steenbeck, 0.2 mm nozzle, at a distance of approximately 10 cm from the substrate) supplied by 2 bar N₂ pressure, followed by 2 minutes drying under nitrogen. This spray-coating/drying cycle was repeated a total of 5 times. In the case where the process atmosphere was controlled, the samples were placed in a custom chamber that was purged with nitrogen for 45 seconds. The photonic sintering treatment (Novacentrix PulseForge 1200) comprised pulse energies ranging from 3107 to 12867 mJ/cm² and between 1 and 6 pulses were delivered.

Material characterization

The thickness and morphology of the printed Zn patterns were characterized using a laser scanning confocal microscope (Keyence VK-X1000). The microstructure of the lines with different treatments was inspected by SEM (JEOL JSM-7500TFE). For SEM inspection of sintered Zn thick films, printed patterns were cleaved after rapid cooling in liquid nitrogen. The resistance of the Zn lines was measured using a tabletop multimeter (Keysight 34401A). To avoid contact resistance effects, 4-wire measurements were performed with custom Kelvin probes. For bending tests, Zn lines were stencil-printed, sintered, and encapsulated as described above if required, the outlines of the samples were laser-cut and the samples were peeled off from the silicon wafer. A custom setup consisting of clamps and a linear motor was used. The adhesion test was performed according to ASTM F1842-15, on 2 \times 2 mm² sintered Zn squares on polyimide, paper and PLA. For the degradation tests, Zn lines were fabricated as described above and soldered to the pads of ZIF connectors using silver epoxy (Epotek E4110). The connection was encapsulated in epoxy resin and the samples were released and

placed in phosphate-buffered saline at 37 °C, while the resistance values were measured with a data logger switching unit (Keysight 34970A).

Temperature coefficient of resistance measurements

Zn resistors were patterned by screen printing and sintered using the two-step process presented above. The resistance was monitored continuously with a digital multimeter (Keysight 34401A), and reference temperature was acquired using a commercial sensor (Sensirion SHT4x). The temperature was varied in a custom-made chamber (or a plastic vial in the case of experiments conducted in PBS) with the help of a hot plate.

Pressure sensors fabrication and characterization

The different designs for the pressure sensors were printed with a laser-cut stencil and treated with the aforementioned sintering process. POMaC was synthesized as previously described. Maleic anhydride, citric acid and 1,8 octanediol (all from Sigma-Aldrich) were mixed at a molar ratio of 3:2:5 in a three-necked flask. The mixture was heated to 160 °C (under nitrogen flow and 200 rpm stirring) until the reagents were fully melted and then reacted at 140 °C for 3 hours. The pre-polymer was dissolved in THF and purified by drop-wise purification in DI water, decanted and dried. The pre-polymer was mixed with 5 wt% of the photoinitiator Irgacure 2959. The POMaC pre-polymer/photoinitiator mixture was then blade-cast with a gap of 500 µm and a speed of 3 mm/s and cured under UV (Proma 140001, 60 W, 365 nm) for 20 minutes. The outlines of the sensors were then cut with a laser engraver (Trotec Speedy 300), they were then gently peeled from the silicon wafer, folded, and cured at 80 °C for 48 h. Concerning the sensor behavior, uniaxial pressures were applied with a pull-tester (Instron 3340) and the capacitance values were recorded using an LCR-meter (E4980A) at 2 MHz. For reference, the Young's modulus of the POMaC was measured with a standard stress-strain test (ASTM D412) and the relative permittivity was estimated by measuring the capacitance of POMaC layers in a parallel plate capacitor configuration with sputtered gold electrodes. In the case of the wireless Zn sensors, the S11 coefficient was measured with a vector network analyzer (NanoVNA V2) with the aid of a custom-made reader coil (silver on FR4). The resonant frequency of the sensor was extracted with a custom script algorithm written in python.

Wirelessly powered circuit

A similar fabrication process to the one described above for the wireless pressure sensors was used. POMaC was used as a bonding layer and was separately blade-cast on a silicon wafer with a polyacrylic acid sacrificial layer. The POMaC was cured under UV, laser-cut, released in DI water, and laminated on the bottom half of the PLA coil. The top half was limited onto the POMaC layer after filling the vias with silver epoxy, and the assembled sensor was cured at 80 °C for 48 h to allow the POMaC to fully polymerize. Finally, the SMD components (green LED and 470 pF capacitor) were connected to the Zn lines using the Zn ink described above mixed with 10 vol% acetic acid.

3.5 Supporting information

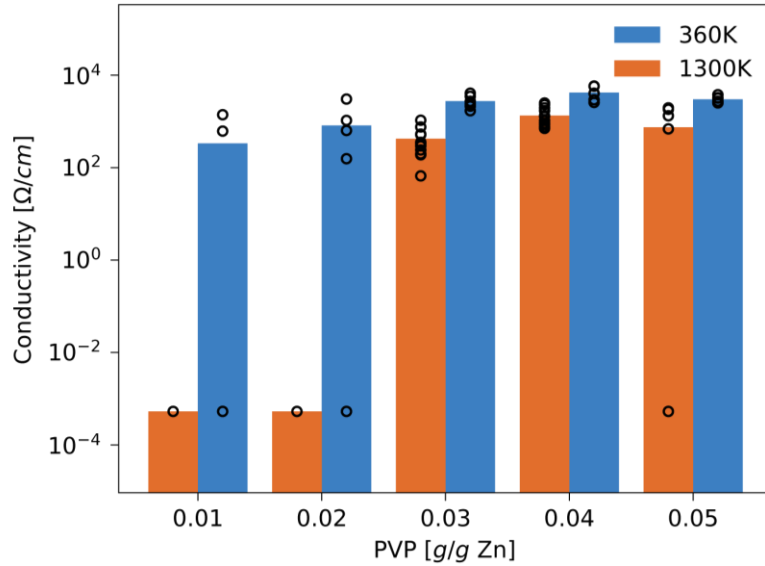


Figure S3.1: Electrical conductivity of lines treated by electrochemical acetic acid sintering as a function of the weight of PVP per weight of Zinc in the solution.

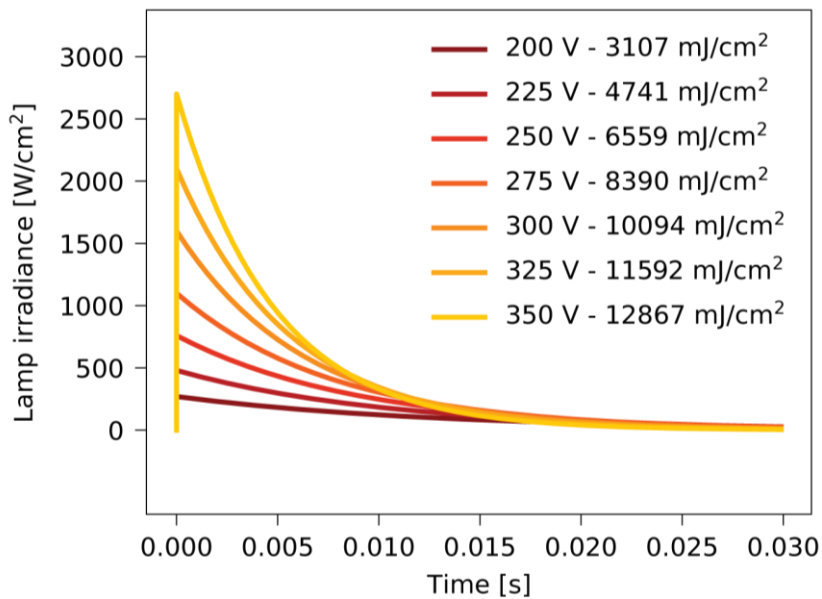


Figure S3.2: Pulses delivered by the PulseForge 1200 photonic sintering lamp as a function of lamp voltage, given as irradiance during the pulse delivery time.

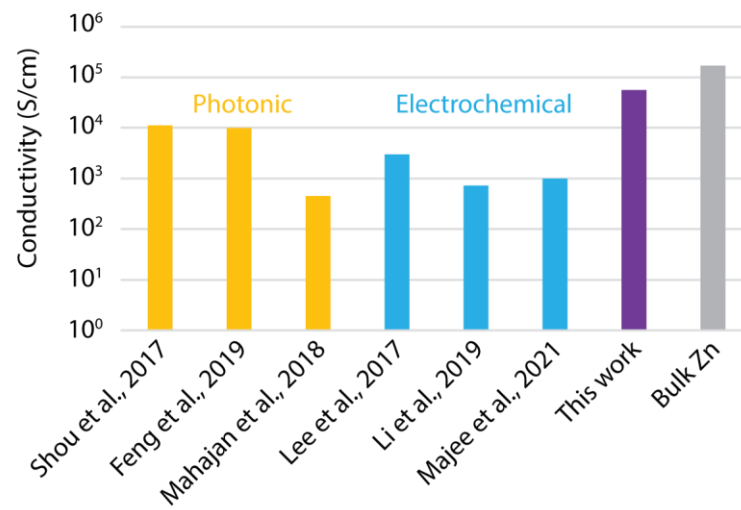


Figure S3.3: Electrical conductivity of the hybrid sintered Zn traces from this work compared to the conductivity of bulk zinc and to examples from the literature for printed zinc using different sintering methods.

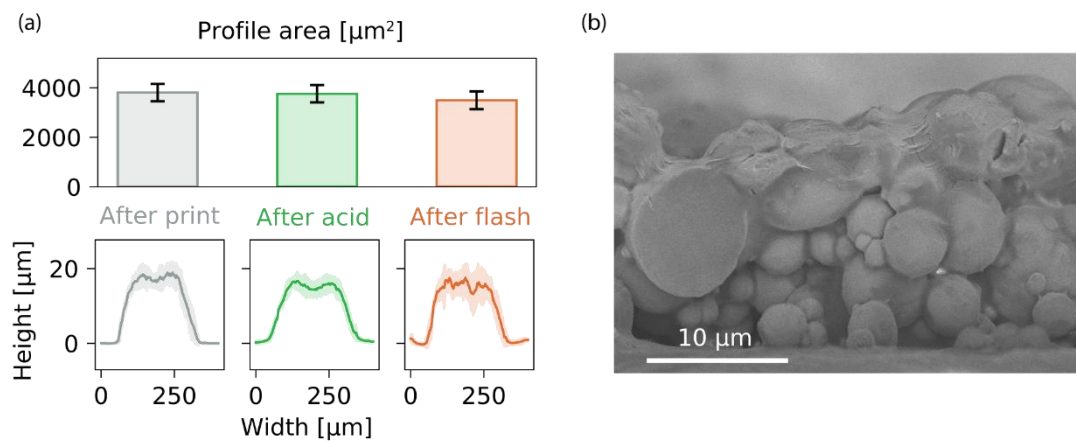


Figure S3.4: Study on profile geometry and microstructure for sintered screen-printed traces. (a) Area and average height of screen-printed profiles after printing, acetic acid sintering, and photonic sintering. (b) SEM cross-section of sintered Zn on polyimide, after freezing in liquid nitrogen and cutting. The sintering and agglomeration of the particles are gradual and localized, particularly in the top 5-10 μm .

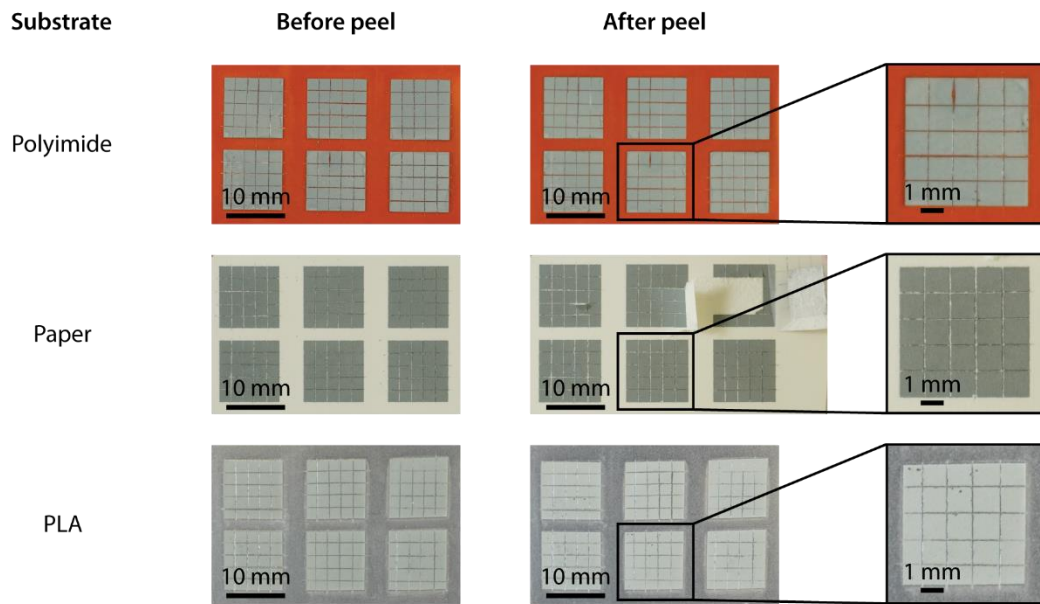


Figure S3.5: Peel test according to ASTM F1842-15 on polyimide, paper and polylactic acid substrates. The sintered zinc layer demonstrated good adhesion properties with the substrates with a classification ranging from 5B to 4B. In the case of paper, the surface part of the substrate peeled during the test, and the zinc layer remained attached to the paper.

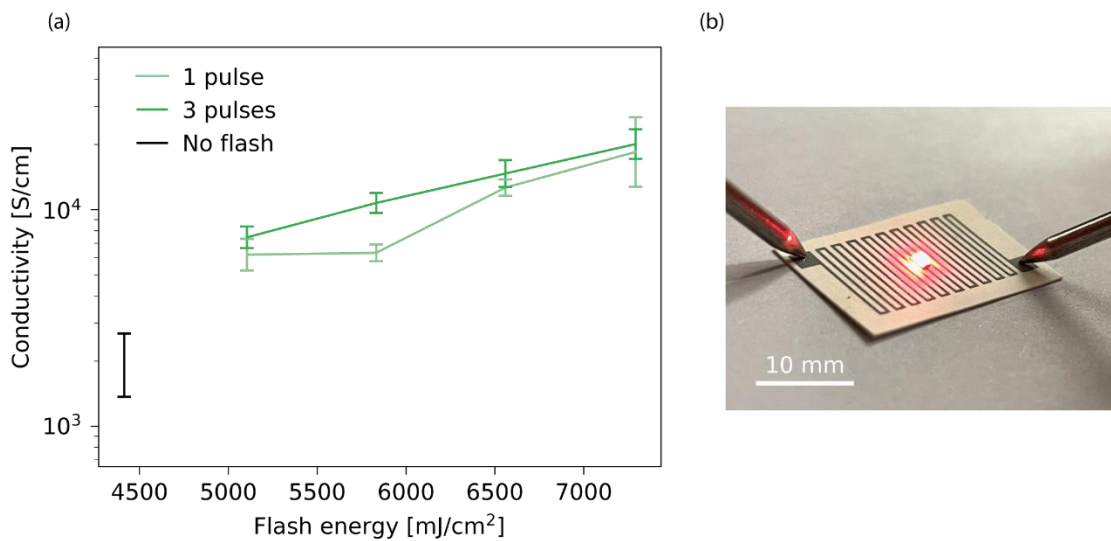


Figure S3.6: Optimization of the hybrid sintering process for paper substrates. (a) Conductivity measured from printed Zn resistors on paper after hybrid sintering, as a function of flash energy and number of pulses. (b) Zn tracks on paper connected to an LED.

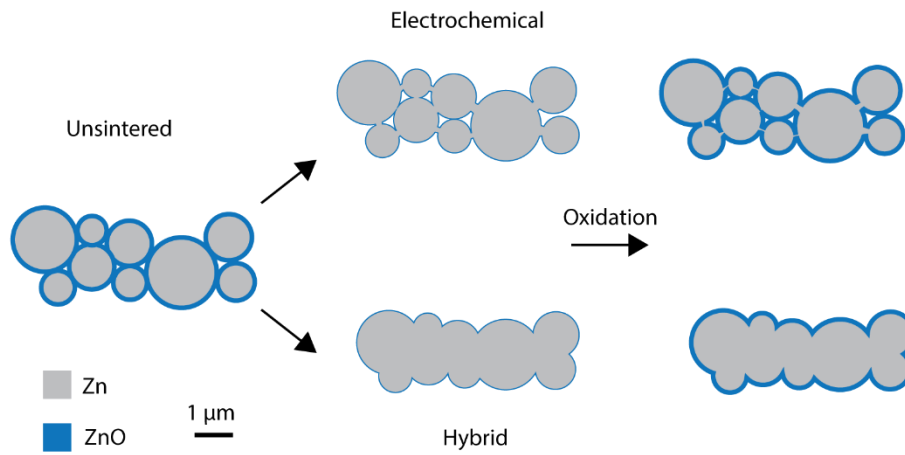


Figure S3.7: Proposed mechanism for the longer durability of photonic sintered Zn in air. The enhanced particle cohesion obtained with hybrid sintering decreases the impact of the zinc reoxidation on the electrical conductivity.

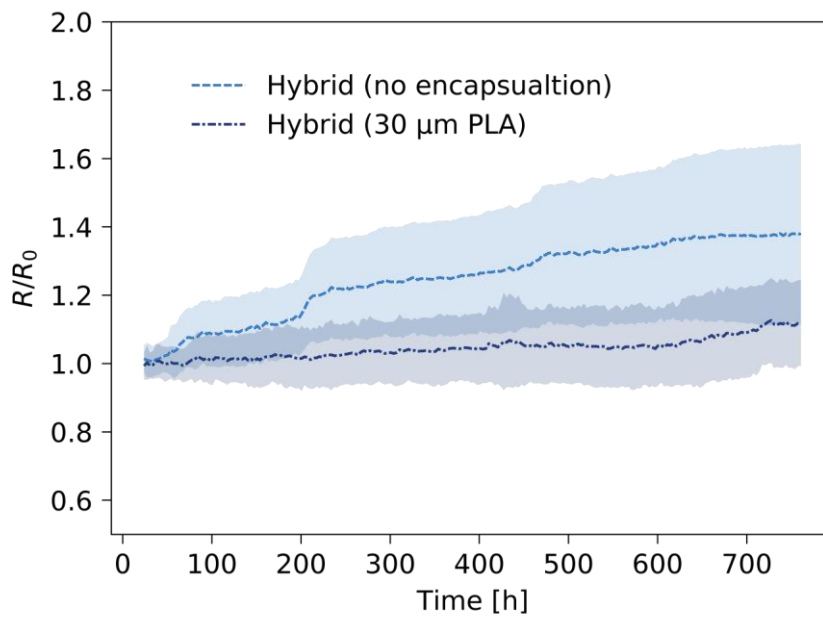


Figure S3.8: Relative change of resistance for Zn lines on PLA after hybrid sintering in air over a period of 31 days, with and without encapsulation.

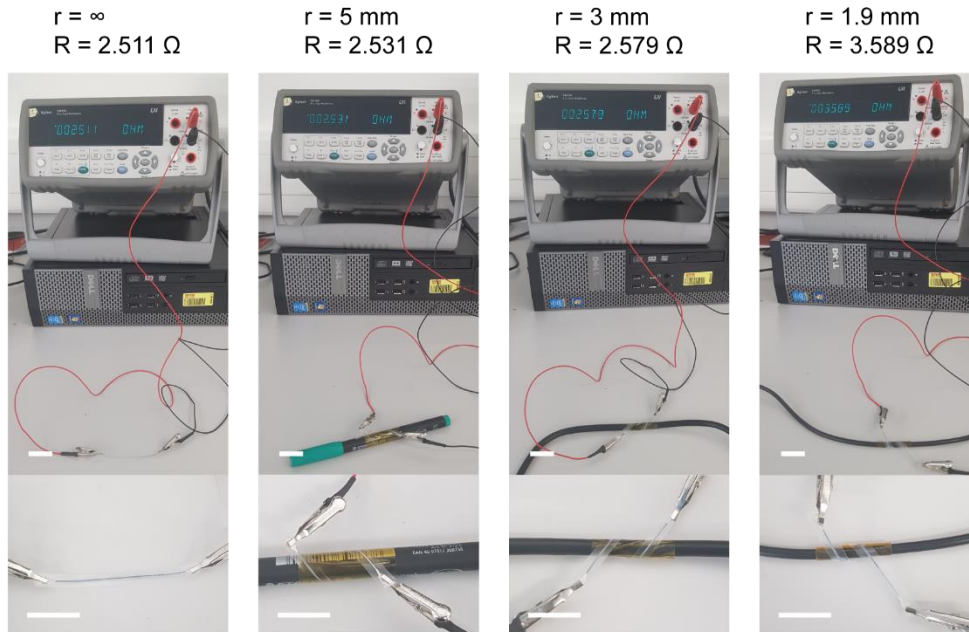


Figure S3.9: Bending of a printed and encapsulated Zn resistor on PLA (50×0.5 mm) at different bending radii. All scale bars are 20 mm.

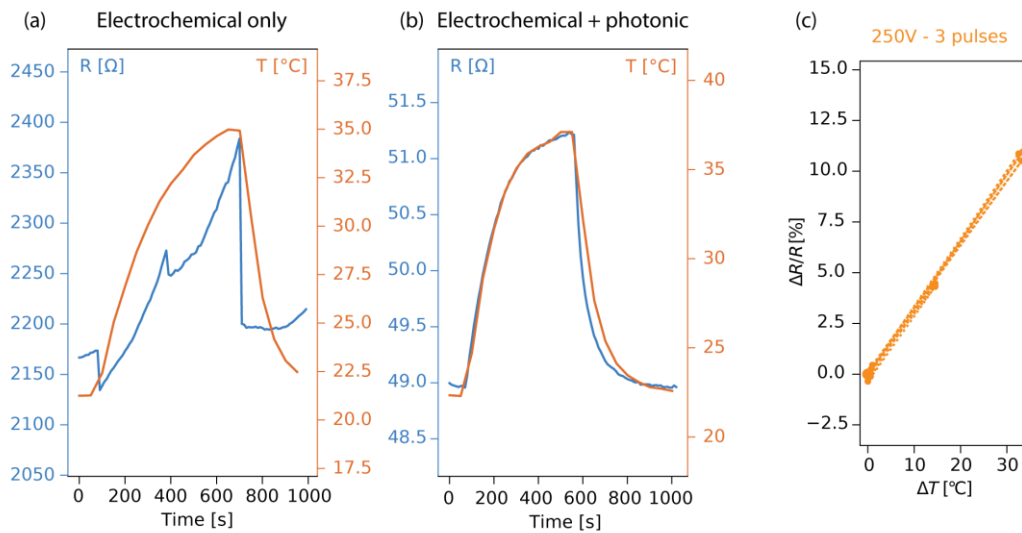


Figure S3.10: Temperature behavior of Zn lines as a function of the sintering process. (a) Heating and cooling of acid sintered only Zn resistor. (b) Heating and cooling of hybrid sintered Zn resistor. (c) Change of resistance with respect to difference from room temperature for a lamp voltage of 250 V and 3 pulses applied.

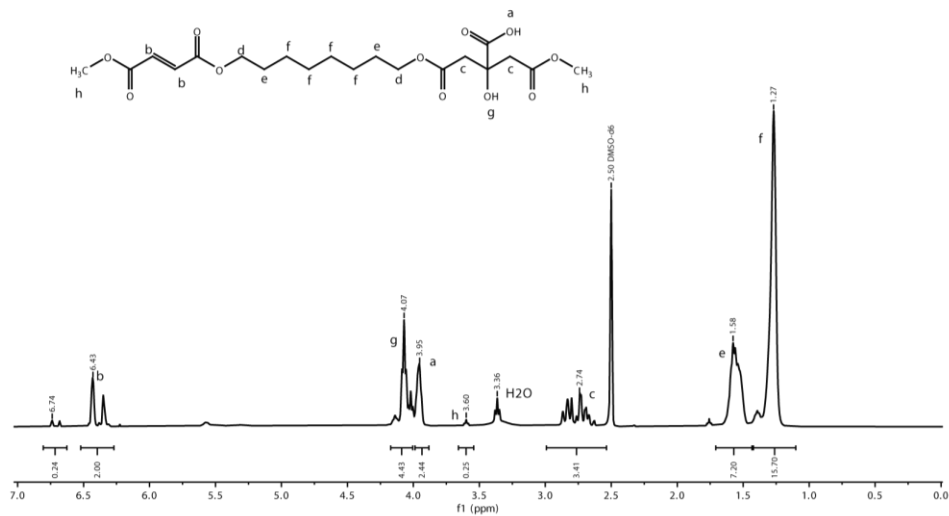


Figure S3.11: $^1\text{H-NMR}$ for the synthesized POMaC pre-polymer. $^1\text{H NMR}$ spectra were recorded on a Bruker AVANCE-400 Ultra Shield instrument at room temperature using $(\text{CD}_3)_2\text{SO}$ as solvent. $^1\text{H NMR}$ chemical shifts are reported relative to the residual proton signal of the solvent.

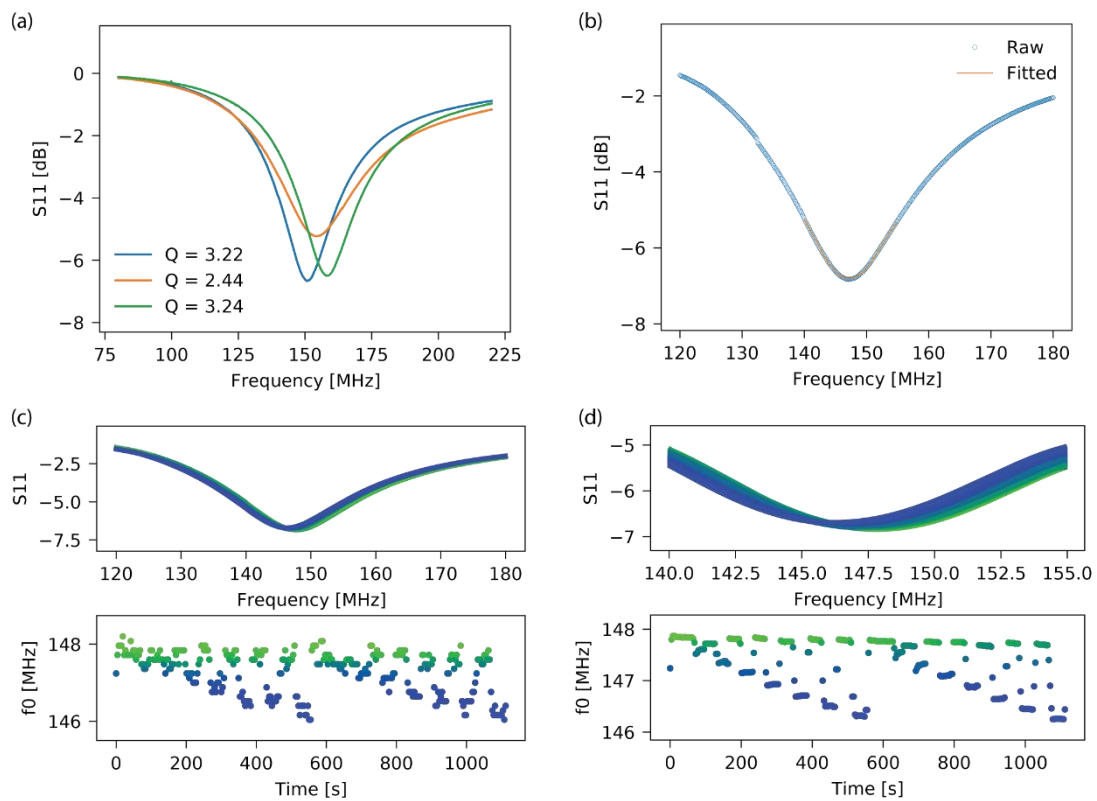


Figure S3.12: Real-time data processing for the S_{11} data of pressure-sensitive wireless circuits. (a) Return loss (S_{11}) of typical transient wireless pressure sensors. (b) 5th-degree polynomial fit used to smooth the resonant frequency signal. (c)

The S_{11} signal and corresponding resonant frequency during application of a calibration force signal, without polynomial fit smoothing. (d) The same data with the polynomial fit smoothing.

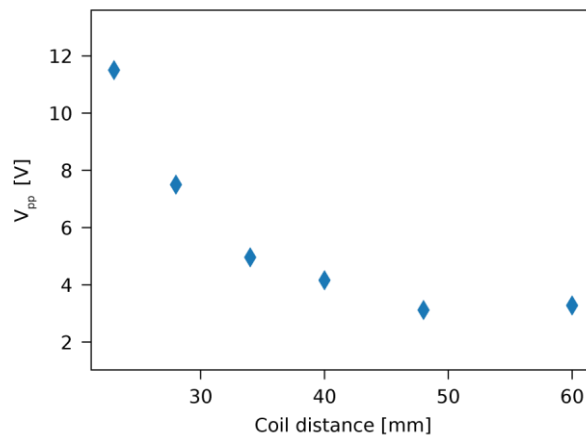
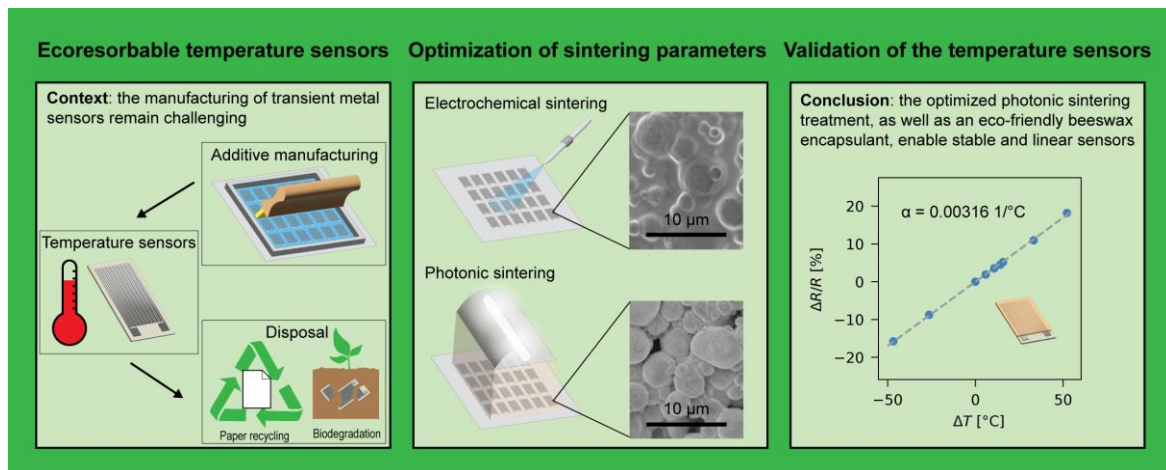


Figure S3.13: Peak-to-peak recorded voltage at the secondary coil (degradable power receiver) as a function of the distance to the primary coil.

Chapter 4 Printed ecoresorbable temperature sensors for environmental monitoring



Electronic waste has become a pressing issue, necessitating sustainable solutions for the disposal of electronic devices. While the development of environmentally degradable electronics has gained attention, the fabrication of stable and performant sensors from biodegradable materials remains challenging. We present printed degradable resistance temperature detectors (RTDs) based on the photonic sintering of a zinc micro-particles ink on a cellulosic substrate. Efficient sintering is attained via a two-step process involving electrochemical oxide removal and pulsed light exposure using a xenon lamp. By optimizing the pulse energy and pulse count, we obtain highly linear zinc-based RTDs with a high temperature coefficient of resistance (TCR). The printed zinc reaches a TCR value of 3160 ppm/K, which represents about 80 % of the value of the bulk material. The dynamic response of the sensors in a range from -20 to 40 °C closely matches the temperature signal recorded by a commercial sensor. The encapsulation of the screen-printed sensors on paper substrate with a biodegradable beeswax coating ensures protection against the interference of moisture. These printed RTDs, fully made of degradable materials, pave the way to the cost-effective manufacturing of eco-friendly yet performant sensors for environmental monitoring.

4.1 Introduction

Precise monitoring of ambient temperature is of critical importance for numerous applications in the agriculture, supply-chain, manufacturing, and health care domains [247–250]. Temperature also often needs to be measured for calibration purposes for other types of sensors exhibiting temperature-dependent responses [251–254]. Several sensor designs have been leveraged for various applications and temperature ranges, including negative temperature coefficient (NTC) thermistors, resistance temperature detectors (RTDs), thermocouples or semiconductor-based sensors [255]. RTDs present the advantage of being based on simple resistive devices that can be reliably microfabricated. Their current challenges center around their integration in novel form factors, such as catheters, bioassays, microrobots and wearables [251,256–258]. However, with the increasing number of connected smart objects and sensors in relation to the development of the internet of things (IoT), concerns about electronic waste generation are being raised. As a consequence, more eco-friendly solutions are urgently needed for the manufacturing and disposal of ubiquitous electronic components. Transient electronics, i.e., circuits or devices that can degrade in a specific environment after their desired period of use without generating harmful byproducts, hold promise to address this challenge [2,3,26]. Due to their increased reactivity and lack of stability when exposed to solvents or high temperatures, the fabrication of microelectronic devices based on degradable materials represents a challenge [67]. Methods to deposit functional layers onto sensitive transient substrates have ranged from the use of a silicone stamp to transfer electronic circuits on the polymeric substrates [1], to shadow-mask deposition techniques to avoid the use of photolithography [147]. These methods have been leveraged to manufacture degradable temperature sensors based on magnesium [21] and silicon nanomembranes [124]. More recently, additive manufacturing methods have emerged as a promising alternative to address this challenge [2]. Printing allows for a more sustainable fabrication process as only the necessary amount of material is deposited, the use of energy-intensive clean room infrastructure and processes is limited or avoided, and scaling up over large area is possible [2,160]. Printing techniques have been leveraged for the production of transient temperature sensors, predominantly based on carbon materials [108,259,260]. However, metal-based RTDs are well established and present advantages (high stability, conductivity and temperature coefficient of resistance (TCR) [261]), yet the additive fabrication of fully degradable metal-based sensors remains challenging. In recent years, there has been a focus on developing annealing methods for printed transient metals that are compatible with degradable substrates, which require low process temperatures [18,185,219,221]. These efforts have centered around zinc, owing to its wide availability in micro- and nanoparticles form and its lower melting temperature among transient metals [214]. However, a printed degradable metallic layer that can serve as resistive temperature sensor for environmental monitoring or biomedical applications has yet to be demonstrated.

In this work, we present for the first time the additive manufacturing and characterization of a biodegradable zinc temperature sensor. We study the temperature behavior of zinc metallic films printed on paper substrates for the development of RTDs made fully of biodegradable materials. Paper is a cellulose-based material that is recyclable and made of renewable materials [262] and is known to be biodegradable, although the exact biodegradation properties will depend on the paper composition, the treatment method for the cellulose fibers and the environmental conditions during degradation [59,60]. Zinc is an ecoresorbable metal [51,263] and dissolves to zinc oxide and zinc hydroxide in the presence of water [82]. The most commonly used sintering process for printed zinc relies on the electrochemical interaction between zinc oxide and acetic acid, which converts the oxide to zinc metal ions [18]. We combine this method with a photonic sintering process, flash lamp annealing, which consists of delivering high-intensity pulsed light to the printed metal lines [236,264]. This allows to selectively heat the printed patterns with minimal effect on the integrity of the cellulosic substrate. We study the influence of the sintering process on the electro-thermal characteristics of the sensors. The application of the optimum parameters enables printed, transient metallic RTDs with a high linearity and TCR. The effect of ambient relative humidity on the response of the sensors is assessed, and an effective passivation against moisture is achieved with a beeswax coating. Beeswax is chosen here for its water-barrier properties and for its biodegradability, which have been thoroughly investigated, notably in soil [50,51]. The encapsulated sensors are characterized at different ambient humidity levels for temperatures up to 40 °C, demonstrating their usability as fully degradable eco-friendly environmental sensors.

4.2 Material and methods

4.2.1 Fabrication

The manufactured zinc RTD on paper substrate is presented in **Figure 4.1(d)**. It consists of a 9.75 mm x 15 mm serpentine resistor with a thickness ranging from 15 to 20 μm and a line width of 250 μm . The resistor was printed from an ink based on Zn microparticles (2 μm average diameter, Sigma Aldrich), polyvinylpyrrolidone (PVP 360K, Sigma Aldrich) as a binder and 1-pentanol (Sigma Aldrich) as the solvent. The ink was deposited on the paper substrate (Powercoat XD 200 μm , ArjoWiggins) by screen printing through a steel mesh (Serilith) using a silicone squeegee and left to dry for one hour (**Figure 4.1(a)**). After drying, a 10 vol% acetic acid was applied to the metal traces (**Figure 4.1(b)**) by spray coating or drop casting, thereby reducing the native zinc oxide layer, whose high melting point impedes an efficient sintering [18]. After drying the acetic acid solution on a hotplate for 5 minutes at 60 $^{\circ}\text{C}$, the samples were placed in a chamber with a glass sapphire window which was purged with nitrogen. Then, to achieve the sintering of the zinc particles, a 30-millisecond photonic flash (Novacentrix Pulseforge 1200) was applied, with pulse energies ranging from 5.1 to 7.3 J/cm^2 (corresponding to lamp voltages between 230 and 260 V), the flash exposure being conducted between one and three times **Figure 4.1 (c)**. Higher pulse energies/number of pulses combinations were not considered as they caused destruction and interruption of the metallic lines. When several energy pulses were used, they were delivered at a frequency of 0.1 Hz, defined to preserve the sample from overheating. This way, the same pulse energy can be delivered several times over, reaching for each light pulse approximately the same maximal temperature in the metallic layer. For samples that were encapsulated, beeswax (Sigma-Aldrich) was melted in a water bain-marie at approximately 80 $^{\circ}\text{C}$ and the samples were dip-coated and left to dry.

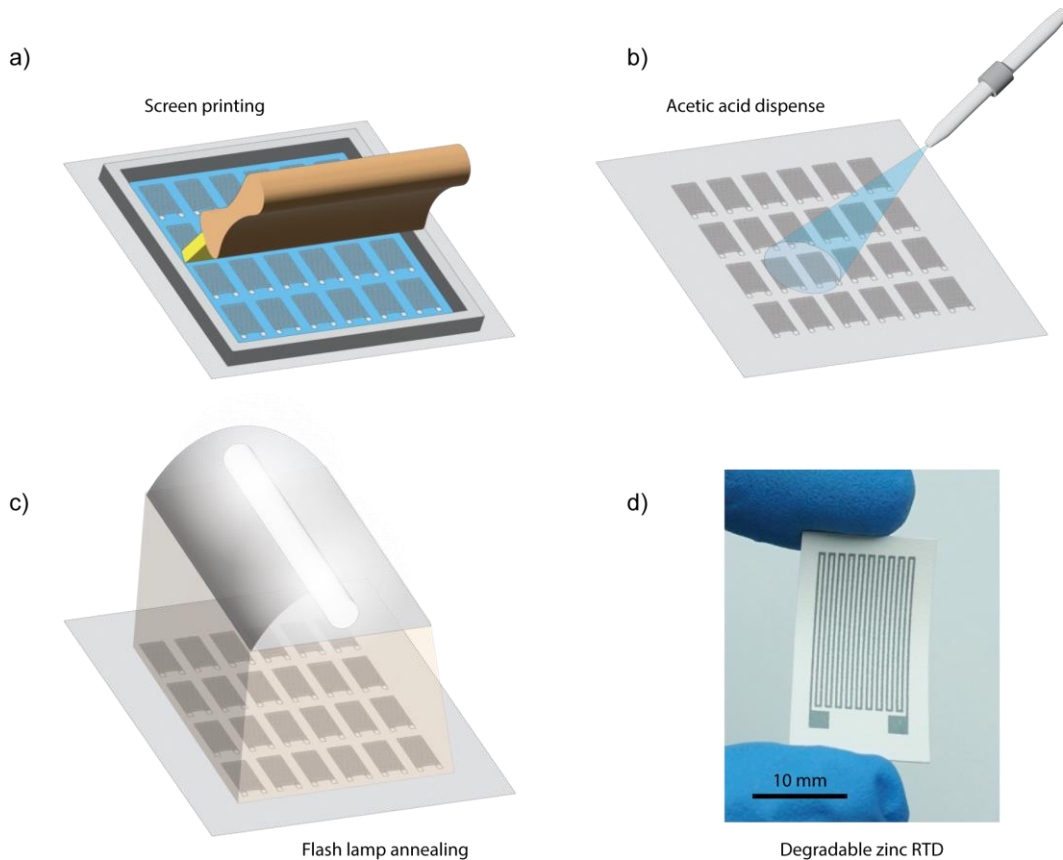


Figure 4.1: Fabrication process of the biodegradable RTD. a) Screen printing of the metallic ink. b) Acetic acid spray dispensing on the printed sensors. c) Photonic sintering step. d) Final sensor after cutting out the paper substrate.

4.2.2 Samples characterization

In order to characterize the electro-thermal behavior of the RTDs, they were placed on a hotplate with a reference temperature and humidity sensor (Sensirion, Digital Humidity and Temperature Sensor, Model SHT4x, operating range: 0-100 %rH, -40-125 °C, relative humidity accuracy: up to ± 1.5 %rH, temperature accuracy: up to ± 0.1 °C, temperature response time: 2 seconds) and were covered (**Figure S4.1(a)**). The resistance of the samples was acquired with a tabletop multimeter (Keysight Digital Multimeter 34401A) and the temperature was set to a specific setpoint (40 °C, 60 °C or 80 °C) until stabilization. After up to 10 minutes, the temperature reached a plateau and the hot plate was turned off, with the samples being left to cool to room temperature. In order to disregard different transient thermal behaviors between the reference sensor and the degradable samples, three steady-state resistance values and the corresponding reference temperatures were extracted from the recorded data: the initial room temperature values, the values at the setpoint temperature, and finally values at room temperature after cooling down (**Figure S4.1(b)**). The behavior of a resistive temperature sensor with a linear behavior is described by the following equation:

$$R(T) = R_0(1 + \alpha(T - T_0))$$

From the values listed above, the temperature coefficient of resistance (TCR) α of the sintered zinc samples and its degree of linearity (in the form of a squared coefficient of correlation) were determined. Further characterization of the samples was conducted in a climatic chamber (Espec Bench-Top Type Temperature & Humidity Chamber SH-661), in which humidity and temperature can be controlled, and the resistance value was recorded with a data acquisition system (Keysight Data Acquisition/Data Logger Switch Unit 34970A). The humidity was varied between 30 and 70 %rH in steps of three hours and the temperature between 20 and 40 °C in steps of one hour. For cooling experiments from room temperature to 0 °C and -20 °C, the samples were placed with the aforementioned reference temperature sensor between ice packs and in a Liebherr FreezeSafe 8260 freezer, respectively.

4.3 Results and Discussion

4.3.1 Influence of flash annealing parameters on temperature behavior

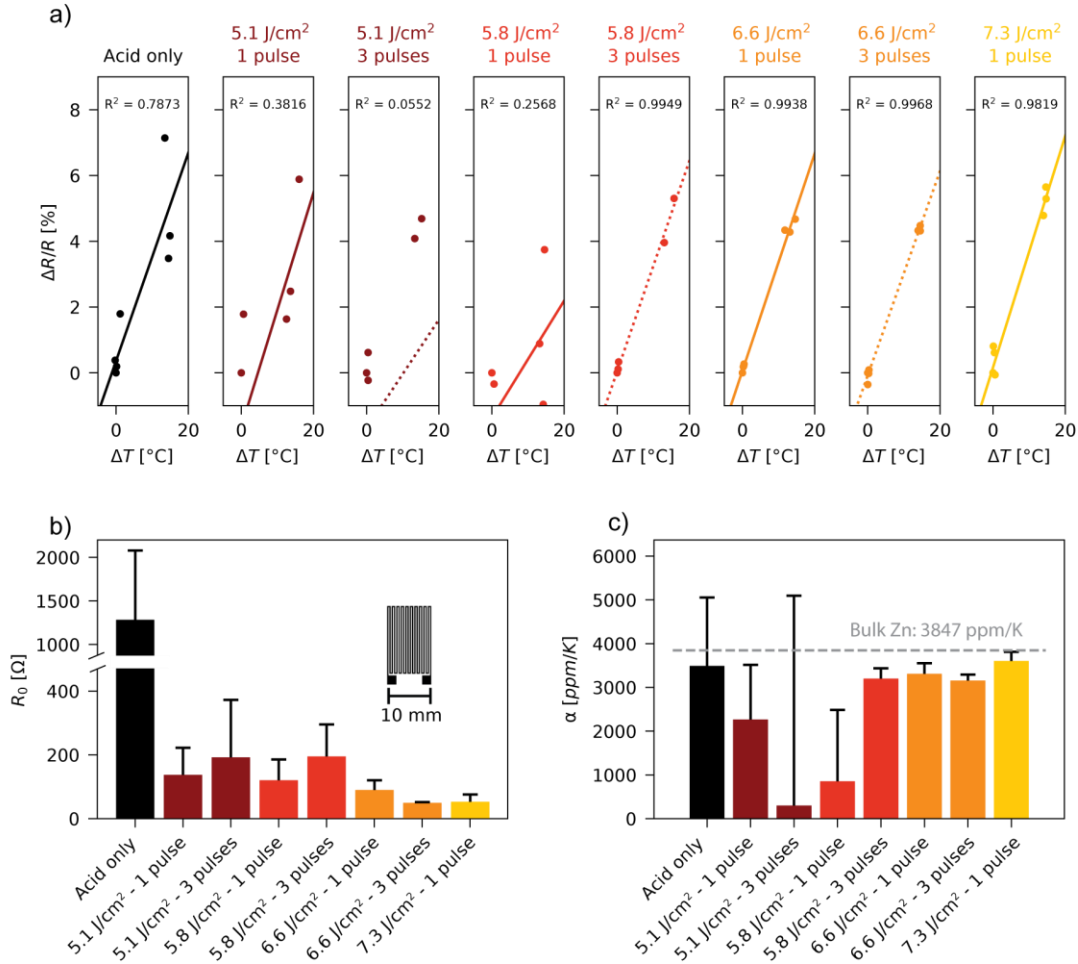


Figure 4.2: Influence of the flash energy and number of pulses on the linearity and repeatability of the temperature response of zinc resistors ($n = 3$). a) Relative change in resistance with respect to change in temperature for different sintering parameters. b) Room temperature resistance as a function of sintering parameters. c) TCR as a function of sintering parameters.

The flash lamp annealing approach was investigated and optimized to obtain printed transient zinc metal traces with electro-thermal properties that are applicable to temperature sensing. **Figure 4.2** shows the influence of the flash lamp parameters (flash photonic energy and number of pulses) on the temperature behavior of the metallic sensing layer. The relative change in resistance is reported with respect to the change in temperature in **Figure 4.2(a)**, this for different photonic treatments ranging from no photonic pulses applied (on the left) to increasing pulse energy (5.1 J/cm² to 7.3 J/cm²) and number of pulses (to the right). For each sintering treatment, a squared correlation coefficient (r^2) is shown. The temperature response of a zinc sensor that was sintered only electrochemically (no photonic sintering) is shown in **Figure 4.2(a)**, on the left. As can be observed, when only electrochemical sintering is used, the RTDs response exhibits a non-linear behavior and a change of baseline resistance. Different competing effects taking place in the zinc layer can potentially explain this unstable behavior and irreversible changes in electrical conductivity. On one hand, raising the temperature of the sensor accelerates re-oxidation of the Zn particles, which may convert the bridges formed between the particles [265] to zinc oxide and reduce conductivity. On the other hand, heating up the resistor during testing may favor evaporation of acetic acid or water residues in the highly porous layer [18], in this case causing an

permanent increase in conductivity. Finally, the presence of polymeric binder in the layer may lead to unstable temperature behavior, as it is known that the purity of the metal layer is paramount for a linear sensing behavior [261]. This can be seen in scanning electron microscope images of the samples, where binder and/or acid residues can be observed around the zinc microparticles after the acetic acid treatment (**Figure S4.2**, on the left).

Flash lamp annealing was therefore applied to achieve sintering of the zinc film and stabilize its electro-thermal response. If sufficient energy is delivered during the photonic treatment (as determined by the combination of pulse intensity and number of pulses), the temperature response drastically changes to a linear behavior with minimal hysteresis, as can be seen in **Figure 4.2(a)**, on the right. When applying a single pulse, at lower pulse energies (below 5.8 J/cm^2) the temperature response of the zinc layer remains similar to what was obtained with electrochemical sintering only, indicating that the sintering remains incomplete. For one pulse applied, there is a threshold point between 5.8 and 6.6 J/cm^2 where the temperature response of the sensor becomes highly linear. At the lower pulse energy of 5.8 J/cm^2 , processing the samples with three light pulses results as well in a linear temperature response with the squared correlation coefficient r^2 increasing from 0.2568 to 0.9949 . Applying three pulses for a pulse intensity of 6.6 J/cm^2 only slightly improved the linearity of the response to temperature compared to the use of a single photonic pulse for which the linearity was already high. However, applying three pulses at 7.3 J/cm^2 caused excessive damage to the zinc layer, resulting in broken resistors. In summary, a drastic shift in the electro-thermal behavior of the zinc films in terms of linearity is observed when sufficient energy is delivered by the flash annealing treatment, suggesting that the microstructure of the films has been stabilized, as could be expected from literature [266]. The change in electro-thermal behavior when delivering more energy during flash lamp annealing can be explained by the metallic layer reaching a temperature high enough to cause sintering and densification of the particles film [185]. As a consequence of the increased cohesion between the particles, the porosity of the film is reduced and the influence of the corrosion in ambient air becomes less important, resulting in more stable RTDs, whereas, in insufficiently sintered films, the limited bridges between particles may be rapidly oxidized with increasing temperatures. Moreover, the elevated temperatures during photonic sintering can cause decomposition of the organic binder, leading to a more homogeneous metallic layer [239,267] with less impurities, which is associated with a higher temperature dependence of the resistivity [268]. This can also be seen in the SEM images of the zinc layer (**Figure S4.2**), where a treatment of three pulses of 6.6 J/cm^2 causes particle fusion and growth and removal of polymeric residue. In parallel, this particles growth results in a decrease of the grain boundary density in the film [269], which can reduce scattering effects and improve temperature sensitivity [270,271]. In summary, the influence of the photonic sintering energy delivered on the temperature response of the printed zinc resistors is thought to be multifactorial, where more effective sintering can lead to increased particle cohesion, reduced grain boundaries and higher homogeneity of the film, contributing to the higher TCR value and the more stable behavior observed.

The sensitivity of the temperature detector scales with the temperature coefficient of resistance of the metal, but also with the initial resistance of the RTD. Increasing the sintering energy causes a decrease in electrical resistivity by one to two orders of magnitude, which translates in an average resistance value going from $1283 \text{ } \Omega$ for electrochemical sintering alone, down to $48.3 \text{ } \Omega$ when the highest total energy is delivered (3 light pulses of 6.6 J/cm^2) as seen in **Figure 4.2(b)**. On the other hand, the benefit and necessity of using higher energy for the sintering on the RTDs characteristics is clearly seen with an increase in the TCR value, and the linearity and reproducibility of their response. This can be visualized in **Figure 4.2(a)** as well as in **Figure 4.2(c)** which display the average and standard deviation of the TCR of the individual sensors. We see that increasing the sintering energy results in high TCR values for the zinc tracks and that the variability between sensors decreases, making the zinc resistors applicable for stable temperature measurements. Among the set of parameters tested, the TCR reaches a maximal value of $3630 \pm 220 \text{ ppm/K}$ for one pulse of 7.3 J/cm^2 , very close to the one of bulk zinc at 3850 ppm/K [241], while 6.6 J/cm^2 , with 1 and 3 pulses, led to a slightly inferior TCR of respectively 3380 and 3050 ppm/K .

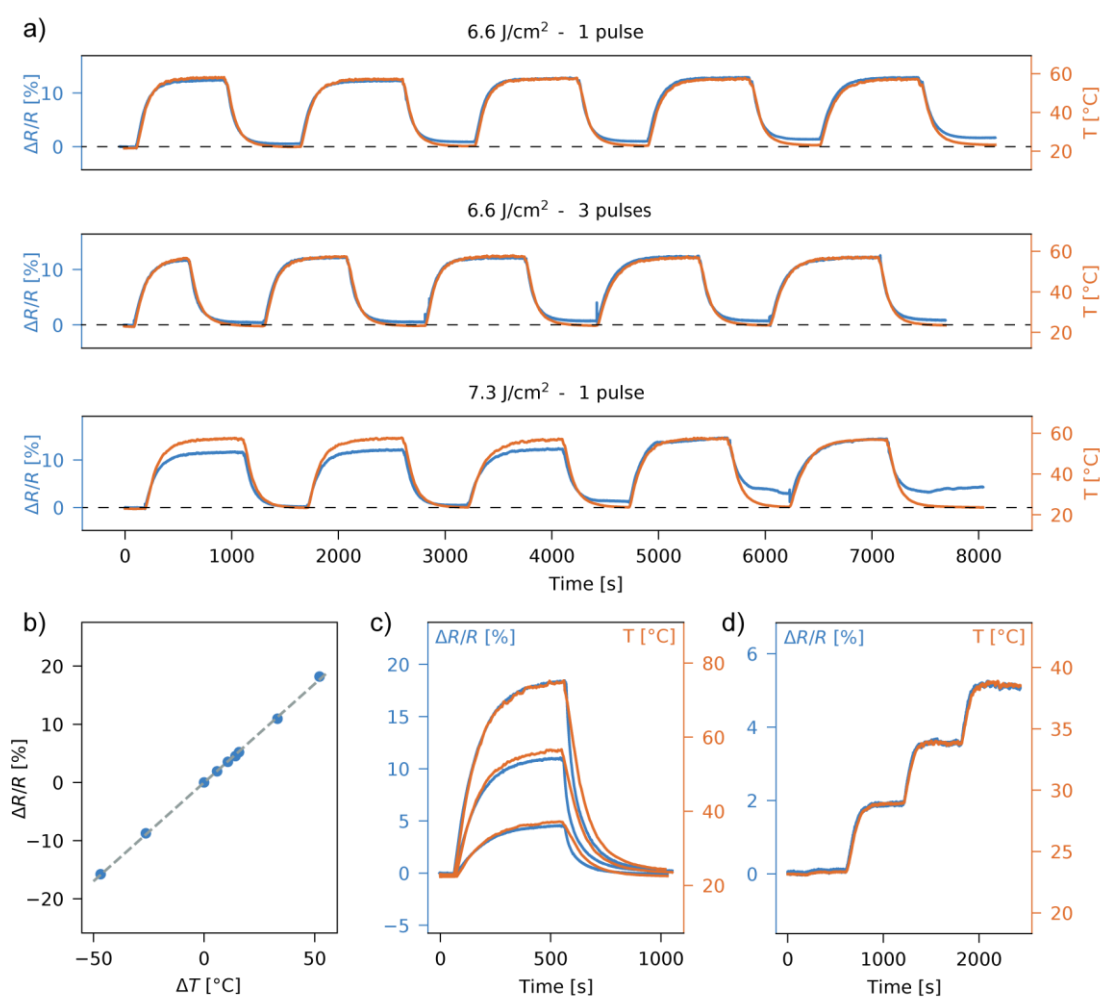


Figure 4.3 Dynamic behavior of the temperature sensors. a) Change in resistance of the zinc traces under cycling between room temperature and 60°C for three different photonic sintering sets of parameters. b) RTDs calibration curve after sintering with optimal parameters. c) Sensor response (blue) and reference temperature (orange) for different variations in temperature. d) Staircase response of the sensor (blue) compared to a commercial sensor (orange).

Further characterization experiments were conducted on zinc samples exposed to the flash parameter combinations yielding the best electro-thermal characteristics: 1 pulse and 3 pulses at 6.6 J/cm², and 1 pulse at 7.3 J/cm². When tested up to a temperature of 60°C, the RTDs that were treated with three pulses of light of 6.6 J/cm² show a slightly more reproducible and reversible behavior between samples (**Figure S4.3**). The stability of the devices was further assessed by cycling the temperature five times, starting from room temperature and going up to a setpoint of 60 °C to, finally, let them cool down to room temperature again. The sensors that were sintered with three repeated pulses show a more repeatable signal and suffer little baseline drift (**Figure 4.3(a)**). The highest pulse energy applied (7.3 J/cm²) yields the worst behavior in terms of baseline stability, consistent with the aforementioned hypothesis that some damage is caused to the metallic layer. The use of a multi-pulse treatment appears to enhance sintering while avoiding excessive damage to the zinc layer. In conclusion, the use of three pulses with an intensity of 6.6 J/cm² was deemed to be optimal for the fabrication by printing of degradable Zn RTDs on paper. As a caveat, the optimum flash lamp annealing conditions will vary depending on the layout and thickness of zinc pattern to be sintered and the substrate used, as all of these parameters will impact the temperature distribution across the metallic layer during sintering and therefore the optimal light pulse parameters [272].

As a demonstration, temperature sensors are manufactured with these optimized parameters (i.e., 3 pulses of 6.6 J/cm²) and their response to temperature are shown in **Figure 4.3(b-d)**. The response of the sensor is

highly linear as a function of temperature with a TCR value of 3160 ± 130 ppm/K is obtained (**Figure 4.3(b)**), over a range of temperatures from -20°C to 40°C . The dynamic measurements conducted at temperatures found in the context of refrigeration and congelation, at 0°C and -20°C respectively, can be found in **Figure S4.4**, as this is relevant for application related to supply-chain monitoring. The sensors are able to precisely track variations in temperature and display low hysteresis, as can be seen in **Figure 4.3(c)** as well. The time dynamics of the step response of the sensors are also comparable to commercial sensors (**Figure 4.3(d)**).

4.3.2 Influence of ambient humidity on the temperature sensors

A common issue with the use of degradable materials such as zinc for electronics is their sensitivity to water [67,221], which may reduce their performance and stability as sensors. To investigate the influence of ambient humidity on the sintered metallic layer, we first fabricated zinc resistors on a $125\ \mu\text{m}$ polyimide film (PI), which shows limited water absorption. The resistance values for these zinc tracks printed and sintered on PI shows a relative change of between 2 and 5 % when humidity is varied between 30 and 70 %rH, as shown in **Figure S4.5**. When measuring the resistance of zinc tracks on paper, while varying the ambient humidity between 30 and 70 %rH at a constant temperature of 20°C , variations in resistance of up to 15 % are registered. This results from the water interaction both in the zinc metallic layer and the paper substrate, which may swell and generate a mechanical load in the zinc layer. For both types of substrates, the changes in resistance are maintained after the humidity level has been lowered back to 30 %rH, which may be due to water remaining in the porous layers or partial degradation of the conductive layer in a humid environment, or microcracks having formed in the metallic layer. The relative change in resistance is greater when the zinc layers are printed on a paper substrate, which suggests that stable sensors can only be reached by fully encapsulating them against humidity. It can also be noted that the influence of the ambient humidity is more important at a higher temperature (as seen in **Figure S4.5**, on the right), due to the higher absolute humidity content.

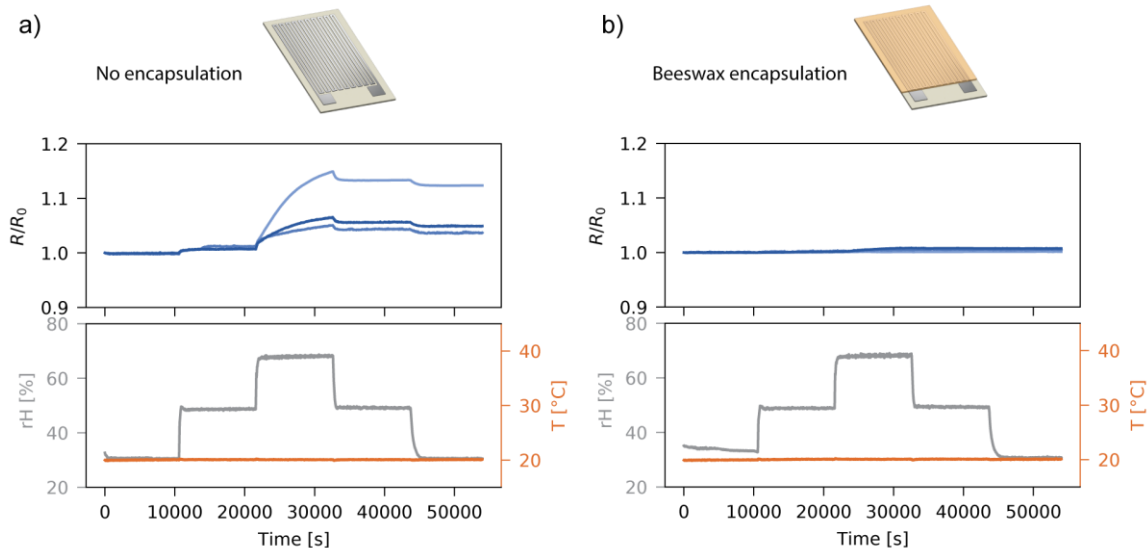


Figure 4.4: Effect of beeswax encapsulation on the interference of humidity. Relative change of resistance (top graphs) when varying ambient humidity while keeping the temperature at 20°C (bottom graphs), in the case where: a) the sensors are not encapsulated and b) the sensors are encapsulated with beeswax ($n = 3$).

We chose to passivate the temperature sensors with beeswax, which, while being a biodegradable and eco-friendly material [273], demonstrates excellent water-barrier properties. Beeswax is already used in food-safe coatings for the preservation of fruit [274–276] and can be applied by dip-coating after heating above its melting temperature of $61\text{--}65^{\circ}\text{C}$. To confirm the barrier properties of the coating, the passivated sensors were subjected to the same ambient humidity cycle, as shown in **Figure 4.4**. The RTDs display little to no sensitivity to humidity, with an average relative change of resistance of 0.47 % after cycling the humidity between 30 and

70 %rH. The behavior of the encapsulated zinc sensors on paper was further tested at temperatures up to 40 °C while maintaining a constant relative humidity, the results being shown in **Figure 4.5**. The sensors respond similarly to the temperature changes, mostly independently of the humidity level, and the exhibited temperature sensitivity corresponds to the TCR that was previously determined without encapsulation. This result highlights the applicability of the manufactured degradable sensors for supply chain monitoring or digital agriculture purposes. One should notice that some drift is observed at the highest humidity level, especially when the temperature approaches 40°C. This evidences that improvements on the temperature resilience of the beeswax coating is required to push the operating temperature limits of the sensors.

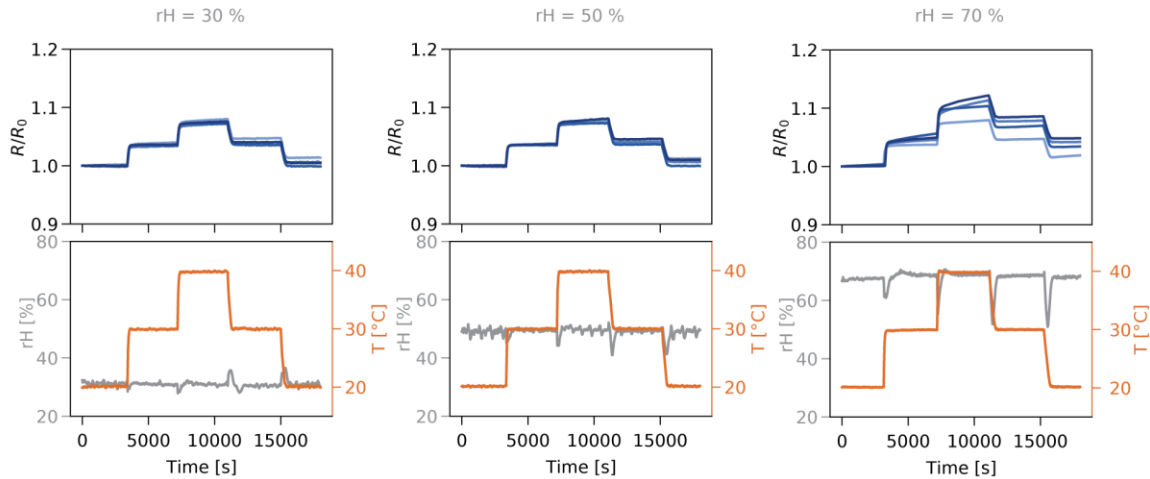


Figure 4.5: Temperature sensing at different humidity levels. Relative change of resistance (top) under varying temperature (bottom) for beeswax-encapsulated sensors at various relative humidity levels: 30 %rH (left), 50 %rH (middle) and 70 %rH (right) ($n = 4$).

4.4 Conclusions

In this work, we show the fabrication and characterization of the first fully printed temperature resistance detector made of degradable metal. The sensors exhibit a linear behavior, with a temperature coefficient of resistance that reaches 80 % of that of bulk zinc, and low hysteresis. To this end, a flash lamp annealing process was leveraged and the influence of the photonic pulse energy as well as the number of pulses delivered on the RTDs electro-thermal characteristics was investigated. For this specific layer stack configuration, it was demonstrated that zinc RTDs exhibited a linear temperature response ($r^2 > 0.99$) when subjected to higher pulse energies and pulse counts above the intensity threshold of 5.8 J/cm². This outcome is likely attributed to a modification of the microstructure of the zinc layer, allowing to minimize the effect of reoxidation in air and corrosion by water vapor, as well as increased crystallinity and purity of the film after the sintering process. Sensors fabricated with optimized process parameters (3 pulses at 6.6 J/cm²) were successfully operated at temperatures ranging from -20 °C to 40 °C, exhibiting a dynamic response which is comparable to that of a commercial sensor. Finally, the implementation of a beeswax coating as encapsulation enabled a reliable operation of the RTD sensor under varying ambient humidity levels, with an unaffected response in the range of 30 to 70 %rH. The sensors, made entirely from biodegradable materials, were shown to function within a temperature range compatible with supply chain monitoring, smart farming and generally applications that may require monitoring of the ambient temperature for a limited period of time. Further developments may include the integration of these RTDs in a fully wireless and biodegradable sensor tag. Finally, this process for zinc could be implemented in the additive fabrication of bioresorbable electronics embedding temperature sensors, systems that will degrade in the body without releasing harmful byproducts.

4.5 Supporting information

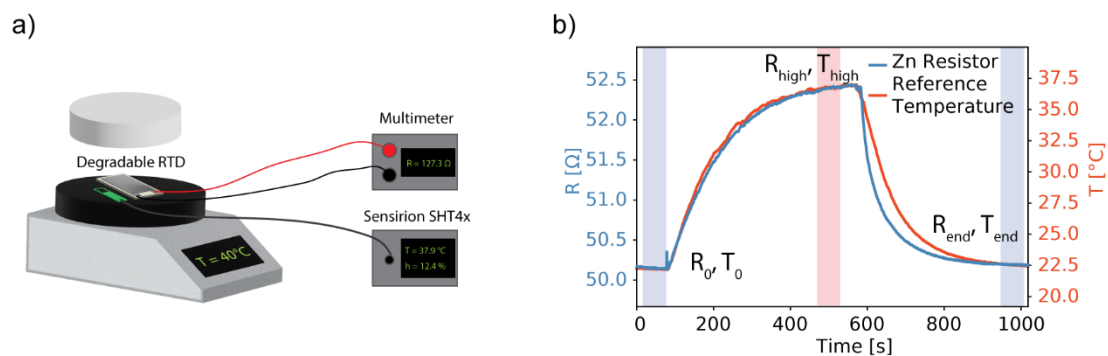


Figure S4.1: Measurement setup and data extraction for the assessment of the degradable RTDs. a) Experimental setup where the degradable RTD and a reference temperature sensor are placed on a hot plate. b) Representative response from a degradable RTD (blue) and reference temperature (orange), where the points in which the data is extracted for further analysis are highlighted.

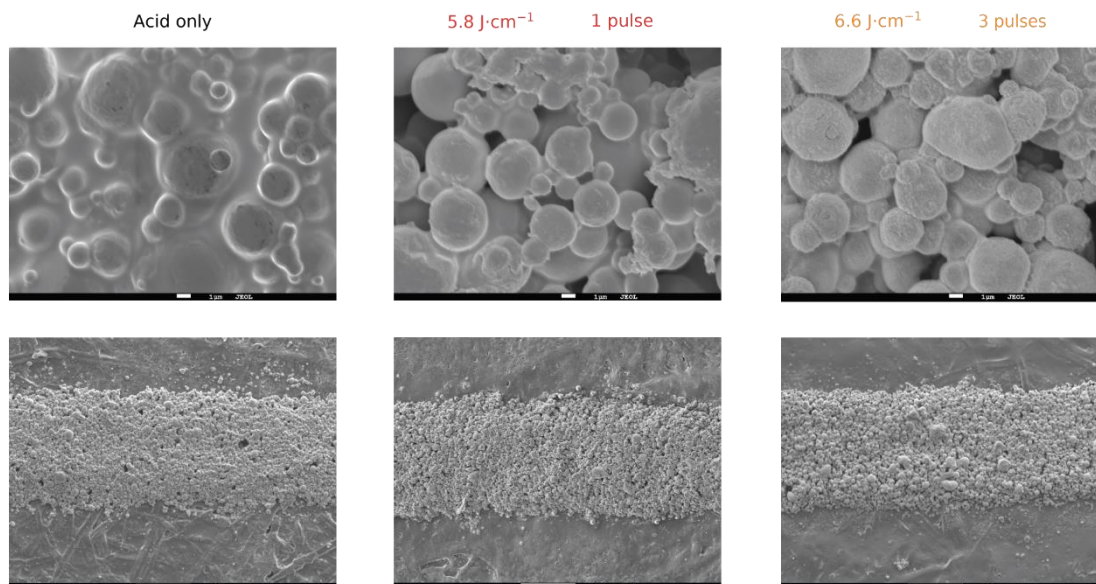


Figure S4.2: SEM images of the zinc layer after different photonic treatments: only electrochemical sintering by application of acetic acid (left), 1 light pulse of 5.8 J/cm^2 (middle) and 3 light pulses of 6.6 J/cm^2 (right).

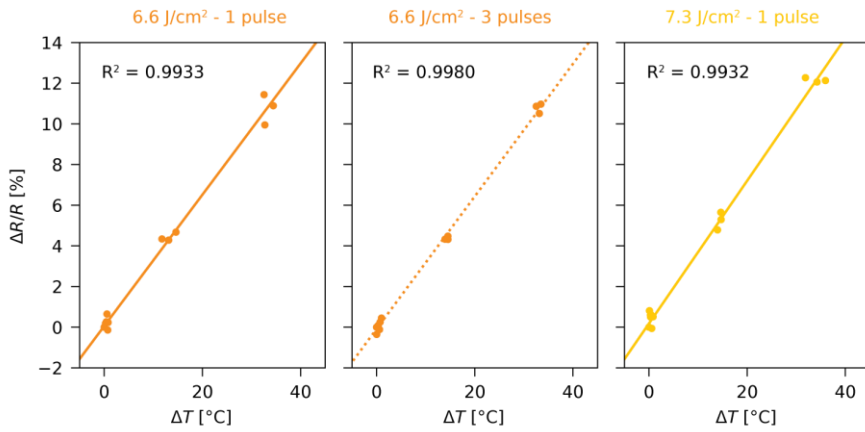


Figure S4.3: Relative change in resistance with respect to change in temperature for different sintering parameters, at room temperature, 40 and 60°C ($n = 3$).

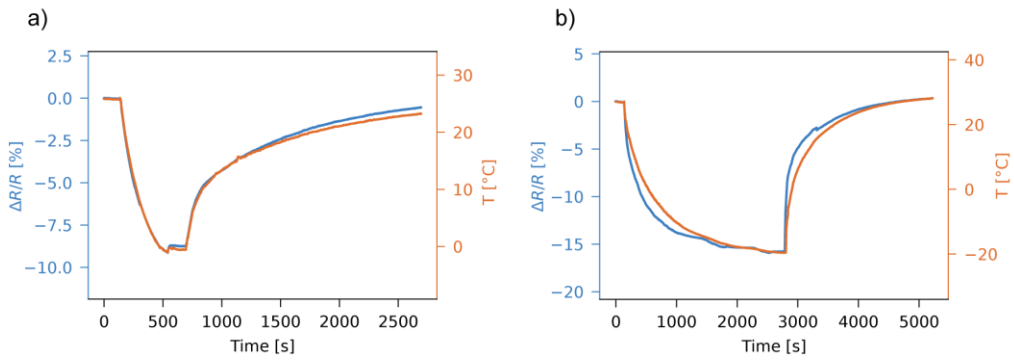


Figure S4.4: Relative change of resistance for temperatures below room temperature. Sensor response (blue) and reference temperature (orange), when cooling the sensor down to 0 °C (a) and -20°C (b).

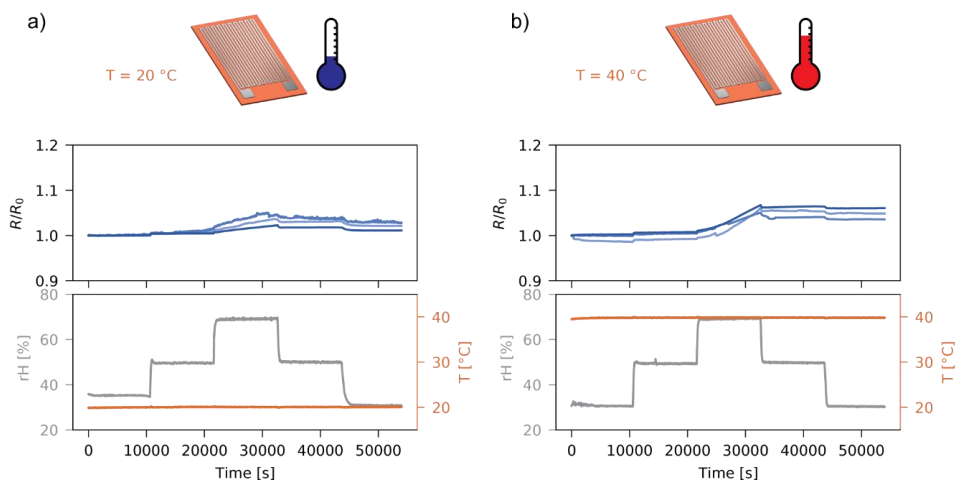
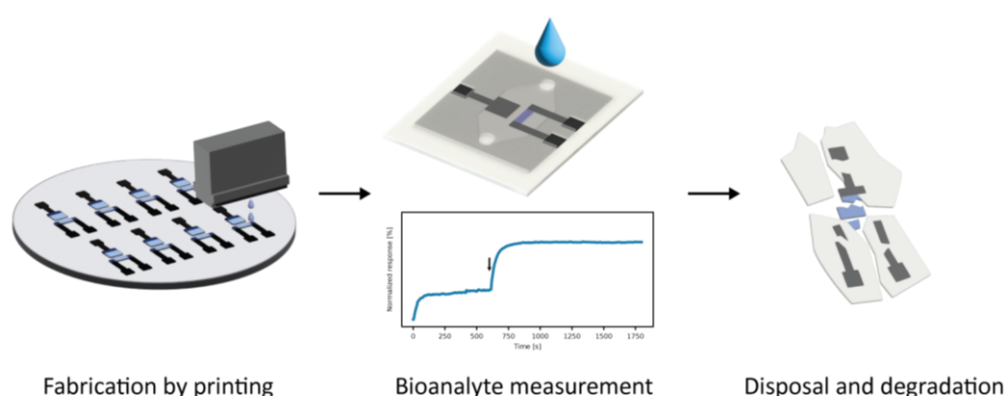


Figure S4.5: Relative change of resistance (top graphs) when varying ambient humidity from 30 to 70 %rH (bottom graphs), for Zn resistors printed on polyimide and without encapsulation, with an ambient temperature of: a) 20 °C and b) 40 °C ($n = 3$).

Chapter 5 Organic electrochemical transistors printed from degradable materials as disposable biochemical sensors



Transient electronics hold promise in reducing electronic waste, especially in applications that require only a limited lifetime. While various degradable electronic and physical sensing devices have been proposed, there is growing interest in the development of degradable biochemical sensors. In this work, we present the development of an organic electrochemical transistor (OECT) with degradable electrodes, printed on an eco- and bioresorbable substrate. The influence of the design and materials for the contacts, channel and gate of the transducer, namely poly(3,4-ethylene dioxythiophene):polystyrene sulfonate (PEDOT:PSS) and carbon, is systematically evaluated for the development of OECT-based transient biosensors. The sensing capabilities of the electrochemical transistors are demonstrated with ionic solutions as well as for the enzyme-based detection of glucose. The disposable OECTs show comparable performance to their non-degradable counterparts. Their integration with highly conductive degradable and printable zinc tracks is studied for the realization of interconnects. These eco-friendly OECTs may find applications as disposable and sustainable biochemical sensors, and constitute a step towards bioresorbable biosensors.

5.1 Introduction

In recent years, interest in seamless, low-cost and reliable biosensors has been steadily increasing, targeting applications in point-of-care testing [277,278], continuous monitoring through wearables [279,280] or implanted biosensors [281]. In this context, organic electrochemical transistors (OECTs) have emerged as a promising alternative to potentiometric, amperometric or ISFET-based sensors [282]. Recent interest in OECTs has been motivated by their compatibility with mechanically compliant substrates [283], high transconductance [284], reference-free operation [285] and simplified microfluidic integration [23]. Precise monitoring of various analytes has been demonstrated leveraging the high signal amplification properties of OECTs. Examples include the sensing of pH [286], electrolytes such as sodium and potassium [287], metabolites including glucose and lactate [288] or neurotransmitters such as dopamine or epinephrine [289,290]. OECTs consist of three terminals (source, drain and gate). The source and drain contacts are usually fabricated with metals such as gold or silver and the channel consists of a conductive polymer layer connecting the source and the drain. The channel is most often based on poly(3,4-ethylene dioxythiophene):polystyrene sulfonate (PEDOT:PSS) [291], although other materials such as polypyrrole have been explored [284]. A variety of materials have been used to fabricate the gate electrode, although silver/silver chloride or platinum are the most common choices for gate fabrication [284]. The gate and channel are in contact with an electrolyte (in liquid or gel form) and cations from the electrolyte diffuse into the channel if a positive gate potential is applied, and de-dope the conductive polymer by compensating the anions of the PSS dopant. This relatively simple architecture is compatible with planar designs and high-density integration into microfluidic systems or complex organic electronics circuits [292].

Advantageously, the fabrication of OECTs, in particular of the conductive channel, is compatible with solution-based fabrication methods and additive manufacturing, enabling cost-efficient manufacturing and rapid prototyping on flexible substrates [23]. This opens new possibilities in terms of the combination of materials that can be used in the manufacturing of OECTs, in particular the use of degradable materials. Degradable electronics refer to electronic systems and components that can degrade in an environment of interest spontaneously, in a controlled amount of time, and without releasing byproducts that are harmful to that environment [26]. With concerning amounts of electronic waste being generated, as well as exploding numbers of connected Internet of Things (IoT) devices [293], there is growing interest in transient electronic systems with a service life of a few days to a few months. Although advances have been made in the manufacturing of fully degradable functional devices, i.e. antennas [214], batteries [229] and physical as well as environmental sensors [108,294], investigations into degradable biosensors remain relatively limited [8].

Advances have been made in proposing new materials for the OECT terminals, in particular the gate electrode, as its properties play a key role in modulating the transistor's behavior. While Ag/AgCl gates offer the advantage of being non-polarizable, Au gates present little electrochemical activity in the range of voltages typical for OECT-based biosensing. Au and PEDOT:PSS gates have been explored for OECT-based biosensors, with the advantage of expanding the possibilities for bio-functionalizing the gate electrode [295,282]. PEDOT:PSS gates and contacts have been investigated, simplifying notably their manufacturing [203]. An all-PEDOT:PSS OECT was presented and shown to measure dopamine concentrations reliably and specifically [296]. Various forms of carbon have also been investigated for the realization of gate electrodes for OECTs [284]. Activated carbon gates, for example, showed increased drain current modulation due to the large specific surface area of the carbon material [285]. Recently, screen-printed carbon-gated OECTs were shown to be suitable for the detection of uric acid after functionalization of the carbon gate with platinum and Uricase [297]. Transient or recyclable materials such as paper [203] have been proposed as substrates for OECTs. Polylactic acid (PLA) [63] and Poly(lactic-co-glycolic acid) [154] (PLGA) have been studied as degradable substrates for OECTs, as well as diacetate cellulose [155]. These studies, however, relied on non-degradable contacts for the operation of the printed OECTs. More recently, Khan et al. proposed a fully printed OECT on cellulose acetate (CA) for the selective detection of glucose [298]. The OECT is made of degradable materials and CA is a biocompatible material that is suitable as a substrate for transient biosensors.

In this work, we present disposable and biocompatible OECTs based on carbon, PEDOT:PSS and PLA as substrate. Challenges in the fabrication of transient electronic devices come from the low-temperature

tolerance [26] of biopolymeric substrates and reaching adhesion of the PEDOT:PSS channel material on the biopolymer [102], which is often deposited from an aqueous solution. A fully additive fabrication process is developed to address these challenges, leveraging screen and inkjet printing. The influence of the gate material choice, as well as the gate geometry, are studied, and these parameters are optimized for the fabrication of transient OECTs for ions and metabolite sensing. The transistor characteristics of the devices as well as their sensing behavior and reproducibility are characterized. Finally, the degradable OECTs are integrated with highly conductive transient zinc metal traces, which are of interest for interconnection with other degradable electronic circuits and could allow, for example, the wireless operation of the biochemical chemical sensors [299].

5.2 Results and discussion

5.2.1 OECTs design and materials

The disposable electrochemical transistors presented in this work are entirely fabricated with environmentally benign and biocompatible materials. The materials used in these devices are amenable to the manufacturing of transient biosensors. Carbon and PEDOT:PSS were chosen in order to respect the aforementioned criterion, and the specific materials combinations are optimized here for two applications: ion sensing and glucose detection. These two analytes rely on different sensing mechanisms, namely diffusion of cations into the conducting channel versus glucose oxidation reactions generating hydrogen peroxide and catalyzed by glucose oxidase [282].

Figure 5.1(a) shows the configuration of the carbon-gated and PEDOT:PSS devices, as described above, as well as the contacts (gate, source and drain) and the voltages that mediate the transistor behavior. A PEDOT:PSS-gated device is shown on the left and a device with a carbon gate on the right. The channel has an effective length of 3 mm and a width of 1 mm, resulting in a W/L ratio of 1/3. The gate geometry, in particular the area ratio between the gate and the channel, was varied. The contacts and channel are arranged in a planar configuration, as this allows for easier microfluidic integration. An optical image of such a device, in this case with a PEDOT:PSS gate electrode is shown in **Figure 5.1(b)**. Based on the measurement to be performed, the test solution was contained either in a polymethylmethacrylate (PMMA) reservoir or a microfluidic channel (**Figure 5.1(c)**), which was fabricated from laser-cut polydimethylsiloxane (PDMS) and polyethylene terephthalate (PET).

As mentioned above, the materials considered in this work to fabricate the transistors are carbon and PEDOT:PSS. Carbon inks have been shown to be degradable in a standard compost [109] and considered to be compatible with implanted use [300]. Moreover, carbon and carbon allotropes in general are of interest for enzymatic detection of molecules due to their high surface area and electron transfer rate [301]. PEDOT:PSS is a biocompatible material [63], has been observed to break-down in moist environments [101], and is considered environmentally benign [302]. The contacts of the OECTs are formed with a screen printable carbon-based paste. The carbon paste is obtained by mixing graphite flakes, carbon black, pentanol and shellac as described in work by Poulin et al. [55]. This formulation was chosen for the water insolubility of the shellac, allowing the contacts to operate in humid environments. The carbon contacts for the source and drain have a resistance of $44.2 \pm 5.3 \Omega$. The channel is fabricated by inkjet printing of a water-based PEDOT:PSS solution, as well as the gate in some configurations. The conductive polymer solution is modified with dimethyl sulfoxide (DMSO), which has been shown to increase PEDOT:PSS conductivity by enhancing PEDOT:PSS cohesion and the creation of PEDOT:PSS-rich domains [303,304], as well as favor stable printing due to its low volatility [305]. The inkjet-printed PEDOT:PSS channel has a thickness of $0.50 \pm 0.05 \mu\text{m}$ and a resistance of $1.54 \pm 0.06 \text{ k}\Omega$ ($n = 3$). The gate electrode is constituted of a carbon contact, which is extended as a gate in some experiments or is in contact with a PEDOT:PSS gate in a second configuration, as seen in **Figure 5.1(a)**. The fabrication process flow is shown in **Figure 5.1(d)**. The degradation of the devices is qualitatively assessed with a degradation test in soil at 55°C (**Figure 5.1(e)**), as previously used for assessing the degradation of PLA substrates [306]. The devices do not undergo visible physical degradation until the third week, when PLA is observed to become opaque and crack, and PEDOT:PSS to break down and fragment. After a month of

degradation, the PLA substrate as well as the carbon contacts have separated in smaller pieces and the PEDOT:PSS channel is almost entirely broken down.

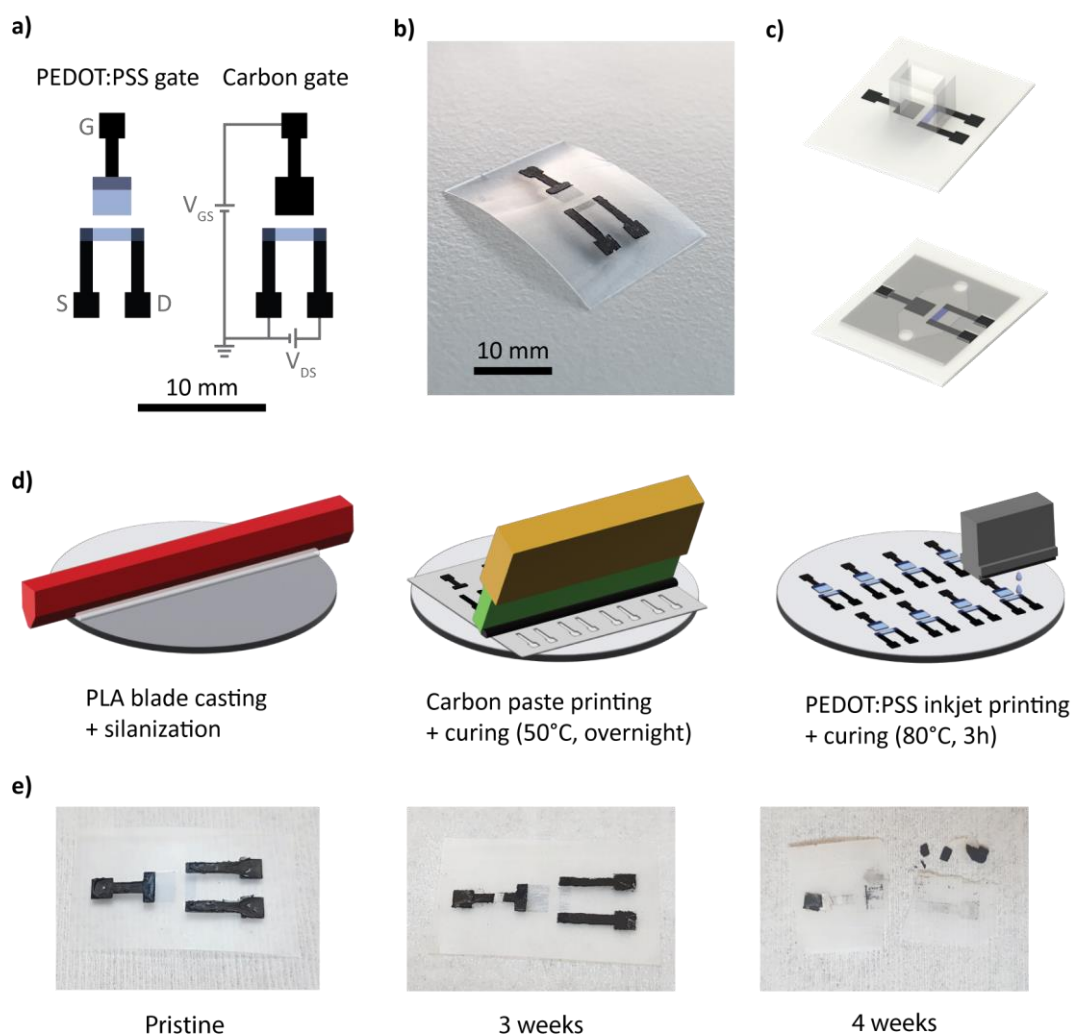


Figure 5.1: Design and fabrication of the degradable OECTs. **a)** Layout of the two OECT designs (PEDOT:PSS-gated and carbon-gated). **b)** Picture of a PEDOT:PSS-gated device. **c)** Recording setups used in the experiments: PMMA reservoir (top) and microchannel (bottom). **d)** Fabrication process for the additive manufacturing of degradable OECTs: (i) PLA substrate casting and surface modification, (ii) carbon paste stencil printing and curing and (iii) inkjet printing of PEDOT:PSS channel and curing. **e)** Degradation of a transient device in soil at different timepoints.

5.2.2 Influence of gate material and geometry

Degradable materials, unsurprisingly, often exhibit higher reactivity in aqueous solutions [26], and thus, we look at the influence of carbon and PEDOT:PSS as gate material on the electrical characteristics of the transistors. This was first evaluated on an inert polyimide (PI) substrate to avoid potential influence from the biodegradable substrate on the OECTs behavior when in an aqueous solution. Indeed, as can be seen in **Figure 5.2(a)** on the left, an OECT with carbon contacts and Ag/AgCl gate electrode displays a very similar behavior as OECTs with the same geometry and channel characteristics seen in the literature [284]. The transconductance maximum is observed at a V_{gs} of approximately -200 mV and a transconductance of 0.389 mS is obtained as seen in **Figure 5.2(b)**, showing the drain current as a function of the gate voltage as well as the transconductance. The transconductance peak for Ag/AgCl gated OECTs is usually found at gate voltages around 0 V, however negative values of a few hundreds of millivolts have been observed in the literature [287,307], in particular when the resistance of the contact was negligible with respect to the resistance of the channel [308]. An explanation for this behavior has been proposed by Paudel et al. [309]. With lower (more negative) source-

drain voltages (V_{ds} is -600 mV in our case), more cations accumulate at the drain electrode, partially de-doping the channel and causing transistor pinch-off at lower (more negative) gate voltages.

The surface properties of the gate electrode are of importance in the transistor behavior achieved. Indeed, contrary to silver/silver chloride (Ag/AgCl) electrodes, which are non-polarizable and operate in a Faradaic regime, polarizable materials such as the ones under consideration here will cause the gate to operate in a capacitive regime [307]. As a consequence, the specific surface of the gate, which has an influence on the double-layer capacitance between the gate and the solution, will affect the transistor behavior [310]. The behavior of the transistors was assessed by measuring their output (drain current I_{ds} – drain voltage V_{ds}) and transfer characteristics (drain current I_{ds} – gate voltage V_{gs}) as well as calculating their transconductance ($g_m = \delta I_{ds} / \delta V_{gs}$). We first look at the influence of the gate material for a fixed geometry and compare it with devices where an Ag/AgCl gate is used. When changing from a non-polarizable Ag/AgCl gate to a polarizable PEDOT:PSS gate, the de-doping behavior is less evident than for an Ag/AgCl gate and happens at higher gate voltages (~400 mV, 0.276 mS), in agreement with previous investigations [285,307]. With the carbon contact as the gate material, a similar behavior to the PEDOT:PSS gate is observed, with a transconductance peak at 700 mV and which reaches a value of 0.376 mS. Although the capacitance of the carbon gates is larger than that of the PEDOT:PSS gates (see **Figure S5.1**), the carbon-gated OECT does not show markedly more efficient modulation and only slightly higher transconductance. This could be due to the capacitance of the system being dominated by the channel [291], as these measurements were conducted with large gates, as well as batch-to-batch variations in the fabrication.

As a further step, we looked at the effect of the gate geometry, as the ratio between the gate and channel areas influences the transistor behavior [311]. For these experiments, we focused on PEDOT:PSS-gated OECTs and varied the aforementioned area ratio ($\gamma = A_{gate}/A_{channel}$) between 0.5 and 2, and the results are shown in **Figure 5.2(c)** and **Figure 5.2(d)**. As seen in the drawings of the designs in **Figure 5.2(c)**, the distance between the gate and the channel also changed, however it has been shown in the literature not to affect the electrical behavior of OECTs [311,312] or their response dynamics [313] at the distances concerned here. As can be seen in **Figure 5.2(c)**, the current modulation behavior is more marked for a larger gate relative to the channel ($\gamma = 2$). Importantly, a peak in transconductance is reached for lower voltages when a large area ratio is used (**Figure 5.2(d)**), as observed in previous research [314]. This is due to the increased capacitance of the gate with increased area, which reduces the voltage loss at the gate, causing a more efficient modulation of the channel current [307]. Therefore, this design ($\gamma = 2$) was chosen for further experiments in order to favor the operation of the transistors at lower voltages and be farther from the voltage threshold at which water electrolysis occurs.

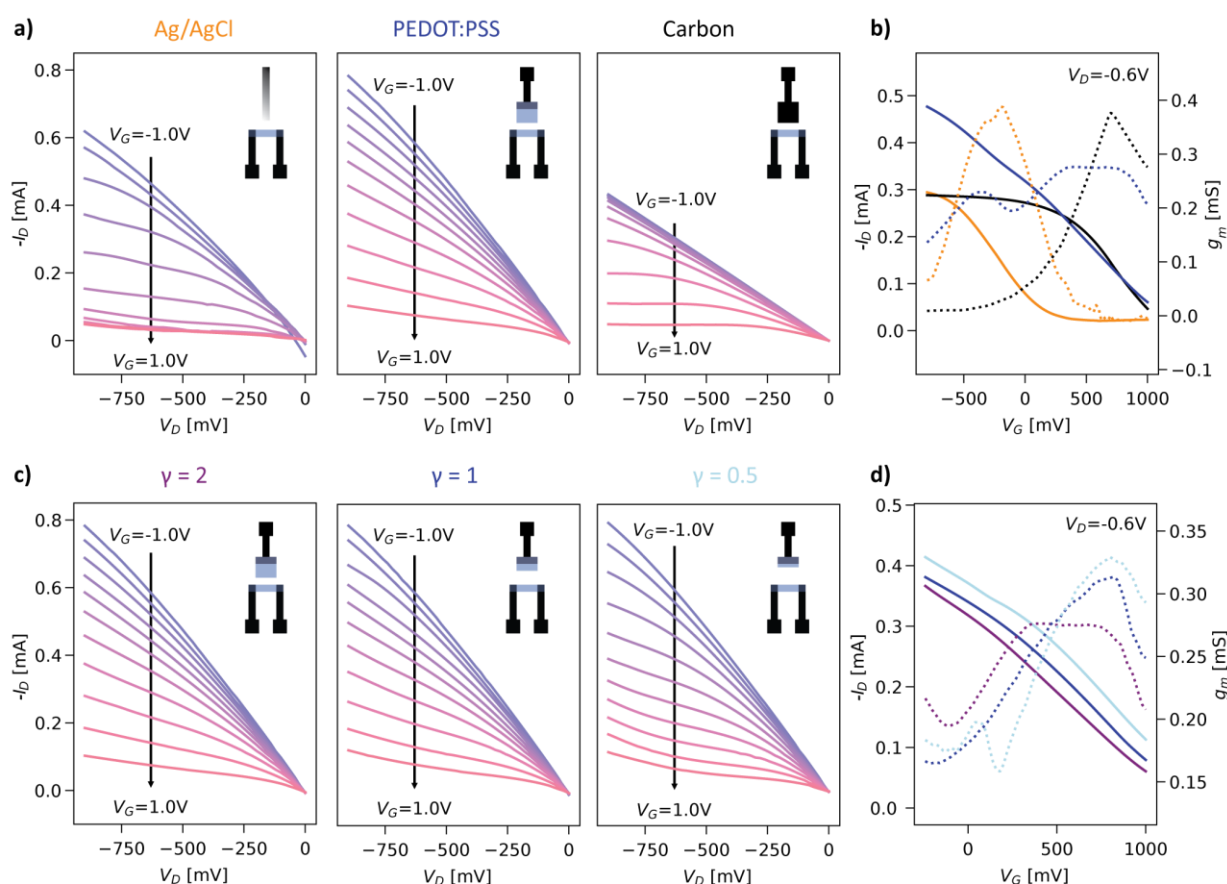


Figure 5.2: Influence of the gate material and dimensions on the behavior of the transistors. a) Output curves for Ag/AgCl, PEDOT:PSS and carbon gates. b) Corresponding transfer curves (solid lines) and transconductance (dotted lines) for the gate materials. c) Output curves for different gate area to channel area ratios: (left) larger gate, $\gamma=2$, (middle) medium gate, $\gamma=1$, (right) smaller gate, $\gamma=0.5$. d) Corresponding transfer curves (solid lines) and transconductance (dotted lines) for the gate-to-channel ratios.

5.2.3 Integration on a biodegradable substrate

With an optimized design for OECTs relying on degradable materials, we transferred their processing on a biodegradable polylactic acid (PLA) substrate. The latter was chosen for its known biodegradability by natural factors, as well as its relative durability in aqueous environments [306]. It effectively strikes a balance between degradability and durability, avoiding for instance a large amount of degradation byproducts immediately fouling the response of the transistor as it comes in contact with the analyte solution. However, its hydrophobicity represents a challenge as the PEDOT:PSS aqueous solution drops deposited by the inkjet printer may not wet the surface, leading to agglomeration and low-quality prints, or delamination of the channel can occur in aqueous media (Supplementary **Figure S5.2**). To circumvent these problems, we study the surface energy of the PLA films and compare it with PI, before and after the use of an oxygen plasma treatment to chemically activate the surface. This was assessed by measuring the contact angle of a droplet of DI water with the substrates and the results are shown in **Figure 5.3(a)**. The contact angle for polyimide substrates considerably decreases when oxygen plasma treatment is used, from $63.9 \pm 5.4^\circ$ for pristine PI to $14.6 \pm 0.7^\circ$ after 120 seconds at 40 W (40 kHz), as seen in Supplementary **Figure S5.3**. Conversely, the water contact angle decrease for PLA for the same treatment is less marked, and the substrate remains relatively hydrophobic, with a contact angle of $45.6 \pm 2.4^\circ$ after 120 seconds of oxygen plasma treatment. To allow for satisfying printing and adhesion of the conductive channel, we functionalized the PLA with 3-aminopropyltriethoxysilane (APTES), an aminosilane allowing it to obtain a more hydrophilic surface. After APTES spin-coating and subsequent oxygen plasma activation, a contact angle of $16.4 \pm 3.2^\circ$ is achieved. Another challenge with the use of transient

substrates such as PLA is the preservation of their integrity during post-processing steps involving heat, especially for extended periods of time. Solution-processed PEDOT:PSS is typically cured at 120 °C [23] for 20 minutes or more. We validated that a curing protocol that is compatible with the degradable substrate (80°C for 3h) would yield the same transistor behavior as when the standard curing protocol is used. The results presented in Supplementary **Figure S5.4** show that the longer curing protocol is adequate not only in terms of obtaining a similar channel electrical conductivity, but also transistor behavior for the PEDOT:PSS channel. This allows to fabricate OECTs with fully transient materials, and their output and transfer characteristics are shown in **Figure 5.3(b) and 3(c)** respectively, for a carbon-gated device. A transconductance of 0.247 mS is achieved, which is comparable with OECTs fabricated on non-transient substrates published in recent works [291]. It is interesting to note that our ink formulation contains (3-glycidyloxypropyl)trimethoxysilane, which was originally added to increase to stability of the channel [315]. However, its full cross-linking is only attained when cured at temperatures above 100 °C [316], and therefore this suggests that the improved adhesion of the PEDOT:PSS to the PLA is largely provided by the aminosilane layer. Finally, the evolution of the transistor behavior of the devices in PBS is evaluated by measuring the transfer behavior repeatedly over approximately one hour, every minute. The results are shown in **Figure S5.5**, and it is observed that the peak transconductance for a PEDOT:PSS-gated device decreases by 20% after 60 measurement cycles. Such a decrease of the current of OECTs has been observed in previous studies and has been inversely linked to the crystallinity of the PEDOT:PSS film [317].

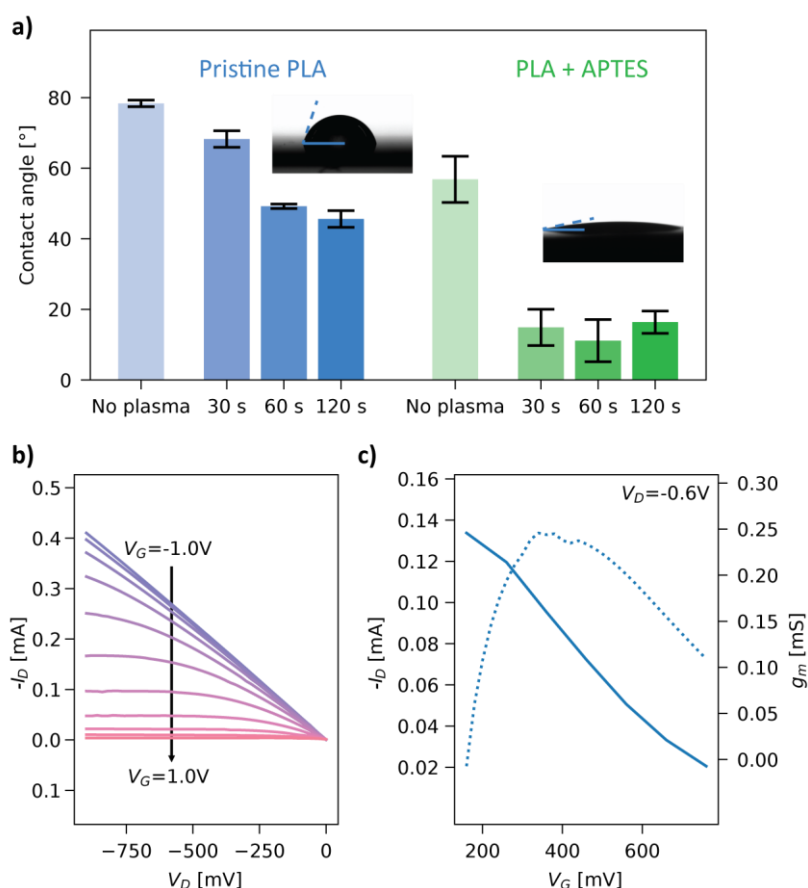


Figure 5.3: Surface modification of PLA to enable to fabrication of fully degradable OECTs. a) Contact angle of DI water on PLA, with and without silanization and as a function of the time of application of oxygen plasma and in inset: contact angle before (left) and after surface (right) modification ($n = 3$ for each treatment). b) and c) Electrical characterization of the transient OECT on PLA, respectively output and transfer curves.

5.2.4 Cation sensing experiments

The degradable OECTs were integrated into a simple microfluidic system to allow for the measurement of decreasing ion concentrations as well as precise control of the ion concentration to which the device is exposed. Prior to measurement, the transistors were flushed with DI water under a gate voltage of 0.6 V for a total of 15 minutes, adapting a protocol reported in the literature to enhance the stability of PEDOT:PSS-based OECTs [315]. Ionic solutions of NaCl, KCl and CaCl₃ respectively, in deionized (DI) water were used, in concentrations ranging from 1 to 100 mM. DI water was injected into the channel via the inlet, followed by increasing concentrations of the test solution every 240 seconds. Finally, decreasing concentrations of the solution were injected after the same time interval, finishing with a DI water injection. These experiments were conducted with both PEDOT:PSS-gated, in **Figure 5.4(a)** and carbon-gated OECTs, in **Figure 5.4(b)**. In the insets, the normalized responses ($n = 3$) for each ion as well as a logarithmic regression of the responses are shown. The sensitivities for each ion were calculated by extracting the steady-state currents from the raw sensor responses and are reported in normalized terms. Indeed, the resistance of the printed PEDOT:PSS channels, and therefore the magnitude of the source-drain current, may vary between devices. Thus, the response is referenced and normalized with respect to the current I_0 measured in the device after stabilization in DI water.

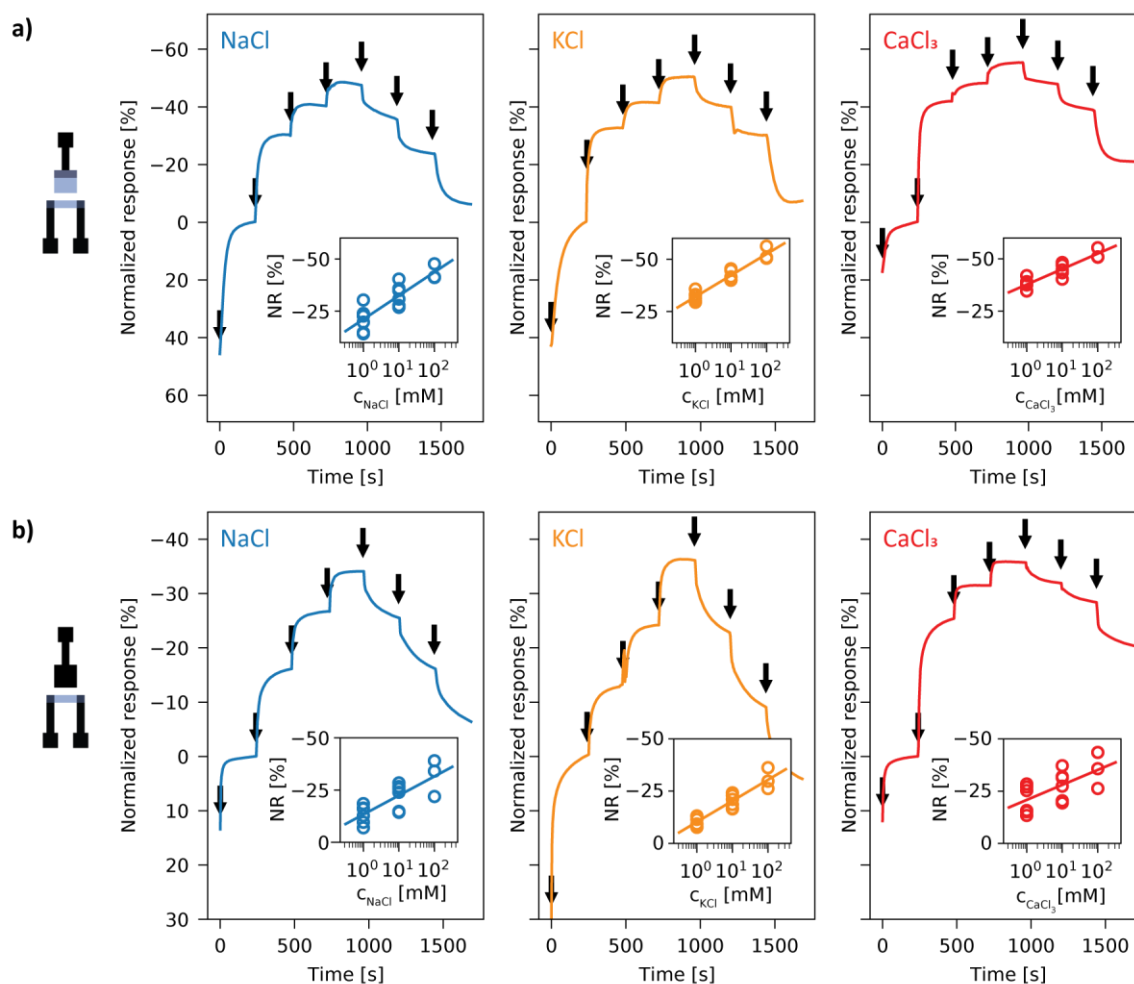


Figure 5.4: Characterization of the OECTs for ion concentrations measurements. Real-time normalized response to varying concentrations of ions, Na⁺ (left), K⁺ (middle), Ca³⁺ (right) with the injections of the different ion concentrations (DI water, 1, 10, 100, 10, 1 mM, DI water) indicated by arrows, and the regression of the normalized currents in the insets ($n = 3$), for PEDOT:PSS-gated OECTs (a) and carbon-gated OECTs (b). The same Y-axis scale was used for all the ions tested.

Independent devices show similar current modulation and the responses scale linearly with the logarithm of the ion concentration. Carbon-gated and PEDOT:PSS-gated OECTs show qualitatively similar behavior. After the final injection of DI water, the source-drain currents of devices return in the vicinity of the I_0 current value. However, in order to re-use a device after a set of measurements, we observed that thorough rinsing with DI water for several minutes was necessary to closely restore the initial current. The relative sensitivities of the OECTs comprising a PEDOT:PSS gate are respectively, for the ions Na^+ , K^+ and Ca^{3+} , $-11.3 \pm 1.8 \text{ \%/dec}$, $-10.2 \pm 0.8 \text{ \%/dec}$ and $-7.4 \pm 1.0 \text{ \%/dec}$. The carbon-gated OECTs display slightly more variability between devices than the PEDOT:PSS-based devices. This could be due to the printing method for the carbon gate (stencil printing) being less repeatable. For the same ions, the carbon OECTs has the following sensitivities (with standard errors): $-9.1 \pm 2 \text{ \%/dec}$, $-10.1 \pm 1.1 \text{ \%/dec}$ and $-7.2 \pm 2.4 \text{ \%/dec}$. Further experiments were conducted with a larger range of concentrations (0.1 mM, 0.5 mM, 1 mM, 5 mM, 10 mM, 50 mM, 100 mM) in order to confirm the sensitivities obtained above for each ion, and the results are reported in **Figure S5.6**. Similar values are obtained for the sensitivities of the devices, with the PEDOT:PSS devices showing slightly higher values, as seen in **Figure 5.4**. Finally, the stabilization of the response of the OECTs to an ion injection was characterized and is shown in **Figure S5.7**. The source-drain current is measured over 20 minutes after ion injection, repeated three times for the same device. After injection both the carbon- and PEDOT:PSS-gated sensors' responses stabilize to reach a plateau. These experiments show that the degradable devices are suitable for the detection of various ions, whether a PEDOT:PSS or carbon gate is used.

5.2.5 Glucose detection and integration with degradable circuits

As a further step, the possibility to use these degradable transistors for the detection of glucose was assessed in the proof-of-concept experiments presented hereafter. These biosensors generally rely on the oxidation of glucose by glucose oxidase (GOx) present on or in the vicinity of the sensor, causing an increase in gate voltage [282]. In this work, glucose concentration measurements were conducted in a PMMA well. Degradable carbon-gated OECTs were used for glucose detection, as carbon benefits from a high surface area and good electron transfer, which is desirable for enzymatic sensing [301]. The GOx enzyme solution in PBS was added to the well, and glucose was subsequently added at increasing concentrations with each injection. An example of a real-time detection experiment for glucose is shown in **Figure 5.5(a)**, with the glucose injections indicated by arrows. The normalized response for three devices is shown in **Figure 5.5(b)**. The relative response of the transistor is non-linear to the logarithm of the glucose concentration, as it has been observed in previous work [318]. In order to determine the limit of detection, a logarithmic regression is carried out in the concentration range from 1 μM to 1 mM, yielding a sensitivity of $-3.4 \pm 0.6 \text{ \%/dec}$ (averaged over the three devices). The limit of detection is estimated as the noise level of the sensor divided by the sensitivity and multiplied by a confidence factor. Considering the standard deviation for the lowest concentration as the noise level and a confidence factor of 3, the limit of detection for glucose can be estimated to be about 5 μM , which is comparable to previous publications on non-transient OECT-based glucose sensors [23,282,319]. It can be seen in **Figure 5.5(b)** that concentrations above 1 mM of glucose show higher device-to-device variations. This could be attributed to the larger amounts of H_2O_2 being released and affecting the PEDOT:PSS layer [320], which would cause a permanent decrease in the current going through the channel. Therefore, the devices can detect glucose in a range from 5 μM to approximately 1 mM.

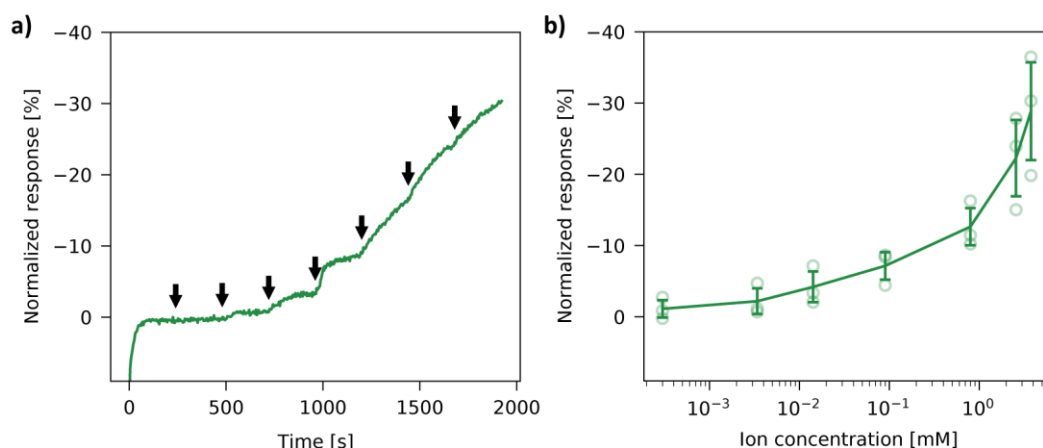


Figure 5.5: Characterization of the OECTs for the enzymatic detection of glucose. a) Real-time glucose sensing (normalized response current) with increasing glucose concentrations (injections of glucose are indicated by arrows), measured in a PMMA well containing glucose oxidase solution. b) Normalized current response (and standard deviation) versus glucose concentrations ($n = 3$).

Finally, we aimed to develop interconnects for the integration of the degradable OECTs with transient electronics. Indeed, the sensor may need to be connected to a readout circuit by conductive traces that are ideally eco- and/or bioresorbable. However, with the relatively high sheet resistance of the carbon ink ($15 \Omega/\text{sq}$), the use of longer carbon traces may considerably increase the resistance of the system, leading to a reduction of the recorded currents and increased noise, as well as a shifting of the transconductance peak to higher gate voltages [308]. Metallic degradable and printable conductors are available and allow to reach higher conductivities [82] and would be therefore suitable for the fabrication of interconnects in a fully printed degradable biosensing platform. The most investigated of such transient metals is zinc, for which methods have been developed [185,321] to obtain conductivities superior to 10^5 S/m . However, the direct integration of zinc as contacts for the OECTs presented here is challenging. Indeed, the zinc oxide layer that naturally forms in air on zinc metal forms a p-n junction with PEDOT, which is a p-type conductive polymer. As a result, a Schottky conduction regime emerges, with limited conductivity below a certain threshold [322,323]. The I-V characteristic of such a junction (formed by stencil-printed Zn and inkjet-printed PEDOT:PSS) is shown in **Figure 5.6(a)** and displays a diode-like behavior. This type of contact is incompatible with the operation of the low-voltage OECTs presented here. However, zinc interconnects can be integrated with the carbon contacts used in the design presented above. The contact between carbon and PEDOT is ohmic, as shown by the linear I-V curve shown in **Figure 5.6(b)**. As a consequence, zinc can be used to fabricate the interconnects of the OECT with carbon creating the contact with PEDOT:PSS. Such OECTs were fabricated and exhibit the same behavior as the carbon-based transistors presented before (Supplementary **Figure S5.4**), demonstrating that the degradable OECTs can be integrated with high-conductivity biodegradable interconnects (**Figure 5.6(c)**). This is of interest, as some transient applications may benefit from wireless operation for example, which is a promising direction for OECT-based devices [299]. It is noted that zinc degrades rapidly in aqueous solutions, and we have shown in a previous study that the zinc interconnects can be encapsulated in PLA and retain their electrical conductivity for several weeks in PBS [321].

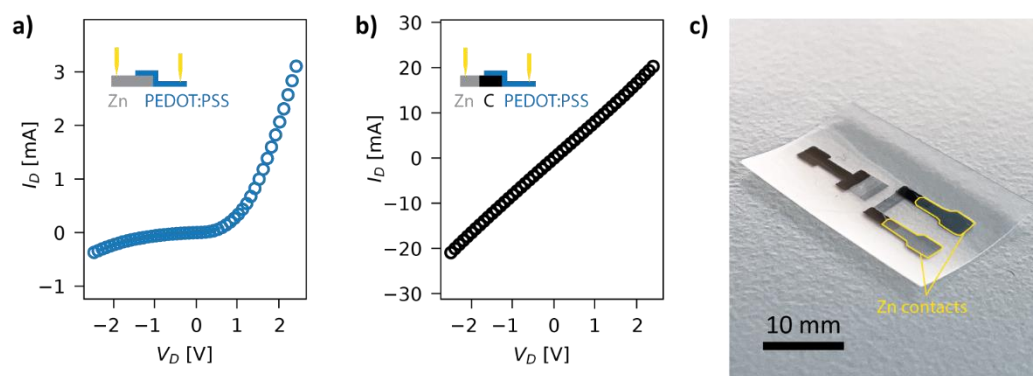


Figure 5.6: Integration of the OECTs with zinc metal traces. a) I - V curve of a Zn-PEDOT:PSS junction. b) I - V curve of a Zn-carbon-PEDOT:PSS junction. c) Example device with carbon contacts for the channel and zinc interconnects.

5.3 Conclusions

In this work, we demonstrate disposable and printed organic electrochemical transistors, which are suitable for the detection of ions and metabolites such as glucose. Their degradation in conditions analogous to industrial composting is observed over a period of one month. The disposable transistors are integrated with highly conductive biodegradable zinc interconnects on an eco- and bioresorbable substrate. The use of PLA as a substrate allows to manufacture sensors that are not only compatible with environmental applications, but can also be used for wearable and implantable applications. Concerning applications in bioresorbable electronics, it must be noted that despite PEDOT:PSS being biocompatible, the pathways and effects of its degradation in the body are not fully known and more investigations are needed on that topic. With an optimized design for the degradable transistors, the fabrication process is adjusted to be compatible with the use of polylactic acid as substrate. A silanization process allows the uniform deposition by inkjet-printing of the water-based PEDOT:PSS inks with good adhesion, enabling the fully additive manufacturing of the disposable transistors. The electrochemical transistor behavior is characterized and shown to be equivalent to non-degradable counterparts with similar design and channel characteristics. Carbon contacts are shown to be suitable for the fabrication of degradable OECTs, and the use of either a carbon or PEDOT:PSS gate to cause a shift in the transconductance peak while maintaining high transconductance values. Moreover, the use of non-polarizable gate materials is shown to decrease the dedoping behavior of the transistors, and a high gate area to be favorable. Sensitivities in the order of 10 %/dec are observed for the detection of sodium, potassium and calcium ions. The ion sensing behavior of the devices is characterized with increasing and decreasing concentrations and is shown to be reproducible across devices. This indicates that the use of degradable materials and inks does not interfere with the sensing mechanisms in the measurement timescales compatible with point-of-care testing with disposable sensors. Although the sensing of several ions is demonstrated in this work, selective ion sensing would require a biocompatible and degradable ion-selective membrane (ISM), which would be an interesting direction for future developments. A proof-of-concept enzymatic detection of glucose is also shown, with linear behavior up to 1 mM. In order to ensure the applicability of the transistors as glucose sensors, more experiments should be conducted to characterize the stability and selectivity of the devices, ideally with the enzyme being immobilized on the sensor. The transistors are shown to be integrated with highly conductive degradable zinc tracks, which opens new possibilities for integration with biodegradable circuits, allowing for instance wireless operation.

5.4 Experimental section

Substrate preparation and characterization

Polyimide foil (125 μm) was treated with oxygen plasma before printing the PEDOT:PSS channel to ensure good adhesion. Polylactic acid substrates were prepared from pellets (Ingeo™ Biopolymer 4032D). The PLA pellets were dissolved in 1,4-dioxane (Sigma Aldrich) at 50°C overnight under stirring until obtention of a homogeneous viscous solution (15 wt%). The solution was blade cast with an automatic film applicator coater (Zehntner ZAA 2300) on a silicon wafer with a gap of 1000 μm and a speed of 2 mm/s. After drying overnight, films of a thickness of approximately 70 μm were obtained. The PLA film surface was activated with oxygen plasma and modified with a silanization process. 3-aminopropyltriethoxysilane (APTES, Sigma Aldrich) was dissolved at 3 wt% in ethanol, spin-coated at 2000 rpm on the PLA films and allowed to cure at 80 °C for 20 mn, after which the excess APTES was rinsed with ethanol. The APTES layer was activated with oxygen plasma before PEDOT:PSS printing. The contact angles of the substrates with different surface treatments were measured with an optical contact angle measuring system (Dataphysics TBU 100) using deionized water as the liquid medium.

OECT fabrication

A shellac-carbon paste was used for the source, drain and, in some experiments, gate contacts and its formulation was described previously [55]. The carbon paste was applied through a stencil mask made of one-sided polyethylene adhesive tape (Nexus G20, 80 μm). The mask was cut to the desired shape with a CO₂ laser (Trotec Speedy300) and applied on the substrate, and the carbon paste was printed with the help of a silicone squeegee. After printing, the mask was peeled off and the carbon contacts were cured in an oven at 50 °C overnight. PEDOT:PSS printing solution was prepared by mixing 1.3 wt% PEDOT:PSS in water (Sigma Aldrich) with 5 wt% dimethyl sulfoxide (Sigma Aldrich) and 1 wt% (3-glycidyloxypropyl)trimethoxysilane. 4 layers of the solution were printed using a Dimatix DMP inkjet printer (Fujifilm) with a drop spacing of 30 μm and keeping the printer plate at 40 °C. The layers were then cured at 80°C for 3 hours or at 120 °C for 20 mn. The thicknesses of the contacts and channel were measured with a laser scanning confocal microscope (Keyence VK-X1000). Zinc interconnects were prepared by stencil printing a Zn microparticles (<5 μm , Sigma Aldrich) mixed with pentanol (Sigma Aldrich) and polyvinylpyrrolidone (360K, Sigma Aldrich). The zinc interconnects were sintered electrochemically to a conductivity of $>10^5$ S/m as described previously [18]. They were then further sintered by photonic sintering with three 30 milliseconds pulses (6.6 J/cm²) [321]. After OECT fabrication, the outlines of the devices were cut with a CO₂ laser and the devices were manually peeled off from the wafer, as explained in a previous publication [321]. All subsequent measurements were done on the released devices.

Test solutions preparation

1X Phosphate-buffered saline (PBS) was prepared with chemicals sourced from Sigma Aldrich at the following concentrations in DI water: NaCl: 137 mM, KCl: 2.7 mM, Na₂HPO₄: 10 mM, KH₂PO₄: 1.8 mM. For potassium and sodium sensing tests, KCl and NaCl solutions were prepared in DI water. Glucose solutions were prepared by mixing glucose with PBS at the desired concentrations. Enzyme solutions were prepared before each experiment by mixing glucose oxidase (from *Aspergillus Niger*, 100 000– 250 000 units/g, Sigma Aldrich) in 1 mL of a PBS and letting them rest at room temperature for 30 minutes.

Devices characterization

The devices were characterized with the test solutions confined in a laser-cut PMMA reservoir maintained on the device with acrylic adhesive, or for real-time measurements, by flowing the solution in a laser-cut PET and PDMS microfluidic channel [22]. For glucose measurements, the enzyme solution was first added to a PMMA well, followed by increasing concentrations of glucose solution. The source and drain contacts were isolated with polyurethane, which was cast from a 25% solution in DMSO, to avoid interaction between the carbon contacts and the electrolyte. The electrical measurements were performed using a semiconductor parameter

analyzer (Agilent 4155A). Prior to measurements, the OECTs were rinsed with 1 ml DI water and left to stabilize in DI water under a gate-drain voltage of 600 mV for 5 minutes, repeated three times. Output curves ($I_{ds}-V_{ds}$) were measured with a medium integration time (20 ms) and varying the source-drain voltage between 0.1 to -0.9 V in steps of -20 mV and the gate-source between -1 and 1 V in steps of 200 mV. Transfer curves ($I_{ds}-V_s$) were measured with a long (320 ms) integration time and repeated 5 times to ensure stabilization of the device behavior, with V_{ds} set to -0.6 V and V_{gs} between -1 and 1 V with steps of 20 mV. The capacitance of the gates was measured by impedance spectroscopy (Metrohm Autolab 8 Series) as described previously [307]. The data were analyzed with custom software written in python.

5.5 Supporting information

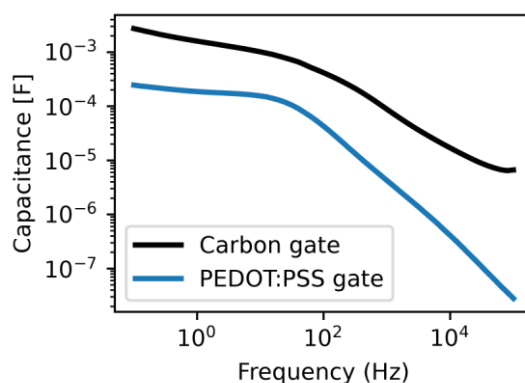


Figure S5.1: Capacitance of the PEDOT:PSS and carbon gates measured in phosphate-buffered saline.

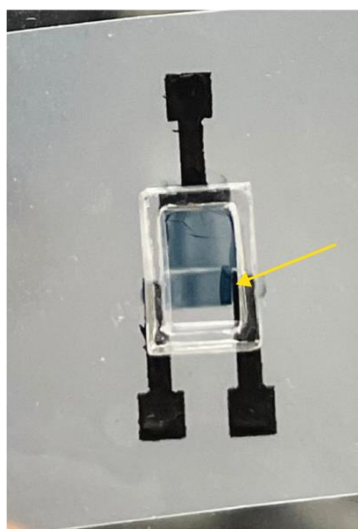


Figure S5.2: Delamination (pointed out by the arrow) of PEDOT:PSS channel and gate in PBS solution, when inkjet printed on a poly(lactic acid) film.

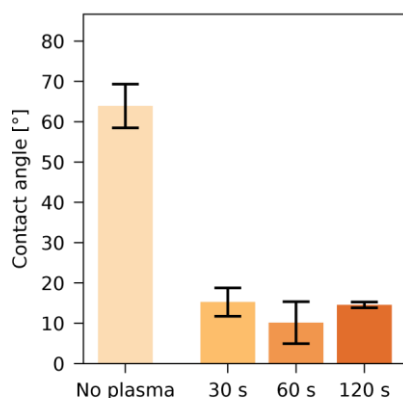


Figure S5.3: Influence of oxygen plasma treatment on a polyimide film on the contact angle of a water droplet, with 40W, 40 kHz oxygen plasma treatments with variable time.

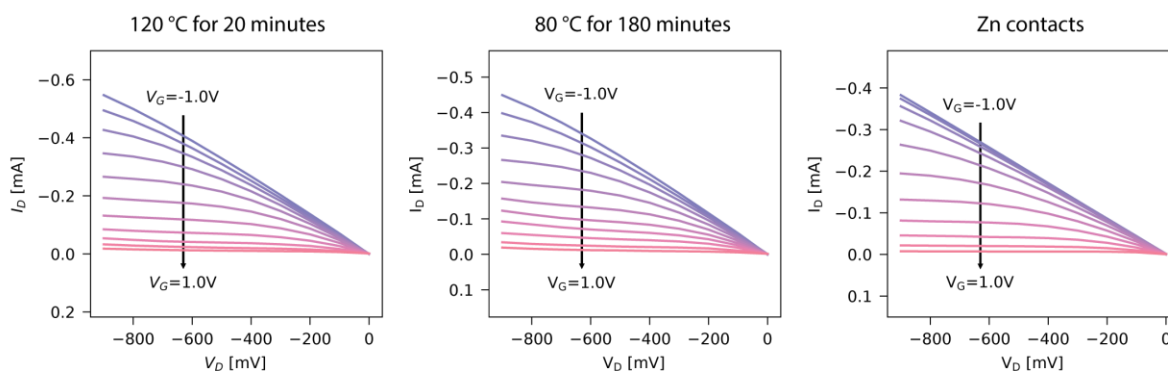


Figure S5.4: Output characteristics of the OECTs (PEDOT:PSS-gated) for different modifications to the fabrication process (with the standard process as a control experiment on the left): changing the curing of the PEDOT:PSS layer to 80 °C for 3 hours (middle) and introducing Zn contacts using the same PEDOT curing protocol (right).

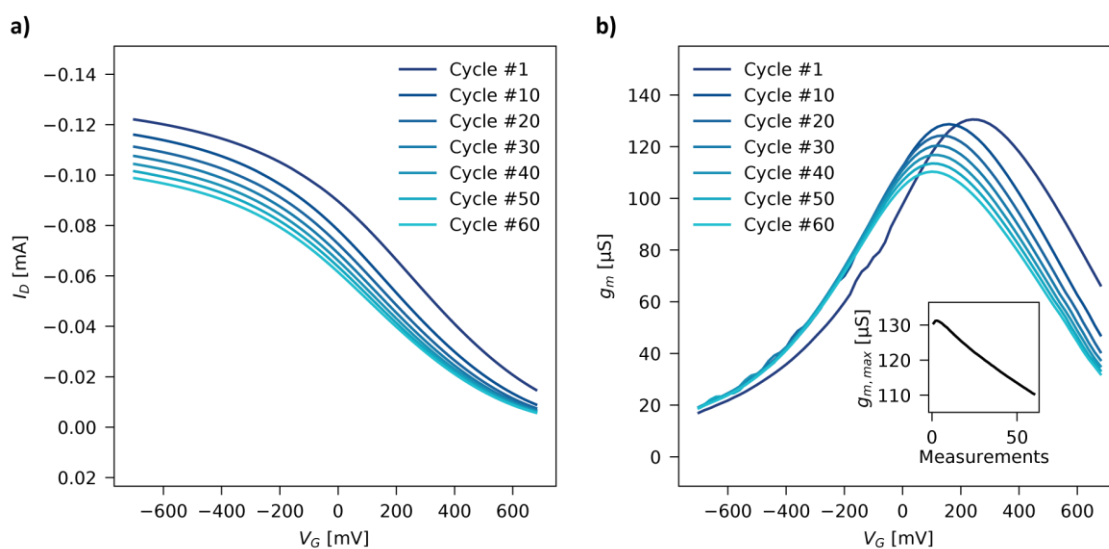


Figure S5.5: Transfer characteristics of the OECTs on PLA after cycling transfer measurements for one hour. (a) Evolution of the transfer behavior after repeated measurements. (b) Evolution of the transconductance after repeated measurements, and the evolution of the maximal transconductance in the inset.

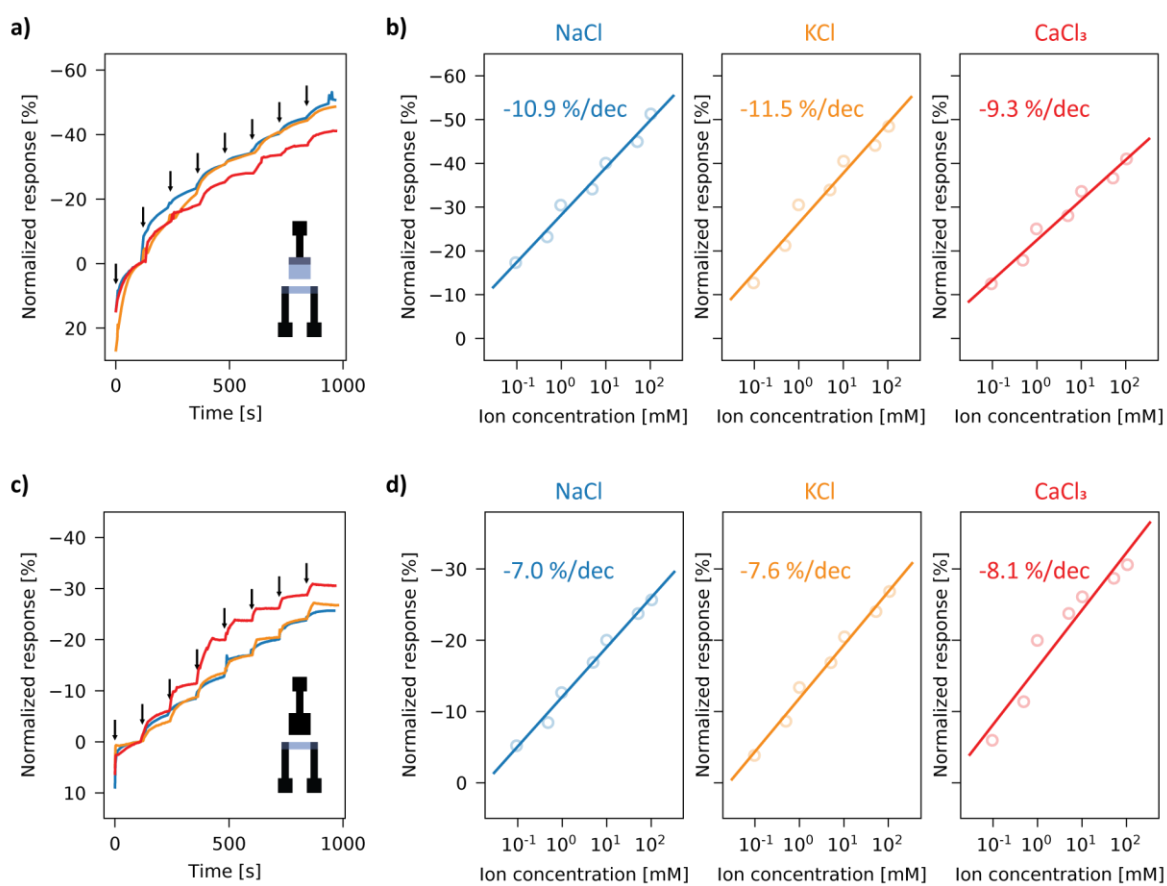


Figure S5.6: Calibration curves for the OECTs for use in ion detection applications, for PEDOT:PSS-gated ((a) and (b)) and carbon-gated ((c) and (d)) devices. (a - c) Real-time normalized response to varying concentrations of ions, Na⁺ (blue), K⁺ (orange), Ca³⁺ (red) with the injections of the different ion concentrations (0.1 mM, 0.5 mM, 1 mM, 5 mM, 10 mM, 50 mM, 100 mM) indicated by arrows. (b - d) Regression of the normalized current responses for each ion.

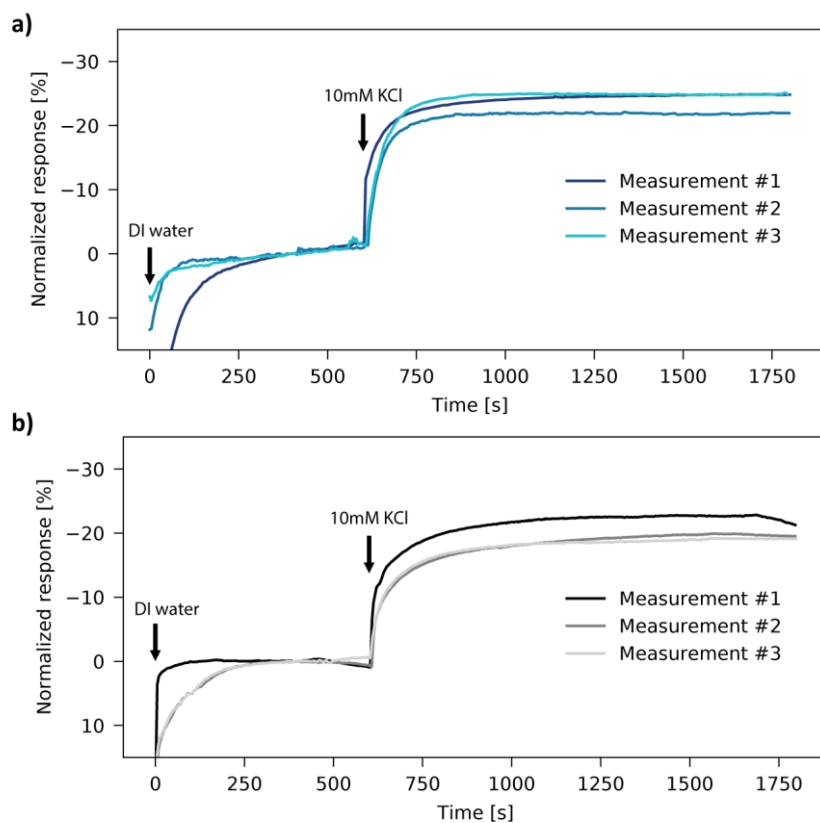
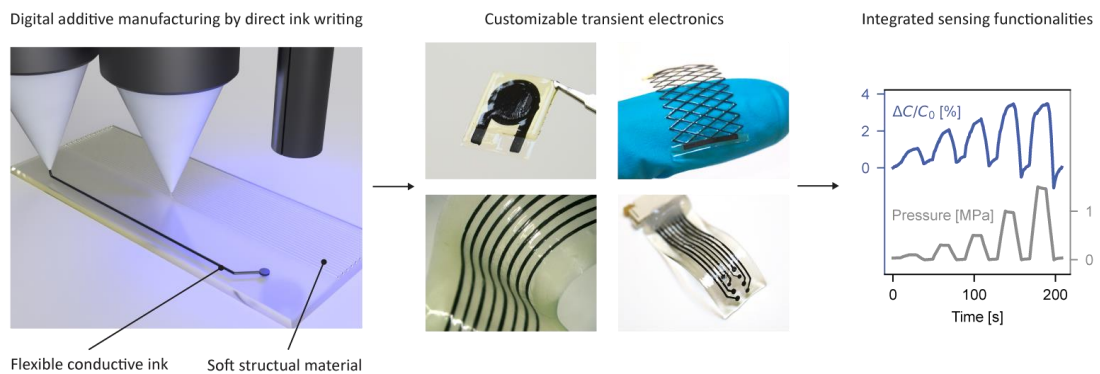


Figure S5.7: Response dynamics and stability of the devices. Response of the devices after injection of 10 mM KCl injection, for 20 minutes, repeated three times, for (a) PEDOT:PSS-gated device and (b) carbon-gated device.

Chapter 6 Digital manufacturing of customizable 3D bioresorbable electronics



Bioresorbable electronics have emerged as a new category of bioelectronics that can degrade within the body, offering tremendous potential for diagnosis, post-surgical monitoring and regeneration applications. Additive manufacturing methods represent a promising approach for patterning transient materials, yet examples of fully printed bioresorbable devices are scarce. This study introduces a fully digital 3D printing approach enabling the prototyping and customization of soft bioelectronics made of transient materials. We investigate the direct ink writing of poly(octamethylene maleate (anhydride) citrate) (POMaC) as an elastomeric matrix and of a shellac-carbon ink as a conductor. We achieve precise and repeatable deposition of both structural and conductive features by optimizing printing parameters, i.e., the dispense gap, printing speed, and inlet pressure. Multi-material 3D printing enables the fabrication of functional transient devices. Notably, pressure and strain sensors are shown to operate in ranges relevant to implanted biomechanical monitoring. 3D printed transient electrodes are demonstrated to be comparable to state-of-the-art devices in terms of impedance behavior. Finally, physical degradation of the materials is confirmed at physiological conditions. These fully digital additive manufacturing processes enable the monolithic fabrication of customizable transient bioelectronics with adaptable functions and geometries.

6.1 Introduction

In the past decade, bioresorbable electronics have garnered significant interest as temporary bioelectronic devices capable of fulfilling monitoring, stimulation, or actuation functions for a limited period of time [1,3,67]. These devices are designed to degrade within the body without causing adverse side effects [5]. This can allow notably to avoid re-operation in cases where only short-term functionality is needed and may help reduce inflammatory response by providing a dissolvable interface with the tissue [29]. This emerging class of implants relies on materials that undergo degradation in biological environments through hydrolysis or enzymatic processes, posing a significant challenge to their fabrication due to this inherent property. Several approaches have been proposed to tackle this challenge, such as mask-based deposition [147], or transfer methods relying on controlled adhesion with a silicone stamp [121] or lamination of films using bioresorbable adhesives [130]. These strategies have resulted in a diverse range of bioresorbable devices, including pressure [84], temperature [124], and strain [146] sensors, electrocorticography (ECoG) electrodes [142], pacemaker leads [137], etc.

Additive manufacturing (AM) has emerged as a promising approach for fabricating bioresorbable electronics [2,159]. Compared to the methods used thus far, additive manufacturing presents the advantage of enhanced compatibility with transient materials. Indeed, transient materials are typically more sensitive to increased temperatures or the use of solvents during the fabrication process. Additive manufacturing also opens the possibility for the monolithic fabrication of bioresorbable electronics, eliminating the need for complex or manual assembly techniques. Furthermore, AM by using 3D printing techniques has proven highly compatible with soft materials, facilitating the fabrication of complex structures using elastomers or hydrogels.[15] The successful integration and operation of bioelectronic implants in the body critically relies on conformability and matching mechanical properties with the local tissue [324,325]. In this context, advancements in the field have prominently focused on the utilization of soft and elastic materials, driving significant progress [326]. Lastly, 3D digital additive manufacturing is being considered for the customization of electronic implants, providing a high degree of adaptation to the anatomy and complex geometries of the human body. The digital aspect of 3D additive manufacturing techniques allows for the seamless translation from a design to a device without adaptation to the process or designing a mask. This facilitates the rapid prototyping of bioelectronics, and allows for the modification of geometries and functions specific to a targeted organ or application. This opportunity has been recognized in the field of neuromuscular interfaces, with the emergence of customizable, additively manufactured bioelectronic implants [158,170,327,328]. Direct-ink writing (DIW), in particular, holds promise for that purpose, thanks to the variety of inks that can be printed [177], enabling the multi-material manufacturing of complex devices using a single printer.

Various materials including transient elastomers and hydrogels have been printed, principally for tissue engineering applications. Efforts on 3D printing bioresorbable elastomers have centered around poly(glycerol sebacate) (PGS). PGS can be rendered polymerizable by ultraviolet (UV) light with the addition of acrylate [40], methacrylate [41] or cinnamate reactive groups [42]. PGS has been 3D printed using methods such as digital light processing [329], 2-photon polymerization [41] or direct ink writing [199,200]. Poly(octamethylene maleate (anhydride) citrate) (POMaC) is a more recently introduced bioresorbable polymer, which is readily UV-curable. Investigations in the printability of POMaC are limited to a recent publication, where POMaC is printed by DIW in the form of a copolymer with poly(ethylene glycol) diacrylate (PEGDA) [202]. Degradable hydrogels (such as PEGDA, alginate or gelatin-based gels) have also been 3D printed to form microfluidic channels [330] or scaffolds to promote regeneration in vivo [331,332], principally using direct ink writing. Integrating electronics on hydrogels is notably difficult due to their mechanical mismatch with typical conductors [328]. Some printable transient hydrogels presented in the literature boast interesting properties, such as shape-memory behavior [333,334] for actuators, or ionic [334,335] or electrical [331,336] conductivity. However, the conductivities obtained for transient hydrogels are typically low (< 1 S/m).

Printable transient materials with higher conductivities have been developed. Metallic pastes based on zinc have been proposed with conductivities exceeding 10^6 S/m [18,185,321]. These have however not been 3D printed yet, likely because they require local sintering approaches to reach an acceptable conductivity. A demonstration of zinc direct ink writing has been recently published [337] however, the structures require

annealing at 600 °C, which is incompatible with transient polymers. Electrically conductive transient pastes that could be compatible with 3D printing and require no complex or high-temperature curing have been proposed. Carbon- and graphite-based transient inks have been 3D printed by direct ink writing [55,338]. Similarly, various ink formulations utilizing molybdenum [223] or tungsten [52] have been developed, exhibiting conductivities in the range of several kS/m. Despite these advancements, the digital 3D additive manufacturing of transient bioelectronics remains a challenge and necessitates the seamless integration of structural and conductive inks in a cohesive fabrication process.

In this work, we pioneer the fully digital additive manufacturing of transient implantable devices by direct ink writing. The DIW of POMaC elastomer is thoroughly studied to achieve precise and repeatable deposition of features with lines in the order of 200-300 μm in width and a thickness of about 50 μm . A slow-degrading, water-resistant shellac-carbon ink is used as a functional material for the formation of conductive traces embedded in a POMaC matrix. The inks are deposited in a multi-nozzle 3D printer, enabling the monolithic fabrication of functional transient electronics within a single machine. The physical degradation behavior of the materials used in this work is studied in physiological conditions. The additive process is exploited to fabricate transient pressure and strain sensors as well as recording electrodes, whose sensing characteristics are evaluated for applications as transient bioelectronics.

6.2 Results and Discussion

6.2.1 Approach and materials

As introduced above, we studied the fabrication of transient bioelectronics by 3D printing, with the aim of enabling the customization of these devices in terms of geometry, design and function. This concept is illustrated in **Figure 6.1(a)**, which shows the pipeline for in-silico customization of transient electronics and their subsequent facile fabrication using direct ink writing. By employing multi-nozzle printing and UV curing within the same machine, the digital design file can be directly translated into a personalized transient electronic device with a specific function and adapted geometry. To demonstrate the capabilities of AM to fabricate a variety of transient bioelectronics, several devices were printed and presented in **Figure 6.1(b-e)**. This includes pressure and strain sensors as well as an electrophysiology array comprising eight electrodes.

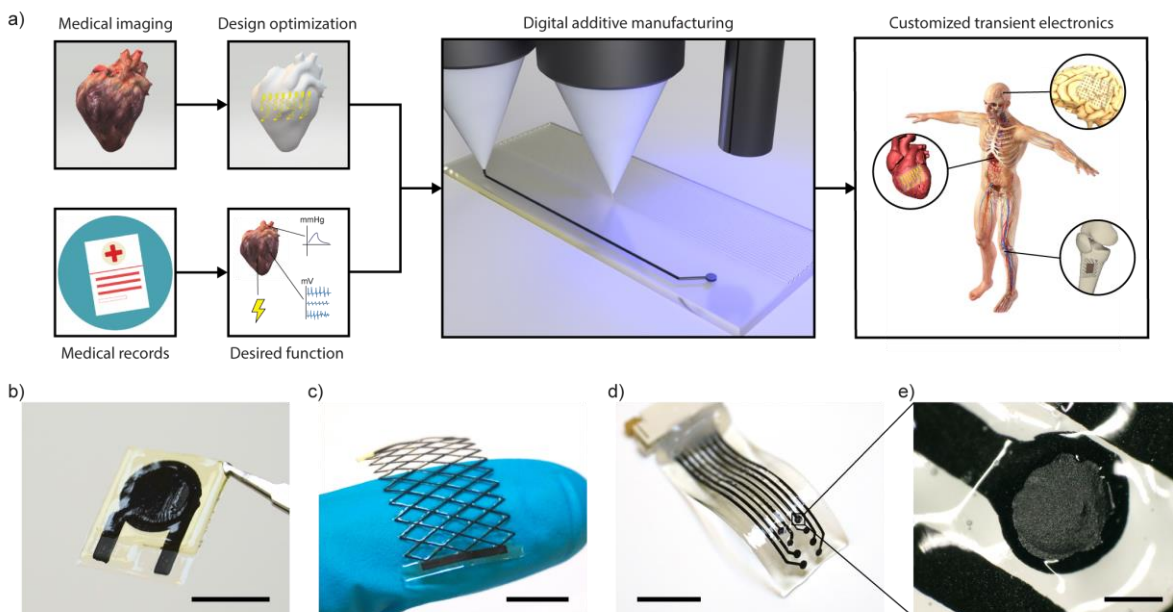


Figure 6.1: Additive manufacturing of customizable transient electronics. (a) Illustration of the concept of using digital additive manufacturing to enable transient implantable electronics with customized forms and functions. (b) DIW printed pressure parallel plate capacitor as pressure sensor (scale bar 10 mm). (c) DIW printed stretchable mesh as strain sensor (scale bar 10 mm). (d) DIW printed electrode array (scale bar 10 mm). (e) Close-up view of an electrode (scale bar 500 μm).

The conductive lines are based on a composite made of shellac, which is a natural bioresorbable resin, and pentanol as a low-volatility solvent to facilitate printing. Conductivity is granted to the composite by carbon and graphite particles, reproducing a degradable conductive ink that was presented in previous work [55]. The soft matrix that supports the carbon patterns and serves as encapsulation as well as soft dielectric in the case of the pressure sensor, is POMaC polymer. Despite the comparatively more established nature of PGS as a 3D printable bioresorbable elastomer, we direct our attention towards POMaC due to several compelling factors. POMaC offers a broader spectrum of mechanical properties compared to photocurable variants of PGS, which have Young's moduli of typically a few hundreds of kPa. Further thermal curing of PGS requires temperatures [339] above 120 °C, which may pose compatibility challenges with transient inks and their binders. POMaC demonstrates excellent compatibility with the fabrication of soft electronics, typically exhibiting a Young's modulus in the range of 0.5 to 1.5 MPa, which is comparable to commonly used polydimethylsiloxane (PDMS) elastomers in flexible and stretchable electronics [340]. Moreover, POMaC offers several advantageous properties that make it a suitable substrate for functional devices. It exhibits remarkable thermal stability for a degradable elastomer, withstanding temperatures exceeding 200 °C [341]. Furthermore, its degradation kinetics are reasonably slow, occurring over the course of months [38]. These characteristics have captured the attention of previous investigations, positioning POMaC as a promising substrate and packaging material for various implantable bioelectronic applications [146,341]. These properties facilitate the integration of conductive inks on the POMaC layer and subsequent encapsulation and curing. First, we seek to optimize the direct ink writing of POMaC polymer.

6.2.2 Synthesis and printing of POMaC pre-polymer

POMaC is obtained through a solvent-free polycondensation reaction of benign monomers (citric acid, 1,8-octanediol and maleic anhydride), which results in a pre-polymer in the form of a viscous gel. POMaC pre-polymer is readily UV-curable owing to the vinyl group in its backbone, thereby avoiding the use of toxic reagents in the synthesis, such as those required for acrylation. In our case, photo-crosslinking is enabled by the addition of 5 wt% Irgacure 2959, a common photo-initiator used in previous investigations on POMaC [146,202]. Further cross-linking can be achieved by thermal curing at 80 °C, causing esterification of the carboxylic acid and hydroxyl groups remaining from the citric acid. The dynamic viscosity of the pre-POMaC as a function of the shear rate is shown in **Figure 6.2(a)** and the gel displays a Newtonian behavior with a viscosity of 165 Pa s. This viscosity is compatible with direct ink writing [177] and may prevent excessive ink flow during UV photopolymerization. Ideal materials for direct ink writing present shear-thinning behavior, allowing easier dispense under pressure and shape fidelity after deposition [15]. Therefore, a thorough investigation of the printability of POMaC pre-polymer was conducted. The printing behavior of the POMaC pre-polymer was systematically studied as a function of selected printing parameters, namely the dispense gap, printing speed and inlet pressure, as depicted in **Figure 6.2(b)**. The parameters were varied respectively between 40 and 100 μm for the dispense gap, 10 and 50 mm/s for the printing speed, and 30 and 80 psi (≈ 207 to 552 kPa). The objective of this analysis was to optimize the resolution and uniformity of the prints, enabling precise 3D deposition of POMaC.

These experiments were conducted with a ceramic nozzle with an internal diameter of 125 μm . For each parameter combination, lines were printed over a 15 mm distance and subsequently cured using the UV LED of the printer. For the photopolymerization, the LED was used at full power, at a working distance of 25 mm (corresponding to an irradiance of 3 W/cm² over 3 mm diameter area) and with a speed of 0.5 mm/s to ensure full curing. The resulting lines were scanned using a confocal laser microscope. This process was repeated four times for each parameter combination, with a scan example shown in **Figure 6.2(c)**. The 3D scan of each printed line allowed us to extract several parameters, including the average line height, average line width, height variability, and width variability. The variabilities were calculated by dividing the standard deviation of the respective metric (height or width) by the average value of that metric across the entire print. The extracted values are displayed in **Figure 6.2(d-e)**. As expected [342], the line width and height monotonically decrease with increasing printer speed (**Figure 6.2(d)**), here for a fixed pressure of 60 psi (≈ 414 kPa). However, when considering the height and width variabilities, it is observed that a minimum value of approximately 5% is reached at a printing speed of 20 mm/s, indicating the most consistent line quality. The dispense gap, on the

other hand, appears to have negligible influence on the printing behavior for values above 40 μm , which is advantageous. This eliminates the need for precise control of the dispense gap with an accuracy of $< 10 \mu\text{m}$, which can be challenging. Therefore, a printing speed of 20 mm/s was selected to maximize line homogeneity and minimize printing defects.

Figure 6.2(e) shows the width and height of printed lines as a function of the pressure and the dispense gap. Regarding the effect of pressure, both the height and width of the printed lines increase linearly with higher inlet pressure, except at 80 psi where instability is observed, due to leakage occurring in the nozzle system. To strike a balance between resolution and layer thicknesses, a pressure of 60 psi was chosen for further prints. For this experiment as well, the dispense gap has minimal influence above 40 μm . The minimal feature width that can be achieved reliably with these parameters is approximately 250 μm , which corresponds to a spreading ratio (line width divided by nozzle diameter) of 2. This could be further improved by adding rheology modifiers to the POMaC ink to obtain a more pronounced shear-thinning behavior, preventing the spreading of the pre-polymer gel after printing [343]. However, the use of such modifiers should be approached cautiously, as their bioresorbability would need to be assessed. Moreover, they could potentially affect the mechanical properties and curing dynamics of the POMaC and could lead to nozzle clogging. In the current approach, the structural stability of the polymer after deposition relies mainly on its high viscosity and immediate application of UV photopolymerization. This methodology has been successfully employed with fast-curing PGS acrylate, achieving spreading ratios on the order of 1.7 [199]. Notably, delaying the UV curing of the lines by 30 minutes resulted in significantly degraded resolution and increased spreading ratio, as depicted in **Figure S6.1**. To enhance print resolution, one possible strategy could be to increase the ratio of maleic anhydride during synthesis, thereby augmenting the presence of vinyl bonds and accelerating the rate of cross-linking. Another approach is to perform the deposition under constant UV illumination, as demonstrated in previous studies [199,200]. However, it should be noted that this would require a considerable reduction in printing speed due to the slower photopolymerization kinetics of POMaC polymers.

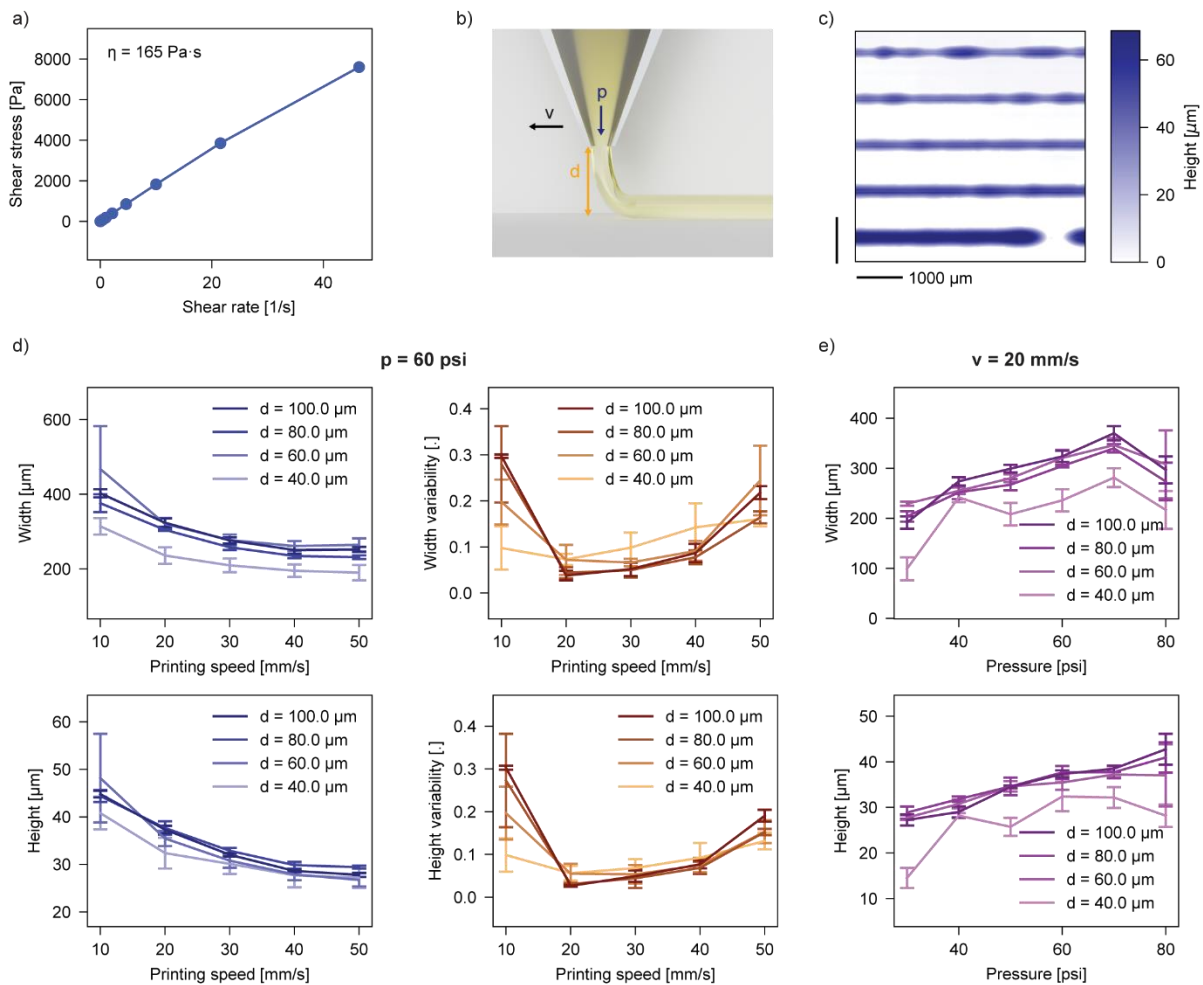


Figure 6.2: Optimization of POMaC patterning by direct ink writing. (a) Shear stress-shear rate behavior of POMaC pre-polymer. (b) Printing parameters that are studied for the optimization of the printing behavior (d : dispense gap, p : inlet pressure, v : printing speed). (c) Example of optically scanned printed lines, with printing speeds from 10 to 50 mm/s (from bottom to top), for a pressure of 60 psi and a dispense gap of 60 μm . (d) Influence of printing speed and dispense gap on the width (top left), width variability (top right), height (bottom left) and height variability (bottom right) of the printed lines for a pressure of 60 psi. (e) Influence of the pressure and dispense gap on the width (top) and height (bottom) of the printed lines for a printing speed of 20 mm/s.

With the aforementioned set of chosen parameters (printer speed: 20 mm/s, pressure 60 psi and a dispense gap of 80 μm), 2D single layers of POMaC polymer were printed and the influence of the interline distance on the layer thickness was examined (**Figure 6.3(a)**). Squares of 10 \times 10 mm were printed with line spacings of 300, 200, 150 and 100 μm , respectively. The optical profilometry scans of the squares are shown in **Figure 6.3(a)**, averaged over three samples. The squares printed with 300 μm line spacing show some raster effects and average $\sim 30 \mu\text{m}$ in thickness. As expected, larger thicknesses can be obtained by decreasing the line spacing, up to over 100 μm for a line spacing of 100 μm . The pre-polymer remains a gel before photopolymerization, and the printed lines favorably flow together during printing, leading to smooth surfaces. This also leads to the presence of shoulders at the edge of the square of approximately 20 μm in thickness in the printed squares, which are more marked when using a line spacing of 100 μm . A line spacing of 200 μm is chosen for further experiments, as it leads to the more uniform prints. This line spacing results in layers of $\sim 50 \mu\text{m}$ thickness.

In order to validate the optimized parameters for the 3D direct-ink-writing of POMaC pre-polymer, up to 10 layers of 10 \times 10 mm were stacked, with every layer being cured by UV before printing the next one. As evidenced in **Figure 6.3(b)**, the layers can be stacked reliably without collapsing or a rough surface preventing further printing (examples of printed stacks can be found in **Figure S6.2**). The thickness of the print scales

linearly with the number of printed layers, each layer averaging $50.3 \mu\text{m}$. This printing method can be used to create patterned surfaces, as shown for instance in **Figure 6.3(c)**, where a grid with lines and holes of $250 \mu\text{m}$ is printed in 10 layers. Topologies in the third dimensions can also be attained repeatably with 3D printed POMaC. Square-base pyramids arrays (each pyramid with a height of 2 mm and a base of $2 \times 2 \text{ mm}$ side, 42 layers total) were printed as an illustration of the capability of producing 3D structures and topologies (**Figure 6.3(d)**). Satisfying shape fidelity is achieved for the 3D fabrication of macroscale structures with features of a few hundred micrometers in size. A confocal microscope scan of the surface of the pyramids is shown in **Figure S6.3**, compared to the original design file.

Finally, the mechanical properties of POMaC can be tuned in terms of Young's modulus according to the curing conditions. To demonstrate this, dogbones (see **Figure 6.3(e)**) were printed with a thickness of $250 \mu\text{m}$ by

stacking 5 layers, and their stress-strain curves to failure were measured (**Figure 6.3(f)**). The Young's modulus increases from $0.59 \pm 0.01 \text{ MPa}$ for the POMaC that underwent only photopolymerization to $1.90 \pm 0.09 \text{ MPa}$ after 48 hours of curing at 80°C . The mechanical properties for the different curing conditions are reported in **Figure S6.4**. The results obtained here indicate stiffer mechanical properties than as in the original publication on the synthesis of POMaC [38] which is likely due to the higher concentration of photo-initiator and longer UV curing time, resulting in more cross-linking. For further experiments, a 48-hour esterification of POMaC at 80°C was conducted following printing and UV curing of the layers.

Achieving conformability to the intricate geometries of organs such as the brain, gut, or heart is crucial for personalized implantable electronics, as it ensures optimal sensing capabilities. The critical radius required for a film to spontaneously wrap around a rounded shape can be described by the following equation [324]:

$$r \geq \sqrt{\frac{Eh^3}{12\gamma(1-\nu^2)}}$$

E corresponds to the Young's modulus of the film, h is the thickness, γ is the surface tension of the fluid and ν , the Poisson ratio of the film. For POMaC, if we consider a Young's modulus in the range of $0.59 - 1.9 \text{ MPa}$ and a Poisson ratio we measured to be 0.48 , and assume a value of 40 mN/m for the surface tension (corresponding to phosphate-buffered saline (PBS) [344]) and a thickness of $\sim 200 \mu\text{m}$, this yields a critical radius between 3.6 and 6.2 mm .

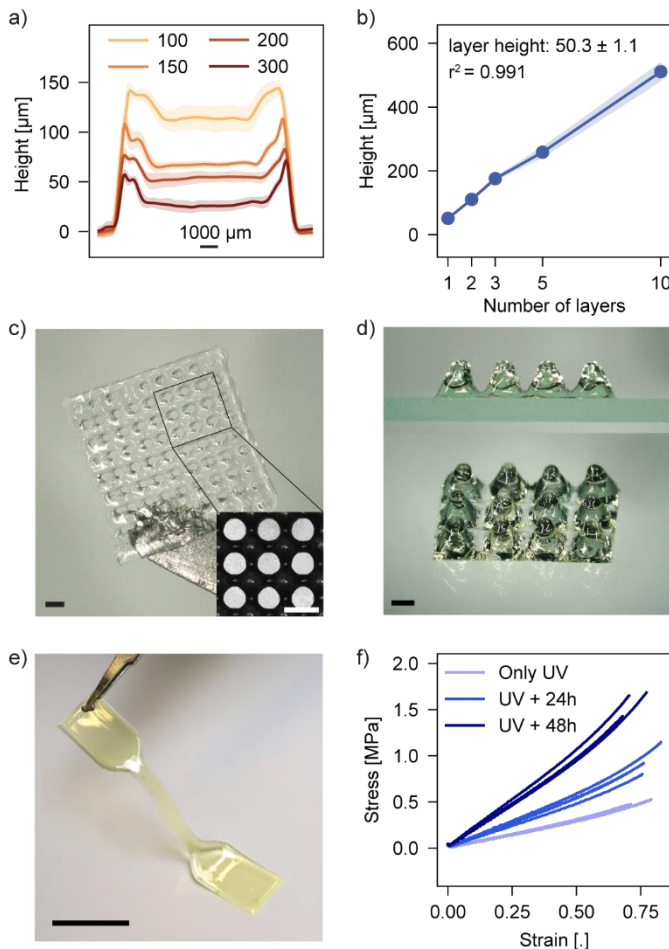


Figure 6.3: 3D direct ink writing of POMaC polymer. (a) Effect of the line spacing on the layer height and shape. (b) Height of the print versus the number of layers printed. (c) Patterned POMaC surface consisting of 10 printed layers, with a zoomed in view of the features in the inset (scale bars: $500 \mu\text{m}$). (d) Example of 3D printed pyramid array (scale bar: 1 mm). (e) 3D printed POMaC dogbone for mechanical properties characterization (f) Stress-strain curves for POMaC with different esterification times after printing and UV curing.

6.2.3 Integration of conductive carbon-based ink

We used a degradable carbon-graphite-shellac composite ink already reported in a recent publication [55], which has a conductivity of around 1000 S/m, to embed electrical functionalities in the POMaC structures. The water-barrier properties of shellac, particularly notable for a bioresorbable material, along with the incorporation of non-oxidizing carbon and graphite components, contribute to the preservation of its conductive properties in aqueous environments. The printing behavior of the carbon ink on POMaC by DIW was systematically investigated, considering the aforementioned dispense parameters and for a fixed pressure of 10 psi, and the results are presented in **Figure S6.5**. As a result of this optimization, lines with an average width of around 300 μm and average height of 30-35 μm are achieved with a printing speed of 30 mm/s and a dispense gap of 60 μm , with satisfying height and width variabilities below 5%. Fully encapsulated carbon lines are shown in **Figure 6.4(a)** and a scanning electron microscope (SEM) image profile section of the 3D printed POMaC and carbon composite is shown in **Figure S6.6**. Notably, this shows that the conductor can be fully encapsulated in POMaC without noticeable diffusion at the interface.

As a next step, the mechanical stability of the printed and encapsulated carbon lines when statically and dynamically bent was evaluated. Bending down to a radius of 1.5 mm leads to an average relative increase of resistance of 3.1 % (**Figure 6.4(b)**). A cyclic bending experiment was also performed at a bending radius of 3 mm, and the resistance over 10'000 cycles decreases by 3 %, as shown in **Figure 6.4(c)**.

In order to measure the durability of their conductivity in an environment reproducing physiological conditions, carbon composite lines encapsulated in POMaC could be immersed in phosphate-buffered saline at 37 °C and their resistance recorded over time. This was attempted, with a similar setup as that presented in Chapter 3. However, recordings were compromised by leaks in the setup, due to the poor adhesion between the epoxy resin used to seal the vial and the soft POMaC elastomer. Further experiments with a watertight setup are needed to evaluate the functional lifetime of the carbon-POMaC electronics in physiological conditions.

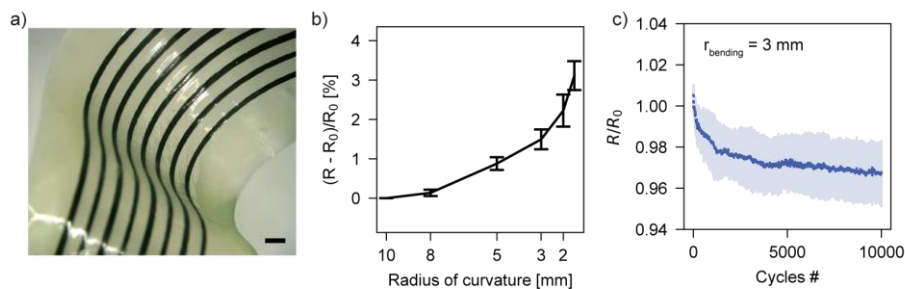


Figure 6.4: Integration of carbon conductors with POMaC. (a) Optical image of fully printed carbon conductors encapsulated in POMaC (scale bar: 1 mm). (b) Relative change of resistance of the carbon tracks on POMaC as a function of the bending radius ($n = 6$). (c) Relative change of resistance during cyclic bending of carbon lines on POMaC (with a bending radius of 3 mm at 1 Hz, $n = 6$).

6.2.4 Fabrication and characterization of 3D printed transient devices

To demonstrate the capabilities offered by this process, we fabricated 3D printed transient sensors. Biomechanical measurements, such as *in vivo* pressure and strain measurements, are of interest for post-surgical monitoring. Devices to measure such parameters have been proposed for transient applications targeting intracranial pressure monitoring [84,127,345] blood vessel deformations [144], cardiovascular postoperative care [128] or tendon healing [146]. By subsequent printing of POMaC and carbon circular electrodes layers, as illustrated in **Figure 6.5(a)**, a parallel plate capacitor with a soft sensing interlayer was fabricated. The device was assessed for pressures ranging up to 1500 kPa, corresponding to values found notably in a normal human knee during movement [346]. **Figure 6.5(b)** shows an example dynamic response in terms of normalized capacitance change to the applied pressure, where it can be seen that the capacitance change tracks the applied pressure. The response curve of the capacitor is reported in **Figure 6.5(c)**, for 10 loading and unloading cycles. The response can be approximated as linear until 1000 kPa, and a sensitivity of 0.0029 %/kPa ($r^2 = 0.93$) can be extracted. Above this pressure, the response reaches a plateau, which might be due to the

relatively thick carbon electrodes clamping the POMaC polymer and limiting deformation. As expected, the sensor sensitivity could be improved by taking approaches to structure or introduce mesoscale porosity in the POMaC dielectric [245]. The design shown here, however, allows for a pressure sensing range that is on the higher end, even for pressure sensors fabricated with conventional methods and materials [347]. To further validate the stability of the pressure sensor, it was subjected to a pressure of 1000 kPa (corresponding to 100 N) for 10'000 cycles at 1 Hz and the result of that experiment is shown in **Figure 6.5(d)**. The unloaded capacitance increases over to first 5000 cycles by 0.54 % and stabilizes, with only 0.18 % variation over the last 5000 cycles.

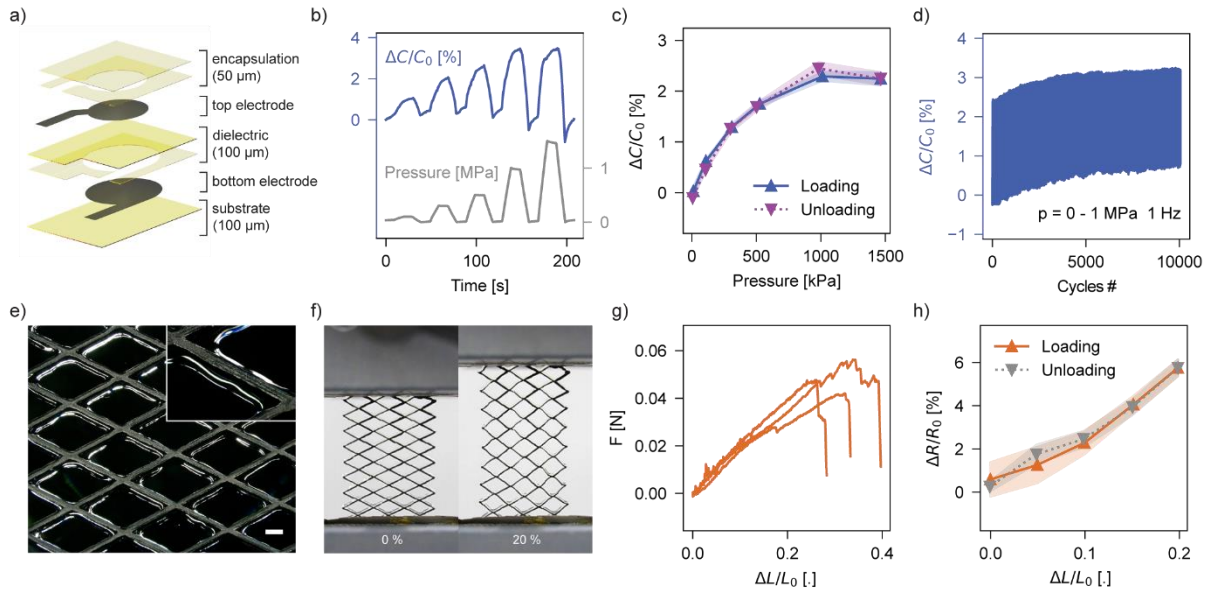


Figure 6.5: Mechanical sensors printed by DIW. (a) Exploded view of the layers printed for the fabrication of a parallel plate capacitive pressure sensor. (b) Relative response of the capacitive sensor (blue) to increasing applied pressures (grey). (c) Response of the capacitive sensor to applied pressures for increasing (blue) and decreasing (purple) loads ($n = 10$ cycles). (d) Response of the capacitive sensor to a cyclic load of 1 MPa at 1 Hz. (e) Optical microscope image of the DIW printed stretchable conductive mesh pattern made of carbon on POMaC (inset: close up view). (f) The printed conductive mesh pattern at rest and under a 20 % axial deformation. (g) Force-relative deformation curves for the mesh pattern. (h) Response in terms of relative resistance change to deformation for a proof-of-concept strain sensor for increasing (orange) and decreasing (grey) relative axial deformations ($n = 10$ cycles).

Stretchability is of interest for implanted electronics, with the soft tissues of the body undergoing deformations of 10-20 % for the heart and tendons, for example [348]. The conductive carbon composite we use in this work is not inherently stretchable, yet the versatility of our additive manufacturing platform permits to engineer stretchability in devices. To this end, we printed a POMaC substrate layer (thickness 100 μm) and a conductive carbon layer patterned in a diamond mesh pattern (as shown in **Figure 6.5(e)**), as stretchable structure. The resulting devices are displayed (unconstrained and under 20 % relative axial deformation) in **Figure 6.5(f)**. The meshes undergo mechanical failure at an average 34 % elongation. Failure is likely due to cracking of the carbon layer and mechanical mismatch with the soft elastomeric substrate (**Figure 6.5(g)**), which lead to local concentration of stresses. As proof of concept, the meshes were used as strain sensors, and their response in terms of resistance change for up to 20 % axial deformation is shown in **Figure 6.5(h)**. The printed strain sensor displays a gauge factor of 0.25 ($r^2 = 0.88$). The gauge factor is low, which is consistent with the use of a structure that serves to limit the strain in the carbon layer and allow to increase the sensing range. Indeed, the design could be optimized for a specific application in terms of deformation range and gauge factor, and the best designs could be rapidly printed and evaluated thanks to the developed additive manufacturing process.

Neuromuscular interfaces allow communication between biological tissues and electronic devices, and perform key monitoring or stimulation functions in clinical applications. Bioresorbable electrodes have been

proposed for applications such as electrocorticography [127,142] or nerve stimulation [131]. We fabricated an electrode array consisting of 8 electrodes of diameter 500 μm , with the array having a surface area of $34 \times 13 \text{ mm}^2$. The electrode array is shown in **Figure 6.6(a)** as well as a SEM image of one electrode, where it can be seen that the carbon composite creates a rough surface with a high effective area. Electrode impedance is a key metric to determine the signal quality and signal-to-noise ratio in ECoG recordings [349]. The impedance spectra of the bioresorbable printed ECoG array in phosphate-buffered solution are shown in **Figure 6.6(b)**. The impedance at 1 kHz is on average $6.5 \pm 1.0 \text{ k}\Omega$, and the cutoff frequency is $79 \pm 36 \text{ Hz}$ ($n = 8$). These characteristics are similar to those from electrodes of the same size found in the literature [350] and therefore suggests that they could be applicable for the recording of biopotentials. Carbon electrodes are also favorable for delivering electrical stimulation, in particular due to their wider electrochemical window compared to Pt electrodes, for instance [351]. A linear sweep voltammetry (LSV) was conducted to confirm this and is shown in **Figure S6.7**, where no water electrolysis occurs between -0.9 and 1.2 V. Cyclic voltammetry (CV) for a representative electrode and conducted within the water window is shown in **Figure 6.6(c)**. The charge storage capacity calculated from the CV measurements is $21.74 \pm 6.15 \text{ mC/cm}^2$ ($n = 4$), which is reasonably high and suggests that these electrodes could be appropriate for electrical stimulation applications [352].

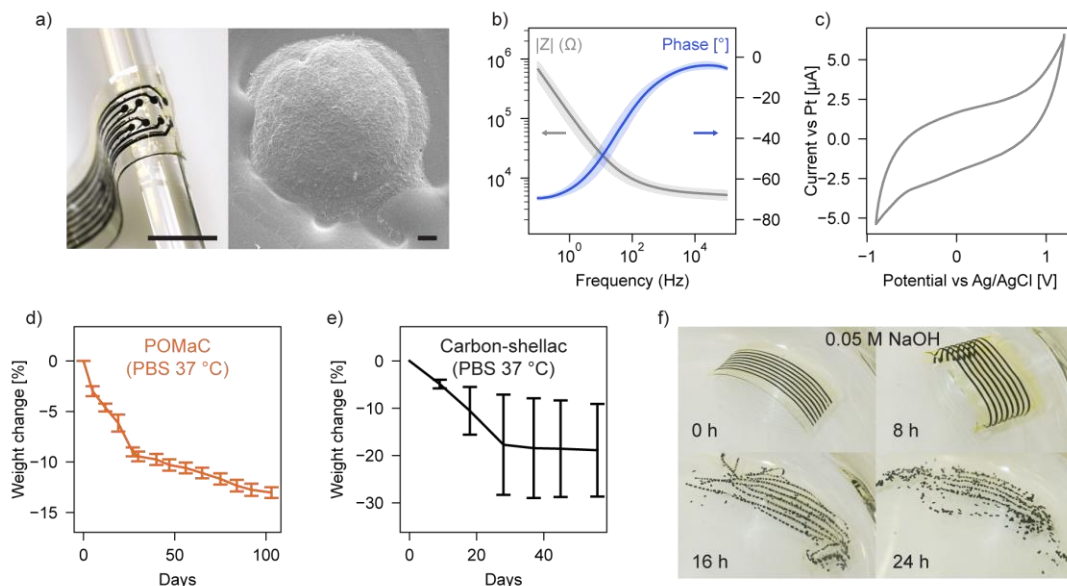


Figure 6.6: Transient printed electrode array and materials degradation study. (a) Image of the electrode array around a 3 mm radius glass rod (scale bar: 10 mm), SEM image of one electrode (scale bars: 100 μm). (b) Magnitude of the electrode impedance versus frequency in PBS ($n = 8$). (c) Cyclic voltammogram for a carbon electrode, at a scan rate of 50 mV/s. (d) Relative weight change of POMaC samples immersed in PBS at 37 $^{\circ}\text{C}$ ($n = 7$). (e) Relative weight change of carbon-shellac samples immersed in PBS at 37 $^{\circ}\text{C}$ ($n = 5$). (f) Accelerated degradation of carbon-shellac lines embedded in POMaC in 0.05 NaOH.

Finally, the materials constituting the devices presented above were studied in terms of their degradation in PBS at 37 $^{\circ}\text{C}$. **Figure 6.6(d)** shows the mass loss percentage for circular POMaC specimen of diameter 18 mm and thickness $267 \pm 8 \mu\text{m}$ as a function of the days of incubation in PBS. POMaC, after photo-crosslinking and 48 h heat curing at 80 $^{\circ}\text{C}$, degrades at an average rate of approximately 0.89 % per week, in line with the published literature [38,341]. The degradation happens at a faster rate in the first three weeks (which may correspond to smaller chains being degraded) and reaches a steadier rate from the third week. Similarly, square carbon-shellac samples of size $10 \times 10 \text{ mm}^2$ and average thickness $33.1 \pm 8.2 \mu\text{m}$ were prepared and incubated in PBS at 37 $^{\circ}\text{C}$ (**Figure 6.6(e)**). An average mass loss rate of 2.6 % per week was observed. However, this corresponds to both surface erosion as well as breaking off of small pieces of conductive composite, which explains the high variability in the data. The degradation of carbon lines in a POMaC structure array was also characterized under conditions of accelerated hydrolysis in 0.05 NaOH (pH 12.7). Images of the degradation of the device are shown in **Figure 6.6(f)** and the POMaC encapsulation dissolves in approximately 16 h, leaving non-hydrolysable carbon particulates.

6.3 Conclusions

In summary, we have demonstrated, for the first time, the full fabrication by digital additive manufacturing of soft implantable sensors and bioelectronics from degradable materials. The easily customizable devices are enabled by the 3D printing of the degradable elastomer POMaC as well as carbon conductive layers, whose printing behavior are thoroughly investigated. The influence of the dispense parameters, e.g. pressure, dispense gap and printer speed, on the morphology of printed layers is studied and optimal parameters are chosen in order to repeatably print features of 200-300 μm in width and layers of thicknesses between 30 and 50 μm . The printing behavior can be modulated by adapting these parameters and could be further modified with a different nozzle size, if smaller features or thicker layers are targeted. The process is shown to be compatible with the fabrication of 3D shapes of several millimeters with no collapse of the layers. An ink based on carbon particles and bioresorbable resin shellac is printed on the degradable elastomer as a conductive. The printed carbon embedded in POMaC is demonstrated to be conformable and can be bent down to 2 millimeters while maintaining its electrical conductivity, and cyclic bending for 10'000 leads to only a small variation in resistance. This platform for transient customized implantable electronics allows the demonstration of functional devices for the acquisition of relevant signals. A multilayer pressure sensor based on a parallel plate capacitor design allows for the monitoring of uniaxial pressures up to 1500 kPa and up to 10'000 cycles at a frequency of 1 Hz, which could be suitable for the recording of human joint pressure during movement. Stretchable conductive patterns are also demonstrated and used in proof-of-concept experiments as strain sensors up to 20 % relative deformation. An 8-electrode array for electrocorticography, electrocardiograph or electromyography is demonstrated. The impedance of the printed electrodes is $6.5 \pm 1.0 \text{ k}\Omega$ at 1 kHz with a cutoff frequency of $79 \pm 36 \text{ Hz}$, which is in line with values obtained for microfabricated non-degradable electrode arrays. Finally, the materials used in this 3D manufacturing platform are shown to degrade in physiological conditions on a timescale of months.

In order to improve the shape fidelity of the printed POMaC, more studies are needed on bioresorbable rheology modifiers and fillers. Moreover, although the use of carbon as a conductive material is hypothesized to allow for a longer functional lifetime than using transient metal, this should be validated with further experiments such as recordings in saline at physiological conditions. Furthermore, the development of inherently stretchable and bioresorbable conductive inks would allow to better take advantage of the mechanical properties of POMaC as a structural material for transient bioelectronics and create fully stretchable implants. In conclusion, this work constitutes a significant advancement towards customized bioelectronics for temporary applications in tissue healing monitoring and post-operative care.

6.4 Experimental Section

POMaC pre-polymer synthesis and characterization

POMaC was synthesized similarly to previous protocols [38]. 1,8 octanediol, citric acid and maleic anhydride (Sigma-Aldrich) were mixed at a molar ratio of 5:2:3 in a 250 ml three-necked flask and heated to 160 °C until full melting of the reagents. The reagents were then polymerized at 140°C for 3 hours under nitrogen flux, with a needle in the third neck to allow for the evacuation of the water resulting from the polycondensation reaction. After cooling to room temperature, the pre-polymer was dissolved in THF and purified by drop-wise purification in DI water for 2 hours, decanted and dried for a week under vacuum. The pre-polymer was then mixed with 5 wt% photoinitiator 2-hydroxy-4'-(2-hydroxyethoxy)-2-methylpropiophenone (Irgacure 2959). The rheology of POMaC was characterized with a DHR-2 Rotational Rheometer (TA Instruments), using a cone and plate geometry.

POMaC printing optimization

A nScript 3Dn-300 printer was used for all the 3D printing experiments conducted in this work. A SmartPumpTM100 attachment was used for the controlled dispense of POMaC pre-polymer, with a zirconia-toughened alumina nozzle (outer diameter: 175 μm , inner diameter: 125 μm). The valve rod position settings for open and closed positions were set to 1.9 and 1.4 mm respectively. For the line dispense optimization, lines of 15 mm were printed on polyimide films and subsequently UV cured at a speed of 0.5 mm/s. For the layer printing optimization, 10 \times 10 mm squares were printed and subsequently UV cured with a speed of 2 mm/s, with the same line spacing as for the printing. UV curing was carried out with the printer UV head at full power and at a distance of 25 mm (365 nm, peak irradiance: 8,000 mW/cm²). Printed shapes were covered in a thin layer of sputtered gold (5 - 10 nm) to ensure opacity and precise surface scanning. The shapes topologies were measured using a laser scanning confocal microscope (Keyence VK-X1000). The height data was corrected for surface shape, the printed lines were automatically detected and the metrics mentioned before were calculated as described. This analysis was carried out in a custom python script. Slicing and generation of printing instructions (in .gcode format) was carried out in Prusa Slicer 2.5.0 and translated project files for the 3Dn-300 printer using custom code written in python.

POMaC pull testing

POMaC dogbones samples were printed in 5 layers, which were each photopolymerized at a speed of 2 mm/s. The samples were printed on a polyimide substrate which was preliminarily covered with a blade-cast layer of polyacrylic acid serving as sacrificial layer. After printing, the samples were exposed to UV light (Proma 140001, 60 W, 365 nm) for 30 minutes to ensure full UV curing of the polymer. The polyimide sheet with the dogbones was placed in DI water overnight and the samples were gently peeled after dissolution of the sacrificial layer and dried in air. Stress strain curves were measured with a 340 Single Column Universal Testing System (Instron) at a strain rate of mm/s.

Carbon ink preparation and printing

The carbon paste was prepared as previously described. Briefly, graphite flakes (7–10 μm , Alfa Aesar, USA), carbon black (Lion Specialty Chemicals Co., Ltd Japan) and 9.5 g of 34 wt.% shellac solution in pentanol (Shellac Orange by Kremer Pigment, Germany) were mixed at a weight ratio of 4:1:9.5 at 5 min at 2350 rpm (DAC600 by Hauschild SpeedMixer, Germany). Direct ink writing of the carbon inks was conducted as for the POMaC inks, with another SmartPumpTM100 attachment on the 3Dn-300 printer, equipped with a 125 μm internal diameter nozzle. Carbon inks were printed on blade-cast POMaC for the printing study and scanned by laser confocal microscopy as described above.

Devices fabrication and characterization

All the devices presented in this work were printed from the POMaC and carbon inks as described above. The carbon ink was left to dry for 20 minutes after subsequent printing of POMaC encapsulation, where relevant. Direct ink writing was performed standard 4-inch single-side polished silicon wafer which was preliminarily covered with a sacrificial layer of spin-coated polyacrylic acid. Silicon wafers were used as carriers to ensure a flat surface during printing. The printed devices were further oven-cured at 80 °C for 48 hours and released from the carriers in DI water overnight. For the functional lifetime tests, carbon interconnects encapsulated in POMaC were immersed in PBS at 37 °C and the resistance values of the lines were continuously acquired with a digital multimeter (Keysight 34401A). The same sample design was used for the flexibility and cyclic bending tests, where a custom mechanical bending setup was used. For the pressure sensors, uniaxial pressures were applied with a single-column Universal Testing System (Instron 3340) and the capacitance values were recorded using an LCR-meter (Agilent E4980A) at 2MHz. Electrochemical characterization of the electrode arrays was conducted on a potentiostat/galvanostat (Metrohm Autolab 8 Series, PGSTAT302N, FRA32M module) in a three-electrode configuration, with an electrode from the array serving as working electrode, a Pt wire as counter electrode and a silver/silver chloride pellet as reference electrode. For impedance spectroscopy, a 10 mV RMS sine wave was used, for frequencies between 0.1 Hz and 100 kHz. LSV measurements were conducted between -2 and 2 V with a scan rate of 50 mV/s, and CV measurements were performed between -0.9 and 1.2 V with a scan rate of 50 mV/s.

Degradation experiments

POMaC samples of 18 mm diameter and thicknesses of $267 \pm 8 \mu\text{m}$ were prepared and incubated in PBS at 37°C in individual 12 ml glass vials. The samples were weighed with a precision scale (Metler Toledo XSR105) after light rinsing in DI water and drying for 2 hours under vacuum at 50°C . Carbon ink square samples with a side dimension of 10 mm and an average thickness of $33.13 \pm 8.18 \mu\text{m}$ were incubated and weighed as described above for the POMaC samples. The accelerated aging test was conducted in 0.05 M NaOH solution at room temperature.

6.5 Supporting information

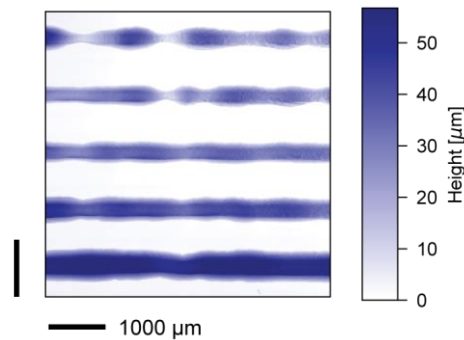


Figure S6.1: Lines of printed POMaC with the same parameters as in Figure 6.2(b) (printing speeds from 10 to 50 mm/s (from bottom to top), for a pressure of 60 psi and a dispense gap of $60 \mu\text{m}$) when curing is delayed by 30 minutes.

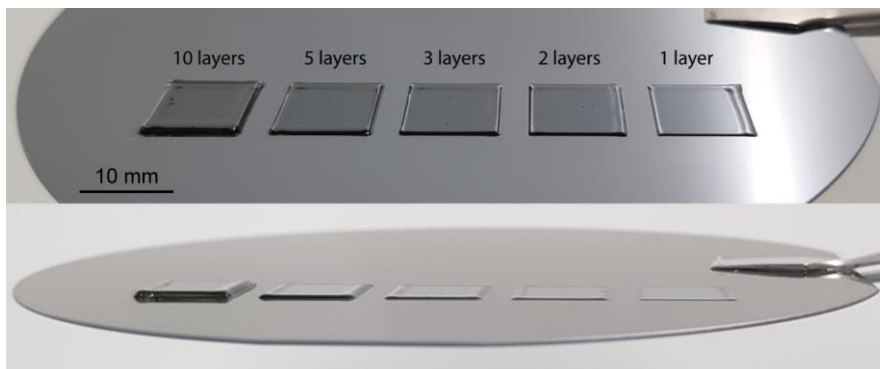


Figure S6.2: POMaC squares printed with increasing number of layers.

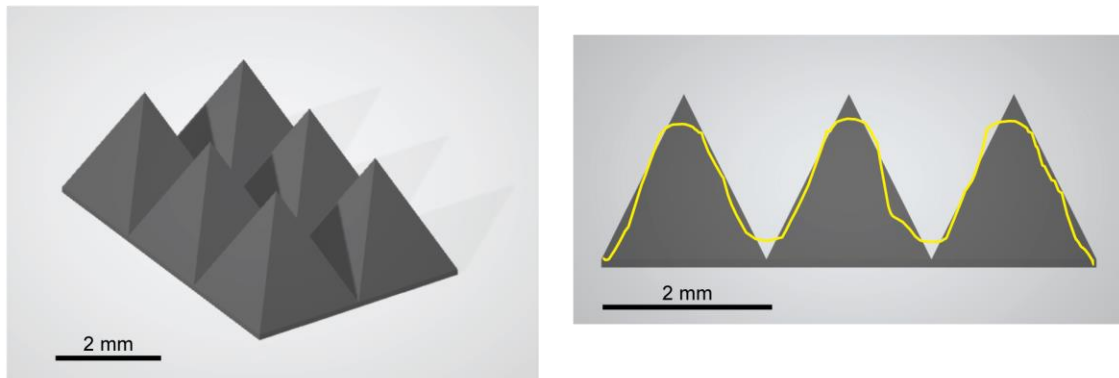


Figure S6.3: 3D design of the POMaC pyramid array, with each pyramid having a 2 x 2 mm base and a height of 2 mm (left). Side view of the pyramids compared to a confocal laser microscope scan of the printed POMaC pyramids, in yellow (right).

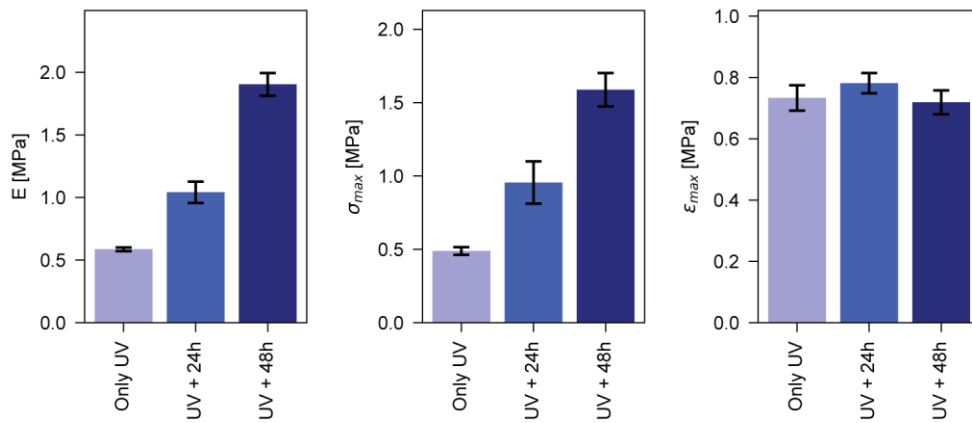


Figure S6.4: Mechanical properties of the POMaC (Young's modulus, failure stress and failure strain) as a function of the esterification time. All were preliminarily fully UV cured.

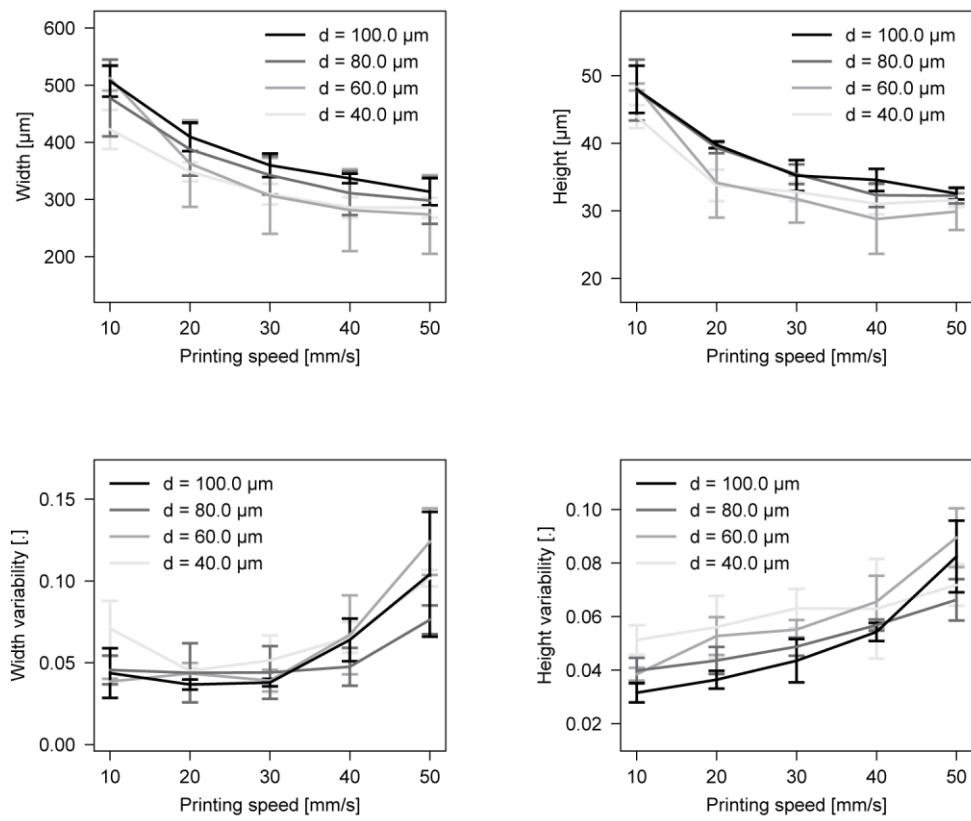


Figure S6.5: Influence of the printing parameters (printing speed and dispense gap) on the shape of printed carbon-shellac lines, for a fixed pressure of 10 psi. Top, right: width. Top, left: height. Bottom, left: relative width variability. Bottom, right: relative height variability.

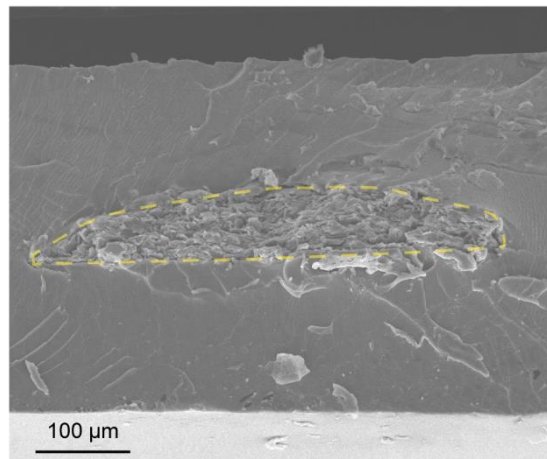


Figure S6.6: SEM image of carbon-shellac conductive ink embedded in POMaC polymer. The contour of the carbon profile is highlighted in yellow.

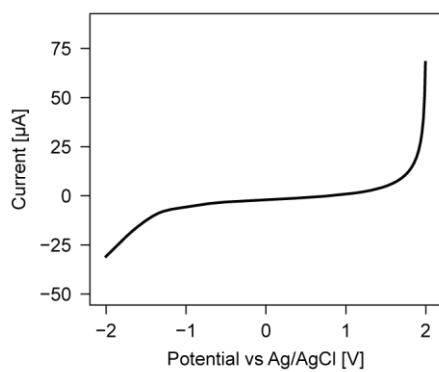


Figure S6.7: Linear sweep voltammetry measurement of a carbon electrode in PBS with potential difference with Ag/AgCl reference between -2 and 2 V.

Chapter 7 Conclusion

This thesis presents several advancements in the fields of additive manufacturing of biodegradable and bioresorbable electronics. In response to challenges regarding material limitations, printing and curing techniques, devices fabrication and characterizations, studies were conducted resulting in progress towards the full additive manufacturing of transient bioelectronics. In this chapter, we summarize the key findings and implications of this work while also providing an outlook on future directions for this research.

7.1 Summary and conclusion

Highly conductive interconnects for eco- and bioresorbable electronics: A novel sintering method for zinc-based ink was developed to overcome challenges related to printable transient metal inks, namely limited conductivity with respect to bulk and poor stability in air. A hybrid two-step sintering process for screen-printed zinc utilizing electrochemical and photonic mechanisms was carefully studied and optimized. The removal of high-melting oxides by electrochemical treatment was shown to be crucial to maximizing the efficiency of the photonic treatment. The influence of the sintering atmosphere, as well as the light pulse count and intensity was investigated to find optimal values and obtain unprecedented conductivity. Conductivity values of $5.6 \cdot 10^6$ S/m were reached for screen printed zinc interconnects, the highest reported value in the state of the art for a transient printed conductor. The batch yield was typically close to 100 %, except for a minority of batches where the acid treatment failed due to the manual nature of the process. The increased efficiency of the process also resulted in a reduction of the photonic energy necessary to attain optimal sintering. This is of particular interest as the process is thus compatible with bioresorbable substrates, which tend to have a very low thermal budget. This was demonstrated on two transient substrates, PVA and PLA, where conductivities in the same order of magnitude were reached. The zinc traces were shown to be stable in ambient air for at least one month, and maintain electrical conductivity for 3-4 weeks as well in physiological conditions when encapsulated in PLA. The interconnects are flexible down to a radius of 3 mm and can be bent repeatedly for 1000 cycles with limited loss in conductivity. This is an important finding, as flexibility of printed patterns is often partially dependent on the binder present in the layer, as has been shown before, and in our case the binder is likely vaporized during the sintering process.

These experiments indicate that the process is suitable for the multi-step fabrication of bioresorbable and biodegradable electronics. This was validated by testing zinc resistors as strain sensors, and as electrodes in parallel plate pressure sensors. The zinc electrodes were shown to be compatible with the deposition and curing at 80 °C for 48 h of POMaC elastomer. The pressure sensors were assessed for forces up to 7 N and showed a sensitivity of 71.4 fF/N (0.035 %/kPa). This value can be explained by the fact that fully cured POMaC is comparatively stiffer than soft dielectrics used in other (non-degradable) pressure sensors. It could be improved by shortening the thermal curing of our elastomer, or by adopting a patterned dielectric approach. Actuation for 1000 cycles caused minimal drift in the response of the sensors. Furthermore, thanks to the high conductivity of the zinc, the capacitive sensors were implemented in a wireless RLC circuit. The chipless sensing device has a footprint of less than 2 cm² and displayed a sensitivity of 320 kHz/N.

Finally, the influence of the sintering process on the temperature characteristics of zinc resistors was investigated for the development of temperature sensors for environmental monitoring. The two-step hybrid sintering process was compared to the electrochemical treatment commonly used in the literature, for zinc resistors printed on paper. The two-step sintered zinc resistors exhibited significantly improved stability under temperature variations and demonstrated a linear response in terms of relative change of resistance ($r^2 > 0.99$).

Hybrid sintering resulted in a high TCR value of $0.00316 \text{ 1/}^\circ\text{C}$, which represents about 80 % of the value for bulk zinc. This is of importance, as it correlates with the sensitivity of the resistance temperature detector. The relative sensitivity that we obtain is superior to examples of microfabricated degradable metallic RTDs based on magnesium, for example. To minimize interference from humidity, a beeswax coating was applied to the sensors by dip-coating. The eco-resorbable temperature sensors were tested from -20°C to 40°C , with relative humidity values ranging from 30 to 70 rH% and were shown to operate with minimal deviation from a reference commercial sensor.

Integration of biochemical sensing function in disposable devices: Specifically, we fabricated organic electrochemical transistors (OECTs) utilizing a PEDOT:PSS conductive channel and degradable carbon-shellac electrodes. These components were printed onto an eco- and bioresorbable PLA substrate. The PEDOT:PSS channel was inkjet-printed while the carbon ink was deposited by stencil printing. The transistor behavior of the devices was evaluated and compared for different gate material choices and device architectures, firstly on an inert polyimide substrate. Carbon and PEDOT:PSS were found to be suitable gate materials for disposable OECTs, exhibiting similar transconductances of approximately $300 \mu\text{S}$. This is likely due to their high effective areas, leading to a high gate capacitance. We also investigated the impact of gate geometry on device performance and observed that larger gates generate a transconductance peak at lower voltages, making them preferable for further experimentation.

To enable the printing of disposable organic electrochemical transistors (OECTs) on a PLA substrate, we addressed the challenges posed by PLA's unfavorable surface properties and low thermal budget. We explored modifications to the process to overcome these limitations. Specifically, we employed a silanization process on PLA, which leads to a highly hydrophilic surface and facilitates the inkjet printing of PEDOT:PSS with performance comparable to reference devices on polyimide. This was also made possible by a reduction of the curing temperature of the PEDOT:PSS to 80°C instead of 120°C , which is compatible with the PLA substrate and does not impact the transistor behavior of the OECTs. The disposable OECTs were assessed as ion sensors and yielded sensitivities in the order of 10 \%/dec for potassium, sodium and calcium ions. This is similar to previous work on OECT made of silver electrodes on a polyimide substrate, indicating minimal negative influence from the degradable materials in our case. Importantly, the sensing behavior remained stable across different devices and repetitions, and the devices exhibited reversibility after washing with DI water. As a proof-of-concept, we also investigated the glucose sensing capability of the devices, achieving a limit of detection of $5 \mu\text{M}$. Although comparable to previous work with glucose-sensitive OECTs with the enzyme attached to the gate, this limit of detection is three order of magnitude higher than in other published works, and could be improved with the use of a mediator such as ferrocene. All in all, these results demonstrate the potential of the disposable OECTs for biochemical sensing applications.

Finally, the OECTs were integrated with highly conductive zinc interconnects enabled by the aforementioned sintering process. However, Zn naturally forms a ZnO passivation when exposed to air. ZnO, being an n-type semiconductor, forms a p-n junction with the PEDOT:PSS channel, which explains why zinc cannot be used directly as contacts for the OECTs. This observation was confirmed by measuring the IV-curves of the ZnO-PEDOT:PSS junction, which exhibits a Schottky barrier behavior. To address this issue, we fabricated OECTs with zinc contacts, but employed a carbon intermediate layer as an interface between the zinc and the PEDOT:PSS. This configuration enabled the devices to have comparable behavior to the reference devices with carbon contacts.

Digital additive manufacturing of customizable transient bioelectronics: Monolithic fabrication of transient bioelectronics in a single machine was achieved, using multi-nozzle direct ink writing and UV curing. This approach takes advantage of the versatility offered by digital additive manufacturing, enabling the creation of bioelectronics with customizable geometry and function. POMaC was chosen as substrate material and its deposition by printing was optimized as a function of the nozzle size, dispense gap and inlet pressure. POMaC pre-polymer is a viscous Newtonian fluid with relatively slow UV curing kinetics, and we demonstrated that its high viscosity is sufficient to maintain shape fidelity after deposition. Features in the order of 200 to $300 \mu\text{m}$

were achieved, as a function of the printing parameters. Layer-by-layer printing was successfully demonstrated with a consistent layer thickness of 50 μm , and 3D topologies were fabricated at scales of a few millimeters.

To introduce electrical functionality, we employed the aforementioned carbon-shellac composite as the conductive layer. This composite maintains its conductivity even in contact with aqueous solutions, making it suitable for fabricating electrodes for electrophysiology applications. The direct ink writing of the composite was also studied. Printed carbon lines encapsulated in POMaC were flexible down to a bending radius of 1.5 mm, and could withstand 10'000 bending cycles at 3 mm with minimal change in resistance. The electrical resistance of the fully printed substrate and interconnects was monitored in PBS at 37 °C and found to degrade at a rate of approximately 5% (relative change of resistance) per hour. Overall, the fabrication process is straightforward and allows for the easy and rapid translation from an *in silico* design to a functional 3D printed construct. The yield for conductive printed lines was observed to be above 90 %, and in the case of interrupted lines, a second pass with the carbon ink was sufficient to obtain fully functional devices.

The ease of customization of transient bioelectronics was demonstrated by fabricating functional devices without requiring adaptation to the fabrication process. A parallel capacitive sensor was fabricated for the monitoring of pressures up to 1500 kPa, achieving a sensitivity of 0.0029 %/kPa. The sensor was tested for cyclic actuation (10'000 cycles) with a 1 MPa pressure at 1 Hz, and its capacitance stabilized after 5000 cycles with only a 0.18% drift in the last 5000 cycles. A stretchable conductive mesh was also printed and tested as a strain sensor for up to 20% deformation with a gauge factor of 0.25. Furthermore, an electrode array was fabricated, showing performance comparable to state-of-the-art electrodes with an impedance of $6.5 \pm 1.0 \text{ k}\Omega$ at 1 kHz and a cutoff frequency of $79 \pm 36 \text{ Hz}$. Finally, the degradation kinetics of POMaC and the carbon-shellac composite in PBS at 37 °C were evaluated. POMaC and the carbon conductive paste were found to exhibit weight loss rates of respectively 0.89 %/week and 2.6 %/week.

7.2 Outlook

This thesis describes advancements in the fabrication of biodegradable and bioresorbable electronics. We address challenges related to additive manufacturing techniques to attain higher performance printed materials and optimized processes. This results in functional printed transient devices incorporating varied sensing functions. The use of additive manufacturing allows for an unprecedented degree of customizability and the creation of 3D topologies. These achievements open new directions for further research, fostering the development of next-generation bioresorbable electronics with enhanced performance, improved integration, and expanded functionality.

The main drawback of the hybrid sintering process presented above is its relative complexity, requiring several acid coats for uniform oxide removal before the photonic treatment. As also mentioned before, this also may compromise the obtained yield, due to the operator-dependant nature of the process. The hybrid sintering method could be considerably improved by introducing the reducing agent in the ink, hopefully maintaining the zinc nano- or microparticles oxide-free during ink storage and printing. This could be achieved by taking inspiration from copper oxide reduction techniques, such as the use of formic acid [188,353,354]. Citric acid solutions also seem to be able to reduce oxides on zinc metal [355]. This will need to be validated with corrosion experiments to validate the timely dissolution of the oxide layer. However, we note that the use of acetic acid already imparts some conductivity to the zinc layers after treatments by causing redeposition of the Zn ions resulting from the oxide layer reduction [18]. The extent to which this contributes to the efficiency of the subsequent photonic sintering is unclear and requires further investigation. However, introducing acetic acid solution directly into the ink is not a viable solution as it causes the ink to solidify within minutes, as we have experimentally confirmed. One potential solution to address the ink stability issue is the use of propionic anhydride, which induces electrochemical sintering of zinc similar to acetic acid [221]. Propionic anhydride is converted to propionic acid in the presence of water, making it suitable for an ink formulation based on an anhydrous organic solvent. However, anhydrides typically react with alcohols to form esters when heated, and an alternative solvent to pentanol should therefore be found. In parallel to that, inks for the direct ink writing of zinc could be developed, to integrate it into the multi-material 3D fabrication platform.

We present disposable biochemical sensors based on PEDOT:PSS, which are entirely made of environmentally benign materials. Although the biodegradation of PLA, carbon or graphite and shellac has been validated, the degradation of PEDOT:PSS polymers *in vivo* or in the natural environment is still unclear [8]. PEDOT or its monomer are not soluble in water and experiments should be conducted to elucidate the potential elimination of PEDOT:PSS by the body as well as its fate in soil. Similarly, while carbon is considered an edible material [356], it is likely to be bioinert and therefore not to be fully bioresorbable. In consequence, the effects of carbon-based composites degradation *in vivo* should be investigated. An alternative approach to avoid these concerns would involve replacing carbon in the inks with degradable metals such as tungsten or molybdenum. Both form thinner oxide layers comparatively to other transient metals and degrade slower; they are therefore suitable for the creation of composites requiring minimal sintering [52,223]. By incorporating degradable metals into shellac composites, higher conductivity can be achieved while leveraging shellac's water-barrier properties to prevent rapid degradation. Another possibility would be to combine transient metals with bioresorbable elastomers, allowing for inherently stretchable, or at least more mechanically compliant, conductors.

POMaC is used as the structural material for personalized transient implants, and had been assessed before as a suitable material for packaging of bioresorbable electronics [146]. As is the case for a lot of bioresorbable materials, it absorbs water readily, swelling up to 20 % in PBS [341]. This can lead to early failure of the device through the creation of strain on the conductive lines, as well as degradation of the conductive material through contact with the aqueous solution. More research is therefore needed into 3D printable bioresorbable polymers with satisfying water barrier properties. An ideal printable transient substrate would show hydrophobic behavior and surface degradation, which allows to provide a better encapsulation and maintain mechanical properties as the material degrades. PGS has been reported to undergo surface erosion and exhibit reduced water absorption compared to POMaC [39]. It is however very challenging to process by printing as its pre-polymer is a wax that melts around 90°C to a thin liquid, and must be cured at 130 °C, leading to structural collapse [343]. We experimented with PGS-POMaC blends, which could be a promising alternative as substrate material and were found to cure at temperatures as low as 100 °C. Another promising avenue for future work on this topic is the use of more hydrophobic polymers, such as PCL or PLA as additives to reduce the water diffusion and uptake. On the topic of additives for POMaC, additives that induce a shear-thinning would hold promise to improve the printing behavior, as this is the ideal rheological behavior for direct ink writing [177]. Cellulose nanocrystals have shown promise as biodegradable (but non-bioresorbable) additives [207], for example, and more research is needed in developing bioresorbable equivalents.

Furthermore, the customizability of transient implants as presented in Chapter 6 can further be exploited and demonstrated. The ability to easily translate *in silico* designs into functional devices and manufacture complex shapes and 3D topologies opens opportunities for optimizing transient implants using sophisticated techniques. Topology optimization [357] as well as generative design [358] have the possibility to incorporate design constraints and automatize the optimization process, leading to structures with enhanced performance. These techniques have been used in conjunction with additive manufacturing, which is best suited for the fabrication of complex designs [359]. With this approach, transient electronic implants could be generated from medical imaging and optimized in terms of layout, mechanical properties, and topology to attain higher recording quality and better conformability. Moreover, the added manufacturing capabilities in the third dimension could be exploited to demonstrate novel sensing or actuation mechanisms in implantable electronics.

Finally, despite advances in the additive manufacturing of transient electronic implants, *in vivo* assessments remain very limited. To address this gap, further research is needed to comprehensively evaluate the long-term functionality and performance of printed bioresorbable implants. Devices should be evaluated *in vitro* in an environment that reproduces their target implantation site as closely as possible. An interesting approach to this end is presented in a recent paper, where a platform is developed for the *in vitro* assessment of spinal cord implants for stimulation [360]. Notably, the spinal cord model is derived from medical imaging and reproduced by additive manufacturing, allowing for a personalized assessment. Such in depth characterization would allow to study the degradation of the transient materials, and to ensure the stability and functionality of the printed devices for a specific application. As a next step, evaluations of these devices in small animal models could be conducted.

References

- [1] Hwang S-W, Tao H, Kim D-H, Cheng H, Song J-K, Rill E, et al. A Physically Transient Form of Silicon Electronics. *Science* 2012;337:1640–4. <https://doi.org/10.1126/science.1226325>.
- [2] Yu X, Shou W, Mahajan BK, Huang X, Pan H. Materials, Processes, and Facile Manufacturing for Bioresorbable Electronics: A Review. *Adv Mater* 2018;30:1707624. <https://doi.org/10.1002/adma.201707624>.
- [3] Fu KK, Wang Z, Dai J, Carter M, Hu L. Transient Electronics: Materials and Devices. *Chem Mater* 2016;28:3527–39. <https://doi.org/10.1021/acs.chemmater.5b04931>.
- [4] Chatterjee S, Saxena M, Padmanabhan D, Jayachandra M, Pandya HJ. Futuristic medical implants using bioresorbable materials and devices. *Biosens Bioelectron* 2019;142:111489. <https://doi.org/10.1016/j.bios.2019.111489>.
- [5] Cha GD, Kang D, Lee J, Kim D. Bioresorbable Electronic Implants: History, Materials, Fabrication, Devices, and Clinical Applications. *Adv Healthc Mater* 2019;8:1801660. <https://doi.org/10.1002/adhm.201801660>.
- [6] Baldé CP, D'Angelo E, Luda V, Deubzer O, Kuehr R. Global Transboundary E-waste Flows Monitor - 2022. U N Univ UNU Int Telecommun Union ITU Int Solid Waste Assoc ISWA BonnGenevaRotterdam 2022.
- [7] Grant K, Goldizen FC, Sly PD, Brune M-N, Neira M, van den Berg M, et al. Health consequences of exposure to e-waste: a systematic review. *Lancet Glob Health* 2013;1:e350–61. [https://doi.org/10.1016/S2214-109X\(13\)70101-3](https://doi.org/10.1016/S2214-109X(13)70101-3).
- [8] Stephen M, Nawaz A, Lee SY, Sonar P, Leong WL. Biodegradable Materials for Transient Organic Transistors. *Adv Funct Mater* 2023;33:2208521. <https://doi.org/10.1002/adfm.202208521>.
- [9] Dong Y, Bao C, Kim WS. Sustainable Additive Manufacturing of Printed Circuit Boards. *Joule* 2018;2:579–82. <https://doi.org/10.1016/j.joule.2018.03.015>.
- [10] Frazza EJ, Schmitt EE. A new absorbable suture. *J Biomed Mater Res* 1971;5:43–58. <https://doi.org/10.1002/jbm.820050207>.
- [11] Staiger MP, Pietak AM, Huadmai J, Dias G. Magnesium and its alloys as orthopedic biomaterials: A review. *Biomaterials* 2006;27:1728–34. <https://doi.org/10.1016/j.biomaterials.2005.10.003>.
- [12] Yang H, Wang C, Liu C, Chen H, Wu Y, Han J, et al. Evolution of the degradation mechanism of pure zinc stent in the one-year study of rabbit abdominal aorta model. *Biomaterials* 2017;145:92–105. <https://doi.org/10.1016/j.biomaterials.2017.08.022>.
- [13] Kim D-H, Viventi J, Amsden JJ, Xiao J, Vigeland L, Kim Y-S, et al. Dissolvable films of silk fibroin for ultrathin conformal bio-integrated electronics. *Nat Mater* 2010;9:511–7. <https://doi.org/10.1038/nmat2745>.
- [14] Wu F, Im M, Yoon E. A flexible fish-bone-shaped neural probe strengthened by biodegradable silk coating for enhanced biocompatibility. 2011 16th Int. Solid-State Sens. Actuators Microsyst. Conf., 2011, p. 966–9. <https://doi.org/10.1109/TRANSDUCERS.2011.5969356>.
- [15] Truby RL, Lewis JA. Printing soft matter in three dimensions. *Nature* 2016;540:371–8. <https://doi.org/10.1038/nature21003>.
- [16] Wallin TJ, Pikul J, Shepherd RF. 3D printing of soft robotic systems. *Nat Rev Mater* 2018;3:84–100. <https://doi.org/10.1038/s41578-018-0002-2>.
- [17] Sanchez-Duenas L, Gomez E, Larrañaga M, Blanco M, Goitandia AM, Aranzabe E, et al. A Review on Sustainable Inks for Printed Electronics: Materials for Conductive, Dielectric and Piezoelectric Sustainable Inks. *Materials* 2023;16:3940. <https://doi.org/10.3390/ma16113940>.
- [18] Lee YK, Kim J, Kim Y, Kwak JW, Yoon Y, Rogers JA. Room Temperature Electrochemical Sintering of Zn Microparticles and Its Use in Printable Conducting Inks for Bioresorbable Electronics. *Adv Mater* 2017;29. <https://doi.org/10.1002/adma.201702665>.
- [19] Liu H, Xiang H, Wang Y, Li Z, Qian L, Li P, et al. A Flexible Multimodal Sensor That Detects Strain, Humidity, Temperature, and Pressure with Carbon Black and Reduced Graphene Oxide Hierarchical Composite on Paper. *ACS Appl Mater Interfaces* 2019;11:40613–9. <https://doi.org/10.1021/acsami.9b13349>.
- [20] Yang Z, Huang T, Cao P, Cui Y, Nie J, Chen T, et al. Carbonized Silk Nanofibers in Biodegradable, Flexible Temperature Sensors for Extracellular Environments. *ACS Appl Mater Interfaces* 2022;14:18110–9. <https://doi.org/10.1021/acsami.2c00384>.
- [21] Salvatore GA, Sülzle J, Dalla Valle F, Cantarella G, Robotti F, Jokic P, et al. Biodegradable and Highly Deformable Temperature Sensors for the Internet of Things. *Adv Funct Mater* 2017;27:1702390. <https://doi.org/10.1002/adfm.201702390>.

-
- [22] Demuru S, Kunnel BP, Briand D. Real-Time Multi-Ion Detection in the Sweat Concentration Range Enabled by Flexible, Printed, and Microfluidics-Integrated Organic Transistor Arrays. *Adv Mater Technol* 2020;5:2000328. <https://doi.org/10.1002/admt.202000328>.
- [23] Demuru S, Huang C-H, Parvez K, Worsley R, Mattana G, Piro B, et al. All-Inkjet-Printed Graphene-Gated Organic Electrochemical Transistors on Polymeric Foil as Highly Sensitive Enzymatic Biosensors. *ACS Appl Nano Mater* 2022;5:1664–73. <https://doi.org/10.1021/acsnm.1c04434>.
- [24] Lee YK, Yu KJ, Song E, Barati Farimani A, Vitale F, Xie Z, et al. Dissolution of Monocrystalline Silicon Nanomembranes and Their Use as Encapsulation Layers and Electrical Interfaces in Water-Soluble Electronics. *ACS Nano* 2017;11:12562–72. <https://doi.org/10.1021/acsnano.7b06697>.
- [25] Yu X, Shou W, Mahajan BK, Huang X, Pan H. Materials, Processes, and Facile Manufacturing for Bioresorbable Electronics: A Review. *Adv Mater* 2018;1707624:1–27. <https://doi.org/10.1002/adma.201707624>.
- [26] Tan MJ, Owh C, Chee PL, Kyaw AKK, Kai D, Loh XJ. Biodegradable electronics: cornerstone for sustainable electronics and transient applications. *J Mater Chem C* 2016;4:5531–58. <https://doi.org/10.1039/C6TC00678G>.
- [27] EN13432, European Committee for Standardization 2015.
- [28] Ryu H, Seo M-H, Rogers JA. Bioresorbable Metals for Biomedical Applications: From Mechanical Components to Electronic Devices. *Adv Healthc Mater* 2021;10:2002236. <https://doi.org/10.1002/adhm.202002236>.
- [29] Li C, Guo C, Fitzpatrick V, Ibrahim A, Zwiernstra MJ, Hanna P, et al. Design of biodegradable, implantable devices towards clinical translation. *Nat Rev Mater* 2020;5:61–81. <https://doi.org/10.1038/s41578-019-0150-z>.
- [30] Burkersroda F von, Schedl L, Göpferich A. Why degradable polymers undergo surface erosion or bulk erosion. *Biomaterials* 2002;23:4221–31. [https://doi.org/10.1016/S0142-9612\(02\)00170-9](https://doi.org/10.1016/S0142-9612(02)00170-9).
- [31] Chen Y, Kim Y-S, Tillman BW, Yeo W-H, Chun Y. Advances in Materials for Recent Low-Profile Implantable Bioelectronics. *Materials* 2018;1–24. <https://doi.org/10.3390/ma11040522>.
- [32] Shin J, Yan Y, Bai W, Xue Y, Gamble P, Tian L, et al. Bioresorbable pressure sensors protected with thermally grown silicon dioxide for the monitoring of chronic diseases and healing processes. *Nat Biomed Eng* 2018;3:37–46. <https://doi.org/10.1038/s41551-018-0300-4>.
- [33] Farah S, Anderson DG, Langer R. Physical and mechanical properties of PLA, and their functions in widespread applications — A comprehensive review. *Adv Drug Deliv Rev* 2016.
- [34] Gentile P, Chiono V, Carmagnola I, Hatton P V. An Overview of Poly (lactic- co -glycolic) Acid (PLGA) -Based Biomaterials for Bone Tissue Engineering. *Int J Mol Sci* 2014;15:3640–59. <https://doi.org/10.3390/ijms15033640>.
- [35] Avgoustakis K. Polylactic- Co -Glycolic Acid (PLGA). *Encycl. Biomater. Biomed. Eng.*, 2005. <https://doi.org/10.1081/E-EBBE-120013950>.
- [36] Woodruff MA, Hutmacher DW. Progress in Polymer Science The return of a forgotten polymer — Polycaprolactone in the 21st century. *Prog Polym Sci* 2010;35:1217–56. <https://doi.org/10.1016/j.progpolymsci.2010.04.002>.
- [37] Hwang S, Lee CH, Cheng H, Jeong J, Kang S, Kim J, et al. Biodegradable Elastomers and Silicon Nanomembranes/ Nanoribbons for Stretchable, Transient Electronics, and Biosensors. *Nano Lett* 2015;2801–8. <https://doi.org/10.1021/nl503997m>.
- [38] Tran RT, Thevenot P, Gyawali D, Chiao J, Tang L, Yang J. Synthesis and characterization of a biodegradable elastomer featuring a dual crosslinking mechanism. *Soft Matter* 2010;2449–61. <https://doi.org/10.1039/c001605e>.
- [39] Wang Y, Ameer GA, Sheppard BJ, Langer R. A tough biodegradable elastomer. *Nat Biotechnol* 2002;20:602–6.
- [40] Nijst CLE, Bruggeman JP, Karp JM, Ferreira L, Zumbuehl A, Bettinger CJ, et al. Synthesis and Characterization of Photocurable Elastomers from Poly(glycerol- co -sebacate). *Biomacromolecules* 2007;8:3067–73. <https://doi.org/10.1021/bm070423u>.
- [41] Pashneh-Tala S, Owen R, Bahmaee H, Reškštytė S, Malinauskas M, Claeysens F. Synthesis, Characterization and 3D Micro-Structuring via 2-Photon Polymerization of Poly(glycerol sebacate)-Methacrylate—An Elastomeric Degradable Polymer. *Front Phys* 2018;6:41. <https://doi.org/10.3389/fphy.2018.00041>.
- [42] Zhu C, Kustra SR, Bettinger CJ. Photocrosslinkable biodegradable elastomers based on cinnamate-functionalized polyesters. *Acta Biomater* 2013;9:7362–70. <https://doi.org/10.1016/j.actbio.2013.03.041>.
- [43] Li Y, Thouas GA, Chen Q-Z. Biodegradable soft elastomers: synthesis/properties of materials and fabrication of scaffolds. *RSC Adv* 2012;2:8229. <https://doi.org/10.1039/c2ra20736b>.
- [44] Rockwood DN, Preda RC, Yücel T, Wang X, Lovett ML, Kaplan DL. Materials fabrication from Bombyx mori silk fibroin. *Nat Protoc* 2011;6:1612–29. <https://doi.org/10.1038/nprot.2011.379>.

-
- [45] Lawrence BD, Omenetto F, Chui K, Kaplan DL. Processing methods to control silk fibroin film bio-material features. *J Mater Sci* 2008;43:6967–85. <https://doi.org/10.1007/s10853-008-2961-y>.
- [46] Li M, Tao W, Kuga S, Nishiyama Y. Controlling molecular conformation of regenerated wild silk fibroin by aqueous ethanol treatment. *Polym Adv Technol* 2003;14:694–8. <https://doi.org/10.1002/pat.409>.
- [47] Min B-M, Jeong L, Lee KY, Park WH. Regenerated Silk Fibroin Nanofibers: Water Vapor-Induced Structural Changes and Their Effects on the Behavior of Normal Human Cells. *Macromol Biosci* 2006;6:285–92. <https://doi.org/10.1002/mabi.200500246>.
- [48] Lawrence BD, Wharram S, Kluge JA, Leisk GG, Omenetto FG, Rosenblatt MI, et al. Effect of Hydration on Silk Film Material Properties: Effect of Hydration on Silk Film Material Properties. *Macromol Biosci* 2010;10:393–403. <https://doi.org/10.1002/mabi.200900294>.
- [49] Wang Y, Wang X, Shi J, Zhu R, Zhang J, Zhang Z. Flexible silk fibroin films modified by genipin and glycerol. *RSC Adv* 2015;5:101362–9. <https://doi.org/10.1039/C5RA19754F>.
- [50] Atreya M, Marinick G, Baumbauer C, Dikshit KV, Liu S, Bellerjeau C, et al. Wax Blends as Tunable Encapsulants for Soil-Degradable Electronics. *ACS Appl Electron Mater* 2022;4:4912–20. <https://doi.org/10.1021/acsaelm.2c00833>.
- [51] Sui Y, Atreya M, Dahal S, Gopalakrishnan A, Khosla R, Whiting GL. Controlled Biodegradation of an Additively Fabricated Capacitive Soil Moisture Sensor. *ACS Sustain Chem Eng* 2021;9:2486–95. <https://doi.org/10.1021/acssuschemeng.0c07615>.
- [52] Kim KS, Maeng W-Y, Kim S, Lee G, Hong M, Kim G, et al. Isotropic conductive paste for bioresorbable electronics. *Mater Today Bio* 2023;18:100541. <https://doi.org/10.1016/j.mtbio.2023.100541>.
- [53] Irimia-Vladu M, Głowacki ED, Schwabegger G, Leonat L, Akpınar HZ, Sitter H, et al. Natural resin shellac as a substrate and a dielectric layer for organic field-effect transistors. *Green Chem* 2013;15:1473–6. <https://doi.org/10.1039/C3GC40388B>.
- [54] Ren D, Yi H, Wang W, Ma X. The enzymatic degradation and swelling properties of chitosan matrices with different degrees of N-acetylation. *Carbohydr Res* 2005;340:2403–10. <https://doi.org/10.1016/j.carres.2005.07.022>.
- [55] Poulin A, Aeby X, Siqueira G, Nyström G. Versatile carbon-loaded shellac ink for disposable printed electronics. *Sci Rep* 2021;11:23784. <https://doi.org/10.1038/s41598-021-03075-4>.
- [56] Ghoshal S, Khan MA, Khan RA, Gul-E-Noor F, Sarwaruddin Chowdhury AM. Study on the Thermo-Mechanical and Biodegradable Properties of Shellac Films Grafted with Acrylic Monomers by Gamma Radiation. *J Polym Environ* 2010;18:216–23. <https://doi.org/10.1007/s10924-010-0182-3>.
- [57] Valappil SP, Misra SK, Boccaccini AR, Roy I. Biomedical applications of polyhydroxyalkanoates, an overview of animal testing and *in vivo* responses. *Expert Rev Med Devices* 2006;3:853–68. <https://doi.org/10.1586/17434440.3.6.853>.
- [58] Lei T, Guan M, Liu J, Lin H, Pfattner R, Shaw L, et al. Biocompatible and totally disintegrable semiconducting polymer for ultrathin and ultralightweight transient electronics. *Proc Natl Acad Sci* 2017. <https://doi.org/10.1073/pnas.1701478114>.
- [59] Fang Z, Zhang H, Qiu S, Kuang Y, Zhou J, Lan Y, et al. Versatile Wood Cellulose for Biodegradable Electronics. *Adv Mater Technol* 2021;6:2000928. <https://doi.org/10.1002/admt.202000928>.
- [60] Alvarez JVL, Larrucea MA, Bermúdez PA, Chicote BL. Biodegradation of paper waste under controlled composting conditions. *Waste Manag* 2009;29:1514–9. <https://doi.org/10.1016/j.wasman.2008.11.025>.
- [61] Béguin P, Aubert J-P. The biological degradation of cellulose. *FEMS Microbiol Rev* 1994;13:25–58. <https://doi.org/10.1111/j.1574-6976.1994.tb00033.x>.
- [62] Huang X, Liu Y, Hwang S, Kang S, Patnaik D, Cortes JF, et al. Biodegradable Materials for Multilayer Transient Printed Circuit Boards. *Adv Mater* 2014;7371–7. <https://doi.org/10.1002/adma.201403164>.
- [63] Mattana G, Briand D, Marette A, Vásquez A, Rooij NF De. Polylactic acid as a biodegradable material for all-solution-processed organic electronic devices. *Org Electron* 2015;17:77–86. <https://doi.org/10.1016/j.orgel.2014.11.010>.
- [64] Zheng Q, Zou Y, Zhang Y, Liu Z, Shi B, Wang X, et al. Biodegradable triboelectric nanogenerator as a life-time designed implantable power source. *Sci Adv* 2016;1–9.
- [65] Li J, Long Y, Yang F, Wang X. Degradable piezoelectric biomaterials for wearable and implantable bioelectronics. *Curr Opin Solid State Mater Sci* 2020;24:100806. <https://doi.org/10.1016/j.cossms.2020.100806>.
- [66] Li R, Wang L, Yin L. Materials and Devices for Biodegradable and Soft Biomedical Electronics. *Materials* 2018;11:2108. <https://doi.org/10.3390/ma11112108>.
- [67] Han WB, Lee JH, Shin J, Hwang S. Advanced Materials and Systems for Biodegradable, Transient Electronics. *Adv Mater* 2020;32:2002211. <https://doi.org/10.1002/adma.202002211>.
- [68] Aslam M, Kalyar MA, Raza ZA. Polyvinyl alcohol: A review of research status and use of polyvinyl alcohol based nanocomposites. *Polym Eng Sci* 2018;58:2119–32. <https://doi.org/10.1002/pen.24855>.

-
- [69] Tang X, Alavi S. Recent advances in starch, polyvinyl alcohol based polymer blends, nanocomposites and their biodegradability. *Carbohydr Polym* 2011;85:7–16. <https://doi.org/10.1016/j.carbpol.2011.01.030>.
- [70] Jiang L, Nath C, Samuel J, Kapoor SG. An enhanced microstructure-level finite element machining model for carbon nanotube-polymer composites. *J Manuf Sci Eng Trans ASME* 2015;137. <https://doi.org/10.1115/1.4028200>.
- [71] Volova T, Shishatskaya E, Sevastianov V, Efremov S, Mogilnaya O. Results of biomedical investigations of PHB and PHB / PHV fibers. *Biochem Eng J* 2003;16:125–33. [https://doi.org/10.1016/S1369-703X\(03\)00038-X](https://doi.org/10.1016/S1369-703X(03)00038-X).
- [72] Giubilini A, Siqueira G, Clemens FJ, Sciancalepore C, Messori M, Nyström G, et al. 3D-Printing Nanocellulose-Poly(3-hydroxybutyrate-co-3-hydroxyhexanoate) Biodegradable Composites by Fused Deposition Modeling. *ACS Sustain Chem Eng* 2020;8:10292–302. <https://doi.org/10.1021/acssuschemeng.0c03385>.
- [73] Ou-Yang Q, Guo B, Xu J. Preparation and Characterization of Poly(butylene succinate)/Polylactide Blends for Fused Deposition Modeling 3D Printing. *ACS Omega* 2018;3:14309–17. <https://doi.org/10.1021/acsomega.8b02549>.
- [74] Koh L, Cheng Y, Teng C, Khin Y, Loh X, Tee S, et al. Mechanical properties and applications of silk fibroin materials. *Prog Polym Sci* 2015;46:86–110. <https://doi.org/10.1016/j.progpolymsci.2015.02.001>.
- [75] Tao H, Kaplan DL, Omenetto FG. Silk materials - A road to sustainable high technology. *Adv Mater* 2012;24:2824–37. <https://doi.org/10.1002/adma.201104477>.
- [76] Qussi B, Suess WG. The Influence of Different Plasticizers and Polymers on the Mechanical and Thermal Properties, Porosity and Drug Permeability of Free Shellac Films. *Drug Dev Ind Pharm* 2006;32:403–12. <https://doi.org/10.1080/03639040600559099>.
- [77] Thombare N, Kumar S, Kumari U, Sakare P, Yogi RK, Prasad N, et al. Shellac as a multifunctional biopolymer: A review on properties, applications and future potential. *Int J Biol Macromol* 2022;215:203–23. <https://doi.org/10.1016/j.ijbiomac.2022.06.090>.
- [78] Ebrahimi B, Mohammadi R, Rouhi M, Mortazavian AM, Shojaee-Aliabadi S, Koushki MR. Survival of probiotic bacteria in carboxymethyl cellulose-based edible film and assessment of quality parameters. *LWT - Food Sci Technol* 2018;87:54–60. <https://doi.org/10.1016/j.lwt.2017.08.066>.
- [79] Zhang B, Montgomery M, Chamberlain MD, Ogawa S, Korolj A, Pahnke A, et al. Biodegradable scaffold with built-in vasculature for organ-on-a-chip engineering and direct surgical anastomosis. *Nat Mater* 2016;15:669–80. <https://doi.org/10.1038/NMAT4570>.
- [80] Li Y, Cook WD, Moorhoff C, Huang WC, Chen QZ. Synthesis, characterization and properties of biocompatible poly(glycerol sebacate) pre-polymer and gel. *Polym Int* 2013;62:534–47. <https://doi.org/10.1002/pi.4419>.
- [81] Kang S, Koo J, Lee YK, Rogers JA. Advanced Materials and Devices for Bioresorbable Electronics. *Acc Chem Res* 2018;51:988–98. <https://doi.org/10.1021/acs.accounts.7b00548>.
- [82] Yin L, Cheng H, Mao S, Haasch R, Liu Y, Xie X, et al. Dissolvable Metals for Transient Electronics. *Adv Mater* 2014;24:645–58. <https://doi.org/10.1002/adfm.201301847>.
- [83] Vojtěch D, Kubásek J, Čapek J. Comparative mechanical and corrosion studies on magnesium, zinc and iron alloys as biodegradable metals. *Mater Tehnol* 2015;49:877–82. <https://doi.org/10.17222/mit.2014.129>.
- [84] Luo M, Martinez AW, Song C, Herrault F, Allen MG. A Microfabricated Wireless RF Pressure Sensor Made Completely of Biodegradable Materials. *J Microelectromechanical Syst* 2014;23:4–13. <https://doi.org/10.1109/JMEMS.2013.2290111>.
- [85] Han H-S, Loffredo S, Jun I, Edwards J, Kim Y-C, Seok H-K, et al. Current status and outlook on the clinical translation of biodegradable metals. *Mater Today* 2019;23:57–71. <https://doi.org/10.1016/j.mat-tod.2018.05.018>.
- [86] Patrick E, Orazem ME, Sanchez JC, Nishida T. Corrosion of tungsten microelectrodes used in neural recording applications. *J Neurosci Methods* 2011;198:158–71. <https://doi.org/10.1016/j.jneumeth.2011.03.012>.
- [87] Huang X. Materials and applications of bioresorbable electronics. *J Semicond* 2018;39:011003. <https://doi.org/10.1088/1674-4926/39/1/011003>.
- [88] Liu Y, Zheng Y, Chen X-H, Yang J-A, Pan H, Chen D, et al. Fundamental Theory of Biodegradable Metals—Definition, Criteria, and Design. *Adv Funct Mater* 2019;29:1805402. <https://doi.org/10.1002/adfm.201805402>.
- [89] Xue D, Yun Y, Tan Z, Dong Z, Schulz MJ. In Vivo and In Vitro Degradation Behavior of Magnesium Alloys as Biomaterials. *J Mater Sci Technol* 2012;28:261–7. [https://doi.org/10.1016/S1005-0302\(12\)60051-6](https://doi.org/10.1016/S1005-0302(12)60051-6).

-
- [90] Li H, Zhao C, Wang X, Meng J, Zou Y, Noreen S, et al. Fully Bioabsorbable Capacitor as an Energy Storage Unit for Implantable Medical Electronics. *Adv Sci* 2019;6:1801625. <https://doi.org/10.1002/advs.201801625>.
- [91] Lee G, Kang S-K, Won SM, Gutruf P, Jeong YR, Koo J, et al. Fully Biodegradable Microsupercapacitor for Power Storage in Transient Electronics. *Adv Energy Mater* 2017;7:1700157. <https://doi.org/10.1002/aenm.201700157>.
- [92] Bowen PK, Drelich J, Goldman J. Zinc Exhibits Ideal Physiological Corrosion Behavior for Bioabsorbable Stents. *Adv Mater* 2013;25:2577–82. <https://doi.org/10.1002/adma.201300226>.
- [93] Yi N, Cheng Z, Yang L, Edelman G, Xue C, Ma Y, et al. Fully Water-Soluble, High-Performance Transient Sensors on a Versatile Galactomannan Substrate Derived from the Endospore. *ACS Appl Mater Interfaces* 2018;10:36664–74. <https://doi.org/10.1021/acsami.8b11682>.
- [94] Schauer A, Redlich C, Scheibler J, Poehle G, Barthel P, Maennel A, et al. Biocompatibility and Degradation Behavior of Molybdenum in an In Vivo Rat Model. *Materials* 2021;14:7776. <https://doi.org/10.3390/ma14247776>.
- [95] Hadrup N, Sørlie JB, Sharma AK. Pulmonary toxicity, genotoxicity, and carcinogenicity evaluation of molybdenum, lithium, and tungsten: A review. *Toxicology* 2022;467:153098. <https://doi.org/10.1016/j.tox.2022.153098>.
- [96] Algieri L, Todaro MT, Guido F, Blasi L, Mastronardi V, Desmaële D, et al. Piezoelectricity and Biocompatibility of Flexible ScxAl(1-x)N Thin Films for Compliant MEMS Transducers. *ACS Appl Mater Interfaces* 2020;12:18660–6. <https://doi.org/10.1021/acsami.0c00552>.
- [97] Da Silva AC, Córdoba De Torresi SI. Advances in Conducting, Biodegradable and Biocompatible Copolymers for Biomedical Applications. *Front Mater* 2019;6:98. <https://doi.org/10.3389/fmats.2019.00098>.
- [98] Stejskal J, Hlavata D, Holler P, Trchov M, Sapurina I, Prokes J. Polyaniline prepared in the presence of various acids : a conductivity study. *Polym Int* 2004;300:294–300. <https://doi.org/10.1002/pi.1406>.
- [99] Le T-H, Kim Y, Yoon H. Electrical and Electrochemical Properties of Conducting Polymers. *Polymers* 2017;9. <https://doi.org/10.3390/polym9040150>.
- [100] Pal RK, Farghaly AA, Collinson MM, Kundu SC, Yadavalli VK. Photolithographic Micropatterning of Conducting Polymers on Flexible Silk Matrices. *Adv Mater* 2016;28:1406–12. <https://doi.org/10.1002/adma.201504736>.
- [101] Dupont SR, Novoa F, Voroshazi E, Dauskardt RH. Decohesion Kinetics of PEDOT:PSS Conducting Polymer Films. *Adv Funct Mater* 2014;24:1325–32. <https://doi.org/10.1002/adfm.201302174>.
- [102] Campos-Arias L, del Olmo R, Peřinka N, Casado N, Vilas-Vilela JL, Mecerreyes D, et al. PEDOT:PSS-based screen-printable inks for H₂O₂ electrochemical detection. *Electrochimica Acta* 2023;439:141615. <https://doi.org/10.1016/j.electacta.2022.141615>.
- [103] Ferlauto L, Vagni P, Fanelli A, Zollinger EG, Monsorno K, Paolicelli RC, et al. All-polymeric transient neural probe for prolonged in-vivo electrophysiological recordings. *Biomaterials* 2021;274:120889. <https://doi.org/10.1016/j.biomaterials.2021.120889>.
- [104] Fanelli A, Ferlauto L, Zollinger EG, Brina O, Reymond P, Machi P, et al. Transient Neurovascular Interface for Minimally Invasive Neural Recording and Stimulation. *Adv Mater Technol* 2022;7:2100176. <https://doi.org/10.1002/admt.202100176>.
- [105] Wang G, Wu W, Yang H, Zhang P, Wang J-Y. Intact polyaniline coating as a conductive guidance is beneficial to repairing sciatic nerve injury. *J Biomed Mater Res B Appl Biomater* 2020;108:128–42. <https://doi.org/10.1002/jbm.b.34372>.
- [106] Huang Z-B, Yin G-F, Liao X-M, Gu J-W. Conducting polypyrrole in tissue engineering applications. *Front Mater Sci* 2014;8:39–45. <https://doi.org/10.1007/s11706-014-0238-8>.
- [107] Poulin A, Aeby X, Nyström G. Water activated disposable paper battery. *Sci Rep* 2022;12:11919. <https://doi.org/10.1038/s41598-022-15900-5>.
- [108] Aeby X, Bourelly J, Poulin A, Siqueira G, Nyström G, Briand D. Printed Humidity Sensors from Renewable and Biodegradable Materials. *Adv Mater Technol* 2022:2201302. <https://doi.org/10.1002/admt.202201302>.
- [109] Aeby X, Poulin A, Siqueira G, Hausmann MK, Nyström G. Fully 3D Printed and Disposable Paper Supercapacitors. *Adv Mater* 2021;33:2101328. <https://doi.org/10.1002/adma.202101328>.
- [110] Ilic IK, Galli V, Lamanna L, Cataldi P, Pasquale L, Annese VF, et al. An Edible Rechargeable Battery. *Adv Mater* 2023;35:2211400. <https://doi.org/10.1002/adma.202211400>.
- [111] Singh R, Bathaei MJ, Istif E, Beker L. A Review of Bioresorbable Implantable Medical Devices: Materials, Fabrication, and Implementation. *Adv Healthc Mater* 2020;9:2000790. <https://doi.org/10.1002/adhm.202000790>.

-
- [112] Allen BL, Kichambare PD, Gou P, Vlasova II, Kapralov AA, Konduru N, et al. Biodegradation of single-walled carbon nanotubes through enzymatic catalysis. *Nano Lett* 2008;8:3899–903. <https://doi.org/10.1021/nl802315h>.
- [113] Tran H, Feig VR, Liu K, Wu H, Chen R, Xu J, et al. Stretchable and Fully Degradable Semiconductors for Transient Electronics. *ACS Cent Sci* 2019;5:1884–91. <https://doi.org/10.1021/acscentsci.9b00850>.
- [114] Irimia-Vladu M, Troshin PA, Reisinger M, Shmygleva L, Kanbur Y, Schwabegger G, et al. Biocompatible and Biodegradable Materials for Organic Field-Effect Transistors. *Adv Funct Mater* 2010;20:4069–76. <https://doi.org/10.1002/adfm.201001031>.
- [115] Serruys PW, Ormiston JA, Onuma Y, Regar E, Gonzalo N, Garcia-garcia HM, et al. A bioabsorbable everolimus-eluting coronary stent system (ABSORB): 2-year outcomes and results from multiple imaging methods. *The Lancet* 2009;373:897–910. [https://doi.org/10.1016/S0140-6736\(09\)60325-1](https://doi.org/10.1016/S0140-6736(09)60325-1).
- [116] Meng B, Wang J, Zhu N, Xu FCY. Study of biodegradable and self-expandable PLLA helical biliary stent in vivo and in vitro. *J Mater Sci* 2006;611–7. <https://doi.org/10.1007/s10856-006-9223-9>.
- [117] Tan L, Yu X, Wan P, Yang K. Biodegradable Materials for Bone Repairs : A Review. *J Mater Sci Technol* 2013;29:503–13. <https://doi.org/10.1016/j.jmst.2013.03.002>.
- [118] Xiang Z, Yen S-C, Xue N, Sun T, Tsang WM, Zhang S, et al. Ultra-thin flexible polyimide neural probe embedded in a dissolvable maltose-coated microneedle. *J Micromechanics Microengineering* 2014;24:065015. <https://doi.org/10.1088/0960-1317/24/6/065015>.
- [119] Boutry CM, Chandralim H, Streit P, Schinhammer M, Hänzi AC, Hierold C. Towards biodegradable wireless implants. *Philos Trans Math Phys Eng Sci* 2012;370:2418–32.
- [120] Boutry CM, Chandralim H, Streit P, Schinhammer M, Hänzi AC, Hierold C. Characterization of miniaturized RLC resonators made of biodegradable materials for wireless implant applications. *Sens Actuators Phys* 2013;189:344–55. <https://doi.org/10.1016/j.sna.2012.08.039>.
- [121] Meitl MA, Zhu Z, Kumar V, Lee KJAE, Feng XUE, Huang YY, et al. Transfer printing by kinetic control of adhesion to an elastomeric stamp. *Nat Mater* 2006;5:33–8. <https://doi.org/10.1038/nmat1532>.
- [122] Hwang S, Huang X, Seo J, Song J, Kim S, Hage-ali S, et al. Materials for Bioresorbable Radio Frequency Electronics. *Adv Mater* 2013;3526–31. <https://doi.org/10.1002/adma.201300920>.
- [123] Tao H, Hwang S, Marelli B, An B, Moreau JE, Yang M, et al. Silk-based resorbable electronic devices for remotely controlled therapy and in vivo infection abatement. *Proc Natl Acad Sci* 2014;119:17385–9. <https://doi.org/10.1073/pnas.1407743111>.
- [124] Kang S, Murphy RKJ, Hwang S, Lee SM, Daniel V, Shin J, et al. Bioresorbable silicon electronic sensors for the brain. *Nature* 2016;530:71–6. <https://doi.org/10.1038/nature16492>.
- [125] Yu KJ, Kuzum D, Hwang S, Kim BH, Juul H, Kim NH, et al. Bioresorbable silicon electronics for transient spatiotemporal mapping of electrical activity Mapping of Electrical Activity from the Cerebral Cortex. *Nat Mater* 2016;15:782–92. <https://doi.org/10.1038/NMAT4624>.
- [126] Bai W, Yang H, Ma Y, Chen H, Shin J, Liu Y, et al. Flexible Transient Optical Waveguides and Surface-Wave Biosensors Constructed from Monocrystalline Silicon. *Adv Mater* 2018;30:1801584. <https://doi.org/10.1002/adma.201801584>.
- [127] Xu K, Li S, Dong S, Zhang S, Pan G, Wang G, et al. Bioresorbable Electrode Array for Electrophysiological and Pressure Signal Recording in the Brain. *Adv Healthc Mater* 2019;8:1801649. <https://doi.org/10.1002/adhm.201801649>.
- [128] Ouyang H, Li Z, Gu M, Hu Y, Xu L, Jiang D, et al. A Bioresorbable Dynamic Pressure Sensor for Cardiovascular Postoperative Care. *Adv Mater* 2021;33:2102302. <https://doi.org/10.1002/adma.202102302>.
- [129] Curry EJ, Ke K, Chorsi MT, Wrobel KS, Miller AN, Patel A, et al. Biodegradable Piezoelectric Force Sensor. *Proc Natl Acad Sci* 2018;115:909–14. <https://doi.org/10.1073/pnas.1710874115>.
- [130] Palmroth A, Salpavaara T, Lekkala J, Kellomäki M. Fabrication and Characterization of a Wireless Bioresorbable Pressure Sensor. *Adv Mater Technol* 2019;4:1900428. <https://doi.org/10.1002/admt.201900428>.
- [131] Koo J, MacEwan MR, Kang S-K, Won SM, Stephen M, Gamble P, et al. Wireless bioresorbable electronic system enables sustained nonpharmacological neuroregenerative therapy. *Nat Med* 2018;24:1830–6. <https://doi.org/10.1038/s41591-018-0196-2>.
- [132] Lee G, Ray E, Yoon H-J, Genovese S, Choi YS, Lee M-K, et al. A bioresorbable peripheral nerve stimulator for electronic pain block. *Sci Adv* 2022;8:eabp9169. <https://doi.org/10.1126/sciadv.abp9169>.
- [133] Koo J, Kim SB, Choi YS, Xie Z, Bandodkar AJ, Khalifeh J, et al. Wirelessly controlled, bioresorbable drug delivery device with active valves that exploit electrochemically triggered crevice corrosion. *Sci Adv* 2020;6:eabb1093. <https://doi.org/10.1126/sciadv.abb1093>.
- [134] Huang Y, Li H, Hu T, Li J, Yiu CK, Zhou J, et al. Implantable Electronic Medicine Enabled by Bioresorbable Microneedles for Wireless Electrotherapy and Drug Delivery. *Nano Lett* 2022;22:5944–53. <https://doi.org/10.1021/acs.nanolett.2c01997>.

-
- [135] Rüegg M, Blum R, Boero G, Brugger J. Biodegradable Frequency-Selective Magnesium Radio-Frequency Microresonators for Transient Biomedical Implants. *Adv Funct Mater* 2019;29:1903051. <https://doi.org/10.1002/adfm.201903051>.
- [136] Zhang Y, Liu F, Zhang Y, Wang J, D'Andrea D, Walters JB, et al. Self-powered, light-controlled, bioresorbable platforms for programmed drug delivery. *Proc Natl Acad Sci* 2023;120:e2217734120. <https://doi.org/10.1073/pnas.2217734120>.
- [137] Choi YS, Yin RT, Pfenniger A, Koo J, Avila R, Benjamin Lee K, et al. Fully implantable and bioresorbable cardiac pacemakers without leads or batteries. *Nat Biotechnol* 2021;39:1228–38. <https://doi.org/10.1038/s41587-021-00948-x>.
- [138] Song JW, Ryu H, Bai W, Xie Z, Vázquez-Guardado A, Nandoliya K, et al. Bioresorbable, wireless, and battery-free system for electrotherapy and impedance sensing at wound sites. *Sci Adv* 2023;9:eade4687. <https://doi.org/10.1126/sciadv.ade4687>.
- [139] Yao G, Kang L, Li C, Chen S, Wang Q, Yang J, et al. A self-powered implantable and bioresorbable electrostimulation device for biofeedback bone fracture healing. *Proc Natl Acad Sci* 2021;118:e2100772118. <https://doi.org/10.1073/pnas.2100772118>.
- [140] Yang Q, Hu Z, Seo M-H, Xu Y, Yan Y, Hsu Y-H, et al. High-speed, scanned laser structuring of multi-layered eco/bioresorbable materials for advanced electronic systems. *Nat Commun* 2022;13:6518. <https://doi.org/10.1038/s41467-022-34173-0>.
- [141] Chang J-K, Fang H, Bower CA, Song E, Yu X, Rogers JA. Materials and processing approaches for foundry-compatible transient electronics. *Proc Natl Acad Sci U S A* 2017;114:E5522–9. <https://doi.org/10.1073/pnas.1707849114>.
- [142] Yu KJ, Kuzum D, Hwang S-W, Kim BH, Juul H, Kim NH, et al. Bioresorbable silicon electronics for transient spatiotemporal mapping of electrical activity from the cerebral cortex. *Nat Mater* 2016;15:782–91. <https://doi.org/10.1038/nmat4624>.
- [143] Pan R, Xuan W, Chen J, Dong S, Jin H, Wang X, et al. Fully biodegradable triboelectric nanogenerators based on electrospun polylactic acid and nanostructured gelatin films. *Nano Energy* 2018;45:193–202. <https://doi.org/10.1016/j.nanoen.2017.12.048>.
- [144] Boutry CM, Beker L, Kaizawa Y, Vassos C, Tran H, Hinckley AC, et al. Biodegradable and flexible arterial-pulse sensor for the wireless monitoring of blood flow. *Nat Biomed Eng* 2019;3:47–57. <https://doi.org/10.1038/s41551-018-0336-5>.
- [145] Feiner R, Dvir T. Tissue-electronics interfaces: From implantable devices to engineered tissues. *Nat Rev Mater* 2017;3. <https://doi.org/10.1038/natrevmats.2017.76>.
- [146] Boutry CM, Kaizawa Y, Schroeder BC, Chortos A, Legrand A, Wang Z, et al. A stretchable and biodegradable strain and pressure sensor for orthopaedic application. *Nat Electron* 2018;1. <https://doi.org/10.1038/s41928-018-0071-7>.
- [147] Dagdeviren C, Hwang SW, Su Y, Kim S, Cheng H, Gur O, et al. Transient, biocompatible electronics and energy harvesters based on ZnO. *Small* 2013;9:3398–404. <https://doi.org/10.1002/smll.201300146>.
- [148] Pan R, Xuan W, Chen J, Dong S, Jin H, Wang X. Nano Energy Fully biodegradable triboelectric nanogenerators based on electrospun polylactic acid and nanostructured gelatin films. *Nano Energy* 2018;45:193–202. <https://doi.org/10.1016/j.nanoen.2017.12.048>.
- [149] Son D, Lee J, Lee DJ, Ghaffari R, Yun S, Kim SJ, et al. Bioresorbable Electronic Stent Integrated with Therapeutic Nanoparticles for Endovascular Diseases. *ACS Nano* 2015:5937–46. <https://doi.org/10.1021/acs.nano.5b00651>.
- [150] Guo Q, Koo J, Xie Z, Avila R, Yu X, Ning X, et al. A Bioresorbable Magnetically Coupled System for Low-Frequency Wireless Power Transfer. *Adv Funct Mater* 2019;29:1905451. <https://doi.org/10.1002/adfm.201905451>.
- [151] Jia X, Wang C, Zhao C, Ge Y, Wallace GG. Toward Biodegradable Mg – Air Bioelectric Batteries Composed of Silk Fibroin – Polypyrrole Film. *Adv Funct Mater* 2016:1454–62. <https://doi.org/10.1002/adfm.201503498>.
- [152] Pal RK, Farghaly AA, Wang C, Collinson MM, Kundu SC, Yadavalli VK. Biosensors and Bioelectronics Conducting polymer-silk biocomposites for flexible and biodegradable electrochemical sensors. *Biosens Bioelectron* 2016;81:294–302. <https://doi.org/10.1016/j.bios.2016.03.010>.
- [153] Xu M, Yadavalli VK. Flexible Biosensors for the Impedimetric Detection of Protein Targets Using Silk-Conductive Polymer Biocomposites. *ACS Sens* 2019. <https://doi.org/10.1021/acssensors.9b00230>.
- [154] Campana A, Cramer T, Simon DT, Berggren M, Biscarini F. Electrocardiographic Recording with Conformable Organic Electrochemical Transistor Fabricated on Resorbable Bioscaffold. *Adv Mater* 2014;26:3874–8. <https://doi.org/10.1002/adma.201400263>.
- [155] Granelli R, Alessandri I, Gkoupidenis P, Vassalini I, Kovács-Vajna ZM, Blom PWM, et al. High-Performance Bioelectronic Circuits Integrated on Biodegradable and Compostable Substrates with Fully

-
- Printed Mask-Less Organic Electrochemical Transistors. *Small* 2022;18:2108077. <https://doi.org/10.1002/smll.202108077>.
- [156] Habas SE, Platt HAS, van Hest MFAM, Ginley DS. Low-cost inorganic solar cells: from ink to printed device. *Chem Rev* 2010;110:6571–94. <https://doi.org/10.1021/cr100191d>.
- [157] Leenen MAM, Arning V, Thiem H, Steiger J, Anselmann R. Printable electronics: flexibility for the future. *Phys Status Solidi A* 2009;206:588–97. <https://doi.org/10.1002/pssa.200824428>.
- [158] Afanasenkau D, Kalinina D, Lyakhovetskii V, Tondera C, Gorsky O, Moosavi S, et al. Rapid prototyping of soft bioelectronic implants for use as neuromuscular interfaces. *Nat Biomed Eng* 2020;4:1010–22. <https://doi.org/10.1038/s41551-020-00615-7>.
- [159] Huo W, Li J, Ren M, Ling W, Xu H, Tee CAT, et al. Recent development of bioresorbable electronics using additive manufacturing. *Curr Opin Chem Eng* 2020;28:118–26. <https://doi.org/10.1016/j.coche.2020.04.002>.
- [160] Huang Q, Zhu Y. Printing Conductive Nanomaterials for Flexible and Stretchable Electronics: A Review of Materials, Processes, and Applications. *Adv Mater Technol* 2019;4:1800546. <https://doi.org/10.1002/admt.201800546>.
- [161] Li J, Liu J, Huo W, Yu J, Liu X, Haslinger MJ, et al. Micro and nano materials and processing techniques for printed biodegradable electronics. *Mater Today Nano* 2022;18:100201. <https://doi.org/10.1016/j.mtnano.2022.100201>.
- [162] Zeng X, He P, Hu M, Zhao W, Chen H, Liu L, et al. Copper inks for printed electronics: a review. *Nanoscale* 2022;14:16003–32. <https://doi.org/10.1039/D2NR03990G>.
- [163] Paul B, Demuru S, Lafaye C, Saubade M, Briand D. Printed Iontophoretic-Integrated Wearable Microfluidic Sweat-Sensing Patch for On-Demand Point-Of-Care Sweat Analysis. *Adv Mater Technol* 2021;6:2000910. <https://doi.org/10.1002/admt.202000910>.
- [164] Mickle AD, Won SM, Noh KN, Yoon J, Meacham KW, Xue Y, et al. A wireless closed-loop system for optogenetic peripheral neuromodulation. *Nature* 2019;565:361–5. <https://doi.org/10.1038/s41586-018-0823-6>.
- [165] Nayak L, Mohanty S, Kumar Nayak S, Ramadoss A. A review on inkjet printing of nanoparticle inks for flexible electronics. *J Mater Chem C* 2019;7:8771–95. <https://doi.org/10.1039/C9TC01630A>.
- [166] Derby B. Inkjet Printing of Functional and Structural Materials: Fluid Property Requirements, Feature Stability, and Resolution. *Annu Rev Mater Res* 2010;40:395–414. <https://doi.org/10.1146/annurev-matsci-070909-104502>.
- [167] Smith M, Choi YS, Boughey C, Kar-Narayan S. Controlling and assessing the quality of aerosol jet printed features for large area and flexible electronics. *Flex Print Electron* 2017;2:015004. <https://doi.org/10.1088/2058-8585/aa5af9>.
- [168] Pu Z, Tu J, Han R, Zhang X, Wu J, Fang C, et al. A flexible enzyme-electrode sensor with cylindrical working electrode modified with a 3D nanostructure for implantable continuous glucose monitoring. *Lab Chip* 2018;18:3570–7. <https://doi.org/10.1039/C8LC00908B>.
- [169] Mattana G, Loi A, Woytasik M, Barbaro M, Noël V, Piro B. Inkjet-Printing: A New Fabrication Technology for Organic Transistors. *Adv Mater Technol* 2017;2:1700063. <https://doi.org/10.1002/admt.201700063>.
- [170] Borda E, Ferlauto L, Schleuniger J, Mustaccio A, Lütolf F, Lücke A, et al. All-Printed Electrocardiography Array for In Vivo Neural Recordings. *Adv Eng Mater* 2020;22:1901403.
- [171] Khan S, Nguyen TP, Thiery L, Vairac P, Briand D. Aerosol Jet Printing of Miniaturized, Low Power Flexible Micro-Hotplates. *Proceedings* 2017;1:316. <https://doi.org/10.3390/proceedings1040316>.
- [172] Cantù E, Tonello S, Abate G, Uberti D, Sardini E, Serpelloni M. Aerosol Jet Printed 3D Electrochemical Sensors for Protein Detection. *Sensors* 2018;18:3719. <https://doi.org/10.3390/s18113719>.
- [173] Herbert R, Lim H-R, Park S, Kim J-H, Yeo W-H. Recent Advances in Printing Technologies of Nanomaterials for Implantable Wireless Systems in Health Monitoring and Diagnosis. *Adv Healthc Mater* 2021;10:2100158. <https://doi.org/10.1002/adhm.202100158>.
- [174] Goh GL, Zhang H, Chong TH, Yeong WY. 3D Printing of Multilayered and Multimaterial Electronics: A Review. *Adv Electron Mater* 2021;7:2100445. <https://doi.org/10.1002/aelm.202100445>.
- [175] Choi J-W, Kim H-C, Wicker R. Multi-material stereolithography. *J Mater Process Technol* 2011;211:318–28. <https://doi.org/10.1016/j.jmatprotec.2010.10.003>.
- [176] Xu X, Goyanes A, Trenfield SJ, Diaz-Gomez L, Alvarez-Lorenzo C, Gaisford S, et al. Stereolithography (SLA) 3D printing of a bladder device for intravesical drug delivery. *Mater Sci Eng C* 2021;120:111773. <https://doi.org/10.1016/j.msec.2020.111773>.
- [177] Saadi M a. SR, Maguire A, Pottackal NT, Thakur MSH, Ikram MMd, Hart AJ, et al. Direct Ink Writing: A 3D Printing Technology for Diverse Materials. *Adv Mater* 2022;34:2108855. <https://doi.org/10.1002/adma.202108855>.

-
- [178] Chong H, Lou J, Bogie KM, Zorman CA, Majerus SJA. Vascular Pressure–Flow Measurement Using CB-PDMS Flexible Strain Sensor. *IEEE Trans Biomed Circuits Syst* 2019;13:1451–61. <https://doi.org/10.1109/TBCAS.2019.2946519>.
- [179] Saleh E, Zhang F, He Y, Vaithilingam J, Fernandez JL, Wildman R, et al. 3D Inkjet Printing of Electronics Using UV Conversion. *Adv Mater Technol* 2017;2:1700134. <https://doi.org/10.1002/admt.201700134>.
- [180] Hong H, Hu J, Yan X. UV Curable Conductive Ink for the Fabrication of Textile-Based Conductive Circuits and Wearable UHF RFID Tags. *ACS Appl Mater Interfaces* 2019;11:27318–26. <https://doi.org/10.1021/acsami.9b06432>.
- [181] Abbel R, van Lammeren T, Hendriks R, Ploegmakers J, Rubingh EJ, Meinders ER, et al. Photonic flash sintering of silver nanoparticle inks: a fast and convenient method for the preparation of highly conductive structures on foil. *MRS Commun* 2012;2:145–50. <https://doi.org/10.1557/mrc.2012.28>.
- [182] Yarali E, Koutsiaki C, Faber H, Tetzner K, Yengel E, Patsalas P, et al. Recent Progress in Photonic Processing of Metal-Oxide Transistors. *Adv Funct Mater* 2020;30:1906022. <https://doi.org/10.1002/adfm.201906022>.
- [183] Huo W, Zhang Z, Wang Z, Wu Z, Li J, Chai Y, et al. Large-Area Transient Conductive Films Obtained through Photonic Sintering of 2D Materials. *Adv Mater Technol* 2022;7:2100439. <https://doi.org/10.1002/admt.202100439>.
- [184] Ouyang J, Cormier D, Williams SA, Borkholder DA. Photonic Sintering of Aerosol Jet Printed Lead Zirconate Titanate (PZT) Thick Films. *J Am Ceram Soc* 2016;99:2569–77. <https://doi.org/10.1111/jace.14272>.
- [185] Feng S, Cao S, Tian Z, Zhu H, Kong D. Maskless Patterning of Biodegradable Conductors by Selective Laser Sintering of Microparticle Inks and Its Application in Flexible Transient Electronics. *ACS Appl Mater Interfaces* 2019. <https://doi.org/10.1021/acsami.9b14431>.
- [186] Magdassi S, Grouchko M, Berezin O, Kamyshny A. Triggering the Sintering of Silver Nanoparticles at Room Temperature. *ACS Nano* 2010;4:1943–8. <https://doi.org/10.1021/nn901868t>.
- [187] Layani M, Grouchko M, Shemesh S, Magdassi S. Conductive patterns on plastic substrates by sequential inkjet printing of silver nanoparticles and electrolyte sintering solutions. *J Mater Chem* 2012;22:14349–52. <https://doi.org/10.1039/C2JM32789A>.
- [188] Hermerschmidt F, Burmeister D, Ligorio G, Pozov SM, Ward R, Choulis SA, et al. Truly Low Temperature Sintering of Printed Copper Ink Using Formic Acid. *Adv Mater Technol* 2018;3:1800146. <https://doi.org/10.1002/admt.201800146>.
- [189] Shi L, Layani M, Cai X, Zhao H, Magdassi S, Lan M. An inkjet printed Ag electrode fabricated on plastic substrate with a chemical sintering approach for the electrochemical sensing of hydrogen peroxide. *Sens Actuators B Chem* 2018;256:938–45. <https://doi.org/10.1016/j.snb.2017.10.035>.
- [190] Demir AG, Monguzzi L, Previtali B. Selective laser melting of pure Zn with high density for biodegradable implant manufacturing. *Addit Manuf* 2017;15:20–8. <https://doi.org/10.1016/j.addma.2017.03.004>.
- [191] Carluccio D, Demir AG, Birmingham MJ, Dargusch MS. Challenges and Opportunities in the Selective Laser Melting of Biodegradable Metals for Load-Bearing Bone Scaffold Applications. *Metall Mater Trans A* 2020;51:3311–34. <https://doi.org/10.1007/s11661-020-05796-z>.
- [192] Feig VR, Tran H, Bao Z. Biodegradable Polymeric Materials in Degradable Electronic Devices. *ACS Cent Sci* 2018;337–48. <https://doi.org/10.1021/acscentsci.7b00595>.
- [193] Tao H, Marelli B, Yang M, An B, Onses MS, Rogers JA, et al. Inkjet Printing of Regenerated Silk Fibroin : From Printable Forms to Printable Functions. *Adv Mater* 2015:4273–9. <https://doi.org/10.1002/adma.201501425>.
- [194] Rider PM, Brook IM, Smith PJ, Miller CA. Reactive Inkjet Printing of Regenerated Silk Fibroin Films for Use as Dental Barrier Membranes. *Micromachines* 2018;46:1–15. <https://doi.org/10.3390/mi9020046>.
- [195] Ghosh BS, Parker ST, Wang X, Kaplan DL, Lewis JA. Direct-Write Assembly of Microperiodic Silk Fibroin Scaffolds for Tissue Engineering Applications. *Adv Funct Mater* 2008:1883–9. <https://doi.org/10.1002/adfm.200800040>.
- [196] Xiao Y, Kalaitzidou K, Yao D, Yeo W-H, Harris TAL. Challenges and Advances in Aerosol Jet Printing of Regenerated Silk Fibroin Solutions. *Adv Mater Interfaces* 2020;7:1902005. <https://doi.org/10.1002/admi.201902005>.
- [197] Vogt L, Ruther F, Salehi S, Boccaccini AR. Poly(Glycerol Sebacate) in Biomedical Applications—A Review of the Recent Literature. *Adv Healthc Mater* 2021;10:2002026. <https://doi.org/10.1002/adhm.202002026>.
- [198] Pashneh-Tala S, Owen R, Bahmaee H, Rekyt S, Malinauskas M, Claeysens F. Synthesis, Characterization and 3D Polymerization of Poly (glycerol sebacate)-Methacrylate - An Elastomeric Degradable Polymer. *Front Phys* 2018;6. <https://doi.org/10.3389/fphy.2018.00041>.

-
- [199] Yeh Y-C, Highley CB, Ouyang L, Burdick JA. 3D printing of photocurable poly(glycerol sebacate) elastomers. *Biofabrication* 2016;8:045004. <https://doi.org/10.1088/1758-5090/8/4/045004>.
- [200] Yeh Y-C, Ouyang L, B. Highley C, A. Burdick J. Norbornene-modified poly(glycerol sebacate) as a photocurable and biodegradable elastomer. *Polym Chem* 2017;8:5091–9. <https://doi.org/10.1039/C7PY00323D>.
- [201] Savoji H, Davenport Huyer L, Mohammadi MH, Lun Lai BF, Rafatian N, Bannerman D, et al. 3D Printing of Vascular Tubes Using Bioelastomer Prepolymers by Freeform Reversible Embedding. *ACS Biomater Sci Eng* 2020;6:1333–43. <https://doi.org/10.1021/acsbiomaterials.9b00676>.
- [202] Wales DJ, Keshavarz M, Howe C, Yeatman E. 3D Printability Assessment of Poly(octamethylene maleate (anhydride) citrate) and Poly(ethylene glycol) Diacrylate Copolymers for Biomedical Applications. *ACS Appl Polym Mater* 2022;4:5457–70. <https://doi.org/10.1021/acsapm.2c00531>.
- [203] Nilsson D. An all-organic sensor–transistor based on a novel electrochemical transducer concept printed electrochemical sensors on paper. *Sens Actuators B Chem* 2002;86:193–7. [https://doi.org/10.1016/S0925-4005\(02\)00170-3](https://doi.org/10.1016/S0925-4005(02)00170-3).
- [204] Tian W, Li Y, Zhou J, Wang T, Zhang R, Cao J, et al. Implantable and Biodegradable Micro-Supercapacitor Based on a Superassembled Three-Dimensional Network Zn@PPy Hybrid Electrode. *ACS Appl Mater Interfaces* 2021;13:8285–93. <https://doi.org/10.1021/acsami.0c19740>.
- [205] Piro B, Tran HV, Thu VT. Sensors Made of Natural Renewable Materials: Efficiency, Recyclability or Biodegradability—The Green Electronics. *Sensors* 2020;20:5898. <https://doi.org/10.3390/s20205898>.
- [206] Koutsioukis A, Belessi V, Georgakilas V. Solid phase functionalization of MWNTs: an eco-friendly approach for carbon-based conductive inks. *Green Chem* 2021;23:5442–8. <https://doi.org/10.1039/D1GC01043C>.
- [207] Williams NX, Bullard G, Brooke N, Therien MJ, Franklin AD. Printable and recyclable carbon electronics using crystalline nanocellulose dielectrics. *Nat Electron* 2021;4:261–8. <https://doi.org/10.1038/s41928-021-00574-0>.
- [208] Pan H, Misra N, Ko SH, Grigoropoulos CP, Miller N, Haller EE, et al. Melt-mediated coalescence of solution-deposited ZnO nanoparticles by excimer laser annealing for thin-film transistor fabrication. *Appl Phys Mater Sci Process* 2009;94:111–5. <https://doi.org/10.1007/s00339-008-4925-0>.
- [209] Omerovi N, Radovi M, Savi SM, Katona J. Preparation of TiO₂ and ZnO dispersions for inkjet printing of flexible sensing devices. *Process Appl Ceram* 2018;12:326–34.
- [210] Schneider J, Hoffmann RC, Soffke O, Jaegermann W, Issanin A, Klyszcz A. A Printed and Flexible Field-Effect Transistor Device with Nanoscale Zinc Oxide as Active Semiconductor Material. *Adv Mater* 2008;20:3383–7. <https://doi.org/10.1002/adma.200800819>.
- [211] Meyers ST, Anderson JT, Hung CM, Thompson J, Wager JF, Keszler DA. Aqueous Inorganic Inks for Low-Temperature Fabrication of ZnO TFTs. *J Am Chem Soc* 2008;130:17603–9. <https://doi.org/10.1021/ja808243k>.
- [212] Härting M, Zhang J, Gamota DR, Britton DT. Fully printed silicon field effect transistors. *Appl Phys Lett* 2009;94:193509. <https://doi.org/10.1063/1.3126958>.
- [213] Shimoda T, Matsuki Y, Furusawa M, Aoki T, Yudasaka I, Tanaka H, et al. Solution-processed silicon films and transistors. *Nature* 2006;440:783–6. <https://doi.org/10.1038/nature04613>.
- [214] Feng S, Tian Z, Wang J, Cao S, Kong D. Laser Sintering of Zn Microparticles and Its Application in Printable Biodegradable Electronics. *Adv Electron Mater* 2019;5:1800693. <https://doi.org/10.1002/aelm.201800693>.
- [215] Lee S, Koo J, Kang S-K, Park G, Lee YJ, Chen Y-Y, et al. Metal microparticle – Polymer composites as printable, bio/eco-resorbable conductive inks. *Mater Today* 2018;21:207–15. <https://doi.org/10.1016/j.mattod.2017.12.005>.
- [216] Mattana G, Briand D. Recent advances in printed sensors on foil. *Mater Today* 2016;19:88–99. <https://doi.org/10.1016/j.mattod.2015.08.001>.
- [217] Khan S, Nguyen TP, Lubej M, Thiery L, Vairac P, Briand D. Microelectronic Engineering Low-power printed micro-hotplates through aerosol jetting of gold on thin polyimide membranes. *Microelectron Eng* 2018;194:71–8. <https://doi.org/10.1016/j.mee.2018.03.013>.
- [218] Shou W, Mahajan BK, Ludwig B, Yu X, Staggs J, Huang X, et al. Low-Cost Manufacturing of Bioresorbable Conductors by Evaporation–Condensation-Mediated Laser Printing and Sintering of Zn Nanoparticles. *Adv Mater* 2017;29:1700172. <https://doi.org/10.1002/adma.201700172>.
- [219] Mahajan BK, Ludwig B, Shou W, Yu X, Fregene E, Xu H, et al. Aerosol printing and photonic sintering of bioresorbable zinc nanoparticle ink for transient electronics manufacturing. *Sci China Inf Sci* 2018;61:1–10. <https://doi.org/10.1007/s11432-018-9366-5>.
- [220] Yi N, Gao Y, Lo Verso A, Zhu J, Erdely D, Xue C, et al. Fabricating functional circuits on 3D freeform surfaces via intense pulsed light-induced zinc mass transfer. *Mater* 2021;50:24–34. <https://doi.org/10.1016/j.mattod.2021.07.002>.

-
- [221] Li J, Xu H, Zhang Z, Hao Y, Wang H, Huang X. Anhydride-Assisted Spontaneous Room Temperature Sintering of Printed Bioresorbable Electronics. *Adv Funct Mater* 2019;1905024. <https://doi.org/10.1002/adfm.201905024>.
- [222] Majee S, Karlsson MCF, Wojcik PJ, Sawatdee A, Mulla MY, Alvi N ul H, et al. Low temperature chemical sintering of inkjet-printed Zn nanoparticles for highly conductive flexible electronic components. *Npj Flex Electron* 2021;5:14. <https://doi.org/10.1038/s41528-021-00111-1>.
- [223] Kim K, Yoo J, Shim J, Ryu Y, Choi S, Lee J, et al. Biodegradable Molybdenum/Polybutylene Adipate Terephthalate Conductive Paste for Flexible and Stretchable Transient Electronics. *Adv Mater Technol* 2022;7:2001297. <https://doi.org/10.1002/admt.202001297>.
- [224] Li J, Luo S, Liu J, Xu H, Huang X. Processing Techniques for Bioresorbable Nanoparticles in Fabricating Flexible Conductive Interconnects. *Mater Basel Switz* 2018;11:1102. <https://doi.org/10.3390/ma11071102>.
- [225] Uva A, Lin A, Babi J, Tran H. Bioderived and degradable polymers for transient electronics. *J Chem Technol Biotechnol* 2022;97:801–9. <https://doi.org/10.1002/jctb.6790>.
- [226] Baumgartner M, Hartmann F, Drack M, Preninger D, Wirthl D, Gerstmayr R, et al. Resilient yet entirely degradable gelatin-based biogels for soft robots and electronics. *Nat Mater* 2020;19:1102–9. <https://doi.org/10.1038/s41563-020-0699-3>.
- [227] Zhao H, Xue Z, Wu X, Wei Z, Guo Q, Xu M, et al. Biodegradable germanium electronics for integrated biosensing of physiological signals. *Npj Flex Electron* 2022;6:63. <https://doi.org/10.1038/s41528-022-00196-2>.
- [228] Xiang H, Li Z, Liu H, Chen T, Zhou H, Huang W. Green flexible electronics based on starch. *Npj Flex Electron* 2022;6:15. <https://doi.org/10.1038/s41528-022-00147-x>.
- [229] Dong Y, Li J, Yang F, Wang Y, Zhang Z, Wang J, et al. Bioresorbable Primary Battery Anodes Built on Core–Double-Shell Zinc Microparticle Networks. *ACS Appl Mater Interfaces* 2021;13:14275–82. <https://doi.org/10.1021/acsami.1c00602>.
- [230] Sharma V, Koivikko A, Yiannacou K, Lahtonen K, Sariola V. Flexible biodegradable transparent heaters based on fractal-like leaf skeletons. *Npj Flex Electron* 2020;4:27. <https://doi.org/10.1038/s41528-020-00091-8>.
- [231] Kamyshny A, Magdassi S. Conductive Nanomaterials for Printed Electronics. *Small* 2014;10:3515–35. <https://doi.org/10.1002/smll.201303000>.
- [232] Mahajan BK, Yu X, Shou W, Pan H, Huang X. Mechanically Milled Irregular Zinc Nanoparticles for Printable Bioresorbable Electronics. *Small* 2017;13:1700065. <https://doi.org/10.1002/smll.201700065>.
- [233] Hong S, Liu C, Hao S, Fu W, Peng J, Wu B, et al. Antioxidant high-conductivity copper paste for low-cost flexible printed electronics. *Npj Flex Electron* 2022;6:17. <https://doi.org/10.1038/s41528-022-00151-1>.
- [234] Polino G, Abbel R, Shanmugam S, Bex GJP, Hendriks R, Brunetti F, et al. A benchmark study of commercially available copper nanoparticle inks for application in organic electronic devices. *Org Electron* 2016;34:130–8. <https://doi.org/10.1016/j.orgel.2016.04.021>.
- [235] Samsonov VM, Alymov MI, Talyzin IV, Vasilyev SA. Size dependence of the melting temperature and mechanisms of the coalescence/sintering on the nanoscale. *J Phys Conf Ser* 2019;1352:012044. <https://doi.org/10.1088/1742-6596/1352/1/012044>.
- [236] Perelaer J, Abbel R, Wünsch S, Jani R, van Lammeren T, Schubert US. Roll-to-Roll Compatible Sintering of Inkjet Printed Features by Photonic and Microwave Exposure: From Non-Conductive Ink to 40% Bulk Silver Conductivity in Less Than 15 Seconds. *Adv Mater* 2012;24:2620–5. <https://doi.org/10.1002/adma.201104417>.
- [237] Abdolmaleki H, Kidmose P, Agarwala S. Droplet-Based Techniques for Printing of Functional Inks for Flexible Physical Sensors. *Adv Mater* 2021;33:2006792. <https://doi.org/10.1002/adma.202006792>.
- [238] Gao L, Chao L, Hou M, Liang J, Chen Y, Yu H-D, et al. Flexible, transparent nanocellulose paper-based perovskite solar cells. *Npj Flex Electron* 2019;3:4. <https://doi.org/10.1038/s41528-019-0048-2>.
- [239] Borodko Y, Lee HS, Joo SH, Zhang Y, Somorjai G. Spectroscopic Study of the Thermal Degradation of PVP-Capped Rh and Pt Nanoparticles in H₂ and O₂ Environments. *J Phys Chem C* 2010;114:1117–26. <https://doi.org/10.1021/jp909008z>.
- [240] Agarwala S, Goh GL, Dinh Le T-S, An J, Peh ZK, Yeong WY, et al. Wearable Bandage-Based Strain Sensor for Home Healthcare: Combining 3D Aerosol Jet Printing and Laser Sintering. *ACS Sens* 2019;4:218–26. <https://doi.org/10.1021/acssensors.8b01293>.
- [241] Pietenpol WB, Miley HA. Electrical Resistivities and Temperature Coefficients of Lead, Tin, Zinc and Bismuth in the Solid and Liquid States. *Phys Rev* 1929;34:1588–600. <https://doi.org/10.1103/PhysRev.34.1588>.
- [242] Kreider KG, Ripple DC, Kimes WA. Thin-film resistance thermometers on silicon wafers. *Meas Sci Technol* 2009;20:045206. <https://doi.org/10.1088/0957-0233/20/4/045206>.

-
- [243] Yang R, Zhang W, Tiwari N, Yan H, Li T, Cheng H. Multimodal Sensors with Decoupled Sensing Mechanisms. *Adv Sci* 2022;9:2202470. <https://doi.org/10.1002/advs.202202470>.
- [244] Guo Z, Kyunglok Kim, Lanzara G, Salowitz N, Peumans P, Chang F-K. Micro-fabricated, expandable temperature sensor network for macro-scale deployment in composite structures. 2011 *Aerosp. Conf., Big Sky, USA: IEEE*; 2011, p. 1–6. <https://doi.org/10.1109/AERO.2011.5747597>.
- [245] Shin Y-K, Shin Y, Lee JW, Seo M-H. Micro-/Nano-Structured Biodegradable Pressure Sensors for Biomedical Applications. *Biosensors* 2022;12:952. <https://doi.org/10.3390/bios12110952>.
- [246] Boutry CM, Nguyen A, Lawal QO, Chortos A, Bao Z. Fully biodegradable pressure sensor, viscoelastic behavior of PGS dielectric elastomer upon degradation. 2015 *IEEE Sens., Busan: IEEE*; 2015, p. 1–4. <https://doi.org/10.1109/ICSENS.2015.7370669>.
- [247] Aung MM, Chang YS. Temperature management for the quality assurance of a perishable food supply chain. *Food Control* 2014;40:198–207. <https://doi.org/10.1016/j.foodcont.2013.11.016>.
- [248] Wu T, Redoute J-M, Yuce MR. A Wireless Implantable Sensor Design With Subcutaneous Energy Harvesting for Long-Term IoT Healthcare Applications. *IEEE Access* 2018;6:35801–8. <https://doi.org/10.1109/ACCESS.2018.2851940>.
- [249] Yin H, Cao Y, Marelli B, Zeng X, Mason AJ, Cao C. Soil Sensors and Plant Wearables for Smart and Precision Agriculture. *Adv Mater* 2021;33:2007764. <https://doi.org/10.1002/adma.202007764>.
- [250] Quintero AV, Molina-Lopez F, Smits ECP, Danesh E, van den Brand J, Persaud K, et al. Smart RFID label with a printed multisensor platform for environmental monitoring. *Flex Print Electron* 2016;1:025003. <https://doi.org/10.1088/2058-8585/1/2/025003>.
- [251] Arata HF, Löw P, Ishizuka K, Bergaud C, Kim B, Noji H, et al. Temperature distribution measurement on microfabricated thermodevice for single biomolecular observation using fluorescent dye. *Sens Actuators B Chem* 2006;117:339–45. <https://doi.org/10.1016/j.snb.2005.11.017>.
- [252] Chung G-S, Jeong J-M. Fabrication of micro heaters on polycrystalline 3C-SiC suspended membranes for gas sensors and their characteristics. *Microelectron Eng* 2010;87:2348–52. <https://doi.org/10.1016/j.mee.2010.04.005>.
- [253] Ali S, Hassan A, Bae J, Lee CH, Kim J. All-Printed Differential Temperature Sensor for the Compensation of Bending Effects. *Langmuir* 2016;32:11432–9. <https://doi.org/10.1021/acs.langmuir.6b02885>.
- [254] Shuaibu Hassan A, Juliet V, Joshua Amriith Raj C. MEMS Based Humidity Sensor with Integration of Temperature Sensor. *Mater Today Proc* 2018;5:10728–37. <https://doi.org/10.1016/j.matpr.2017.12.356>.
- [255] Tranca D-C, Rosner D, Tataroiu R, Stegaru SC, Surpateanu A, Peisic M. Precision and linearity of analog temperature sensors for industrial IoT devices. 2018 17th *RoEduNet Conf. Netw. Educ. Res. RoEduNet, Cluj-Napoca: IEEE*; 2018, p. 1–6. <https://doi.org/10.1109/ROEDUNET.2018.8514122>.
- [256] Miyakawa N, Legner W, Ziemann T, Telitschkin D, Fecht H-J, Friedberger A. MEMS-based micro-thruster with integrated platinum thin film resistance temperature detector (RTD), heater meander and thermal insulation for operation up to 1,000°C. *Microsyst Technol* 2012;18:1077–87. <https://doi.org/10.1007/s00542-012-1441-0>.
- [257] Gourikutty SBN, Choong D, Lim R, Damalerio MRNB, Oh J, Kim Y, et al. Temperature detection system for Renal Denervation Catheter application. 2020 *IEEE 22nd Electron. Packag. Technol. Conf. EPTC, Singapore, Singapore: IEEE*; 2020, p. 198–202. <https://doi.org/10.1109/EPTC50525.2020.9315073>.
- [258] Salowitz NP, Guo Z, Kim S-J, Li Y-H, Lanzara G, Chang F-K. Microfabricated Expandable Sensor Networks for Intelligent Sensing Materials. *IEEE Sens J* 2014;14:2138–44. <https://doi.org/10.1109/JSEN.2013.2297699>.
- [259] Falco A, Sackenheim PS, Romero FJ, Becherer M, Lugli P, Salmerón JF, et al. Fabrication of low cost and low impact RH and temperature sensors for the internet of environmental-friendly things. *Mater Sci Eng B* 2021;267:115081. <https://doi.org/10.1016/j.mseb.2021.115081>.
- [260] Bali C, Brandmaier A, Ganster A, Raab O, Zapf J, Hübler A. Fully Inkjet-Printed Flexible Temperature Sensors Based on Carbon and PEDOT:PSS1. *Mater Today Proc* 2016;3:739–45. <https://doi.org/10.1016/j.matpr.2016.02.005>.
- [261] Arman Kuzubasoglu B, Kursun Bahadır S. Flexible temperature sensors: A review. *Sens Actuators Phys* 2020;315:112282. <https://doi.org/10.1016/j.sna.2020.112282>.
- [262] Tobjörk D, Österbacka R. Paper Electronics. *Adv Mater* 2011;23:1935–61. <https://doi.org/10.1002/adma.201004692>.
- [263] Li W, Liu Q, Zhang Y, Li C, He Z, Choy WCH, et al. Biodegradable Materials and Green Processing for Green Electronics. *Adv Mater* 2020;32:2001591. <https://doi.org/10.1002/adma.202001591>.
- [264] Hwang H-J, Oh K-H, Kim H-S. All-photonic drying and sintering process via flash white light combined with deep-UV and near-infrared irradiation for highly conductive copper nano-ink. *Sci Rep* 2016;6:19696. <https://doi.org/10.1038/srep19696>.

-
- [265] Nwoko VO, Uhlig HH. Logarithmic Oxidation Kinetics of Zinc. *J Electrochem Soc* 1965;112:1181. <https://doi.org/10.1149/1.2423394>.
- [266] Chinelatto ASA, Chinelatto AL, Ojaimi CL, Ferreira JA, Pallone EM de JA. Effect of sintering curves on the microstructure of alumina–zirconia nanocomposites. *Ceram Int* 2014;40:14669–76. <https://doi.org/10.1016/j.ceramint.2014.06.055>.
- [267] Bogatyrev VM, Borisenko NV, Pokrovskii VA. Thermal Degradation of Polyvinylpyrrolidone on the Surface of Pyrogenic Silica 2001;74:6.
- [268] Belsler RB, Hicklin WH. Temperature Coefficients of Resistance of Metallic Films in the Temperature Range 25° to 600°C. *J Appl Phys* 1959;30:313–22. <https://doi.org/10.1063/1.1735158>.
- [269] Zhu KN, Ruan Q, Godfrey A. The kinetics of grain growth in near-micrometre grain size copper produced by spark plasma sintering. *IOP Conf Ser Mater Sci Eng* 2015;89:012060. <https://doi.org/10.1088/1757-899X/89/1/012060>.
- [270] Singh A. Grain-size dependence of temperature coefficient of resistance of polycrystalline metal films. *Proc IEEE* 1973;61:1653–4. <https://doi.org/10.1109/PROC.1973.9345>.
- [271] Dukarov SV, Petrushenko SI, Sukhov VN. Inner size effect of temperature coefficient of resistance in Cu, Ag, V and Mo films. *Vacuum* 2022;202:111148. <https://doi.org/10.1016/j.vacuum.2022.111148>.
- [272] Jang Y-R, Joo S-J, Chu J-H, Uhm H-J, Park J-W, Ryu C-H, et al. A Review on Intense Pulsed Light Sintering Technologies for Conductive Electrodes in Printed Electronics. *Int J Precis Eng Manuf-Green Technol* 2021;8:327–63. <https://doi.org/10.1007/s40684-020-00193-8>.
- [273] Hossain ME, Khan MI, Ketata C, Islam MR. Comparative Pathway Analysis of Paraffin and Beeswax for Industrial Applications. *J Charact Dev Nov Mater* n.d.:13.
- [274] Zhang Y, Bi J, Wang S, Cao Q, Li Y, Zhou J, et al. Functional food packaging for reducing residual liquid food: Thermo-resistant edible super-hydrophobic coating from coffee and beeswax. *J Colloid Interface Sci* 2019;533:742–9. <https://doi.org/10.1016/j.jcis.2018.09.011>.
- [275] Nasrin TAA, Rahman MA, Arfin MS, Islam MN, Ullah MA. Effect of novel coconut oil and beeswax edible coating on postharvest quality of lemon at ambient storage. *J Agric Food Res* 2020;2:100019. <https://doi.org/10.1016/j.jafr.2019.100019>.
- [276] Yilmaz F, Dagdemir E. The effects of beeswax coating on quality of Kashar cheese during ripening. *Int J Food Sci Technol* 2012;47:2582–9. <https://doi.org/10.1111/j.1365-2621.2012.03137.x>.
- [277] Jain S, Nehra M, Kumar R, Dilbaghi N, Hu TonyY, Kumar S, et al. Internet of medical things (IoMT)-integrated biosensors for point-of-care testing of infectious diseases. *Biosens Bioelectron* 2021;179:113074. <https://doi.org/10.1016/j.bios.2021.113074>.
- [278] Shrivastava S, Trung TQ, Lee N-E. Recent progress, challenges, and prospects of fully integrated mobile and wearable point-of-care testing systems for self-testing. *Chem Soc Rev* 2020;49:1812–66. <https://doi.org/10.1039/C9CS00319C>.
- [279] Kim J, Campbell AS, de Ávila BE-F, Wang J. Wearable biosensors for healthcare monitoring. *Nat Biotechnol* 2019;37:389–406. <https://doi.org/10.1038/s41587-019-0045-y>.
- [280] Song Y, Mukasa D, Zhang H, Gao W. Self-Powered Wearable Biosensors. *Acc Mater Res* 2021;2:184–97. <https://doi.org/10.1021/accountsr.1c00002>.
- [281] Rodrigues D, Barbosa AI, Rebelo R, Kwon IK, Reis RL, Correlo VM. Skin-Integrated Wearable Systems and Implantable Biosensors: A Comprehensive Review. *Biosensors* 2020;10:79. <https://doi.org/10.3390/bios1007079>.
- [282] Liao J, Si H, Zhang X, Lin S. Functional Sensing Interfaces of PEDOT:PSS Organic Electrochemical Transistors for Chemical and Biological Sensors: A Mini Review. *Sensors* 2019;19:218. <https://doi.org/10.3390/s19020218>.
- [283] Sophocleous M, Contat-Rodrigo L, Garcia-Breijo E, Georgiou J. Organic Electrochemical Transistors as an Emerging Platform for Bio-Sensing Applications: A Review. *IEEE Sens J* 2021;21:3977–4006. <https://doi.org/10.1109/JSEN.2020.3033283>.
- [284] Rivnay J, Inal S, Salleo A, Owens RM, Berggren M, Malliaras GG. Organic electrochemical transistors. *Nat Rev Mater* 2018;3:17086. <https://doi.org/10.1038/natrevmats.2017.86>.
- [285] Tang H, Kumar P, Zhang S, Yi Z, Crescenzo GD, Santato C, et al. Conducting Polymer Transistors Making Use of Activated Carbon Gate Electrodes. *ACS Appl Mater Interfaces* 2015;7:969–73. <https://doi.org/10.1021/am507708c>.
- [286] Scheiblin G, Coppard R, Owens RM, Mailley P, Malliaras GG. Referenceless pH Sensor using Organic Electrochemical Transistors. *Adv Mater Technol* 2017;2:1600141. <https://doi.org/10.1002/admt.201600141>.
- [287] Ghittorelli M, Lingstedt L, Romele P, Crăciun NI, Kovács-Vajna ZM, Blom PWM, et al. High-sensitivity ion detection at low voltages with current-driven organic electrochemical transistors. *Nat Commun* 2018;9:1441. <https://doi.org/10.1038/s41467-018-03932-3>.

-
- [288] Tang H, Yan F, Lin P, Xu J, Chan HLW. Highly Sensitive Glucose Biosensors Based on Organic Electrochemical Transistors Using Platinum Gate Electrodes Modified with Enzyme and Nanomaterials. *Adv Funct Mater* 2011;21:2264–72. <https://doi.org/10.1002/adfm.201002117>.
- [289] Tang H, Lin P, Chan HLW, Yan F. Highly sensitive dopamine biosensors based on organic electrochemical transistors. *Biosens Bioelectron* 2011;26:4559–63. <https://doi.org/10.1016/j.bios.2011.05.025>.
- [290] Mak CH, Liao C, Fu Y, Zhang M, Tang CY, Tsang YH, et al. Highly-sensitive epinephrine sensors based on organic electrochemical transistors with carbon nanomaterial modified gate electrodes. *J Mater Chem C* 2015;3:6532–8. <https://doi.org/10.1039/C5TC01100K>.
- [291] Friedlein JT, McLeod RR, Rivnay J. Device physics of organic electrochemical transistors. *Org Electron* 2018;63:398–414. <https://doi.org/10.1016/j.orgel.2018.09.010>.
- [292] Rashid RB, Ji X, Rivnay J. Organic electrochemical transistors in bioelectronic circuits. *Biosens Bioelectron* 2021;190:113461. <https://doi.org/10.1016/j.bios.2021.113461>.
- [293] Elahi H, Munir K, Eugeni M, Atek S, Gaudenzi P. Energy Harvesting towards Self-Powered IoT Devices. *Energies* 2020;13:5528. <https://doi.org/10.3390/en13215528>.
- [294] Lemaire E, Moser R, Borsa CJ, Briand D. Green paper-based piezoelectronics for sensors and actuators. *Sens Actuators Phys* 2016;244:285–91. <https://doi.org/10.1016/j.sna.2016.04.024>.
- [295] Macchia E, Romele P, Manoli K, Ghittorelli M, Magliulo M, Kovács-Vajna ZM, et al. Ultra-sensitive protein detection with organic electrochemical transistors printed on plastic substrates. *Flex Print Electron* 2018;3:034002. <https://doi.org/10.1088/2058-8585/aad0cb>.
- [296] Gualandi I, Tonelli D, Mariani F, Scavetta E, Marzocchi M, Fraboni B. Selective detection of dopamine with an all PEDOT:PSS Organic Electrochemical Transistor. *Sci Rep* 2016;6:35419. <https://doi.org/10.1038/srep35419>.
- [297] Galliani M, Diacci C, Berto M, Sensi M, Beni V, Berggren M, et al. Flexible Printed Organic Electrochemical Transistors for the Detection of Uric Acid in Artificial Wound Exudate. *Adv Mater Interfaces* 2020;7:2001218. <https://doi.org/10.1002/admi.202001218>.
- [298] Khan S, Ali S, Khan A, Wang B, Bermak A. Printing Sensors on Biocompatible Substrates for Selective Detection of Glucose. *IEEE Sens J* 2021;21:4167–75. <https://doi.org/10.1109/JSEN.2020.3032539>.
- [299] Bonacchini GE, Omenetto FG. Reconfigurable microwave metadevices based on organic electrochemical transistors. *Nat Electron* 2021;4:424–8. <https://doi.org/10.1038/s41928-021-00590-0>.
- [300] Gutierrez CA, Meng E. Low-cost carbon thick-film strain sensors for implantable applications. *J Micromechanics Microengineering* 2010;20:095028. <https://doi.org/10.1088/0960-1317/20/9/095028>.
- [301] Cho I-H, Kim DH, Park S. Electrochemical biosensors: perspective on functional nanomaterials for on-site analysis. *Biomater Res* 2020;24:6. <https://doi.org/10.1186/s40824-019-0181-y>.
- [302] Song JH, Park J, Kim SH, Kwak J. Vitamin C-Induced Enhanced Performance of PEDOT:PSS Thin Films for Eco-Friendly Transient Thermoelectrics. *ACS Appl Mater Interfaces* 2023;15:2852–60. <https://doi.org/10.1021/acsami.2c17263>.
- [303] Lee I, Kim GW, Yang M, Kim T-S. Simultaneously Enhancing the Cohesion and Electrical Conductivity of PEDOT:PSS Conductive Polymer Films using DMSO Additives. *ACS Appl Mater Interfaces* 2016;8:302–10. <https://doi.org/10.1021/acsami.5b08753>.
- [304] Lingstedt LV, Ghittorelli M, Lu H, Koutsouras DA, Marszalek T, Torricelli F, et al. Effect of DMSO Solvent Treatments on the Performance of PEDOT:PSS Based Organic Electrochemical Transistors. *Adv Electron Mater* 2019;1800804. <https://doi.org/10.1002/aelm.201800804>.
- [305] Sun Y, Zhang Y, Liang Q, Zhang Y, Chi H, Shi Y, et al. Solvent inkjet printing process for the fabrication of polymer solar cells. *RSC Adv* 2013;3:11925. <https://doi.org/10.1039/c3ra22659j>.
- [306] Karamanlioglu M, Robson GD. The influence of biotic and abiotic factors on the rate of degradation of poly(lactic) acid (PLA) coupons buried in compost and soil. *Polym Degrad Stab* 2013;98:2063–71. <https://doi.org/10.1016/j.polymdegradstab.2013.07.004>.
- [307] Koutsouras DA, Torricelli F, Gkoupidenis P, Blom PWM. Efficient Gating of Organic Electrochemical Transistors with In-Plane Gate Electrodes. *Adv Mater Technol* 2021;6:2100732. <https://doi.org/10.1002/admt.202100732>.
- [308] Han S, Polyravas AG, Wustoni S, Inal S, Malliaras GG. Integration of Organic Electrochemical Transistors with Implantable Probes. *Adv Mater Technol* 2021;6:2100763. <https://doi.org/10.1002/admt.202100763>.
- [309] Paudel PR, Kaphle V, Dahal D, Radha Krishnan RK, Lüssem B. Tuning the Transconductance of Organic Electrochemical Transistors. *Adv Funct Mater* 2021;31:2004939. <https://doi.org/10.1002/adfm.202004939>.
- [310] Tarabella G, Santato C, Yang SY, Iannotta S, Malliaras GG, Cicoira F. Effect of the gate electrode on the response of organic electrochemical transistors. *Appl Phys Lett* 2010;97:123304. <https://doi.org/10.1063/1.3491216>.

-
- [311] Cicoira F, Sessolo M, Yaghmazadeh O, DeFranco JA, Yang SY, Malliaras GG. Influence of Device Geometry on Sensor Characteristics of Planar Organic Electrochemical Transistors. *Adv Mater* 2010;22:1012–6. <https://doi.org/10.1002/adma.200902329>.
- [312] Gualandi I, Marzocchi M, Scavetta E, Calieni M, Bonfiglio A, Fraboni B. A simple all-PEDOT:PSS electrochemical transistor for ascorbic acid sensing. *J Mater Chem B* 2015;3:6753–62. <https://doi.org/10.1039/C5TB00916B>.
- [313] Ramuz M, Margita K, Hama A, Leleux P, Rivnay J, Bazin I, et al. Optimization of a Planar All-Polymer Transistor for Characterization of Barrier Tissue. *ChemPhysChem* 2015;16:1210–6. <https://doi.org/10.1002/cphc.201402878>.
- [314] Basiricò L, Cosseddu P, Scidà A, Fraboni B, Malliaras GG, Bonfiglio A. Electrical characteristics of ink-jet printed, all-polymer electrochemical transistors. *Org Electron* 2012;13:244–8. <https://doi.org/10.1016/j.orgel.2011.11.010>.
- [315] Bidinger SL, Han S, Malliaras GG, Hasan T. Highly stable PEDOT:PSS electrochemical transistors. *Appl Phys Lett* 2022;120:073302. <https://doi.org/10.1063/5.0079011>.
- [316] Mantione D, del Agua I, Schaafsma W, ElMahmoudy M, Uguz I, Sanchez-Sanchez A, et al. Low-Temperature Cross-Linking of PEDOT:PSS Films Using Divinylsulfone. *ACS Appl Mater Interfaces* 2017;9:18254–62. <https://doi.org/10.1021/acsami.7b02296>.
- [317] Kim S-M, Kim C-H, Kim Y, Kim N, Lee W-J, Lee E-H, et al. Influence of PEDOT:PSS crystallinity and composition on electrochemical transistor performance and long-term stability. *Nat Commun* 2018;9:3858. <https://doi.org/10.1038/s41467-018-06084-6>.
- [318] Pappa A-M, Curto VF, Braendlein M, Strakosas X, Donahue MJ, Fiocchi M, et al. Organic Transistor Arrays Integrated with Finger-Powered Microfluidics for Multianalyte Saliva Testing. *Adv Healthc Mater* 2016;5:2295–302. <https://doi.org/10.1002/adhm.201600494>.
- [319] Ma X, Chen H, Zhang P, Hartel MC, Cao X, Dilemiz SE, et al. OFET and OECT, Two Types of Organic Thin-Film Transistor Used in Glucose and DNA Biosensors: A Review. *IEEE Sens J* 2022;22:11405–14. <https://doi.org/10.1109/JSEN.2022.3170405>.
- [320] Giaretta JE, Duan H, Farajikhah S, Oveissi F, Dehghani F, Naficy S. A highly flexible, physically stable, and selective hydrogel-based hydrogen peroxide sensor. *Sens Actuators B Chem* 2022;371:132483. <https://doi.org/10.1016/j.snb.2022.132483>.
- [321] Fumeaux N, Briand D. Zinc hybrid sintering for printed transient sensors and wireless electronics. *Npj Flex Electron* 2023;7:14. <https://doi.org/10.1038/s41528-023-00249-0>.
- [322] Sharma BK, Khare N, Ahmad S. A ZnO/PEDOT:PSS based inorganic/organic heterojunction. *Solid State Commun* 2009;149:771–4. <https://doi.org/10.1016/j.ssc.2009.02.035>.
- [323] Khan MU, Hassan G, Raza MA, Bae J, Kobayashi NP. Schottky diode based resistive switching device based on ZnO/PEDOT:PSS heterojunction to reduce sneak current problem. *J Mater Sci Mater Electron* 2019;30:4607–17. <https://doi.org/10.1007/s10854-019-00753-y>.
- [324] Vomero M, Porto Cruz MF, Zucchini E, Ciarpella F, Delfino E, Carli S, et al. Conformable polyimide-based μ ECoGs: Bringing the electrodes closer to the signal source. *Biomaterials* 2020;255:120178. <https://doi.org/10.1016/j.biomaterials.2020.120178>.
- [325] Dubey A, Ray S. Cortical Electrocochlogram (ECoG) Is a Local Signal. *J Neurosci* 2019;39:4299–311. <https://doi.org/10.1523/JNEUROSCI.2917-18.2019>.
- [326] Minev IR, Musienko P, Hirsch A, Barraud Q, Wenger N, Moraud EM, et al. Electronic dura mater for long-term multimodal neural interfaces. *Science* 2015;347:159–63. <https://doi.org/10.1126/science.1260318>.
- [327] Wang P, Wu EG, Uluşan H, Phillips AJ, Hays MR, Kling A, et al. Direct-print three-dimensional electrodes for large-scale, high-density, and customizable neural interfaces 2023:2023.05.30.542925. <https://doi.org/10.1101/2023.05.30.542925>.
- [328] Zhou T, Yuk H, Hu F, Wu J, Tian F, Roh H, et al. 3D printable high-performance conducting polymer hydrogel for all-hydrogel bioelectronic interfaces. *Nat Mater* 2023;22:895–902. <https://doi.org/10.1038/s41563-023-01569-2>.
- [329] Wu Y-L, D'Amato AR, Yan AM, Wang RQ, Ding X, Wang Y. Three-Dimensional Printing of Poly(glycerol sebacate) Acrylate Scaffolds via Digital Light Processing. *ACS Appl Bio Mater* 2020;3:7575–88. <https://doi.org/10.1021/acsabm.0c00804>.
- [330] Song KH, Highley CB, Rouff A, Burdick JA. Complex 3D-Printed Microchannels within Cell-Degradable Hydrogels. *Adv Funct Mater* 2018;28:1801331. <https://doi.org/10.1002/adfm.201801331>.
- [331] Prasopthum A, Deng Z, M. Khan I, Yin Z, Guo B, Yang J. Three dimensional printed degradable and conductive polymer scaffolds promote chondrogenic differentiation of chondroprogenitor cells. *Biomater Sci* 2020;8:4287–98. <https://doi.org/10.1039/D0BM00621A>.

-
- [332] Gao F, Xu Z, Liang Q, Li H, Peng L, Wu M, et al. Osteochondral Regeneration with 3D-Printed Biodegradable High-Strength Supramolecular Polymer Reinforced-Gelatin Hydrogel Scaffolds. *Adv Sci* 2019;6:1900867. <https://doi.org/10.1002/advs.201900867>.
- [333] Sun W, Williamson AS, Sukhnandan R, Majidi C, Yao L, Feinberg AW, et al. Biodegradable, Sustainable Hydrogel Actuators with Shape and Stiffness Morphing Capabilities via Embedded 3D Printing. *Adv Funct Mater* 2023;2303659. <https://doi.org/10.1002/adfm.202303659>.
- [334] Wang W, Li Z, Xu H, Qiao L, Zhang X, Zhao Y, et al. Highly stretchable, shape memory and antioxidant ionic conductive degradable elastomers for strain sensing with high sensitivity and stability. *Mater Des* 2022;222:111041. <https://doi.org/10.1016/j.matdes.2022.111041>.
- [335] Huo R, Bao G, He Z, Li X, Ma Z, Yang Z, et al. Tough Transient Ionic Junctions Printed with Ionic Microgels. *Adv Funct Mater* 2023;33:2213677. <https://doi.org/10.1002/adfm.202213677>.
- [336] Park J, Lee S, Lee M, Kim H-S, Lee JY. Injectable Conductive Hydrogels with Tunable Degradability as Novel Implantable Bioelectrodes. *Small* 2023;19:2300250. <https://doi.org/10.1002/smll.202300250>.
- [337] Zhu C, Schorr NB, Qi Z, Wygant BR, Turney DE, Yadav GG, et al. Direct Ink Writing of 3D Zn Structures as High-Capacity Anodes for Rechargeable Alkaline Batteries. *Small Struct* 2023;4:2200323. <https://doi.org/10.1002/sstr.202200323>.
- [338] Brooks S, Cartwright Z, Merckle D, Weems AC. 4D Aliphatic photopolymer polycarbonates as direct ink writing of biodegradable, conductive graphite-composite materials. *Polym Compos* 2021;42:5134–43. <https://doi.org/10.1002/pc.26211>.
- [339] Li Y, Cook WD, Moorhoff C, Huang W-C, Chen Q-Z. Synthesis, characterization and properties of biocompatible poly(glycerol sebacate) pre-polymer and gel: Biocompatible poly(glycerol sebacate) pre-polymer and gel. *Polym Int* 2013;62:534–47. <https://doi.org/10.1002/pi.4419>.
- [340] Moučka R, Sedláčik M, Osička J, Pata V. Mechanical properties of bulk Sylgard 184 and its extension with silicone oil. *Sci Rep* 2021;11:19090. <https://doi.org/10.1038/s41598-021-98694-2>.
- [341] Turner BL, Twiddy J, Wilkins MD, Ramesh S, Kilgour KM, Domingos E, et al. Biodegradable elastomeric circuit boards from citric acid-based polyesters. *Npj Flex Electron* 2023;7:1–14. <https://doi.org/10.1038/s41528-023-00258-z>.
- [342] Zhou L, Gao Q, Fu J, Chen Q, Zhu J, Sun Y, et al. Multimaterial 3D Printing of Highly Stretchable Silicone Elastomers. *ACS Appl Mater Interfaces* 2019;11:23573–83. <https://doi.org/10.1021/acsami.9b04873>.
- [343] Ruther F, Roether JA, Boccaccini AR. 3D Printing of Mechanically Resistant Poly (Glycerol Sebacate) (PGS)-Zein Scaffolds for Potential Cardiac Tissue Engineering Applications. *Adv Eng Mater* 2022;24:2101768. <https://doi.org/10.1002/adem.202101768>.
- [344] Rijn P, Wang H, Böker A. Ultra-sound assisted formation of biodegradable double emulsion capsules from hen egg white. *Soft Matter* 2011;7:5274. <https://doi.org/10.1039/c1sm05093a>.
- [345] Lu D, Yan Y, Deng Y, Yang Q, Zhao J, Seo M, et al. Bioresorbable Wireless Sensors as Temporary Implants for In Vivo Measurements of Pressure. *Adv Funct Mater* 2020;30:2003754. <https://doi.org/10.1002/adfm.202003754>.
- [346] Zhou T. Analysis on the biomechanical characteristics of knee joint with meniscus injury. *Healthc Technol Lett* 2018;5. <https://doi.org/10.1049/htl.2018.5048>.
- [347] Wang H, Li Z, Liu Z, Fu J, Shan T, Yang X, et al. Flexible capacitive pressure sensors for wearable electronics. *J Mater Chem C* 2022;10:1594–605. <https://doi.org/10.1039/D1TC05304C>.
- [348] Feiner R, Dvir T. Tissue–electronics interfaces: from implantable devices to engineered tissues. *Nat Rev Mater* 2017;3:1–16. <https://doi.org/10.1038/natrevmats.2017.76>.
- [349] Chung T, Wang JQ, Wang J, Cao B, Li Y, Pang SW. Electrode modifications to lower electrode impedance and improve neural signal recording sensitivity. *J Neural Eng* 2015;12:056018. <https://doi.org/10.1088/1741-2560/12/5/056018>.
- [350] Boehler C, Carli S, Fadiga L, Stieglitz T, Asplund M. Tutorial: guidelines for standardized performance tests for electrodes intended for neural interfaces and bioelectronics. *Nat Protoc* 2020;15:3557–78. <https://doi.org/10.1038/s41596-020-0389-2>.
- [351] Vomero M, Castagnola E, Ciarpella F, Maggiolini E, Goshi N, Zucchini E, et al. Highly Stable Glassy Carbon Interfaces for Long-Term Neural Stimulation and Low-Noise Recording of Brain Activity. *Sci Rep* 2017;7:40332. <https://doi.org/10.1038/srep40332>.
- [352] Schiavone G, Kang X, Fallegger F, Gandar J, Courtine G, Lacour SP. Guidelines to Study and Develop Soft Electrode Systems for Neural Stimulation. *Neuron* 2020;108:238–58. <https://doi.org/10.1016/j.neuron.2020.10.010>.
- [353] Liu J, Ji H, Wang S, Li M. The low temperature exothermic sintering of formic acid treated Cu nanoparticles for conductive ink. *J Mater Sci Mater Electron* 2016;27:13280–7. <https://doi.org/10.1007/s10854-016-5476-3>.

-
- [354] Woo K, Kim Y, Lee B, Kim J, Moon J. Effect of Carboxylic Acid on Sintering of Inkjet-Printed Copper Nanoparticulate Films. *ACS Appl Mater Interfaces* 2011;3:2377–82. <https://doi.org/10.1021/am2002907>.
- [355] Larba R, Boukerche I, Alane N, Habbache N, Djerad S, Tifouti L. Citric acid as an alternative lixiviant for zinc oxide dissolution. *Hydrometallurgy* 2013;134–135:117–23. <https://doi.org/10.1016/j.hydromet.2013.02.002>.
- [356] Ruiz-Valdepeñas Montiel V, Sempionatto JR, Campuzano S, Pingarrón JM, Esteban Fernández de Ávila B, Wang J. Direct electrochemical biosensing in gastrointestinal fluids. *Anal Bioanal Chem* 2019;411:4597–604. <https://doi.org/10.1007/s00216-018-1528-2>.
- [357] Wang X, Xu S, Zhou S, Xu W, Leary M, Choong P, et al. Topological design and additive manufacturing of porous metals for bone scaffolds and orthopaedic implants: A review. *Biomaterials* 2016;83:127–41. <https://doi.org/10.1016/j.biomaterials.2016.01.012>.
- [358] Ghilan A, Chiriac AP, Nita LE, Rusu AG, Neamtu I, Chiriac VM. Trends in 3D Printing Processes for Biomedical Field: Opportunities and Challenges. *J Polym Environ* 2020;28:1345–67. <https://doi.org/10.1007/s10924-020-01722-x>.
- [359] Wang Z, Zhang Y, Bernard A. A constructive solid geometry-based generative design method for additive manufacturing. *Addit Manuf* 2021;41:101952. <https://doi.org/10.1016/j.addma.2021.101952>.
- [360] Schiavone G, Fallegger F, Kang X, Barra B, Vachicouras N, Roussinova E, et al. Soft, Implantable Bioelectronic Interfaces for Translational Research. *Adv Mater* 2020;32:1906512. <https://doi.org/10.1002/adma.201906512>.

Curriculum Vitae

DATE OF BIRTH 22nd April 1992
PHONE NUMBER 079 424 99 50
MAIL nicolas.fumeaux@bluewin.ch
NATIONALITY Swiss

EDUCATION

04/2019 – present **EPFL, Lausanne**
PhD in Microengineering

02/2017 – 03/2018 **Harvard Medical School, Boston**
Master's thesis

09/2015 – 02/2017 **EPFL, Lausanne**
Bioengineering Master, Minor in Neuroprosthetics

02/2014 – 07/2014 **EPFL, Lausanne**
Mechanical Engineering Bachelor,
6th semester (Swiss Mobility)

09/2011 – 02/2014 **ETH, Zürich**
Mechanical Engineering Bachelor,
Semester 1-5

LANGUAGES

French Mother tongue
German Fluent
English Fluent
Italian Intermediate

WORK EXPERIENCE

04/2019 – present **PhD Researcher, EPFL, Neuchâtel**
- Additive manufacturing of bioresorbable implantable electronics
- Scientific papers writing, conferences presentations, supervision of several student projects, teaching

06/2018 – 02/2019 **Intern in the Biosignal team at Mindmaze, Lausanne**
- Preparation of clinical study, EEG experiments: recordings, analysis of movement correlates, machine learning

02/2017 – 03/2018 **Graduate Student Researcher at MGH, Boston**

-
- Detection and prediction from EEG in a rat model of epilepsy, fabrication of light delivery device for in vivo applications
 - 09/2017 – 12-2017 **Lab Immersion in the LNE, EPFL**
 - Simulation (in COMSOL), microfabrication and testing of electrodes for retinal electroporation
 - 01/2016 – 12/2016 **Internship in G-Therapeutics, Lausanne**
 - Implementation of a sensor fusion algorithm for further use in a robotic rehabilitation device
 - Programming GUI and control of a robotic platform for neuroprosthetics development in mice and rats
 - 08/2014 – 01/2016 **Internship and work in Courtine-Lab (G-Lab), EPFL**
 - Development of a rehabilitation environment for patients at CHUV (control of robotic interface, sensor integration in VR scenarios in Unity)
 - 09/2013 – 02/2014 **Teaching assistant (Structural mechanics), ETH Zürich**
 - Weekly exercise sessions and intermediary quizzes correction

AWARDS AND GRANTS

- 06/2022 **Innosuisse Business Concept Lausanne**, best startup and La Forge prize
- 09/2021 **Cleveland NeuroDesign**, selected for an entrepreneurial seminar based on the BioDesign methodology
- 10/2017 **Prize for the best average** during the Master of Bioengineering
- 02/2016 **Bertarelli Fellowship in Translational Neuroscience and Neuroengineering**
- 09/2015 **Outstanding ETHZ Bachelor Award**
- 06/2011 **Physics and applied mathematics prize**
 (Lycée-Collège des Creusets)

PUBLICATIONS

- Fumeaux, N., Almeida, C. P., Demuru, S., & Briand, D. (2023). Organic electrochemical transistors printed from degradable materials as disposable biochemical sensors. *Scientific Reports*, 13(1).
- Fumeaux, N., Kossairi, M., Bourely, J., & Briand, D. (2023). Printed ecoresorbable temperature sensors for environmental monitoring. *Micro and Nano Engineering*, 20, 100218.
- Fumeaux, N., & Briand, D. (2023). Zinc hybrid sintering for printed transient sensors and wireless electronics. *Npj Flexible Electronics*, 7(1), 14.
- Fumeaux, N., Ebrahim, S., Coughlin, B. F., Kadambi, A., Azmi, A., Xu, J. X., ... & Cash, S. S. (2020). Accurate detection of spontaneous seizures using a generalized linear model with external validation. *Epilepsia*, 61(9), 1906-1918.

Mignardot, J.B., Le Goff, C.G., Van Den Brand, R., Capogrosso, M., Fumeaux, N., Vallery, H., Anil, S., Lanini, J., Fodor, I., Eberle, G. and Ijspeert, A., (2017). A multidirectional gravity-assist algorithm that enhances locomotor control in patients with stroke or spinal cord injury. *Science Translational Medicine*, 9(399), p.eaah3621.

Von Zitzewitz, J., Asboth, L., Fumeaux, N., Hasse, A., Baud, L., Vallery, H. and Courtine, G., (2016). A neuro-robotic platform for locomotor prosthetic development in rats and mice. *Journal of neural engineering*, 13(2), p.026007.

van den Brand, R., Mignardot, J. B., von Zitzewitz, J., Le Goff, C., Fumeaux, N., Wagner, F., ... & Courtine, G. (2015). Neuroprosthetic technologies to augment the impact of neurorehabilitation after spinal cord injury. *Annals of physical and rehabilitation medicine*, 58(4), 232-237.

CONFERENCES

Fumeaux, N., Di Stadio, D., Briand D., Additive manufacturing of transient metal for bioresorbable sensing implants. *Swiss Printed Electronics Day*, July 4 2023, Geneva (Switzerland). *Poster presentation

Bourelly, J., De Sousa, L., Fumeaux, N., Briand, D., Biodegradable materials as sensitive coatings for humidity sensing in S-band microwave frequencies. *Micro and Nano Engineering*, September 19-23 2022, Leuven (Belgium). *Oral presentation

Fumeaux, N., Kossairi, M., Bourelly, J., Briand, D., Sintering of fully degradable printed Zn resistors for temperature sensing applications. *Micro and Nano Engineering*, September 19-23 2022, Leuven (Belgium). *Oral presentation

Fumeaux, N., Briand D., Additive manufacturing for bioresorbable implantable electronics. *Spring Meeting of the European Materials Research Society*, May 23-25 2022, Honolulu (USA). *Oral presentation

Fumeaux, N., Demuru S., Briand D., Organic Electrochemical Sensing Transistors Fabricated on Soft Bioresorbable Substrates. *Spring/Fall Meeting of the European Materials Research Society*, November 27-December 4 2020, Virtual. *Oral presentation